

EXPLORING RADIO PULSARS WITH NEW TECHNOLOGIES

Dissertation

zur

Erlangung des Doktorgrades (*Dr. rer. nat.*)

der

Rheinischen Friedrich–Wilhelms–Universität, Bonn

vorgelegt von

Pablo TORNE TORRES

aus

Granada, Spain

Bonn, 08.09.2016

Angefertigt mit Genehmigung der Mathematisch-Naturwissenschaftlichen Fakultät
der Rheinischen Friedrich-Wilhelms-Universität Bonn

1. Referent: Prof. Dr. Michael Kramer
2. Referent: Prof. Dr. Frank Bertoldi
Tag der Promotion: 20.12.2016
Erscheinungsjahr: 2017

Diese Dissertation ist auf dem Hochschulschriftenserver der ULB Bonn unter
http://hss.ulb.uni-bonn.de/diss_online elektronisch publiziert

Abstract

by Pablo Torne

for the degree of

Doctor rerum naturalium

Pulsars are rapidly-rotating, highly-magnetized compact neutron stars. Their strong gravitational and magnetic fields, together with the stability of their rotations and the precision with which we can measure them using radio telescopes make pulsars unique laboratories for a wide variety of physical experiments. This thesis presents an investigation of the application of new receiver technologies and observing techniques at different radio wavelengths to the search for and study of pulsars.

Discovering new pulsars always expands our capabilities to do new science. In general, the most exciting pulsars are those in binary systems because of their potential in high-precision tests of General Relativity and other gravity theories, and for constraining the Equation-of-State of ultra-dense matter. I present a search for pulsars in the Galactic Centre, where the probabilities of finding pulsar binaries, including the long-sought pulsar-black hole system, are high. The data were taken with the Effelsberg 100-m radio telescope and used high radio frequencies between 4.85 and 18.95 GHz to partially overcome the strong scattering in the direction to the centre of the Galaxy. With approximately 50 per cent of the results reviewed, no new pulsars have been discovered. We carried out a study of the sensitivity limits of the survey, finding that our sensitivity to Galactic Centre pulsars is highly reduced by the contributions to the total system noise of the Galactic Centre background and the atmosphere. We conclude that the paucity of detections in this and perhaps also previous similar surveys is likely due to insufficient sensitivity, and not a lack of pulsars in the region.

In March 2013, a radio magnetar, one of the rarest types of pulsars, became suddenly visible from the Galactic Centre. I led two multifrequency observing campaigns on this source, SGR J1745–2900, in order to study its radio emission properties. Four different observatories were involved (including simultaneous observations): the Nançay 94-m equivalent, the Effelsberg 100-m, the IRAM 30-m, and the APEX 12-m radio telescopes, allowing us to cover a frequency range from 2.54 to 472 GHz. The observations at the short millimetre range made use of new broad-band instrumentation never before used for pulsar observations. These observations resulted in the detection of SGR J1745–2900 from 2.54 to 291 GHz, providing measurements of its variable flux density, its also-varying spectrum, and evidence for polarized millimetre emission. The detections above 144 GHz are the highest radio frequency detections of pulsed emission from neu-

tron stars to date, results that set new constraints on the still poorly-understood radio emission mechanism of pulsars.

Since the study of the properties of pulsar emission at very high radio frequencies is relevant for understanding the radio emission process, further observations of a sample of six normal pulsars between 87 and 154 GHz were carried out using the IRAM 30-m. The initial results of this ongoing project include the detections of PSR B0355+54 up to 138 GHz, together with flux density measurements. For the other five pulsars, no obvious detections were achieved. Above 87 GHz, our detections of PSR B0355+54 are the highest-frequency detections of emission from a normal pulsar in the radio band, showing that normal pulsars continue emitting in the short millimetre regime. We found no evidence of a flattening or turn-up in the spectrum, a feature that could provide information about the emission mechanism. The intensity of this pulsar apparently decreases at and above 87 GHz, but our results suffer from uncertainties in the calibration and the possible intrinsic intensity variability of the pulsar. Forthcoming precise calibration information about the instrument will allow us to revisit the data providing stronger conclusions on the the nature of PSR B0355+54's apparent varying intensity at the millimetre wavelengths.

In addition to the scientific exploitation of the these four telescopes, I investigated technical aspects of two next-generation radio receivers planned for the the Effelsberg 100-m: the new Ultra-Broad-Band receiver (UBB), and the future Phased Array Feed (PAF). The tests for the UBB included the investigation of its optimum focusing set-up and its frequency-dependent system noise. We found the optimum focus to be that which optimized the gain at the highest frequencies of its operating band. We have also shown that the sensitivity of the UBB was significantly lower when the receiver is installed at the telescope (by a factor ~ 3) in comparison to measurements taken in the laboratory. Our investigation points to strong Radio Frequency Interference (RFI) as the cause of this sensitivity deficit. I also designed and carried out the first scientific experiment with the UBB during its commissioning: a search for pulsars in detected gamma-ray sources with the *Fermi* Large Area Telescope (LAT) with no associated counterparts. No new radio pulsars were discovered in this survey, but the data analysis demonstrated that large parts of the observing frequency range (~ 50 – 80 per cent) were unusable due to persistent RFI. We also showed that the strong RFI in the local environment made the receiver enter often into saturation. For the PAF, our tests at Effelsberg on a sample element of the future Checkerboard PAF MkII array confirmed that the front-end should be able to operate at Effelsberg without a persistent saturation by RFI. Overall, the results confirm that these new receivers can be used in electromagnetically-polluted areas, but require careful designs of the electronics in order to strongly suppress those frequency ranges particularly polluted by man-made radio signals.

For my parents Mercedes and Pablo

Contents

1	Introduction	3
1.1	Pulsar basics	3
1.1.1	Discovery and initial theories	3
1.1.2	Formation	4
1.1.3	Basic model of pulsars	5
1.1.4	Properties of pulsars	7
1.1.4.1	Spin evolution, age, and magnetic field strength	7
1.1.4.2	Emission properties	8
1.1.5	The pulsar population	9
1.1.5.1	Normal pulsars	10
1.1.5.2	Recycled or millisecond pulsars	10
1.1.5.3	RRATs	10
1.1.5.4	Magnetars	12
1.2	Radiation mechanism	13
1.2.1	High-energy emission	14
1.2.2	Coherent radio emission	14
1.3	Propagation effects in the interstellar medium	17
1.3.1	Dispersion	17
1.3.2	Scattering	18
1.3.3	Scintillation	20
1.4	Highlights of pulsar science	22
1.5	Scope and structure of this thesis	25
2	Methods and techniques	27
2.1	Introduction	27
2.2	Instrumentation	27
2.3	Pulsar searching	29
2.3.1	RFI and data cleaning	30
2.3.2	Dedispersion	30
2.3.3	Barycentering	31
2.3.4	Periodicity search	33
2.3.4.1	Candidate Selection	33
2.3.4.2	Harmonic summing	34
2.3.4.3	Acceleration search	35
2.3.4.4	Candidate sifting	36
2.3.5	Folding and candidate optimization	36
2.3.6	Candidate evaluation methods	37
2.3.7	Searches for transient emission	37
2.3.8	Overview of a pulsar searching pipeline	39

2.4	Millimetre pulsar data reduction	39
2.4.1	Red noise and RFI removal	42
2.4.2	Flux density calibration of IRAM 30-m data	43
2.5	Use and commissioning of new receivers	49
2.6	Summary and future work	50
3	Searching for pulsar binaries in the Galactic Centre with the Effelsberg 100-m radio telescope	51
3.1	Introduction	52
3.2	Observations and data analysis	54
3.2.1	Observations	54
3.2.2	Data analysis	57
3.2.2.1	Pulsar searching pipeline	57
3.2.2.2	Analysis of the acceleration detection capabilities of the pipeline	59
3.2.2.3	Challenges of searching at high radio frequencies	64
3.2.2.4	Candidate examination	66
3.3	Results	66
3.4	Discussion	69
3.5	Summary	73
4	Simultaneous multifrequency radio observations of the Galactic Centre magnetar SGR J1745–2900	75
4.1	Introduction	76
4.2	Observations and data reduction	77
4.2.1	Nançay and Effelsberg	77
4.2.2	IRAM 30-m	77
4.2.3	APEX	78
4.3	Results	80
4.3.1	Detections and profiles	80
4.3.2	Flux density and spectral index	80
4.3.3	Single pulses	80
4.4	Summary and Discussion	84
5	Detection of the magnetar SGR J1745–2900 up to 291 GHz with evidence of polarized millimetre emission	87
5.1	Introduction	88
5.2	Observations and data analysis	89
5.3	Results and discussion	90
5.3.1	Detections, flux density and spectrum	90
5.3.2	Linear polarization	93
5.4	Summary	97

6	Pulsar observations at 3 and 2 mm	99
6.1	Introduction	100
6.2	Observations and data reduction	102
6.3	Results and discussion	104
6.4	Future work	109
7	New instrumentation for pulsar observations	111
7.1	Introduction	112
7.1.1	Telescope gain and sensitivity	112
7.1.2	Field-of-View: the problem of surveying with large single dishes	113
7.2	Phased Array Feeds	114
7.2.1	Introduction	114
7.2.2	The Effelsberg PAF project	116
7.2.2.1	Survey speed analysis	117
7.2.2.2	Challenges of the project	119
7.2.2.3	Tests of Checkerboard MkII LNA robustness against RFI	119
7.2.3	Summary	122
7.3	Ultra-Wide-Bandwidth receivers	123
7.3.1	Introduction	123
7.3.2	An Ultra-Broad-Band (UBB) receiver for Effelsberg	123
7.3.2.1	Commissioning of the UBB at Effelsberg	124
7.3.2.2	RFI and UBB sensitivity	125
7.3.2.3	Focusing optimization	128
7.3.3	Summary	129
7.4	Other instruments for pulsar observations	134
7.4.1	Effelsberg high frequency receivers	134
7.4.2	IRAM 30-m and the Large Millimetre Telescope	134
7.4.3	Atacama Large Millimetre/submillimeter Array	135
7.4.4	Square Kilometre Array	135
7.5	Conclusions	136
8	Summary and future work	139
8.1	Summary	139
8.2	Future Work	140
	Bibliography	145
	Acknowledgements	159
	Curriculum Vitae	165

List of Figures

1.1	Basic representation of a pulsar	6
1.2	$P - \dot{P}$ diagram of the known pulsar population	11
1.3	Sketch of the coherence breakdown effect on a pulsar spectrum	16
1.4	Multifrequency spectrum of the Crab pulsar	16
1.5	Sketch of the effects of an inhomogeneous ISM on pulsar radiation	19
2.1	Overview of a radio telescope system for pulsar observations.	28
2.2	Comparison of S/N versus error DM trial at 1.39, 4.85, and 87 GHz	32
2.3	Explanation of a pulsar candidate evaluation plot	38
2.4	Explanation of a single pulse search diagnostic plot	40
2.5	Block diagram of the pulsar searching process	41
2.6	Red noise subtraction by a running mean filter	43
2.7	Details in the Fourier space of IRAM 30-m data	44
2.8	Example profiles of SGR J1745–2900 before and after cleaning	45
2.9	S/T_A^* values for the IRAM 30-m	47
3.1	Maximum detectable pulsar spin frequency in the accelerated search	62
3.2	Pulsar signal recovery simulation under extreme accelerations	63
3.3	Example of candidate at a $DM \neq 0$ produced by RFI	65
3.4	SGR J1745-2900 harmonic candidate detected in the blind search	67
3.5	Single pulse diagnostic plot with single pulses from SGR J1745–2900	68
3.6	Survey luminosity limits extrapolated to 1.4 GHz	71
4.1	Profiles of SGR J1745–2900 between 2.54 and 225 GHz (July 2014)	81
4.2	Spectrum of SGR J1745–2900 (July 2014)	82
4.3	Single pulses from SGR J1745–2900 between 87 and 154 GHz	83
5.1	Profiles of SGR J1745–2900 between 2.54 and 291 GHz (March 2015)	92
5.2	Spectrum of SGR J1745–2900 (March 2015)	94
5.3	Polarisation evidence in SGR J1745–2900’s emission at mm-wavelengths	95
6.1	Profiles of PSR B0355+54 between 4.85 and 138 GHz	106
6.2	Spectrum of PSR B0355+54 from 80 MHz up to 154 GHz	108
7.1	Illustration comparing the sky illumination with different receivers	115
7.2	PAF single element installed at the Effelsberg 100-m	121
7.3	Schematic of the set-up for the Checkerboard PAF element RFI tests	122
7.4	RFI in a typical UBB observation in the range 835–898 MHz	126
7.5	Saturation evidence in the UBB bandpass	127
7.6	Optimum focusing set-up vs. frequency across the UBB bandwidth	129
7.7	Gain vs. frequency at different focusing points of the UBB (BB01-Lat)	130

- 7.8 Gain vs. frequency at different focusing points of the UBB (BB01-Lon) . 131
- 7.9 Gain vs. frequency at different focusing points of the UBB (BB02-Lat) . 132
- 7.10 Gain vs. frequency at different focusing points of the UBB (BB02-Lon) . 133

List of Tables

2.1	S/T_{A}^* values for the IRAM 30-m	46
2.2	Data extracted from one IRAM 30-m calibration scan using MIRA	48
3.1	Observations of the Galactic Centre survey with the Effelsberg 100-m	54
3.2	Summary of the Galactic Centre survey data and searching parameters	59
3.3	Survey flux density limits per frequency band and segmentation step	70
4.1	Observations and flux densities of SGR J1745–2900 (July 2014)	79
5.1	Observations of SGR J1745–2900 (March 2015)	96
5.2	Flux densities of SGR J1745–2900 (March 2015)	96
6.1	List of observed pulsars at short mm-wavelengths	103
6.2	Flux densities of PSR B0355+54 from 80 MHz to 154 GHz	107
7.1	Technical specifications of Effelsberg’s Checkerboard PAF MkII	117
7.2	Survey speed of different receivers for the Effelsberg 100-m	118
7.3	Challenges for the PAF project at Effelsberg	120

Nomenclature

Frequently Used Symbols

α	Inclination angle
β	Degradation factor (or impact angle)
B	Magnetic flux density
B_s	Magnetic flux density at the surface
c	Speed of light
δ	Pulse duty cycle
d	Distance
D	Diameter
e	Eccentricity (or electron charge or numerical constant)
E	Energy
G	Gravitational constant
i	Inclination
I	Moment of inertia
k	Wavenumber
k_B	Boltzmann's constant
λ	Wavelength
L	Luminosity
μ	Magnetic dipole moment
m	Modulation index (or mass)
M	Mass
ν	Frequency
n	Breaking index (or refractive index)
N	Numerical density
Ω	Angular frequency
P	Period
P_B	Orbital period
ρ	Density (or emission cone angular radius)
r_{em}	Emission height
R	Radius
S	Flux density
τ_c	Characteristic age
τ_s	Scattering time scale
θ	Bending angle
t	Time
T	Age of a pulsar (or temperature or time)
T_B	Brightness temperature
v	Velocity
W	Pulse width

Frequently Used Acronyms

ADC	Analogue to Digital Converter
APEX	Atacama Pathfinder EXperiment
AXP	Anomalous X-ray Pulsar
DFT	Discrete Fourier Transform
DM	Dispersion Measure
FFT	Fast Fourier Transform
IF	Intermediate Frequency
IRAM	Institut de Radioastronomie Millimétrique
ISM	Inter Stellar Medium
LNA	Low Noise Amplifier
LO	Local Oscillator
LOS	Line of Sight
MPIfR	Max Planck Institute for Radio Astronomy
MSP	Millisecond pulsar
PAF	Phased Array Feed
PFB	Polyphase Filter Bank
PSR	Pulsar
RF	Radio Frequency
RFI	Radio Frequency Interference
RFM	Radius-to-Frequency Mapping
RRAT	Rotation RAdio Transient
RVM	Rotation Vector Model
S/N	Signal-To-Noise ratio
SGR	Soft Gamma Repeater
SSB	Solar System Barycentre
UBB	Ultra-Broad-Band receiver
UWB	Ultra-Wideband-Bandwidth receiver

Introduction

1.1 Pulsar basics

1.1.1 Discovery and initial theories

The history of pulsars is one of those wonderful examples in science when a theoretical prediction is demonstrated correct years after it has been announced. It began when [Baade & Zwicky \(1934\)](#) proposed that a compact star consisting mainly of neutrons¹ could form in a supernova explosion. Indeed, pulsars are highly magnetized, rotating neutron stars formed in supernova explosions. However, they were not discovered until 33 years after the publication of Baade and Zwicky's theory, only then confirming the existence of neutron stars.

Pulsars were discovered in 1967 by Jocelyn Bell and her supervisor Antony Hewish. It was a serendipitous discovery while they were studying interplanetary scintillation by observing compact radio sources ([Hewish et al., 1964, 1966](#)). What initially appeared to be interference by terrestrial radio signals was soon identified as a celestial source, and turned out to arguably be one of the greatest discoveries in physics: the first *pulsar*, named CP1929 with a spin period $P = 1.337$ s ([Hewish et al., 1968](#)).

The name *pulsar* derives from the combination of the words *pulsating star*, alluding to the fact that these objects are most often detected as a train of pulses when observed, in contrast to a *steady* image or spectrum which is a more common view of astronomical objects.

The first theories to try to explain the new mysterious pulsating sources appeared already in the discovery paper by [Hewish et al. \(1968\)](#). Radial pulsations from white dwarfs or neutron stars were tentatively proposed as possible reasons for the observed radio pulses. Several other theories followed rapidly. In summary, the theories can be divided into three groups: those explaining the pulsations by means of radial pulsations ([Hewish et al., 1968](#); [Thorne & Ipser, 1968](#)), those explaining them by orbital motions in binary systems ([Saslaw et al., 1968](#); [Burbidge & Strittmatter, 1968](#)), or related to the rotation of an object ([Ostriker & Tassoul, 1968](#); [Gold, 1968](#)).

New observational data soon settled the question about the origin of the pulsations. By 1970, only three years after the discovery of the first pulsar, 40 had already been discovered. As the number of pulsars with different characteristics increased, some theories started to have difficulties to explain the phenomenon. The detection of the slow-down of pulsars (i.e. their spin periods increase) ([Richards & Comella, 1969](#); [Cole, 1969b,a](#)) ruled out the theories based on binary systems, because due to the emission

¹The neutron itself was discovered only two years before by [Chadwick \(1932\)](#).

of gravitational waves, the periodicity would be expected to decrease as the two bodies spiral in and shorten their orbital period (Pacini & Salpeter, 1968). The discovery of the Vela pulsar (Large et al., 1968) and the Crab pulsar (Staelin & Reifenstein, 1968; Comella et al., 1969), with periods of $P \simeq 89$ and 33 ms, respectively, ruled out the theories based on radial pulsations of white dwarfs because they could not explain such short periods. Finally, a rotating neutron star with a magnetic axis misaligned with respect to the rotation axis was the model that better explained the observed properties of the new pulsating radio sources (Gold, 1968), solving the mystery of the origin of the newly discovered pulsars.

1.1.2 Formation

Pulsars are neutron stars formed in cataclysmic core-collapse supernova explosions. This type of supernova occurs at the end of the life of massive stars ($M \gtrsim 9 M_{\odot}$, Heger et al., 2003) when, after undergoing a series of evolutionary stages in which the Hydrogen is converted into heavier elements through nuclear fusion processes, an iron (^{56}Fe)-rich core is formed. Having the largest binding energy of all elements, iron does not release energy when fused, and the star's radiative pressure from nuclear processes, that was balancing the enormous self-gravitational inward pull, starts decreasing. Electron degeneracy pressure² can support the dense iron core against the gravity inward pull, but only until the core reaches the Chandrasekhar mass ($M \simeq 1.4 M_{\odot}$). At this point, neither the radiative pressure nor the electron degeneracy pressure are enough to support the star's own gravitational inward pull. When this occurs, the gravity force violently compresses the star, and the core reaches energies high enough to trigger inverse β -decay processes between the protons and electrons, forming neutrons. The rapid compression increases the density drastically and the infalling matter rebounds on the core. This produces a shock wave that expels most of the mass of the dying star in what is one of the most extreme explosions known in the Universe. The highly-compressed ultra-dense core may survive the explosion.

If the mass of the ultra-dense core formed in the supernova is below the Tolman-Oppenheimer-Volkoff limit (Oppenheimer & Volkoff, 1939; Tolman, 1939), *neutron* degeneracy pressure halts further gravitational collapse and what is formed is a neutron-rich dense core (a neutron star). If the core of the dead star is above this limit, not even the neutron degeneracy pressure can sustain the enormous gravitational force, and the core collapses further and forms a *black hole*.

The state of matter in the interior of neutron stars is unknown. The density inside these stars reaches values above that of nuclear matter, not reproducible in laboratory experiments on Earth. Furthermore, the neutron star composition depends on the Equation-of-State (EoS), that relates the pressure and density inside the star, and the correct EoS for neutron stars is still unknown. Canonical values for a neutron star mass and radius are $1.4 M_{\odot}$ (approximately the Chandrasekhar mass) and ~ 10 km (Lattimer

²*Degeneracy pressure* arises directly from the quantum mechanic laws; more precisely, it is the Pauli exclusion principle that prevents identical fermions to occupy a same quantum state what translates into an incredible supporting pressure that can balance enormous gravitational inward pulls.

& Prakash, 2001), respectively. With an average density $\langle\rho\rangle = 6.6 \cdot 10^{17} \text{ kg m}^{-3}$, such small radii are only about three times the Schwarzschild radius, which shows how close neutron stars are to being black holes.

With further simple arguments, if we assume a progenitor star of $10 M_{\odot}$ and use the mass–radius relationship for massive stars $R/R_{\odot} = 1.33(M/M_{\odot})^{0.555}$ (Demircan & Kahraman, 1991), by conservation of the angular momentum and magnetic flux, the newly born star’s angular velocity would be increased roughly by 10^{12} , and its magnetic field strength by 10^{10} . Therefore, the neutron star that remains after the supernova will be very rapidly rotating and highly magnetized.

1.1.3 Basic model of pulsars

To interpret the basic configuration of a pulsar, we shall follow a simple model outlined initially by Pacini (1967) and Gold (1968) and extended by Goldreich & Julian (1969) based on the work by Deutsch (1955). In this model, a dipolar magnetic field co-rotates with the neutron star, inducing an electric field³. Assuming that the star is an excellent conductor, the distribution of charged particles inside it will reconfigure to counteract the induced electric field until a force-free state is reached. If there is a vacuum outside the neutron star, the particles on the surface will feel a large electric force (than can easily exceed gravity by orders of magnitude!). Such a force can strip charged particles from the star surface filling up the vacuum region outside the star. This effect will lead to a dense plasma surrounding the neutron star that will feel the same electromagnetic field that the star interior. The plasma will rigidly co-rotate with the star as if it were just a continuation of the star itself, forming the *pulsar magnetosphere*.

The co-rotation can only be sustained up to a distance where the speed reaches the speed of light. This maximum distance is called the *light cylinder radius* (see e.g. Lorimer & Kramer, 2005)

$$R_{\text{LC}} = \frac{c}{\Omega} = \frac{cP}{2\pi} \simeq 4.77 \cdot 10^4 \left(\frac{P}{s}\right) \text{ [km]}, \quad (1.1)$$

where $\Omega = 2\pi/P$ is the rotational angular frequency, and P is the pulsar spin period. The light cylinder divides a pulsar magnetosphere into two regions, one with closed magnetic field lines (those inside the light cylinder radius), and another one with open magnetic field lines (those crossing the light cylinder radius).

The open field lines define two regions on the neutron star surface (centred at the magnetic axis) known as the *polar caps*. They are of particular interest, because the charged particles stripped from these regions can be trapped by the open magnetic field lines, accelerated to relativistic velocities, and radiate in a beam of conical shape that sweeps across space as the star rotates. If this beam crosses the line of sight

³This model assumes a magnetic axis aligned with the rotation axis. This is not a realistic configuration for pulsars because in this case we would no detect pulsations. However, the case of an oblique rotator has been analysed in the literature showing that results are basically unaltered (Kapoor & Shukre, 1998).

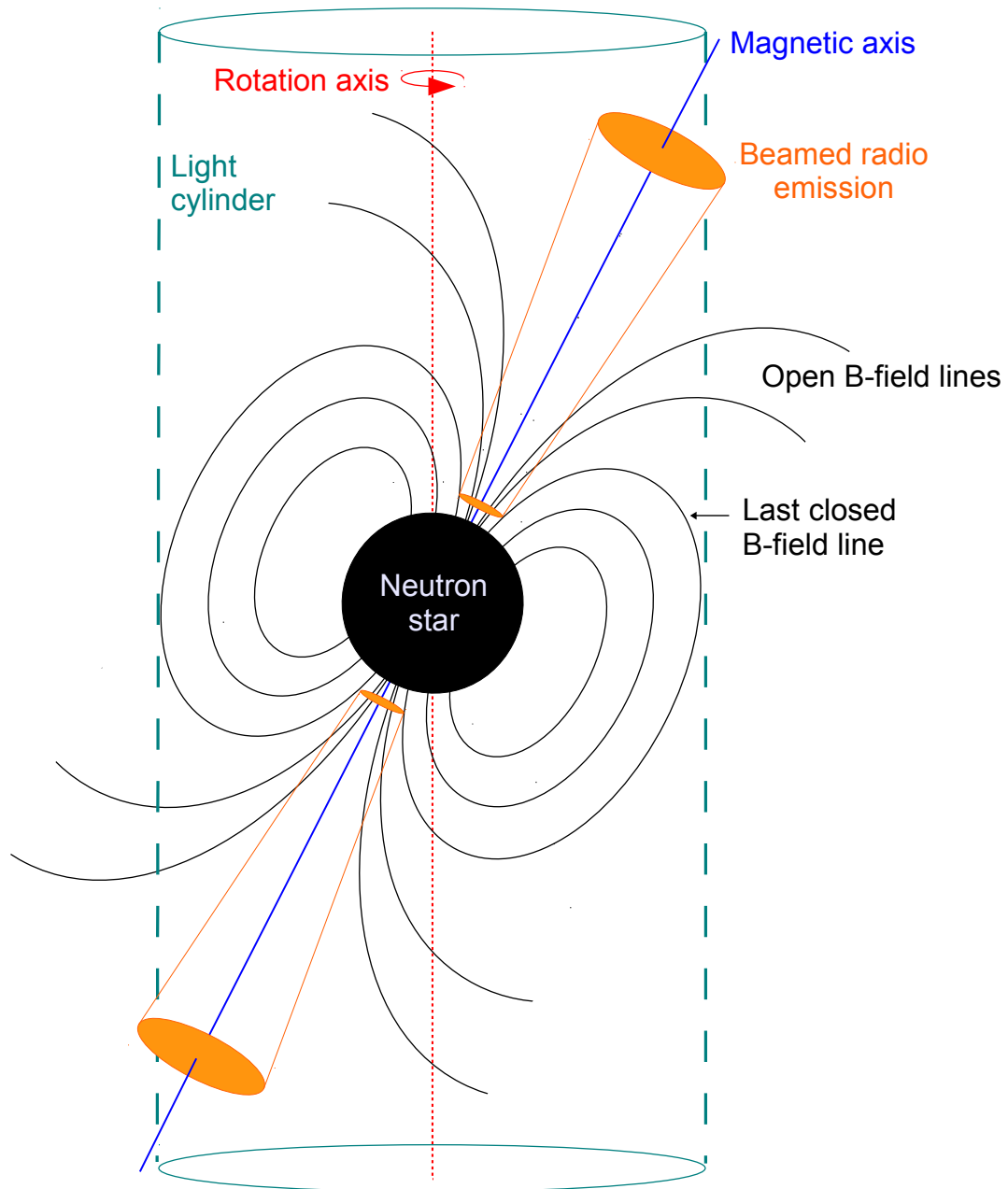


Figure 1.1: Basic representation of a pulsar. The radio emission is produced by charged particles accelerated above the polar regions. When the magnetic axis and the rotation axis are misaligned, a *lighthouse effect* is produced. If the beam crosses the line of sight to the Earth, we may observe pulses of radiation as the neutron star rotates. Figure adapted from Lorimer & Kramer (2005). Figure not to scale.

to the Earth, we may observe pulses of electromagnetic radiation as the star rotates. Figure 1.1 shows a representation of this basic pulsar model.

1.1.4 Properties of pulsars

Following our basic model of pulsars as rotating neutron stars with a dipolar magnetic field, we can infer several properties of these objects from a very small set of observables; mainly the spin period, P , and the ratio of change in spin period, $\dot{P} = dP/dt$. We will present here some of these relationships following the discussion of [Lorimer & Kramer \(2005\)](#).

1.1.4.1 Spin evolution, age, and magnetic field strength

Pulsars have very stable rotations, but their spin periods increase with time due to the loss of rotational kinetic energy. We can relate the increase of spin period, \dot{P} , with the ratio of loss of rotational kinetic energy, \dot{E} (also known as *spin-down luminosity*),

$$\dot{E} \equiv -\frac{dE_{\text{rot}}}{dt} = -\frac{(dI\Omega^2/2)}{dt} = -I\Omega\dot{\Omega} = 4\pi^2 I \dot{P} P^{-3}, \quad (1.2)$$

where E_{rot} is the rotational kinetic energy of the pulsar, and $I = kMR^2$ is the moment of inertia of the star, with a canonical value (assuming a sphere of uniform density⁴), of $I = 10^{38} \text{ kg m}^2$.

The loss of rotational kinetic energy is mostly due to dipole magnetic radiation, and the relation between spin period and spin period evolution can be expressed by equating the spin-down luminosity and the magnetic dipole emission. In a general form it can be expressed as a power law,

$$\dot{\Omega} = -\frac{2}{3c^3} \frac{\mu^2 \sin^2 \alpha}{I} \Omega^n, \quad (1.3)$$

where μ is the magnetic dipole moment, α is the inclination angle between the magnetic and rotation axes, and n is the braking index. The braking index for pure magnetic dipole radiation is $n = 3$, but in reality there can be other factors contributing to the spin-down of a pulsar, like for example the production of a particle wind. If μ , I and α are constant, the braking index can be calculated if both the first and second derivatives of the spin frequency of the pulsar, $\dot{\nu}$ and $\ddot{\nu}$, can be measured,

$$n = \nu \ddot{\nu} / \dot{\nu}^2. \quad (1.4)$$

Real measured values of the braking index for pulsars range between $0.9 < n < 2.9$ (see [Lyne et al., 2015](#), and references therein), with even a measurement above $n = 3$ recently reported by [Archibald et al. \(2016\)](#).

Assuming $n \neq 1$, we can use Equation 1.3 to obtain the age of a pulsar, T . Expressed in terms of the spin period instead of the rotational angular frequency,

⁴A neutron star probably does not have a uniform density, and k depends on the density profile. Anyway, for our simple modelling this assumption is enough, for which $k = 0.4$.

$$T = \frac{P}{(n-1)\dot{P}} \left[1 - \left(\frac{P_0}{P} \right)^{n-1} \right], \quad (1.5)$$

where P_0 is the pulsar spin period at birth. A common quantity estimated from Equation 1.5 is the *characteristic age* of a pulsar, τ_c . It is obtained assuming that the spin-down is only due to magnetic dipole radiation (i.e. $n = 3$), and that the spin period at birth is much smaller than the current value,

$$\tau_c \equiv \frac{P}{2\dot{P}}. \quad (1.6)$$

Although obtaining a direct measurement of the magnetic field strength is not possible, we can get an estimation if we assume that the rotational kinetic energy loss is purely from magnetic dipole radiation (see e.g. Jackson, 1962),

$$B_s = \sqrt{\frac{3c^3}{8\pi^2} \frac{I}{R^6 \sin^2 \alpha} P \dot{P}}, \quad (1.7)$$

where B_s is the magnetic field strength at the surface of the star, R is the radius of the star, and α is the angle between the rotation axis and the magnetic axis.

1.1.4.2 Emission properties

We can obtain some additional information about the magnetosphere and the emission by measuring other observables of the pulses. Although we lack of a complete theoretical model for the pulsar magnetosphere and the plasma processes responsible for the emission, there are a number of models (many of them phenomenological) that we can use to describe the observations (for a recent review, see Melrose & Yuen, 2016).

Despite the complication due to the dependency with the geometrical configuration of the magnetic axis with respect to the rotation axis, the width of the emission beam can be used to measure the diameter of the open field lines region,

$$\cos \rho = \cos \alpha \cos(\alpha + \beta) + \sin \alpha \sin(\alpha + \beta) \cos \left(\frac{W}{2} \right), \quad (1.8)$$

where ρ is the emission cone angular radius, α is the inclination angle of the magnetic axis to the rotation axis, β (called the impact angle or impact parameter) is the angle at the smallest distance between the observed cut through the beam and the magnetic axis, and W is the measured pulse width. Both α and β can be estimated from polarization measurements assuming the so-called Rotation-Vector-Model (RVM, Radhakrishnan & Cooke, 1969).

The pulse width of many pulsars decrease with observed frequency. To explain this effect, a model in which the high frequency emission is produced deeper in the pulsar magnetosphere (i.e. closer to the neutron star surface) than the lower frequencies was proposed, namely the *radius-to-frequency mapping* (RFM, Cordes, 1978). From the boundary of the polar cap that, at the same time, relates to the pulsar spin period through the light cylinder radius (see Equation 1.1), we can estimate the *emission*

height. A simplified expression from fitting observations leads to (Kijak & Gil, 1998, 2003),

$$r_{\text{em}}^{\text{KG}} = 400 \pm 80 \left(\frac{\nu}{\text{GHz}} \right)^{-0.26 \pm 0.09} \left(\frac{\dot{P}}{10^{-15}} \right)^{0.07 \pm 0.03} \left(\frac{P}{s} \right)^{0.30 \pm 0.05} \text{ [km]}, \quad (1.9)$$

where $r_{\text{em}}^{\text{KG}}$ is the height at which the emission leaves the magnetosphere⁵.

The energetics of a pulsar can also be estimated. Assuming that the intensity is constant in the emission cone and that the spectrum of the pulsar follows a power law, we can calculate the luminosity of the emission (see e.g. Lorimer & Kramer, 2005),

$$L = \frac{4\pi d^2}{\delta} \sin^2 \left(\frac{\rho}{2} \right) \int_{\nu_1}^{\nu_2} S_{\text{mean}}(\nu) d\nu, \quad (1.10)$$

where d is the distance to the pulsar, $\delta = W/P$ is the pulsar duty cycle, and $\int_{\nu_1}^{\nu_2} S_{\text{mean}}(\nu) d\nu$ is the integrated mean flux density in the frequency range of interest. A more commonly-used related quantity is the *pseudo-luminosity*, a simplification of the calculation of L that uses only the mean flux density at one given frequency and the distance,

$$L_\nu = S_\nu d^2. \quad (1.11)$$

Finally, the brightness temperature of the emission region, T_{B} , can be calculated relating the measured flux density to an equivalent *black body*. Using the Rayleigh-Jeans approximation and using the speed of light to estimate the maximum size of the emitting region that produces a pulse of duration Δt ,

$$T_{\text{B}} = \frac{S_{\text{peak}}}{2\pi k_{\text{B}}} \left(\frac{\nu \Delta t}{d} \right)^2, \quad (1.12)$$

where S_{peak} is the peak flux density measured for a given pulse and k_{B} is the Boltzmann constant.

Although the number of assumptions made to derive these relationships is somewhat significant, these expression gives us reasonable approximations to try to understand the basics of the properties of pulsars and their emission. Apart from being a starting point for our studies, these derived properties allow us to compare and categorize pulsars into different types or “families”.

1.1.5 The pulsar population

At the moment of writing, there are 2536 pulsars known (see the Australian Telescope National Facility (ATNF) pulsar catalogue⁶, Manchester et al., 2005). Pulsars can be categorized in many different ways, for example by their spin-down luminosity,

⁵It is not totally clear if the radiation leaves the magnetosphere at a different place from where it is produced (see e.g. Barnard & Arons, 1986; McKinnon, 1997).

⁶<http://www.atnf.csiro.au/people/pulsar/psrcat/>

magnetic field strength, or their age. As most of the pulsar properties can be inferred from the spin period and its derivative (see Section 1.1.4), a common representation of the pulsar population is a plot of P versus \dot{P} . These two quantities, furthermore, are evolving with the pulsar age and other processes, like binary interactions. Thus, the so-called “ $P - \dot{P}$ diagram” is like a Hertzsprung-Russell diagram for pulsars. Figure 1.2 shows a $P - \dot{P}$ diagram of the known pulsar population.

1.1.5.1 Normal pulsars

Normal pulsars make up the central bulk in the $P - \dot{P}$ diagram, with spin periods between 100 ms and a few seconds, and characteristic ages between ~ 1 kyr and ~ 1 Gyr. The youngest and most energetic pulsars tend to show, in addition to radio, gamma-ray emission, and are in many cases related to a supernova remnant.

As discussed in Section 1.1.4, pulsars slow down with time steadily consuming their spin-down luminosity, a process that make them move to the lower-right end in the $P - \dot{P}$ diagram. At a certain point, their spin-down luminosity is not enough to feed the radiative mechanism and pulsars fade out and stop emitting. The so-called *death line* marks approximately the region of the $P - \dot{P}$ diagram where this occurs. However, the death-line is model-dependent, and other factors in addition to the dipole magnetic emission may be relevant to the emissivity, like for instance the configuration of the magnetic field of the pulsar. For this reason, it is more precise to consider a region or *death valley* rather than a single death-line (Chen & Ruderman, 1993).

1.1.5.2 Recycled or millisecond pulsars

Pulsars in binary systems can interact with their companion stars. If the companion star expands during its evolution and the pulsar accretes matter, angular momentum is also transferred to the pulsar, spinning it up (Alpar et al., 1982; Bhattacharya & van den Heuvel, 1991). This process is called *recycling* and can bring back to life very old pulsars that had already crossed the death line and stopped emitting. Such “recycled pulsars” can reach very short spin periods of the order of one millisecond. Hence, these recycled fast-spinning pulsars are referred to as *millisecond pulsars* (MSPs). An important characteristics of MSPs is that they tend to show a lower magnetic field than that of the normal population. Consequently, their magnetic dipole emission is lower than for other pulsars, and their spin period can be extremely stable over very long periods of time. Such rotational stability makes MSPs some of the most precise clocks found in nature, and enable unique physics experiments to be performed with astonishing precision (see Section 1.4). The MSP family populate the lowest left corner of the $P - \dot{P}$ diagram.

1.1.5.3 RRATs

The so-called Rotating RAdio Sources (RRATs) are pulsars that show sporadic emission. They were discovered in 2006 (McLaughlin et al., 2006) reporting the detection

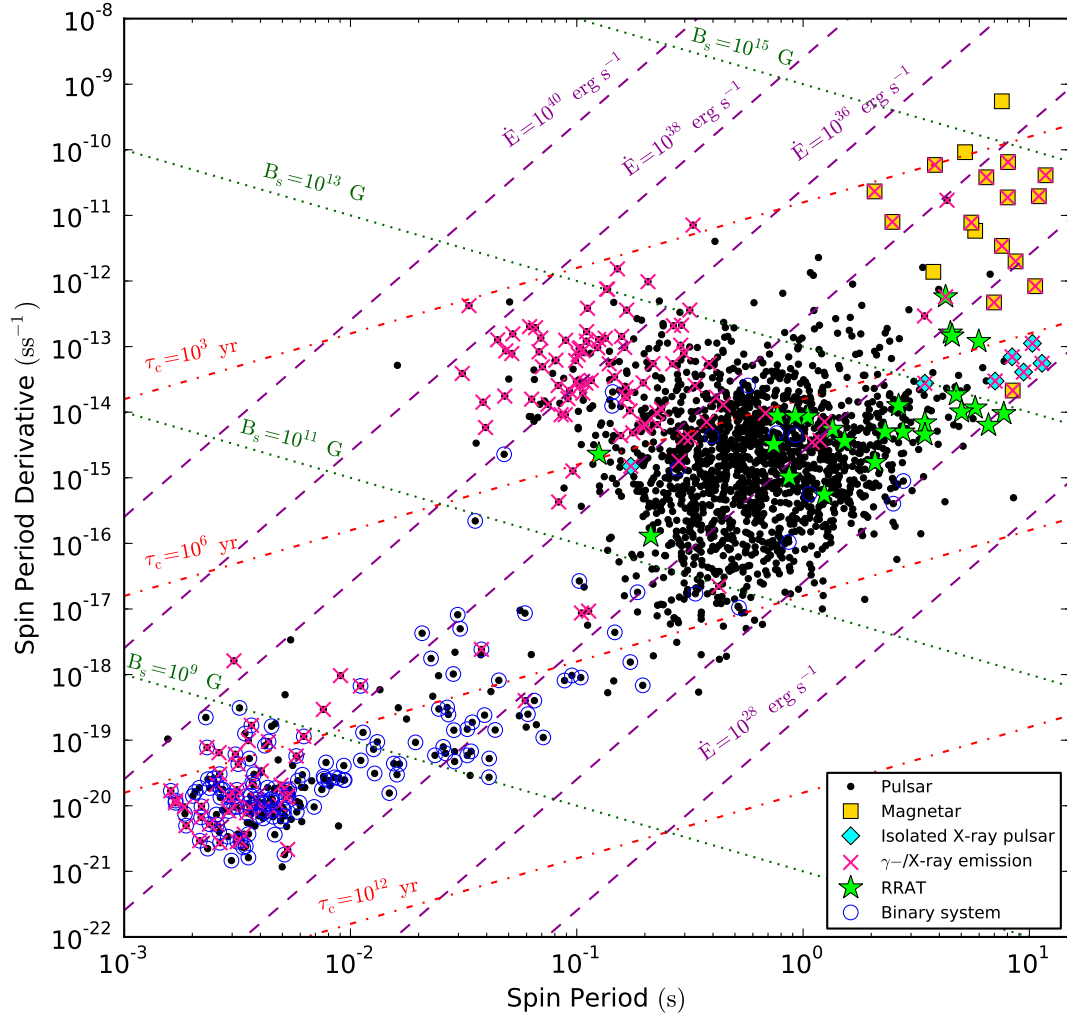


Figure 1.2: $P - \dot{P}$ diagram of the known pulsar population^a. Pulsars are represented by black dots. Soft-Gamma-Repeater (SGR) and Anomalous X-ray pulsars (AXP), also known as magnetars, are plotted as golden squares. Pulsars for which only pulsed thermal X-ray emission is observed are cyan diamonds. Rotating Radio Transient (RRATs) are represented by green stars. A pink cross over a pulsar indicates that high energy (γ - or X-ray) emission is observed. Those pulsars with companions, i.e.: in binary systems^b, are marked with a blue circle.

^aData from the Australian Telescope National Facility (ATNF) pulsar catalogue, (Manchester et al., 2005). Available at <http://www.atnf.csiro.au/people/pulsar/psrcat/>.

^bThere are two triple systems known, PSR B1620-26 (Sigurdsson et al., 2003) and PSR J0337+1715 (Ransom et al., 2014), that for simplicity are included here into the “binary systems” family.

of 11 of these objects and, currently, more than a hundred are known (see the RRATALOG⁷). RRATs are identified as radio pulsars because the characteristics of their radio pulses are highly consistent with rotating neutron stars (e.g. Keane et al., 2011), for example showing periodicities in the range 0.1–7.7 s. The fraction of time their emission in visible varies broadly from source to source, from less than one pulse to hundreds per hour. The nature of RRATs within the pulsar population is still unclear. It has been suggested that they could be just pulsars with large variability in the intensity of their emission, for which only the strongest pulses are detected from Earth (Weltevrede et al., 2006). Another possibility fitting with their variable emission is that RRATs are linked with magnetars (e.g. Lyne et al., 2009). This scenario is supported by the position of some RRATs in the $P - \dot{P}$, indicating high magnetic fields and in the region between the pulsar and magnetar populations. Additional evidence comes from the characteristics of the extended emission around PSR J1819-1458, suggesting a high magnetic source of energy (Rea et al., 2009). Both proposals are not exclusive and noting that RRATs also populate part of the bulk of normal pulsars in the $P - \dot{P}$, it could be possible that what we detect as RRATs are more than one population: highly variable pulsars far enough or highly magnetized neutron stars with intrinsic variable emission.

1.1.5.4 Magnetars

At the top right region of the $P - \dot{P}$ diagram we can identify another family of objects. They are isolated, and show long periods and rapid spin evolution, indicating low characteristic ages and high magnetic field strengths. These young, very magnetized pulsars are known as *magnetars*⁸, and show the strongest magnetic fields known in the universe (reaching $10^{14} - 10^{15}$ G).

Magnetars are short lived and their population is very small. Currently, only 23 of these objects are known (see the Magnetar Catalogue⁹, Olausen & Kaspi, 2014), and the population estimations predict no more than a few dozens of these objects in the Galaxy (Lyne & Graham-Smith, 2012).

There are different subcategories within the magnetar family (for a recent review, see Turolla et al., 2015). Some of these objects show stable X-ray pulsations with periods between 6–12 s and X-ray luminosities *higher* than the spin-down luminosity, and make up the subcategory of Anomalous X-ray Pulsars (AXPs). Other magnetars emit pulsations in soft gamma-rays typically following a large gamma-ray outburst, and are called Soft Gamma-ray Repeaters (SGRs). Although known to be neutron stars, these objects were not directly related to radio pulsars until Halpern et al. (2005) reported the detection of radio emission from the AXP XTE J1810–197; relation undoubtedly confirmed after the discovery of radio pulsations from this same source by Camilo et al. (2006).

As the number of known magnetars grew and their characteristics were studied in

⁷<http://astro.phys.wvu.edu/rratalog/rratalog.txt>

⁸From the combination of *magnetic star*.

⁹<http://www.physics.mcgill.ca/~pulsar/magnetar/main.html>.

more detail, the distinct separation in subcategories became blurred. A number of SGRs showed characteristics like those of AXPs (Kouveliotou et al., 1998, 1999) and vice versa (Gavriil et al., 2002), and a few objects had simultaneously radio pulsar and AXP behaviour (Camilo et al., 2006, 2008). Furthermore, some magnetars show low magnetic field strength (Rea et al., 2013c, 2014) more typical of radio pulsars; and some radio pulsars show strong magnetic fields closer to the magnetar ones (Ng & Kaspi, 2011). These discoveries suggest that normal pulsars and magnetars are connected and that, perhaps, their differences and similarities respond to different stages in the evolution of some neutron stars (e.g. Kaspi, 2010; Lyne et al., 2015).

There are important peculiarities of magnetars when compared to canonical pulsars. As already mentioned, they can show high-energy luminosities larger than their spin-down luminosity, therefore requiring of an additional energy source to power their radiation apart from rotational kinetic energy. The accepted model is that the additional energy source is the *decay of the magnetic field* (Duncan & Thompson, 1992; Thompson & Duncan, 1995).

Among the 23 magnetars known, only *four* have shown radio pulsations (Camilo et al., 2006, 2008; Levin et al., 2010; Eatough et al., 2013c). The family of radio emitting magnetars is therefore the rarest among the pulsar population. Interestingly, their radio emission characteristics show differences with that of the normal pulsar population. For instance, magnetars show a large variability in pulse profile shape, intensity, or polarization properties, both in long and short time scales, and their radio spectrum, in contrast to the steep spectrum of most pulsars, is roughly flat and can also vary significantly (see e.g. Chapters 4 and 5).

The fact that they show a flat spectrum make of magnetars unique sources to study pulsars at very high radio frequencies. In the radio band, above ~ 50 GHz only radio magnetars are bright enough to be detected and studied with current facilities (with the only exception of PSR B0355+54 that has been detected up to 138 GHz in this thesis, see Chapter 6). This particular characteristic motivated a considerable part of the work presented in this dissertation, focused on measuring the radio emission properties at a wide range of frequencies of the recently discovered Galactic Centre radio magnetar, SGR J1745–2900 (Mori et al., 2013; Kennea et al., 2013; Shannon & Johnston, 2013; Eatough et al., 2013c; Rea et al., 2013a). The results of that research are presented in detail in Chapters 4 and 5.

1.2 Radiation mechanism

There are many caveats about the exact mechanism (or mechanisms) responsible of the observed broadband emission from pulsars. It is not the aim of this this thesis to analyse the different proposed theories, but to offer *observational evidence* about the properties of pulsar and magnetar radio emission that any valid model has to be able to explain. However, for the sake of completeness I include a short overview on the topic and show with one example case how emission models can be tested with observations (for additional information about pulsar emission and proposed mechanisms, see e.g.

Michel, 1982; Lorimer & Kramer, 2005; Lyne et al., 2015; Melrose & Yuen, 2016; Eilek & Hankins, 2016).

1.2.1 High-energy emission

Pulsars are relatively cool objects. Although born with temperatures of $\sim 10^{12}$ K, the emission of large quantities of neutrinos cools down these stars rapidly to temperatures $\sim 10^6$ K. The thermal emission from pulsar surfaces peaks in the X-ray band and can be observed in many cases. However, pulsars have been detected across all the electromagnetic spectrum, from radio to γ -rays, and they must have an important component of non-thermal emission as well. The non-thermal component responsible of the high-energy emission is believed to be produced by synchrotron and curvature emission, with possibly also a component of inverse-Compton of photons emitted from the hot star surface (Lyne et al., 2015). Motivated in part by the usual phase misalignment between the pulses received in radio and high-energy, it is thought that the high-energy emission is produced in a different region than the radio emission, in the the so-called *outer gaps*, regions adjacent to the open magnetic fields lines extending to the light cylinder limits.

1.2.2 Coherent radio emission

The case of pulsar radio emission is more complex. Brightness temperatures of the radio pulses have typical values of $T_B \sim [10^{25} - 10^{26}]$ K, but values as high as $T_B \sim 10^{41}$ K have been observed (Hankins & Eilek, 2007). No incoherent process can produce such high T_B values, and some sort of coherent mechanism that can boost the radiation is required. *What is exactly this underlying coherent mechanism is still unknown.* Different possible mechanisms have been proposed during the almost five decades since the discovery of pulsars, with three main groups of models. One group relies on antenna mechanisms, in which the charged particles are emitting in groups inside volumes small enough to enable the radiation in-phase (Komesaroff, 1970; Sturrock, 1971; Ruderman & Sutherland, 1975; Cheng & Ruderman, 1977). A second group proposes relativistic plasma emission, in which some kind of plasma instability raises a turbulence in the plasma capable of producing radio emission (e. g Arons & Barnard, 1986; Asseo, 1993). The third group comprises maser mechanisms with processes capable of storing energy temporally (some kind of negative absorption) that is released coherently (Zhelezniakov & Shaposhnikov, 1979; Luo & Melrose, 1992; Melrose, 1978; Kazbegi et al., 1991). For a recent review of the proposed mechanisms of pulsar emission, see Melrose & Yuen (2016).

Bunched particles emission and possible coherence breakdown

One particular model of pulsar emission that can be tested in the context of this thesis is the coherent curvature emission of bunched particles. Despite some arguments against the plausibility of this model (Melrose, 1992; Lesch et al., 1998), it is still perhaps the most favoured by the observers (see e.g. Rankin, 1983, 1990; Mitra & Rankin, 2011).

In a nutshell, electric currents due to a large electric potential above the polar caps accelerate particles to very high velocities. These accelerated particles emit gamma-ray photons able to decay into pairs of electron-positrons. The process of particle acceleration, emission of gamma-ray photons, and decay into electron-positron pairs is repeated in what is called a “cascade” of creation of electric particles. Some of those particles would lead to groups (or “bunches”) being accelerated *close together*. The proximity of the particles is key because by moving closely together (roughly in a volume $\lesssim \lambda/2$), the emission of the individual particles adds in phase, amplifying the intensity of the emission of N individual particles up to by N^2 in an ideal case, producing the enhanced radio emission that we observe.

This “bunched particles” model makes a prediction about the behaviour of the intensity of the pulsar emission at very high frequencies, *that could be tested with observations at sufficiently high frequencies*. The model predicts that the efficiency of the coherence should decrease with increasing frequency (due mainly to the necessity of keeping particles densely packed in subsequently smaller volumes), which would lead to an intensity of pulsar emission that would decrease with frequency. This effect is sometimes referred as “coherence breakdown” (Michel, 1978, 1982). In addition to the coherent emission it is logical to consider the incoherent emission from the particles that are moving without the need of being in bunches. Considering the radiation mechanism as curvature emission, the incoherent component would show a spectrum shape very similar to that of synchrotron emission. The resulting spectrum of a pulsar emission is then a combination of both coherent and incoherent components and, if the model is correct, would lead to a region of the spectrum where the transition between the components produces a flattening or turn-up in the spectrum (see Figure 1.3).

A strong observational evidence supporting turn-ups in pulsar spectra comes from the shape of the Crab pulsar spectrum (see Figure 1.4). The intensity detected at infrared and optical wavelengths is orders of magnitude stronger than the decaying precedent radio emission. The gap between the maximum radio frequencies at which the Crab pulsar has been detected (≈ 43 GHz, Hankins et al., 2015) and the infrared wavelengths may hinder the breakdown region where the spectrum changes from a decreasing to an increasing flux, but this has not yet been observed. Moreover, Wielebinski et al. (1993) and Kramer et al. (1996, 1997a) have reported apparent flattening and turn-ups in some of the few pulsars observed at very high radio frequencies (up to ~ 40 GHz), although the results are not significant enough to indubitably confirm the effect.

Sampling the spectrum of pulsar emission at all possible wavelengths is a powerful method to infer the mechanisms behind the emission, especially when models predicts certain recognizable features or shapes. Nevertheless, the part of the radio spectrum between a few gigahertz and infrared wavelengths is highly under sampled, mainly due to the faintness of pulsars in that region. For this reason, and taking advantage of new higher-sensitivity receivers, this thesis work is partly focused on the acquisition and study of pulsar data in those under-explored parts of pulsar radio spectrum (see Chapters 4, 5 and 6), in order to test the bunched particles model, set new observational constraints to *any* emission model, and understand better the pulsar radiative

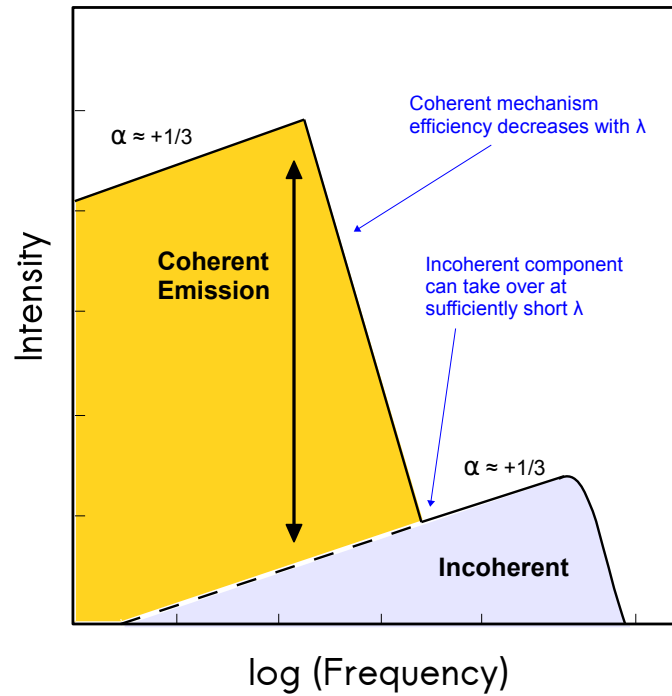


Figure 1.3: Illustration of the coherence breakdown effect in the spectrum of a pulsar as predicted by Michel (1978, 1982). An incoherent component of emission can become dominant at sufficiently high frequencies (estimated between radio and infrared wavelengths) and produce a recognizable flattening or turn-up of the intensity. Figure adapted from Michel (1982).

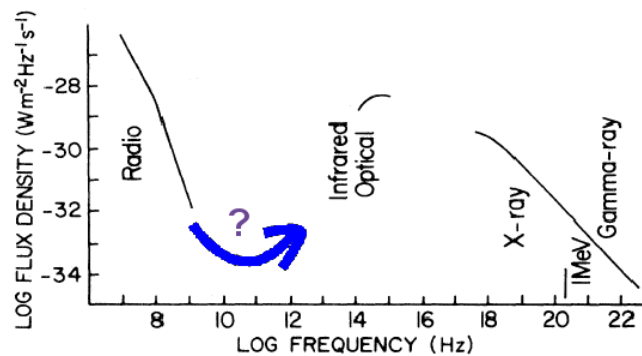


Figure 1.4: Spectrum of the Crab Pulsar across the electromagnetic spectrum. The intensity detected at infrared and optical wavelengths is of much higher magnitude than the decreasing precedent radio emission. The gap between the radio and infrared may hinder the breakdown region predicted by (Michel, 1978, 1982). Figure adapted from Smith (1977).

mechanism.

1.3 Propagation effects in the interstellar medium

The broadband electromagnetic radiation emitted by a pulsar travels through the interstellar medium (ISM) on its way to the Earth. The ISM is not empty; it is mostly a cold, ionised plasma, in many cases inhomogeneous and turbulent. The pulsar radiation interacts with the charged particles of the ISM as it propagates through it, in particular with the free electrons¹⁰. As a result, the signal gets dispersed, can be scattered and can suffer of intensity modulations. Furthermore, if the pulsar signal is polarized (as it is commonly the case), and there is a magnetic field along the line of sight, the polarization properties of the pulsar signal are also affected. While these propagation effects generally complicate the detection and study of pulsar signals, at the same time provide a means to obtain valuable information about the ISM. The next sections explain the basics of the relevant propagation effects for the work presented in this thesis: dispersion, scattering, and scintillation.

1.3.1 Dispersion

In vacuum, an electromagnetic (EM) wave of any frequency will travel at exactly the speed of light. This occurs because the refractive index of vacuum is one, and the velocity of the EM wave is

$$v_g = cn, \quad (1.13)$$

where v_g is its group velocity, c is the speed of light, and n is the refractive index of the medium where the EM travels. However, since the ISM is not empty its refractive index is not equal to 1. The refractive index of the ISM (as a cold, ionised plasma) depends on the so-called *plasma frequency* (see e.g. [Wilson et al., 2013](#)),

$$n = \sqrt{1 - \frac{\nu_p^2}{\nu^2}}, \quad (1.14)$$

where ν_p is the plasma frequency, and ν is the frequency of the EM wave. Combining equations 1.13 and 1.14,

$$v_g = c \sqrt{1 - \frac{\nu_p^2}{\nu^2}}. \quad (1.15)$$

The plasma frequency, ν_p , depends on the density of free electrons in the plasma (see e.g. [Lorimer & Kramer, 2005](#)),

$$\nu_p = \sqrt{\frac{N_e e^2}{\pi m_e}} \simeq 8.978 \left(\frac{N_e}{\text{cm}^{-3}} \right)^{0.5} \quad [\text{kHz}], \quad (1.16)$$

¹⁰The radiation also interacts with the ions, but we neglect here this effect because the ion's high mass with respect to the electrons ($m_{\text{ion}} \simeq 2000 m_e$) decrease their contribution by this same factor.

where N_e is the number of free electrons, and e and m_e are the electric charge and mass of the electron, respectively.

These simple relations show that the group velocity of an EM wave travelling in a medium will depend on the free electron content and the specific frequency of the EM wave. Since the pulsar radiation is broadband, Equation 1.15 implies that the different frequencies will propagate at different velocities through the ISM. As a result, the low frequencies arrive to the observer delayed in time with respect to the high frequencies. This frequency-dependent time delay is known as *dispersion*.

Expanding in series Equation 1.15 and using Equation 1.16, we can calculate the time delay between two frequencies,

$$\Delta t = \frac{e^2}{2\pi c m_e} \left[\frac{1}{\nu_1^2} - \frac{1}{\nu_2^2} \right] \int_0^L N_e(l) dl, \quad (1.17)$$

The first factor is a constant usually referred as the *dispersion constant*

$$\mathcal{D} \equiv \frac{e^2}{2\pi c m_e} \simeq 4.1488056 \cdot 10^3 \text{ MHz}^2 \text{ pc}^{-1} \text{ cm}^3 \text{ s}. \quad (1.18)$$

The integral of the number of free electrons along the line of sight is called *dispersion measure*, DM,

$$\text{DM} = \int_0^L N_e(l) dl. \quad (1.19)$$

From equations 1.17, 1.18, and 1.19 we can write

$$\Delta t \approx 4.15 \cdot 10^6 \left[\frac{1}{\nu_1^2} - \frac{1}{\nu_2^2} \right] \text{DM} \text{ [ms]}. \quad (1.20)$$

which corresponds to the time delay in ms between the frequencies ν_1 and ν_2 expressed in MHz.

One remark from this analysis is the fact that if we can measure the distance to a pulsar with precision (for example through astrometric measurements, precise timing, or spectroscopy), we can obtain the average electron density in the line of sight to that pulsar. Similarly, knowing the average electron content in the line of sight we can estimate the distance to a pulsar. Some of the most complete models of the electron content in the Milky Way are based on pulsar DM and distance measurements (Taylor & Cordes, 1993; Cordes & Lazio, 2002), and their precision can be continuously improved as new pulsars are discovered and more accurate measurements of DM values and distances become available.

1.3.2 Scattering

As was already mentioned, the ISM is not homogeneous. Differences in the electron densities between the observer and a pulsar, as well as relative motion between the observer, the pulsar, and the inhomogeneous ISM regions will cause distortions of the originally coherent EM wave front (see Figure 1.5). The multi-path propagation and

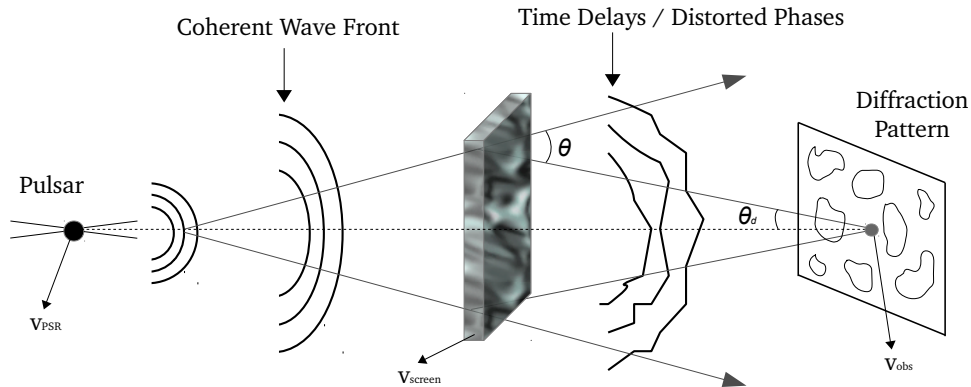


Figure 1.5: Sketch showing the effects of an inhomogeneous ISM (represented by a thin screen model) on pulsar radiation. The initially coherent wave front gets distorted as a result of multi-path propagation and differences in the refractive index of the medium (from variations of the electron density, see Equation 1.14 and 1.16). The differences in electron density can be inherent to the medium (e.g. if crossing an HII region or supernova shock front), to turbulence, or due to relative motion between the pulsar, the inhomogeneous medium, and the observer. The multi-path propagations translates into time delays of the radiation reaching the observer (scattering) and into phase differences that can lead to constructive or destructive interference (scintillation). Figure adapted from Lorimer & Kramer (2005).

differences in the refractive index of different paths result in different time delays of the signal arriving at the observer. Such effect produces *scattering* of the signal

To describe the effect, a simple model is usually adopted in which a thin “scattering screen”, representing the averaged effects of all the inhomogeneities in the line of sight, is placed middle way between the pulsar and the observer (Scheuer, 1968). The calculations depend on the turbulence spectrum of the ISM, typically assumed to be a Kolmogorov spectrum. Under these assumptions and using simple geometrical relations, the observer of a scattered point-like source will see a diffuse disk with angular radius (see e.g. Lorimer & Kramer, 2005)

$$\theta_d = \frac{\theta}{2}, \quad (1.21)$$

where θ is the bending angle of the wavefront at the scattering screen (see Figure 1.5), and an exponentially decaying angular intensity distribution,

$$I(\theta)d\theta \propto \exp(-\theta^2/\theta_d^2) 2\pi\theta d\theta. \quad (1.22)$$

Since the light rays observed after being bended an angle θ will arrive with a

geometrical time delay, $\Delta t(\theta) = \theta^2 d/c$, with respect to the rays taking the direct path travelling a distance d from the pulsar to the Earth, we can derive that the observed intensity as a function of time,

$$I(t) \propto \exp(-c\Delta t/\theta_d^2 d) \equiv \exp(-\Delta t/\tau_s) \quad (1.23)$$

where

$$\tau_s \equiv \theta_d^2 \frac{d}{c} \propto \Delta N_e^2 d^2 f^{-4} \quad (1.24)$$

is referred as the scattering time scale, i.e. a one-side exponential function that represents the distortion of the pulsed emission due to the scattering. This expression gives us important information about the scattering effect in pulsar emission. First, the temporal scattering of the emission is proportional to the square of the variations in electron density and the square of the distance to the pulsar. Secondly, the scattering decreases rapidly with frequency, as the fourth power. Consequently, a way to decrease the deleterious effects of scattering is to use high frequency observations. This is particularly useful where the scattering is expected to be strong like, for instance, when observing pulsars in the Galactic Centre (Cordes & Lazio, 1997, see Chapter 3).

1.3.3 Scintillation

The same geometrical time delays that causes scattering results in waves arriving at the observer plane with different phases, $\Delta\phi \sim 2\pi\tau_s$. The constructive and destructive interference pattern will produce a modulated variation of the detected intensity of the source. To produce interference, the phases of the waves must differ less than 1 radian. This means that there is a limiting bandwidth (also called *scintillation bandwidth* or *decorrelation bandwidth*) in which waves show the intensity variations. The condition for interference is (see e.g. Lorimer & Kramer, 2005),

$$2\pi\Delta\nu\tau_s \sim 1, \quad (1.25)$$

implying that $\Delta\nu \propto 1/\tau_s \propto \nu^4$.

The effects of scintillation can differ depending on the different scales of the electron density inhomogeneities in the ISM and the distance to the pulsar. Following this dependency, scintillation can be classified in *weak* and *strong* scintillation, and the strong scintillation is subcategorised in *diffractive* and *refractive*. The regime can be determined calculating the *field coherence scale*, s_0 , (i.e. the size of a circular region on the scattering screen centred at the source with phase differences less than 1 rad), and comparing it to the first Fresnel zone, l_F . Following Lorimer & Kramer (2005), (see also Cordes & Lazio, 1991)

$$s_0 = \frac{1}{k\theta_d}, \quad (1.26)$$

where $k = 2\pi/\lambda$ is the wavenumber, and

$$l_F = \sqrt{\frac{d}{k}}. \quad (1.27)$$

If $s_0 \gg l_F$ the distortions are caused only by small phase perturbations within the Fresnel zone, producing weak scintillation. Otherwise, the signal can suffer of larger phase perturbations, which lead to strong scintillation.

Using the velocity of the relative motion of the pulsar, V_{ISS} , we can estimate the observable effects of the scintillation on the intensity of the signal. Most pulsar observations occur in the strong regime (and this is also the case for the observations presented in this thesis), and we focus here on this case. Typically, the estimated quantity is the standard deviation, σ_S , of the mean flux density, which can be used to obtain the so-called *modulation index*

$$m = \frac{\sigma_S}{\langle S \rangle}. \quad (1.28)$$

The modulation index of strong diffractive scintillation depends on the number of scintles within the observation, both in time (N_t) and frequency (N_f),

$$m_{\text{DISS}} = \sqrt{\frac{1}{N_t N_f}}, \quad (1.29)$$

where

$$N_t \approx 1 + \kappa \frac{T_{\text{obs}}}{\Delta t_{\text{DISS}}}, \quad (1.30)$$

$$N_f \approx 1 + \kappa \frac{\Delta \nu}{\Delta \nu_{\text{DISS}}}, \quad (1.31)$$

$$\Delta t_{\text{DISS}} = \frac{s_0}{V_{\text{ISS}}}, \quad (1.32)$$

and

$$\Delta \nu_{\text{DISS}} \sim 11 \left(\frac{\nu}{\text{GHz}} \right)^{4.4} \left(\frac{d}{\text{kpc}} \right)^{-2.2} [\text{MHz}], \quad (1.33)$$

being T_{obs} the length of the observation, Δt_{DISS} the scintillation time scale, $\Delta \nu$ the observation bandwidth, $\Delta \nu_{\text{DISS}}$ is the scintillation bandwidth, and κ is a parameter empirically estimated in the range 0.1–0.2. Furthermore, if the refractive scale $l_R = l_F^2/s_0 \gg l_F$, strong refractive scintillation must also be taken into account. Strong refractive scintillation produces intensity modulations with an index

$$m_{\text{RISS}} = \left(\frac{l_F}{s_0} \right)^{-1/3}, \quad (1.34)$$

in longer time scales, of the order of

$$\Delta t_{\text{RISS}} = \frac{l_R}{V_{\text{ISS}}}. \quad (1.35)$$

1.4 Highlights of pulsar science

Pulsars, apart from being intrinsically fascinating objects, are excellent high-precision tools to carry out different astronomical and physics experiments. The key of the success of many pulsar-based experiments is the incredible stability of the rotations of neutron stars and the high accuracy that we can achieve measuring the arrival times of the pulses. After monitoring a pulsar regularly (usually covering a non-continuous time span of a year or more), we can build in most cases an exact model of the pulsar system, capable of keeping track of *every single* rotation of the pulsar. The technique by which a pulsar is monitored and a high-precision model is built is called *pulsar timing*, and it is at the heart of most of the applications of pulsars as physical tools (for a detailed description of the pulsar timing technique, see Lorimer & Kramer, 2005). Below we outline some of outstanding applications of pulsars to (astro)physics.

Plasma physics and ISM properties

The plasma properties and electrodynamics inside the pulsar magnetosphere are still poorly understood. However, they are an interesting topic of study because the regimes of gravity and magnetic field strength are very extreme there and not reproducible in laboratory experiments on Earth. Through the study of the pulse characteristics (brightness temperature, structure, polarization, arrival times, intensity modulation, etc.) it is possible to obtain information about the properties of the plasma and emission process responsible for the emission (e.g. Kramer et al., 1997b). In this thesis, the properties of the radio emission from a magnetar and a normal pulsar have been measured up to regimes of frequency never explored before (see Chapters 4, 5, 6), providing new constraints to pulsar emission models.

Additionally, by studying the propagation effects on the radio emission from pulsars we can measure the properties of the Galactic interstellar medium, like the electron density, its distribution, or the magnetic field component along the line of sight. Since pulsars are broadly distributed in the Galaxy, and we receive their emission from many different directions, this information can be used to build models of those quantities in the Milky Way (e.g. Noutsos et al., 2008; Cordes & Lazio, 2002).

Tests of gravity theories

Einstein's theory of General Relativity (GR) is at the moment the best description of gravity. The theory has been thoroughly verified in the weak-field regime with experiments in the Solar System (e.g. Will, 2001). In the *strong-field regime*, where deviations are more likely to occur if GR is not the absolute description of gravity, pulsars are excellent (and unique) tools to test GR and other gravity theories. For example, the discovery of the first binary pulsar (PSR B1913+16; Hulse & Taylor, 1975) allowed for *the first time* the measurement of a number of special- and relativistic effects in the orbit, including the decay in the orbital period consistent with the energy loss due to the emission of gravitational waves (Taylor & Weisberg, 1982). The tests of gravity theories continued as more binary pulsars were discovered. Currently, the observations

of the double pulsar provide the most stringent tests of GR in the strong-field regime (Kramer et al., 2006b). Alternative gravity theories, in particular those including a scalar-field contribution, are also strongly constrained by pulsar observations (Freire et al., 2012; Antoniadis et al., 2013). The ideal systems to further constrain gravity theories are pulsars orbiting black holes (Wex & Kopeikin, 1999; Liu et al., 2012, 2014; Psaltis et al., 2016), although unfortunately no such system has yet been detected. The discovery of a pulsar-black hole binary is one of the main drivers of the pulsar survey presented in Chapter 3.

Gravitational Waves

The emission of Gravitational Waves (GWs) is a prediction of GR that was indirectly¹¹ confirmed more than 30 years ago by long-term observations of the first binary pulsar system (Taylor & Weisberg, 1982). A next step was to achieve *direct detections* of GWs, something finally accomplished in 2015 using the Laser Interferometer Gravitational-Wave Observatory, or LIGO, (Abbott et al., 2016)¹².

Pulsars can also be used to *directly* detect GWs by using an array of them distributed in different locations of the sky, a configuration called a *Pulsar Timing Array* (PTA). The signal from GWs will distort the space-time between the pulsars and the Earth, producing a correlated modification of the arrival times of the pulses that can be measured with very high precision timing (e.g. Jenet et al., 2005). The gravitational frequency range where PTAs are sensitive is much lower than for ground-based experiments like LIGO, or even space-based interferometers like the Evolved Laser Interferometer Space Antenna (eLISA). This makes PTAs complementary tools to explore the gravitational universe, and the only means to detect stochastic gravitational wave background from supermassive black hole binary mergers (Sesana et al., 2008). Efforts are ongoing worldwide with three major projects analysing PTA data: the North American Nanohertz Observatory for Gravitational Waves (NanoGRAV, McLaughlin, 2013), the European Pulsar Timing Array (EPTA, Kramer & Champion, 2013), and the Parkes Pulsar Timing Array (PPTA, Hobbs, 2013). A global collaboration embracing those three projects and building the most complete and sensitive dataset works under the International Pulsar Timing Array (IPTA, Manchester, 2013). From the current status of the work, the estimations are that PTAs may start detecting GWs in the next few years (Jenet et al., 2005).

Stellar astrophysics

Pulsars are the remnants of the varied stellar and binary evolution in the Galaxy and they can be used to develop, test, and improve stellar evolution models. The history of many pulsar systems can be inferred from those models, although there are still pulsars that impose challenges to current evolutionary theories. A good example

¹¹We call it an indirect detection of GWs because what is observed is the decay of the orbital period due to GW emission, and not the GWs directly.

¹²Arguably one of the most important accomplishments of this century.

are isolated MSPs, MSPs in eccentric binaries (Champion et al., 2008), or the triple pulsar system (Ransom et al., 2014). Such systems have led to the development of new formation mechanisms for MSPs, like hierarchical triple-systems (Champion et al., 2008; Freire et al., 2011; Portegies Zwart et al., 2011), or rotationally-delayed collapse of fast-spinning white dwarfs (Freire & Tauris, 2014). Another example of the synergy between pulsar observations and stellar evolution theories was the discovery of the so-called transitional MSPs (or tMSPs). These kind of binary systems, in combination with previous indication given by the detection of millisecond pulsations in some low-mass X-ray binaries, have provided a strong evidence for the recycling theory of pulsars (Archibald et al., 2009; Papitto et al., 2013; Stappers et al., 2014).

Physics of ultra-dense matter

The physics of supra-nuclear matter are unknown. Neutron stars offers unique laboratories to study the composition and state of matter above the nuclear density, opening the possibility of deriving the correct Equation-of-State (EoS) for this case. The EoS can be constrained with precise measurements of neutron stars radii and masses. The measurements of a neutron star radius is possible but usually cannot achieve high precision due mainly to systematics in the measurements methods (e.g. Miller & Lamb, 2016). In contrast, the measurements of neutron star masses can achieve incredible precisions (e.g. Freire et al., 2011). In fact, some of the most stringent constraints on the EoS of cold, supra-nuclear matter are set by the two most massive neutron stars known, with masses of $\approx 2 M_{\odot}$ (Demorest et al., 2010; Antoniadis et al., 2013).

The pulsar population and distribution

The population studies of pulsars in the Galaxy need to extrapolate from the known population. Although at the moment of writing more than 2500 pulsars are known (see the ATNF catalogue, Manchester et al., 2005), the surveys leading to those discoveries have suffered from a number of bias due to sensitivity or hardware limitations, or radio frequency interference (e.g. Lorimer et al., 2015; Lazarus et al., 2015). Current all-sky surveys using state-of-the-art technologies (see e.g. Barr et al., 2013b; Keith et al., 2010) and new processing methods are more sensitive to all kind of pulsars, and will be able to discover many new systems with decreased biases. Reconstructing the underlying galactic pulsar population and distribution has many applications. For instance, it enables more precise predictions of the merger rate of binary neutrons stars, which is fundamental to understand the detection event rates of new gravitational wave detectors (e.g. Abbott et al., 2008). Furthermore, a better estimate of the pulsars in the Galaxy is a valuable input for optimally designing the observing strategies and data reduction techniques for new surveys, like those planned with new radio telescopes like MeerKAT or the Square Kilometre Array.

1.5 Scope and structure of this thesis

This thesis presents an investigation of the application of new receiver technologies and observing techniques at different radio wavelengths to the search for and study of pulsars.

In **Chapter 2** we examine the methods and techniques used through this thesis, including an overview of the systems to obtain pulsar data, the methodology for pulsar searching, the data analysis of the millimetre wavelength observations, and the methodology of technical work applied when commissioning new receivers.

In **Chapter 3** we present a new pulsar survey of the Galactic Centre carried out with the Effelsberg 100-m radio telescope, consisting of 110 pointings during a four-year time span, using four different observing frequencies and a specifically-designed pipeline capable of detecting pulsars in extreme binaries, e.g. orbiting black holes.

In **Chapter 4** the results of simultaneous multifrequency observations of the recently discovered magnetar in the Galactic Centre (SGR J1745–2900) are presented, which include the detection of the source and the measurement of its emission properties from 2.54 up to 225 GHz, being the study of pulsar radiation at the highest radio frequency to that date.

In **Chapter 5** we present the results of a second multifrequency observational campaign on SGR J1745–2900, made with excellent weather conditions, with detections up to 291 GHz, and evidencing the strong variability of the magnetar also at short millimetre wavelengths. Furthermore, we detect clear evidence of a high degree of linear polarization in the magnetar radio emission at frequencies up to 154 GHz.

In **Chapter 6** we present the results from a project to study the characteristics of normal pulsar radio emission up the highest radio frequencies to date, between 87 and 154 GHz. This includes the detection of PSR B0355+54 up to 138 GHz, together with flux density measurements; results that demonstrate that pulsars can continue to emit well within the short millimetre regime.

In **Chapter 7** we present the commissioning works related to the next generation of low-frequency radio receivers planned for the 100-m Effelsberg radio telescope, namely the Ultra-Broad-Band receiver (UBB) and the Phased Array Feed (PAF).

In **Chapter 8** we present a summary and our conclusions, and discuss future research plans.

Methods and techniques

2.1 Introduction

The scientific experiments carried out in this thesis work can be divided into *searching* for new pulsar systems, and *investigating* the properties of the radio emission of some pulsars of particular interest. The most remarkable differences and innovations in the methods used here are: the use of new instrumentation for the observations, some of it never applied to pulsar experiments before, that allowed the detections of pulsars and magnetars up to the highest radio frequencies to date (reaching 154 and 291 GHz, respectively, see Chapters 4, 5, and 6); the simultaneous observing campaigns involving up to three observatories (the 94-m equivalent Nançay radio telescope, the 100-m Effelsberg radio telescope, and the 30-m dish at Pico Veleta), enabling an instantaneous (non-continuous) frequency coverage of up to ~ 300 GHz; the use of a newly developed pulsar searching pipeline, with acceleration on Graphic Processor Units (GPUs) and sensitive to extreme pulsar binaries; and new data reduction methods, key to allow and optimize the detections of pulsars in the millimetre wavelength observations and to obtain their absolute flux density.

This chapter presents the relevant techniques and methodologies used throughout this thesis, and is organized as follows. Section 2.2 describes the instrumentation typically used to carry out pulsar observations. Sections 2.3 and 2.4 focus on the data analysis methods, in particular on pulsar searching algorithms and the reduction of pulsar data obtained at millimetre wavelengths, respectively. Finally, in section 2.5 we briefly describe the methodology of technical work done for the next generation of radio receivers planned for the Effelsberg 100-m. Section 2.6 summarizes and comments on future work.

2.2 Instrumentation

Pulsars are among the weakest astronomical sources in the radio band. In order to detect them in reasonable integration times we require of radio telescopes with very high sensitivities, meaning generally those with very large collecting areas. Furthermore, pulsars are steep spectrum sources and so, they are best observed at low frequencies (below ~ 3 GHz) where they are brighter. For these reasons, the most suited instruments for pulsar observations are typically large single dishes like the Effelsberg 100-m, the Lovell 76-m, the Parkes 64-m, the Arecibo 305-m, or the 100-m Robert C. Byrd Green Bank Telescope. Apart from the large collecting areas, the advances in electronic technologies are allowing the construction of new receivers with very low system

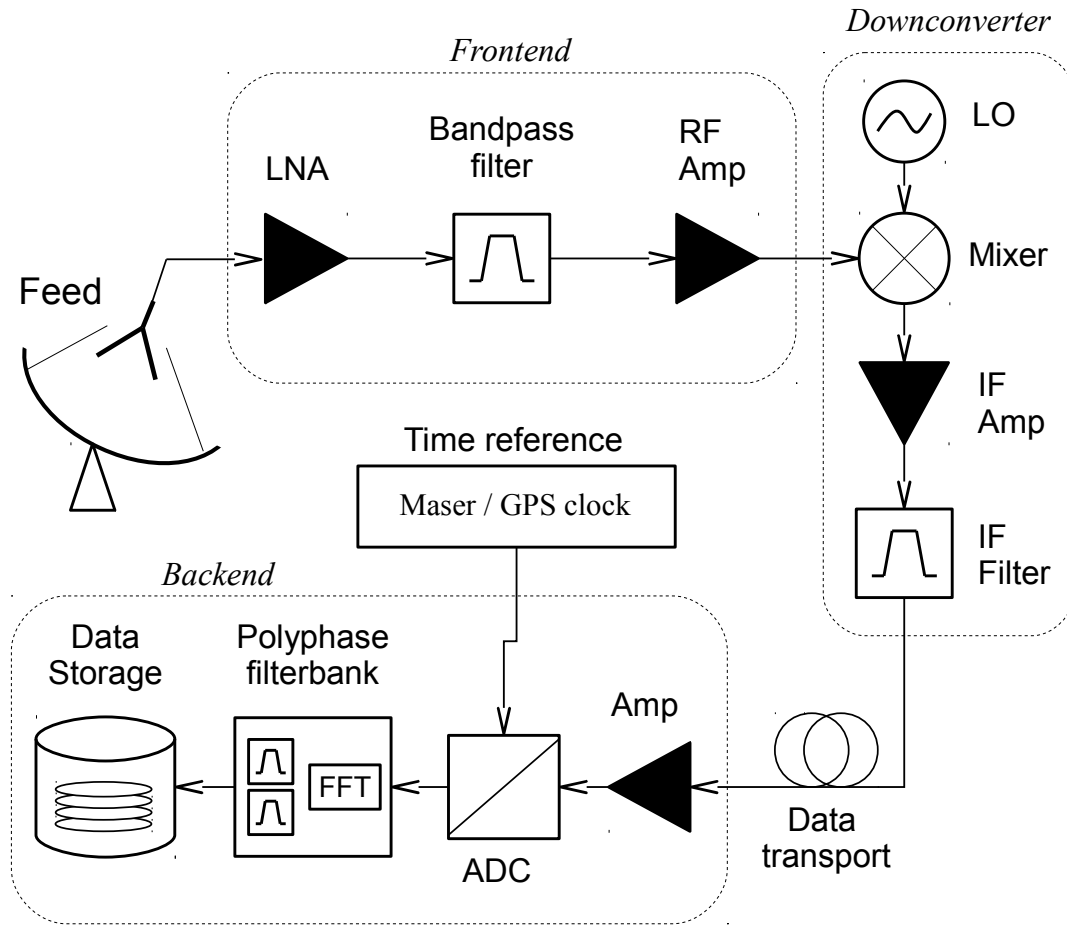


Figure 2.1: Overview of a radio telescope system for pulsar observations.

temperatures and large instantaneous bandwidths, which also improves the sensitivity (see section 7.1 for more details).

The general set-up of an instrument (a radio telescope) for pulsar observations is sketched in Fig. 2.1. The system is divided into two main parts: the frontend and the backend. Although there is no fixed agreement on what exactly comprises the frontend and backend, it is common to separate them in the *down conversion* stage, where the Radio Frequency (RF) signal is mixed and translated to a lower frequency, called the Intermediate Frequency (IF), where extra analogue processing can be made more easily.

The frontend starts at the feed, where the signal collected and focused by the telescope surface is converted from an electromagnetic wave into voltages. The next step is a signal amplification by a Low-Noise Amplifier (LNA), typically cryogenically cooled to avoid adding unwanted extra thermal noise. This step is extremely important, as the addition of extra noise at this point can have a large impact in the sensitivity of the receiver as a whole. After the LNA, there are usually filters to reject the frequencies that are not of interest, and perhaps also known persistent Radio Frequency Interference

(RFI). After the filtering, additional amplification may also be present.

The analogue processing of RF signals at high frequencies is more challenging than at low ones. Low-noise electronic components operating at high radio frequencies are difficult to build and, in addition, high frequency signals suffer of a strong attenuation when propagating on cables. A solution is to “translate” the signal to a lower frequency. This change of frequency is the role of the *mixer*, a device that multiplies the original signal by a stable sinusoidal wave of a frequency close to the original one, produced by a Local Oscillator (LO). As a result of this multiplication, several *exact copies* of the original signal are produced at different carrier frequencies. From those copies, there is one of particular interest that occurs at a carrier frequency $\nu_{\text{IF}} = \nu_2 - \nu_1$, where ν_2 is the frequency of the original signal and ν_1 the frequency of the LO. That copy at ν_{IF} is isolated after the mixer by a bandpass filter, and further signal transport is then possible avoiding the strong attenuation on the cables and using electronic devices operating at a lower, fixed frequency range.

The backend will receive the electric analogue signal and convert it to the digital domain with an Analogue-to-Digital converter (ADC) at the Nyquist frequency. The ADC requires of a high-quality clock reference to keep the sampling time and add precise timestamps. The most common pulsar backend device for pulsar search observations is a Polyphase Filter Bank (PFB). In a PFB, discrete blocks of data are Fourier transformed (typically by using a Fast Fourier Transform, FFT, see Section 2.3.4), producing spectra every a few microseconds. The blocks of data are weighted by a sinc function to decrease the spectral leakage (an artefact of the FFT in which the power of a strong signal can spread over several bins in the power spectrum) before applying the FFT. For the purposes of pulsar searching no polarization information is required, and the output from each polarisation channel is sum in quadrature. Finally, the stream of spectra including a header with information about the observation is written to disk for off-line processing.

2.3 Pulsar searching

Pulsar searching is the data analysis technique used to discover new pulsars in a dataset. It normally implies that no information about the properties of potential pulsars present in the data is known a-priori, such as the spin period, its derivative, DM, or orbital parameters in the case of binary systems. The searching process includes all the steps required to go from the raw data recorded by our observing system to a deliverable, normally a plot or a score from which a human or an artificial intelligence software make a decision of whether a detected signal is actually from a rotating neutron star or not.

The main necessary steps to detect pulsar signals are the dedispersion of the raw data, Fourier transform of the dedispersed time series, search for periodicities in the Fourier domain, and the sifting and folding of the candidates. The Fourier analysis can be complemented by a time domain analysis searching for individual pulsations. Additionally, the cleaning of the data, for example from Radio Frequency Interference

(RFI) or undesired instrumental effects, can greatly improve the detectability of weak pulsar signals. The next sections give an overview of the pulsar searching methodology, and explains the tools utilized in the new pulsar searching pipeline that we developed for this thesis.

2.3.1 RFI and data cleaning

Our radio telescopes not only detect astronomical signals, but also most of the terrestrial interference produced by the receiver electronics and all kind of services emitting in the observing frequency range (or close). All the undesired signals present in our data are considered RFI. The RFI signals are usually much stronger than the pulsar signals, and likely contain periodicities. Therefore, RFI easily translate into candidates in a pulsar search. If not dealt with properly, RFI can produce so many candidates that real weaker pulsar signals can be lost in the analysis.

One powerful method to detect and excise RFI is to exploit the fact that such signals will typically not be dispersed. This means that by analysing the raw data without applying dedispersion (see Section 2.3.2), the significant signals both in the time series and the Fourier series will likely be RFI. A list of time intervals and Fourier bins affected by RFI can be created, usually called a “mask”, that later on is used to “clip” those data segments by substituting them with zeros, the mean of the time series, or noise that mimic the average statistics of the data.

The pulsar data analysis software `PRESTO`¹, extensively used in this thesis, includes a powerful tool that analyses observations in blocks, calculates statistics, and by comparing the data with the statistics, creates automatically a mask of RFI for a given observation. The program is called `rfifind`. In addition to the masked data detected by `rfifind`, we developed an automated code that searches for periodic RFI at a $DM=0$, and creates a list of all the found periodicities so they can be excluded from the analysis.

One particularity of this thesis is the use of high and very high radio frequencies for the observations (most of them are carried out at ~ 5 , 8 and above 87 GHz). At such high radio frequencies the dispersion effect is greatly reduced, and can be even negligible at the millimetre regime (see Fig. 2.2). To properly identify RFI and differentiate between terrestrial RFI and astronomical signals has been one of the major issues faced during this thesis (see section 3.2.2.3).

2.3.2 Dedispersion

As already described in section 1.3.1, the broadband emission from pulsars suffers of dispersion as it travels through the ISM from the neutron star to our telescope. To mitigate it, we make use of the frequency-channelized data, calculating the dispersive time delays introduced by the ISM at each frequency channel with respect to a reference frequency, and shifting each frequency channel accordingly (see Eq. 1.20).

¹<http://www.cv.nrao.edu/~sransom/presto/>

When searching for new pulsars, we do not know the amount of free electrons between our telescope and the neutron star. Therefore, we perform a brute force search in DM, assuming a number of different trial values and applying the dispersion correction for each case. The step value, ΔDM , can be chosen by calculating the amount of pulse smearing across the full observation bandwidth and equalling it to the sampling time on the data (see e.g. Lorimer & Kramer, 2005),

$$\Delta\text{DM} = 1.205 \cdot 10^{-7} t_{\text{samp}} \left(\frac{\nu^3}{\Delta\nu} \right) \text{ [pc cm}^{-3}\text{]} \quad (2.1)$$

where t_{samp} is the sampling time of the observation (in ms), ν is the centre frequency (in MHz), and $\Delta\nu$ is the total bandwidth (in MHz). For each trial DM, we perform a search for periodic signals, as described in the next sections.

Figure 2.2 shows a comparison of the impact of an incorrect trial DM on the detection Signal-to-Noise ratio (S/N) of a pulsar for different test cases and different observing set-ups. As the observing frequency increases, the dispersion decreases rapidly. Part of this thesis uses observations at very high radio frequencies, where the dispersion effect is negligible. The lack of dispersion can have some disadvantages, as in these cases it is not possible to distinguish RFI from celestial signals by using the dispersion effect (see Section 3.2.2.3), nor can the DM be used to estimate a distance to a pulsar.

To dedisperse pulsar observations we make use of programs like `prepdata` or `prepsubband`, from the PRESTO pulsar analysis suite. Alternatively, `dedisperse` from SIGPROC² or the Python-based SIGPYPROC³ also include efficient dedispersion routines. PRESTO also includes a useful tool, `DDplan.py`, to calculate optimum ΔDM values from the characteristics of an observation.

2.3.3 Barycentering

The Earth, due to its rotation and orbit around the solar system barycentre, is in motion relative to other celestial objects. If an observation is short ($T_{\text{obs}} \lesssim 30 \text{ min}$), the effects of this relative movement can usually be neglected. However, for longer observations, or if the observations are taken with satellite-based instruments in orbit around the Earth, this relative movement can result in varying arrival times of the pulses and thus of the observed spin period of a pulsar. This varying time delays decrease the purity of the periodicity of the received pulses, affecting their detectability in the periodicity search step (see section 2.3.4).

A solution consists in correcting the time series recorded at the observatory (called the *topocentric* dataset) to obtain a time series as if the observatory were placed at the Solar System Barycentre (SSB), which is a very good approximation to an inertial reference frame. This correction is called *barycentering* and it can be done by software such as `prepdata` from PRESTO, in combination with the software TEMPO⁴, which includes

²<http://sigproc.sourceforge.net/>

³<http://www3.mpifr-bonn.mpg.de/staff/ebarr/sigpyproc/Introduction.html>

⁴<http://tempo.sourceforge.net/>

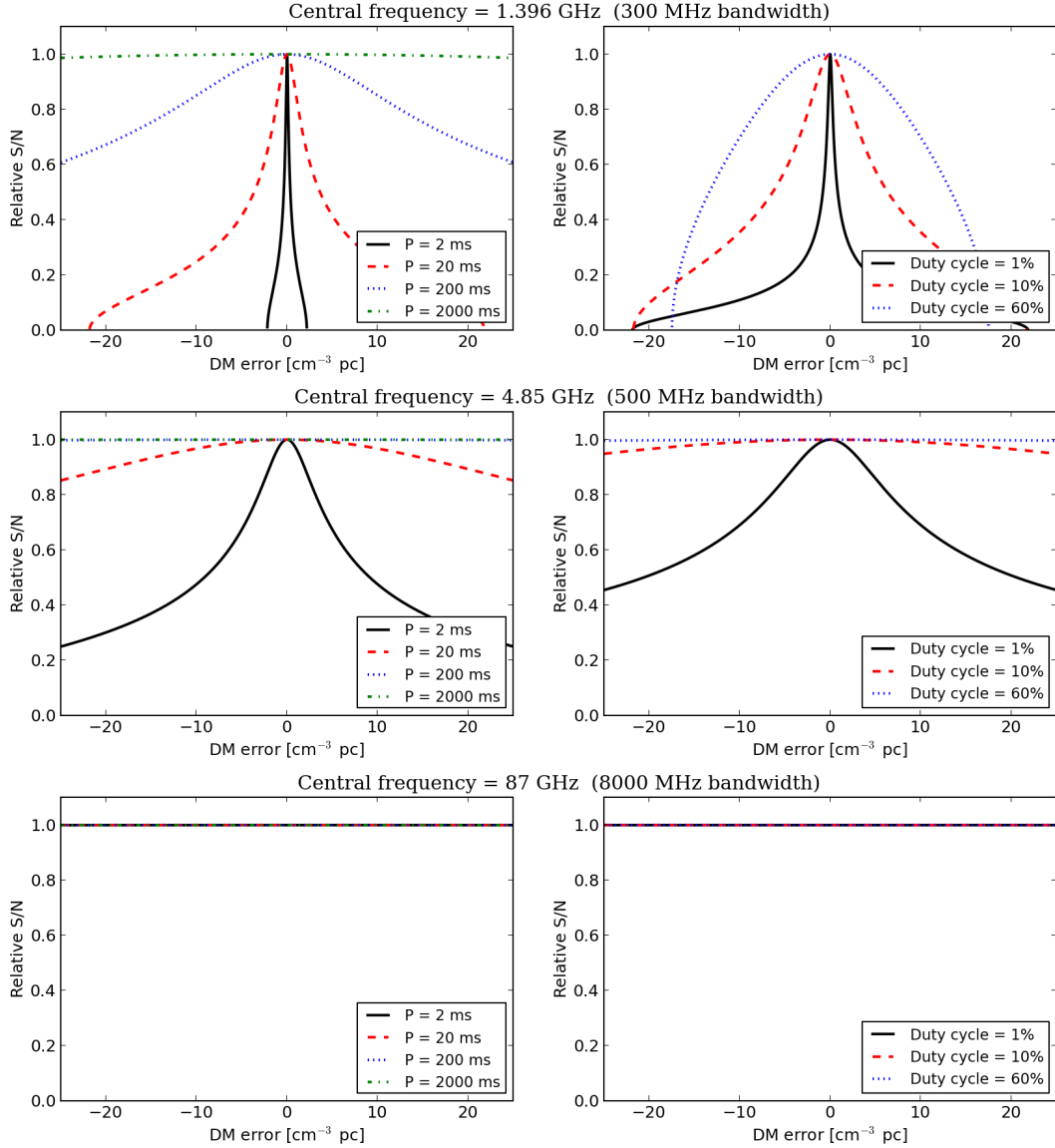


Figure 2.2: Relative S/N of recovered pulsar signals as a function of error in the assumed DM with respect to the real value. *Upper-left:* Comparison of relative S/N for four different hypothetical pulsars with periods 2, 20, 200, and 2000 ms and a duty cycle of 5 per cent for an observation centred at 1.396 GHz with 300 MHz of bandwidth (a typical set-up for L-band observations at Effelsberg). *Upper-right:* Comparison of relative S/N for a pulsar with a period of 20 ms with different duty cycles of 1, 10, and 60 per cent, for observations centred at 1.396 GHz with 300 MHz of bandwidth. *Middle-panels:* Same example as in the upper panels but for observations centred at 4.85 GHz and a bandwidth of 500 MHz (one of the two main frequencies used in our Galactic Centre pulsar survey, see Chapter 3). By comparison with the upper panels, it can be noticed how the effects of dispersion decrease as the observing frequency increases, reducing the impact of an error in the assumed DM of the pulsar. *Lower-panels:* Same example as in upper panels but for observations centred at 87 GHz with 8 GHz of bandwidth (a set-up used in our observations at 3 mm, see Chapters 4, 5, and 6). In this case the effects of dispersion are negligible.

a precise model of the solar system and can compute the necessary time corrections for a given dataset.

2.3.4 Periodicity search

To detect the periodic pulses we can make use of the Fourier transform, searching for features in the frequency spectrum. With this method we are able to identify periodicities even if they are buried in noise in the time domain. Nowadays, the astronomical data are stored in digital form, and the Discrete Fourier Transform (DFT) is used to transform the data to the frequency domain. Due to the large number of samples that pulsar data can have, a computationally efficient DFT algorithm is desirable. The Fast Fourier Transform (FFT) is the most widely utilized algorithm given its computational efficiency. For a data set of N discrete values, the number of operations required by the FFT is $\sim N \log N$, in contrast to $\sim N^2$ that are required by the DFT. Different libraries performing the FFT algorithm can be downloaded as open source code. For this work, we have made use of the FFTW library⁵.

To facilitate some of the subsequent steps, that rely on statistical analysis, it is desirable a dataset with Gaussian noise properties. However, due to variations in the electronics, RFI, or external sources like, for instance, the atmospheric contribution when observing at very high radio frequencies, the data will generally have a non negligible (or even large) component of non-Gaussian noise. In particular, *red noise*⁶ can be prominent, and can affect significantly the detectability of pulsars with slow rotating periods (Lazarus et al., 2015). A good way to reduce the red noise component is to fit the slope of the Fourier series in small blocks and subtract it. Similarly, one can apply for example running mean or running median filters in the time or frequency domain.

Finally, the normalization of the Fourier series (so it has a root mean square of one) is helpful; this way, the S/N of a Fourier bin is equivalent to its power. It is a common practice to normalize the Fourier series before looking for significant periodic signals for further analysis.

Code to perform all these transformations exist as part, for example, of the PRESTO suite. The specific programs are called `realfft`, which, based on the FFTW library, applies the FFT to a time series, and `rednoise`, which reduces the red noise (with the method of fitting a slope in blocks) and normalize the spectrum. Additionally, we wrote Python routines to apply running mean or running median filtering in the time domain.

2.3.4.1 Candidate Selection

Once we have transformed a dataset into the Fourier domain, we need to decide what features of the spectrum are promising and worth analysing further. The usual way is to set a threshold of power (or S/N) over which a peak in the spectrum is considered

⁵<http://www.fftw.org/>

⁶Red noise refers to noise that has increasing power at the low frequencies of the spectrum.

significant. The threshold should be low enough to detect as many periodic signals as possible while at the same time reducing the chances of selecting peaks produced purely by noise. We can make use of the statistics of the noise in the data to calculate a good threshold value. The following assumes Gaussian noise. The power in an individual bin is the sum of the squares of the real and imaginary parts of the complex Fourier values, and when harmonic summing is applied (see section 2.3.4.2), it will be the sum of the powers in m harmonics. For this general case, the probability of a sum of m harmonics to be over a given threshold power \mathcal{P}_{\min} (also referred as *false-alarm probability*) is citep[see e.g.]lorkra05

$$p(\mathcal{P} > \mathcal{P}_{\min}) = \sum_{j=0}^{m-1} \frac{\mathcal{P}^j}{j!} \exp(-\mathcal{P}_{\min}). \quad (2.2)$$

By setting the probability such that less than one false positive is obtained after a given number of trials, we can obtain a threshold power to consider a detection, $\mathcal{P}_{\text{threshold}}$. If we prefer to work with Fourier amplitudes, it can be shown that an equivalent threshold $(S/N)_{\min}$ is (see e.g. Lorimer & Kramer, 2005)

$$(S/N)_{\min} = \frac{\sqrt{\ln(n_{\text{trials}})} - \sqrt{\pi/4}}{1 - \pi/4}, \quad (2.3)$$

where n_{trials} correspond to the number of bins in the Fourier series, multiplied by the number of harmonic summing stages, and by the number of DM trials. In the case that acceleration search is performed (see section 2.3.4.3), the number of acceleration trials must also be included in n_{trials} . Finally, to account for RFI it is a good practice to increase the calculated threshold about 5 to 10 per cent.

we made use of the routine `accelsearch` of PRESTO for the candidate selection in our surveys. Another commonly used software for this purpose is `seek` from the suite SIGPROC.

2.3.4.2 Harmonic summing

The power of pulsar signals in the Fourier domain will spread over a number of harmonics that accompany the fundamental. This occurs because the pulses received from a rotating neutron star are normally far from a sinusoidal shape. In fact, pulsar profiles have typically short duty cycles and can have many sharp components, which translates into a rich spectral harmonic content (see e.g. Fig. 6.1).

The technique used to recover the total power of a periodic signal summing a fundamental with its harmonics is called “harmonic summing”. It is an important and powerful method that can increase considerably the significance of a detection when searching a Fourier spectrum for signals that could be a pulsar. Harmonic summing of up to 16 harmonics is included in the candidate selection routine `accelsearch` of PRESTO.

2.3.4.3 Acceleration search

Some of the most interesting pulsars known (and yet to be discovered) are in binary systems. When a pulsar is in a binary orbit it suffers a varying acceleration due to its orbital motion, resulting in a varying velocity at different parts of the orbit. The line-of-sight (LOS) component of the velocity will modify the observed spin period of the pulsar due to the Doppler shift,

$$P(t) = P_0 \left(1 + \frac{v_{\text{LOS}}(t)}{c} \right), \quad (2.4)$$

where $P(t)$ is the observed spin period of the pulsar, P_0 is its intrinsic spin period, $v_{\text{LOS}}(t)$ is the velocity along the line-of-sight, and c is the speed of light. Similarly, the acceleration will affect the derivative of the spin period, with a relation (in a first order approximation)

$$P'(t) = P_0 \left(1 + \frac{a_{\text{LOS}}(t)}{c} \right), \quad (2.5)$$

where $P'(t)$ is the first derivative of the spin period, and $a_{\text{LOS}}(t)$ the acceleration component along the line-of-sight.

The effect of a varying spin period during an observation is a spread of the power of the periodic signal over several adjacent bins in the Fourier spectrum. To increase our sensitivity to pulsars in binary systems suffering an acceleration, we utilize a matched-filtering technique included in the `accelsearch` routine of `PRESTO` (Ransom et al., 2002). The algorithm calculates how the power of the signal will spread for a given acceleration, a , assumed to be constant across the observation⁷. A parameter corresponding to the maximum number of bins in the Fourier series that will be used in the cross-correlation with the matched filters can be input to `accelsearch`,

$$z = \frac{a T_{\text{obs}}^2}{P c}, \quad (2.6)$$

where a is the acceleration of the pulsar, T_{obs} is the length of the observation, P the pulsar's spin period.

Including acceleration searches in large ranges of z (or a) can be computationally very expensive, but it is required to be sensitive to pulsar in exotic systems (like double neutron stars, pulsar-black holes or pulsars in very tight orbits). Those exotic systems are the main objective of the surveys carried out in this thesis. For this reason, the newly developed pulsar searching pipeline includes a version of `accelsearch`⁸ modified to work on Graphic Processor Units (GPUs). By running the code on GPUs (tested on an Nvidia K20), a speed up of up to a factor 22x was achieved compared to single-threaded CPU⁹. This improvement was crucial in order to be able to process the large dataset of the Effelsberg Galactic Centre pulsar survey (presented in chapter 3) in a

⁷The constant acceleration assumption is a good approximation for observations that are less than about 10 per cent of the full orbital period (Ransom et al., 2003, see also Ng et al. (2015)).

⁸https://github.com/jintaoluo/presto2_on_gpu

⁹Intel Xeon CPU E5-2640

reasonable time. Furthermore, this way the pipeline included large acceleration ranges, making us sensitive to the most extreme pulsar systems; including pulsars in orbit with the supermassive black hole at the centre of the Milky Way.

2.3.4.4 Candidate sifting

The potential pulsars and other significant periodic signals (for instance from RFI) will be usually detected in different trials of DM and acceleration values, with different S/N. Sometimes, the total number of candidates that pass the threshold for further analysis can reach values of up to several thousand in one observation. In order to bring the number of candidates down to manageable numbers it is necessary to sift them.

A typical sifting algorithm checks for duplicate periodicities found at different DM and acceleration trials and keeps only one instance of each where the detection S/N is maximum. In addition, it checks for and remove harmonically related candidates, applies more restrictive significance thresholds, or reject periodicities too short or too long to be pulsars. The final list of candidates will be folded (see section 2.3.5) and inspected in more detail. For the data analysis done in this thesis, the candidate sifting is performed by the `sifting.py` module of PRESTO.

Computer-aided and artificial intelligence algorithms allow for an automatic, very fast evaluation of large numbers of candidates (Eatough et al., 2010). When these tools are available, it can be reasonable to allow a larger number of candidates pass through the sifting step, for example decreasing the significance thresholds or allowing wider period ranges for the selected candidates (e.g. Morello et al., 2014).

2.3.5 Folding and candidate optimization

In most cases, the signals detected in a periodicity search are very weak. To increase the S/N and evaluate better the properties of such signals, the raw data is dedispersed to the discovery DM and folded modulo detection period, creating an average profile of the emission of the source (also known as *folded profile* or *integrated profile*). This averaging process is referred to as *folding*.

When folding, the time resolution of the integrated profile is controlled by selecting the number of phase bins, n_{bins} , across one period. Then, for each sample in the time series we calculate to which phase bin it corresponds to and add it to it. Once all the samples has been added to their corresponding bin, each bin is normalized by the total number of samples added to it.

The folding is usually done in segments in time (called sub-integrations) and frequency (called sub-bands). This is useful to obtain information about the persistence and broadband properties of the detected signal in time and frequency, respectively. Those two properties are important because pulsars are generally expected to be broadband and persistent in time. In contrast, much of the RFI signals do not fulfil those two characteristics.

During the folding, the properties of the signal may be optimized by an extra search in the parameter spaces of period, period derivative (related to the acceleration, see

Eq. 2.5), or DM, trying to maximize the S/N or the Chi-square (χ^2) of the profile (see e.g. Lorimer & Kramer, 2005). In the case that the pulsar properties are known, for example from a timing analysis, the folding step can make use of an ephemeris to calculate with more precision to which bin of the integrated profile each time sample corresponds to. With this method the pulse smearing that can occur by imprecisions in the pulsar parameters is greatly reduced, obtaining the maximum S/N and fidelity to the received pulses.

The most common software to perform efficient folding of pulsar observations are `dspsr` from the `DSPSR`¹⁰ software suite, or `prepfold` from `PRESTO`. For our data analysis we mainly used `prepfold` and `dspsr`.

2.3.6 Candidate evaluation methods

The information of a periodic signal that passes the threshold of significance and is folded includes the integrated profile, and a list of the signal properties (like period, period derivative, S/N of the Fourier power, S/N of the integrated profile, acceleration, best DM, etc.). To evaluate candidates it is common to use a graphical representation of this information. The most common plots include a S/N (or χ^2) versus DM curve, and waterfall plots of intensity versus rotational phase, both across the observation time and frequency. Figure 2.3 shows and describes an example of a candidate evaluation plot produced by `prepfold` from `PRESTO`. After the information about a candidate is gathered and plotted, the final decision on the validity of the signal as a pulsar or not is made by humans. However, a pulsar survey can produce enormous quantities of candidates, making reviewing manually all of them a very tedious and time-consuming task.

In order to improve our discovery capabilities in pulsar surveys (especially in large scale ones), and support the humans in the process, there are additional tools. A good example is computer-aided Artificial Intelligence (AI) algorithms for the automatic evaluation and filtering of candidates. These AI programs can learn from real and simulated datasets and evaluate candidates automatically at astonishing speeds. In this thesis, we have made use of two AI algorithms to review and score the candidates of the surveys carried out. One of the tools is the Pulsar Evaluation Algorithm for Candidate Extraction (PEACE) (Lee et al., 2013), and the other one is the Pulsar Image-based Classification System (PICS) AI (Zhu et al., 2014). These tools were not used as a substitution of the manual candidate check (in which the ~ 100 most significant candidates per observation are always examined), but as a complement in order to increase the discovery probabilities of weak pulsar signals.

2.3.7 Searches for transient emission

The searching process in the Fourier domain relies on the periodicity of the pulsations. Nevertheless, not all pulsars show clear periodicities due, for instance, to intermittency or intensity variations between different pulses that could make some of them too weak

¹⁰<http://dspsr.sourceforge.net/>

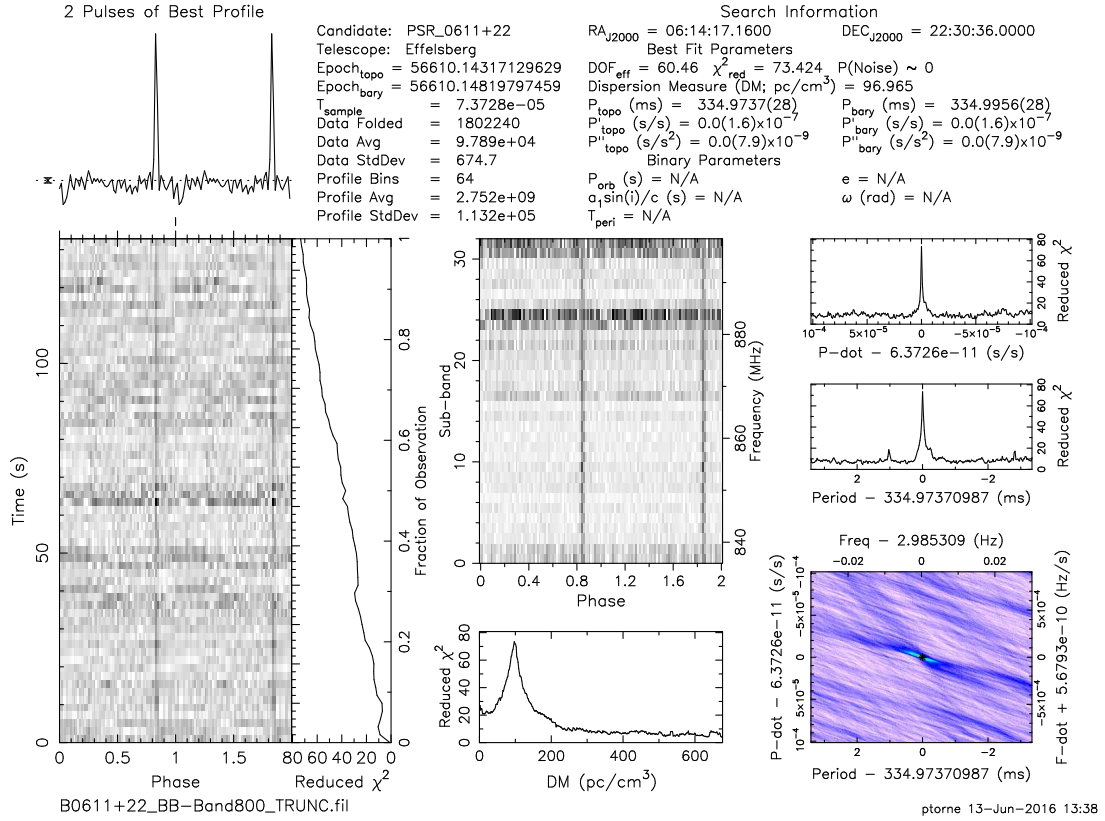


Figure 2.3: Example of candidate evaluation plot produced by `prepfold` (with a detection of PSR B0611+22). *Top-left*: Integrated pulse, shown twice. *Top-right*: Candidate and observation details including name, telescope, epoch, data time sampling, data statistics, position, period and period derivatives (for topocentric and barycentric references), and binary parameters if applicable. *Lower-left*: Waterfall plot showing the intensity as a function of rotational phase and observing time, together with a representation of the reduced χ^2 of the integrated profile accumulated during the observation length. *Middle-centre*: Waterfall plot of the intensity as a function of rotational phase versus frequency. *Middle-bottom*: Reduced χ^2 as a function of trial DM. *Lower-right*: Waterfall plot of reduced χ^2 for the integrated profile as a function of folding period and period derivative. *Middle-right*: Two plots with one-dimensional cuts (on the zero reference) from the waterfall plot shown in the lower-right panel.

to be detected. A periodicity search may not be effective to detect such sources and alternatives are needed.

A solution consist on searching in the time domain for the emission of the individual bursts or pulses emitted from the neutron star, called *single pulses*. The usual method to detect them is to use matched filters that add the intensity of contiguous time samples, checking the summed intensity against the noise statistics. Similarly to what we discussed in section 2.3.4.1, choosing a good threshold to decide what events are significant is important to avoid too many false positives. Assuming Gaussian statistics for the time series, and accounting for probable RFI present in the data, a proper threshold for a standard single pulse search is about $(S/N)_{\text{thres}} \simeq 6$ (Cordes & McLaughlin, 2003; Lorimer & Kramer, 2005).

Throughout this thesis, the Python routine from PRESTO called `single_pulse_search.py` has been the method used for searching transient emission in our pulsar observations. `single_pulse_search.py` is also able to produce diagnostic plots from the results. Figure 2.4 shows a diagnostic plot from a single pulse search on PSR B2111+46 as an example.

2.3.8 Overview of a pulsar searching pipeline

The different steps described in the previous sections can be applied individually, but it is more common to use a control script that performs all the necessary steps to go from raw data to a candidate list and/or evaluation plots in an automated way. Such control codes are typically referred to as *pulsar searching pipelines*. To perform the pulsar surveys presented in this thesis, we wrote a searching pipeline based on the PRESTO software. This code had been installed in several different computers, including the Max Planck large-scale supercomputer *Hydra*¹¹. The pipeline has been used to process a Galactic Centre survey done with the Effelsberg 100-m radio telescope (see Chapter 3), search for radio pulsars in unassociated gamma-ray sources (see Section 7.3.2.1), and in two collaborative projects searching for radio pulsations from newly discovered gamma-ray pulsars (Clark et al., 2015), and from the globular cluster 47 Tuc (Ridolfi et al. submitted). Figure 2.5 shows a block diagram with an overview of the pulsar searching pipeline.

2.4 Millimetre pulsar data reduction

A substantial fraction of the observations driving this thesis are carried out in the millimetre band, between ~ 3 mm and 0.6 mm (87–472 GHz) using the IRAM 30-m radio telescope, and to a lesser extend, the APEX 12-m radio telescope. Observations of pulsars at such high radio frequencies are very uncommon due to pulsar’s steep spectrum and faintness, and we faced several challenges for reducing and calibrating the millimetre pulsar data. The main ones and the adopted solutions are discussed in the next sections.

¹¹<http://www.mpcdf.mpg.de/services/computing/hydra>

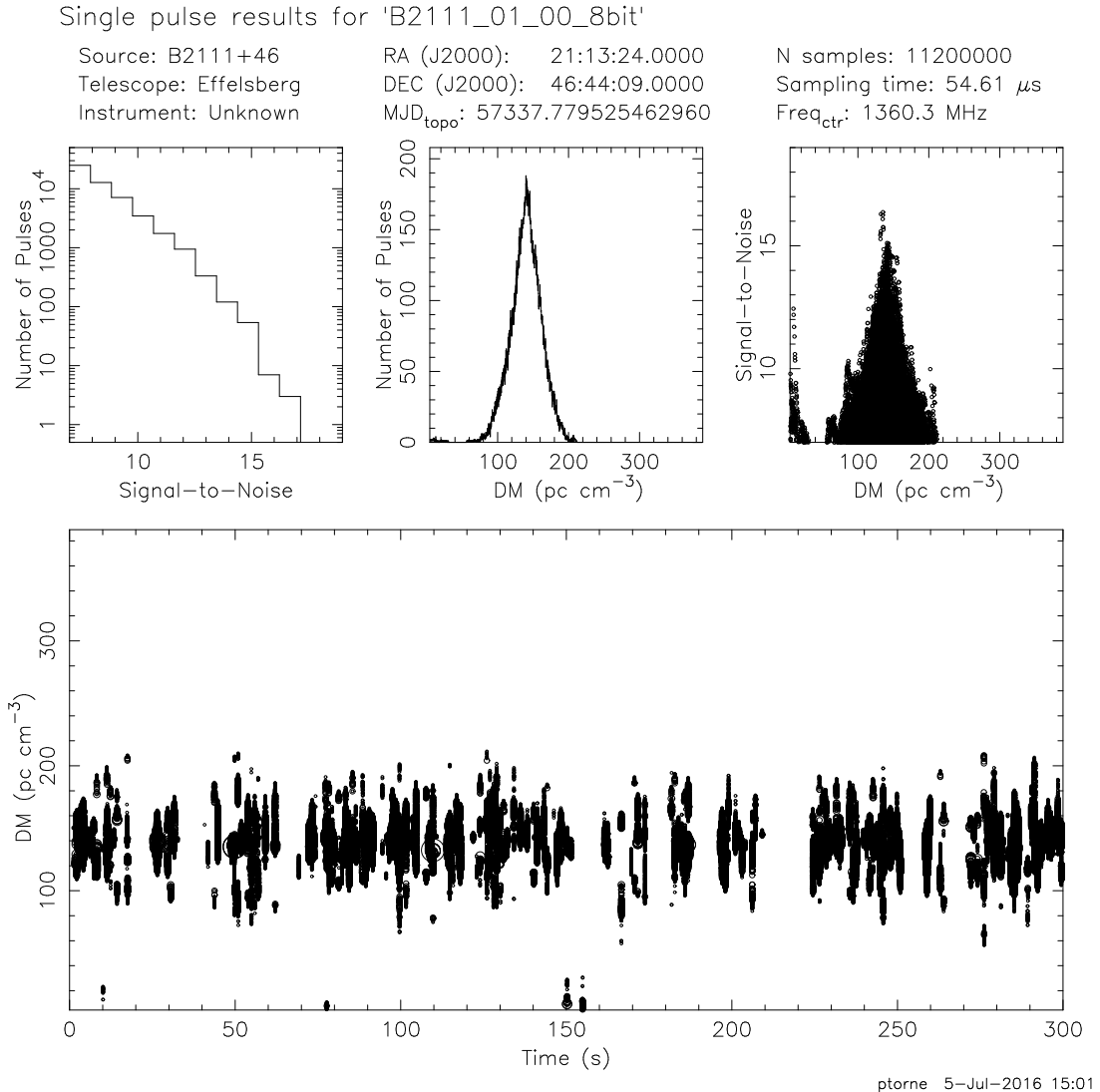


Figure 2.4: Example of single pulse diagnostic plot from PRESTO's `single_pulse_search.py` showing the results of a transient emission search from PSR B2111+46. The top part shows information about the source, telescope and instrument used, epoch, position, and observational properties. *Upper-left*: A histogram of the S/N of the detected pulses. *Upper-centre*: Histogram of the DM of the detected pulses. *Upper-right*: A plot of S/N versus DM for all detected pulses. *Lower*: Waterfall representation of the detected single pulse events (with the size of the circles proportional to their S/N) as a function of DM and observing time. The events clustered around $DM = 141 \text{ pc cm}^{-3}$ are single pulses from the pulsar (that has a real $DM = 141.26 \text{ pc cm}^{-3}$). The events close to $DM = 0 \text{ pc cm}^{-3}$ are most likely produced by RFI.

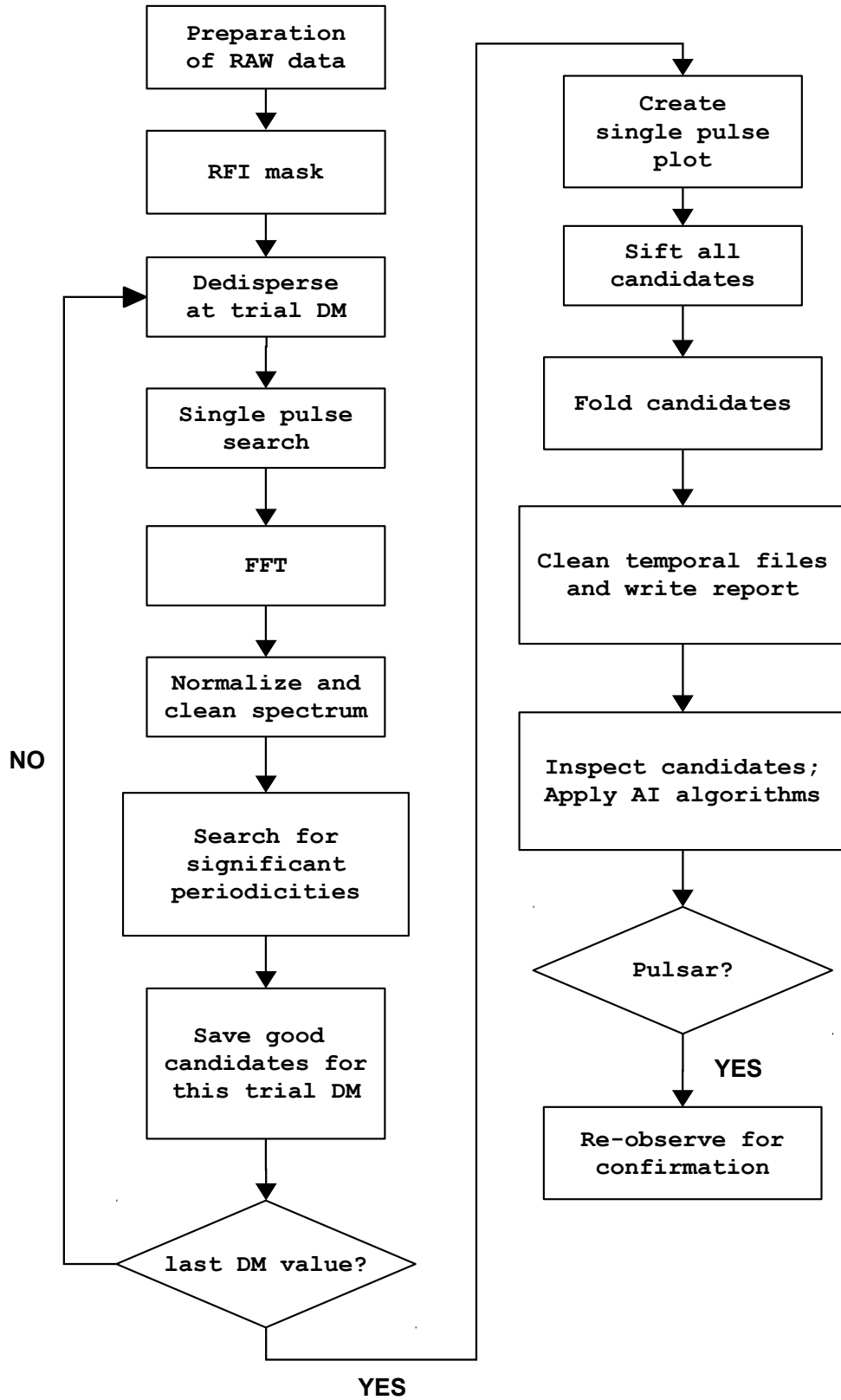


Figure 2.5: Overview of the process of pulsar searching, following the data flow of the pulsar searching pipeline developed for this thesis.

2.4.1 Red noise and RFI removal

One of the main problems when analysing our millimetre pulsar observations was the significant amount of red noise present in the data. This noise component is produced mainly by changes in the atmospheric conditions within the observations, and need to be mitigated in order to allow the detections and analysis of the faint pulsar signals. One effect of the red noise is a non-flat off-pulse region in the folded profiles. As a result, the detection S/N can be greatly reduced, and in extreme cases a weak signal can be totally hindered. In the case of carrying out blind periodicity searches, the red noise can reduce the detection S/N of the periodicities in the Fourier series, which could lead to a pulsar signal being missed by the search algorithms (see Sec. 2.3.4.1). This decrease in detectability caused by the excess of red noise is particularly severe for the detection and study of long period pulsars, like the Galactic Centre magnetar SGR J1745–2900 ($P \simeq 3.765$ s, see Chapters 4 and 5). But also when studying other faster-rotating pulsars (see Chapter 6) the subtraction of the red noise also proved to be a necessary step in order to improve the detection S/N of the weak signals (see Chapter 6).

Normally, in observations at millimetre wavelengths a “switching technique” is used to measure and subtract the atmospheric and receiver noise contributions and, with them, the red noise. In its simplest form, the telescope is continuously positioned on and off source and both measurements are subtracted to obtain the source temperature. For our pulsar observations, the switching techniques are not appropriate. By using for instance position or beam switching, half of the integration time we would be off-source, with the consequent decrease in the sensitivity of the observations. This is a big drawback when trying to detect the extremely weak pulsar signals. Thus, we did not make use of any switching technique for our observations and observed in “total power mode”, i.e., integrating always on-source (the pulsars) and recording long coherent time series that maximize our sensitivity. The drawback of this observing mode is that the red noise needs to be removed manually.

Our solution to this problem consists in the attenuation of the red noise by filtering it. Two different strategies were studied and utilized. Applying filters in the time domain, e.g. a running mean filtering, proved to be very effective. The other option is to work in the Fourier domain, fitting the spectrum slope in blocks and subtracting it. However, these red noise cleaning methods can affect the pulsar signals producing artefacts in the resulting folded profiles (for example, dipping the pulse below the off-pulse mean level). Such artefacts have to be avoided, specially when trying to measure the absolute flux density of the sources.

Two different methods to clean the data from excess of red noise while avoiding artefacts on the folded profiles were used here. The first one consists on filtering by fitting a moving window and subtracting the baseline slope and a 1 Hz sinusoidal signal¹². This method was successfully applied to the observations of SGR J1745–2900 done in July 2014 (see Chapter 4). The second method applies a running mean filtering

¹²In addition to the red noise, a very strong RFI signal at 1 Hz with several powerful harmonics (most likely related to the cryogenerator) is often present in the IRAM 30-m data.

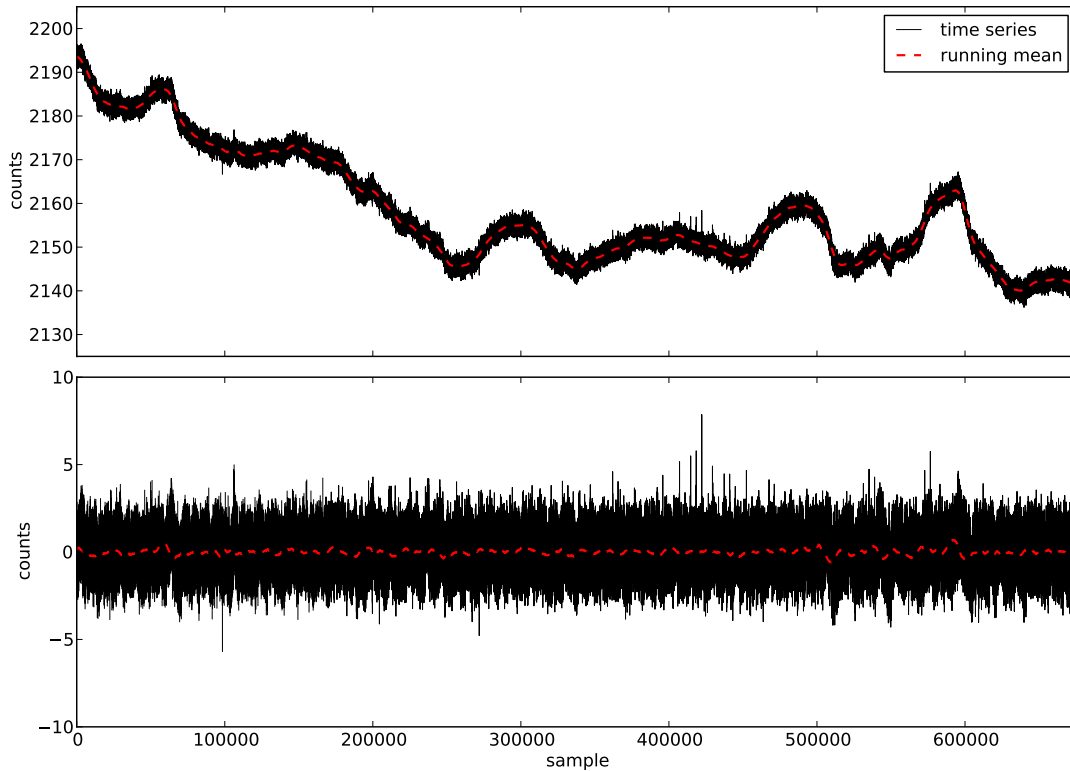


Figure 2.6: Example of time domain red noise subtraction using a running mean filter. *Upper plot:* A raw time series of an observation at a central frequency of 101 GHz of the magnetar SGR 1745-2900 with the IRAM30-m . The slow variations in mean count level due to atmospheric changes during the observation are evident. *Lower plot:* The resulting data after applying the running mean subtraction with a window of 8.3 seconds. The variations are significantly removed and, with them, most of the red noise in the data.

while protecting the individual pulses (calculated from an ephemeris) by extrapolating the running mean vector over the pulse regions. This second method proved also to be very effective, and was used in the observations done in March 2015 (see Chapter 5).

Figures 2.6 and 2.7 show examples of the filtering methods in time and frequency, respectively. Figure 2.8 shows a comparison of folded profiles with and without the red noise filtering applied. All this demonstrates the importance of the red noise subtraction algorithms to obtain successful and high S/N detections in pulsar observations done at very high radio frequencies.

2.4.2 Flux density calibration of IRAM 30-m data

Another challenge was to obtain the absolute flux density calibration of the data. The standard software to observe and reduce data from the IRAM 30-m (e.g. MIRA, CLASS,

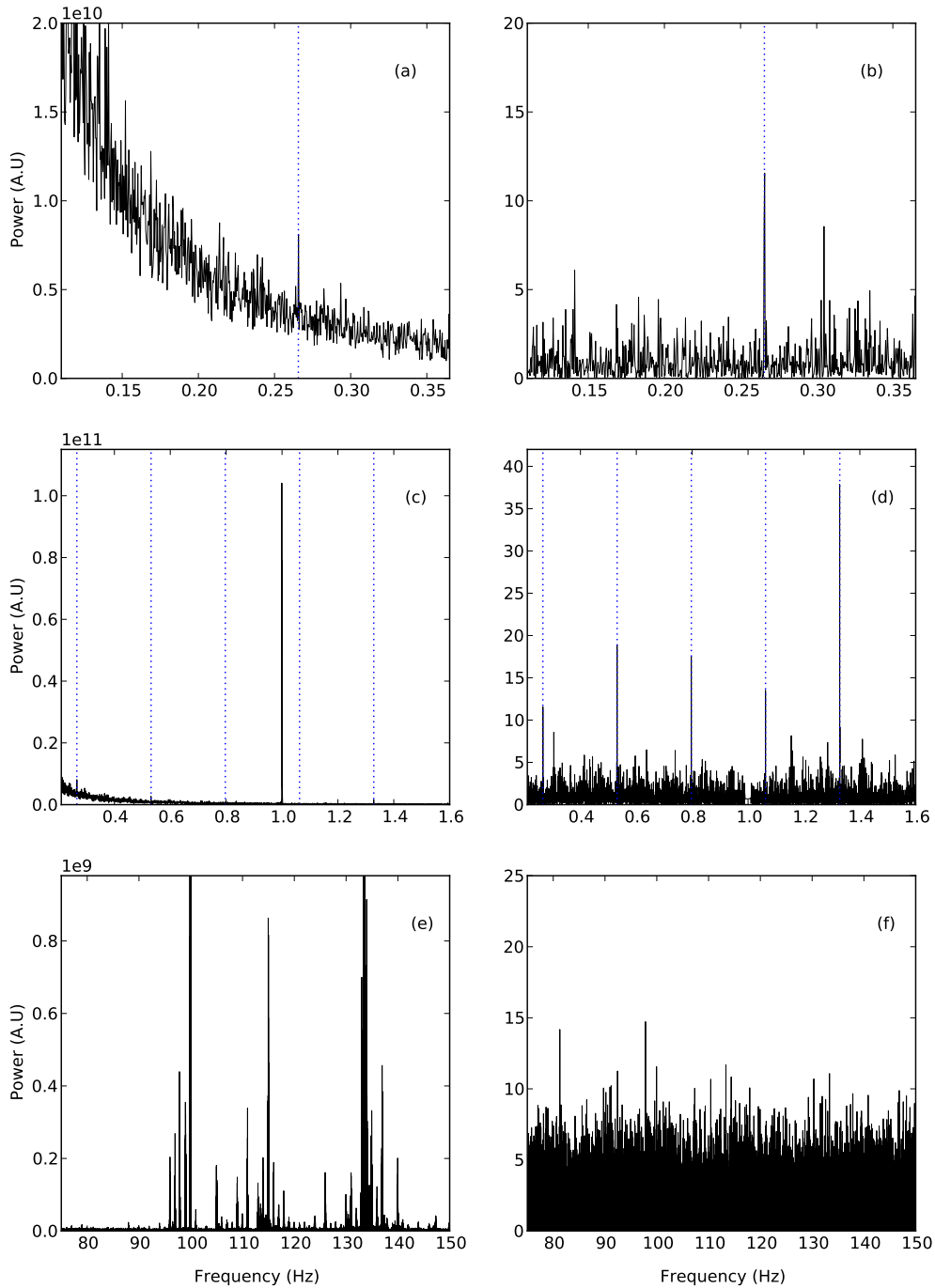


Figure 2.7: Red noise reduction and normalization of an observation of SGR J1745–2900 with IRAM 30-m at 101 GHz using a Fourier domain technique. The three panels on the left show the raw data with no filtering applied, while the panels on the right show the same regions after applying the `rednoise` algorithm from PRESTO. Panels (a) and (b) show the low frequencies, highly affected by rednoise. Panels (c) and (d) zoom to the region of the dominant RFI signal at 1 Hz (manually excised from the data). Panels (e) and (f) show an example of the rest of the strong RFI usually present in the data. Note that the fitting window of `rednoise` is small enough to fit and subtract broadband RFI. The vertical dotted lines mark the fundamental and harmonics of the magnetar SGR J1745–2900.

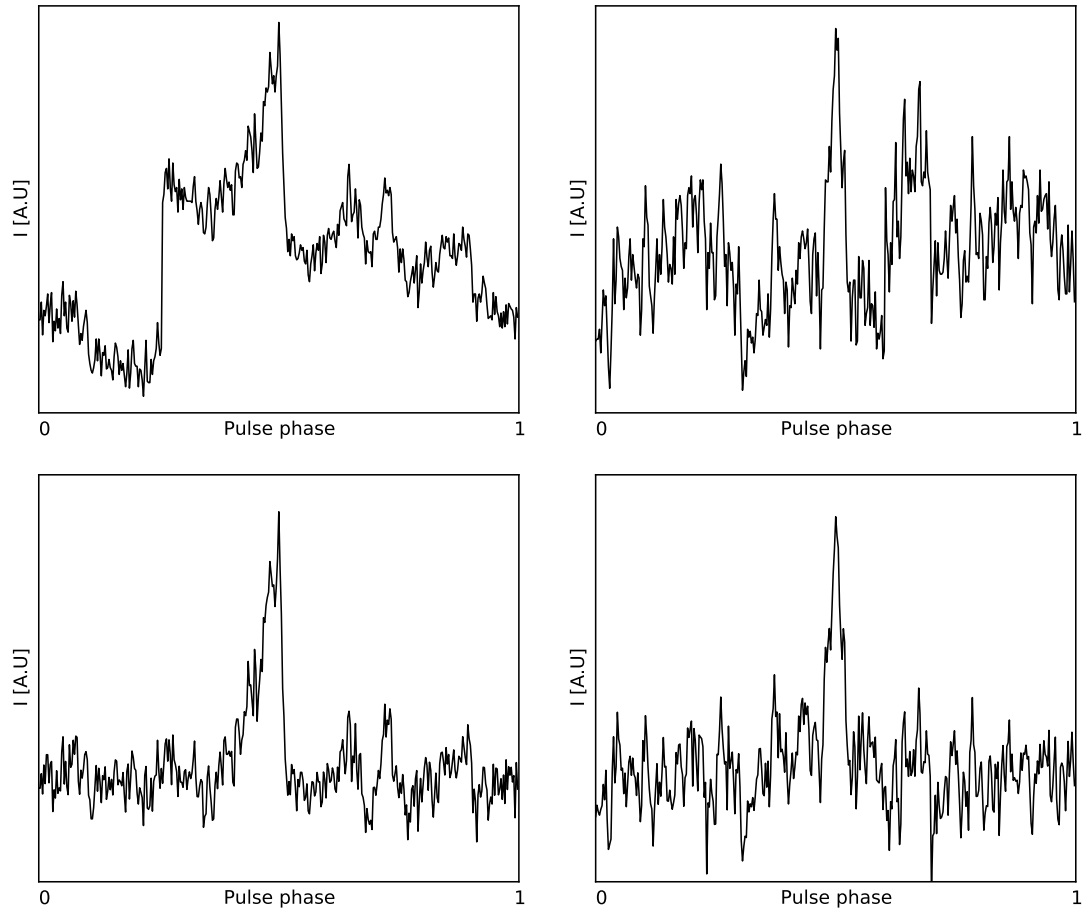


Figure 2.8: Two examples of the integrated profile of the magnetar SGR J1745–2900 before and after the red noise subtraction. *Upper-left panel:* Integrated profile from an observation on 4 March 2015 at 87 GHz, with no red noise removal applied. *Lower-left panel:* Integrated profile of the same observation as in panel upper-left with the red noise removal applied. *Right panels:* Another example from an observation on 9 March 2015, at 101 GHz. Without the red noise subtraction, the detections would have been much less significant, with the risk of even not exceeding the minimum S/N to consider a detection.

Table 2.1: Summary of the S/T_A^* values for the IRAM 30-m.

ν (GHz)	S/T_A^* (Jy/K)	Uncertainty (per cent)
86	5.9	10
145	6.4	10
210	7.5	20
260	8.4	30
340	10.9	30

GILDAS) include routines to calibrate the observations in a very easy and almost automatic way. Unfortunately, the pulsar observations produced files that were too big to be processed efficiently with these standard software (they worked too slowly or ran into memory problems). My solution consisted on manually calculating the conversion factors from backend counts to flux density units, following the IRAM technical report by Kramer (1997). This required extracting the necessary information from the telescope calibration scans and calculating the scaling factors (from count to Jansky) using custom written code.

The methodology to calibrate our IRAM 30-m data is as follows. First, we select the good calibration scans close to the pulsar observations by reviewing the notes taken during the observing session¹³. A calibration scan was always done just before and after each pulsar observation. Then, we use the MIRA software to extract the necessary information from each calibration scan, and write it into a text file. Table 2.2 shows an example of the extracted information.

Following Kramer (1997), the antenna temperature, T_A^* , can be calculated as

$$T_A^* = \frac{P_{\text{sou}} \cdot T_{\text{cal}}}{G} \text{ [K]}, \quad (2.7)$$

where P_{sou} is the source power in counts, T_{cal} is the calibration temperature in Kelvin, and G is the gain measured in counts. These values are all measured and available when a calibration scan is done with the telescope. The IRAM institute provides a telescope efficiency analysis of the 30-m telescope, which yields the conversion factors from antenna temperature to flux density, S/T_A^* , in units of Jy/K. The information can be looked up in the online wiki of the observatory¹⁴. We summarize it in table 2.1. These S/T_A^* conversion factors are tabulated for certain frequencies only, which are not always the central frequencies used in our observations. By fitting a second-degree polynomial to the available S/T_A^* values (which results in a very good fit) and extrapolating, we obtain values of S/T_A^* at any given frequency of interest within the range 82–330 GHz (see Fig. 2.9).

There are three additional steps that need to be taken into account for a precise flux density calibration. First, because the pulsar observations are relatively long,

¹³For keeping updated observing logs we made use of the very useful Telescope Archive for Public Access System (TAPAS). More information at <https://tapas.iram.es/tapas/>.

¹⁴<http://www.iram.es/IRAMES/mainWiki/Iram30mEfficiencies>

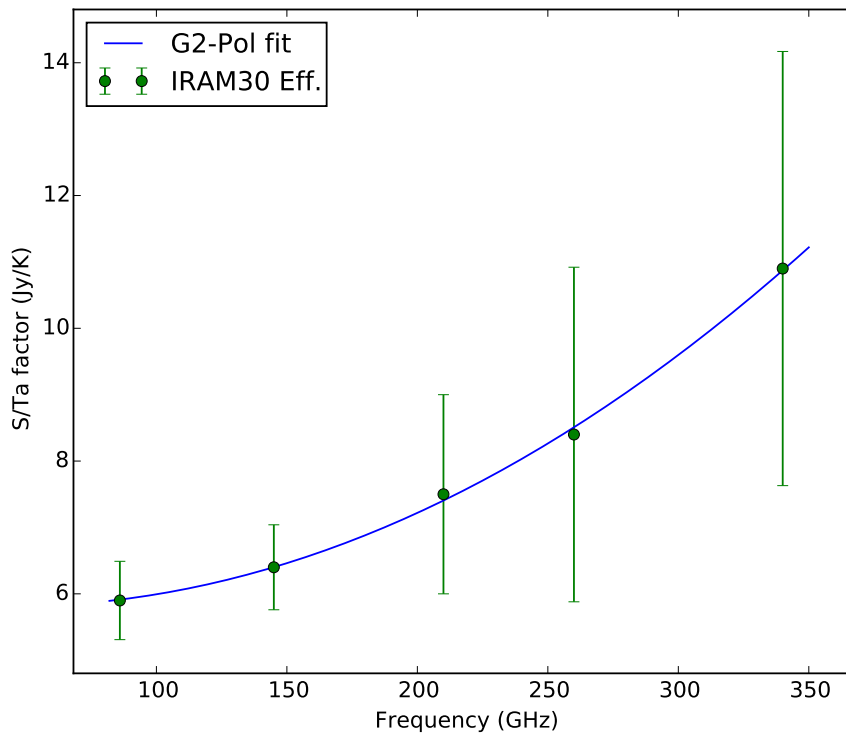


Figure 2.9: Second order polynomial fit on the S/T_A^* provided by IRAM to extrapolate to our frequencies of interest.

Table 2.2: Example of the information extracted from one IRAM 30-m calibration scan using MIRA (Date: 2015-03-04; UTC: 06:53:04.000; Scan: 55; Source: J1745-2900). The columns show the channel number (8 in total, from the 4 central frequencies simultaneously recorded, 2 polarization channels each), receiver code name, backend name and channel, the calibration temperature, the measurement of the gain, the opacity at zenith, the system temperature, the number of counts measured for the room temperature absorber (hot load) and the sky, the telescope elevation, and the receiver temperature. For display purposes, the number of digits in the values have been reduced. The tables used in the numerical analysis use higher precision.

Channel	Receiver	Backend	T_{cal} (K)	G (counts)	τ_z	T_{sys} (K)	P_{hot} (counts)	P_{sky} (counts)	Elevation (deg)	T_{rec} (K)
Channel 0	E0HLS	BBC/1	287.065	438850411	0.02966	109.825	594916340	156065929	23.89	58.012
Channel 1	E0HUS	BBC/2	285.722	413682054	0.03306	124.240	579491702	165809647	23.89	68.047
Channel 2	E0VLS	BBC/3	289.136	399899518	0.02645	106.350	537710857	137811338	23.89	57.673
Channel 3	E0VUS	BBC/4	285.193	423945007	0.03392	118.537	586027750	162082742	23.89	62.604
Channel 4	E1HLS	BBC/5	276.440	333338476	0.04803	137.246	480366481	147028004	23.89	58.766
Channel 5	E1HUS	BBC/6	269.520	380809056	0.05726	154.684	570612322	189803265	23.89	63.621
Channel 6	E1VLS	BBC/7	275.279	395039713	0.04991	125.175	553890165	158850452	23.89	47.785
Channel 7	E1VUS	BBC/8	268.862	363224762	0.05840	144.140	531863612	168638849	23.89	54.619

the measured quantities to perform the calibration (T_{cal} , G , etc.) vary during the observation span. Thus, we interpolate linearly between the values obtained just before and after each pulsar observation and calculate the values corresponding to the middle of the observation. Secondly, the T_{cal} value read from a calibration scan by MIRA is calculated for the zenith, and does *not*¹⁵ take into account the airmass¹⁶ correction. This correction is needed when a source is observed at an elevation lower than 90 deg, because the atmosphere will absorb part of the radiation. The effect is particularly important in our observations, not only because the atmosphere has a significant impact at (sub)millimetre wavelengths, but also because one of our sources of interest, the magnetar SGR J1745–2900, is always seen from the IRAM 30-m observatory at very low elevations (< 25 deg). Therefore, the signal absorption by the atmosphere can be large. The airmass correction is applied to T_{cal} ,

$$T'_{\text{cal}} = T_{\text{cal}} \cdot \exp \left[\frac{\tau_z}{\sin(\text{elevation})} \right] \quad [\text{K}] \quad (2.8)$$

where τ_z is the measured opacity at zenith. Secondly, the gain of the 30-m telescope has a dependence with elevation and frequency (Greve et al., 1998; Peñalver, 2012), resulting in a decrease in gain at lower elevations and toward the highest frequencies. Most of our observations are done at very low elevations and up to very high frequencies, and this gain distortion can reach values of up to ~ 30 per cent. We coded the empirical model presented in Peñalver (2012), calculating the correct gain, G' , as a function of the telescope elevation and observing frequency.

The final *calibration factors*, K , to convert from counts to absolute flux density, are calculated as

$$K = \left(\frac{T'_{\text{cal}}}{G'} \right) \cdot S/T_{\text{A}}^*(\nu) \quad [\text{Jy/count}] \quad (2.9)$$

and, finally, the source absolute flux density, S_{sou} , is

$$S_{\text{sou}} = K \cdot P_{\text{sou}} \quad [\text{Jy}]. \quad (2.10)$$

2.5 Use and commissioning of new receivers

Most of this thesis is driven by the use of new receiver technologies in radio astronomy. Apart from the broadband “Eight MIXer Receiver” used at IRAM 30-m (see Chapters 4, 5, and 6), I worked on the commissioning of the new Ultra-Broad-Band receiver (UBB) and Phased Array Feed (PAF) for the Effelsberg 100-m radio telescope (see Chapter 7). The work with the receivers to be installed at Effelsberg was mostly engineering work, differing somewhat in the methodology from how scientific projects are usually carried out.

¹⁵H. Wiesemeyer, private communication. We note that the airmass corrections are applied in CLASS.

¹⁶Airmass refers to the amount of Earth’s atmosphere that a celestial signal passes through along the line of sight.

The methodology of commissioning new RF receivers focuses on systematic technical tests in order to measure their specifications, both in laboratory measurements and after their installation on the telescope, and to compare them with the design requirements. This includes, for example, measurements of the beam shape, pointing and focus corrections, as well as of different figures-of-merit, i.e. the receiver and system temperature, frequency response, gain, or interference characteristics. The dependence of those characteristics on telescope elevation or RFI situation is also of interest.

Occasionally, modifications to the electronics and/or backends may be necessary, for instance if the RFI environment changes and create stability or sensitivity issues after a receiver has been built (see e.g. Section 7.3.2.2). In these cases, the technical tests are repeated after the adjustments, to verify that the specifications of the upgraded receiver maintain the design requirements.

2.6 Summary and future work

This chapter has presented the main methods and techniques used throughout this thesis, in particular the pulsar search algorithm and the data reduction of millimetre wavelength observations. The main challenges arose from the use of newly developed receivers, technologies that in some cases were applied to the observations of pulsars for the first time (like the EMIR receiver of the IRAM 30-m telescope). In this sense, we had to deal with problems for which, in many cases, we had little or no previous experience. Some examples are the large amount of red noise present in the millimetre pulsar data, the absolute flux density calibration of the IRAM 30-m data, or the fact that the effects of dispersion in the ISM are minimal or negligible at very high radio frequencies.

The pulsar searching observations and data reduction follow a standard methodology whose principles have not changed in decades. However, during this thesis we make use of the most modern algorithms and hardware, which improved our analysis speed and sensitivity to pulsar binaries considerably. New areas where improvement is possible have at the same time been identified. One is the quantitative assessment of the impact of the red noise on the detection of slow spinning pulsars in a blind search performed on our high frequency surveys. This effect is not taken into account in the sensitivity limits presented here or in any other similar work (with exception of [Lazarus et al. \(2015\)](#) for the P-ALFA L-band survey with the Arecibo telescope). A second pending task is the development of a robust method to distinguish RFI from celestial signals when the effect of dispersion is not of help. This should reduce significantly the uncertainty that we face when detecting a “pulsar-like signal” in our high frequency surveys (see Section 3.2.2.3).

The PAF and the UBB receivers at Effelsberg are currently under commissioning, and will be made available to the scientific community after the tests are completed. The commissioning works follow systematics measurements of the specifications and robustness against RFI of the systems. This includes a combination of engineering and scientific work. More details about these commissioning test are presented in Chapter 7.

Searching for pulsar binaries in the Galactic Centre with the Effelsberg 100-m radio telescope

This chapter is based on an article in preparation to be submitted to Monthly Notices of the Royal Astronomical Society when completed. I am the lead author of the article. My main contributions include the development of the pulsar searching pipeline, its installation in the Max-Planck-Gesellschaft's supercomputer Hydra, the processing of the data, the review of the pulsar candidates, the simulations of the impact of extreme accelerations on the signal recovery, and the writing of the article. Most observations were undertaken prior to this work as part of a Galactic Centre pulsar monitoring campaign. I observed on two occasions.

The full list of authors is:

P. Torne, R. P. Eatough, R. Karuppusamy, M. Kramer, and B. Klein

Abstract

Pulsars located in the innermost region of the Milky Way can be excellent tools to improve our understanding of gravity and the Galactic Centre environment. The high stellar densities of the Galactic Centre, that includes many massive stars, increases the probabilities of finding there exotic binaries like pulsars in orbit with stellar-mass black holes or the supermassive black hole Sgr A* itself. Those extreme systems would provide unique laboratories for black hole physics and to test General Relativity. However, and despite many efforts surveying the centre of the Galaxy, only six pulsars have been discovered within 15 arcmin from Sgr A*, and none of them in binary systems. This paucity of discoveries highly contrasts with the high number of pulsars predicted to exist in the region. With the objective of finding the elusive Galactic Centre pulsars, we present a new, multiepoch survey of the Galactic Centre at four different central frequencies, 4.85, 8.35, 14.60, and 18.95 GHz, using the Effelsberg 100-m radio telescope. The data analysis included acceleration searches to increase our sensitivity to binary pulsars. At the moment of writing, 100 per cent of the observations were processed, 100 per cent of the results from the analysis through single pulses were reviewed, and 23 per cent of the candidates from the periodicity search have been inspected, with no new discoveries until now. Although the lack of more discoveries is certainly puzzling, we conclude that we cannot rule out the possibility that the non-detections are simply due to a lack of sufficient sensitivity in our survey.

3.1 Introduction

The Galactic Centre (GC) is a region of particular interest to find pulsars. It contains a $\sim 4.3 \cdot 10^6 M_{\text{sun}}$ compact object at its centre, coincident with the radio source Sgr A*, believed to be a supermassive black hole (SMBH) at a distance of 8.3 kpc (Eckart & Genzel, 1996; Gillessen et al., 2009). Furthermore, the stellar densities in the GC are large and contain many massive stars (Genzel et al., 2010; Pfuhl et al., 2014), the progenitors of neutron stars and black holes. The presence of these massive stars are an indirect indication that pulsars should exist in the GC, and recent works based on previous observations and population analysis estimate in up to ~ 1000 the number of pulsars in the GC (Pfahl & Loeb, 2004; Wharton et al., 2012). Assuming that pulsars are formed in or arrive at the GC, the high stellar densities of the region will increase the interactions between objects. Such interactions have the potential to create a very rich menagerie of binary pulsar systems. Therefore, it is reasonable to expect not only a high number of pulsar binaries in the GC, but also an increased probability of exotic systems, like for instance pulsars orbiting black holes (Faucher-Giguère & Loeb, 2011).

If a detected pulsar in the GC is in a close orbit¹ with Sgr A* or even a lower mass black hole, General Relativity (GR) and other theories of gravity could be tested to an unprecedented precision (Wex & Kopeikin, 1999; Liu et al., 2012, 2014; Psaltis et al., 2016). Additionally, any pulsar, even isolated, is a potential precision tool to study the GC medium properties (e.g. Eatough et al., 2013c; Schnitzeler et al., 2016), and will help to understand better the GC stellar population and evolutionary history.

Many authors have surveyed the GC for pulsars in the past (e.g. Johnston et al., 1995; Kramer et al., 2000; Manchester et al., 2001; Klein, 2005; Johnston et al., 2006; Deneva et al., 2009; Macquart et al., 2010; Bates et al., 2011; Eatough et al., 2013a). In spite of the efforts, only six pulsars were found within 15 arcmin from Sgr A*, none of them in binary systems (Johnston et al., 2006; Deneva et al., 2009; Eatough et al., 2013c). Before the detection of the GC radio magnetar SGR J1745–2900 in 2013 (Mori et al., 2013; Kennea et al., 2013; Eatough et al., 2013c; Shannon & Johnston, 2013), the lack of detections close to the centre of the Galaxy was explained by the strong scattering predicted in the direction of the GC. The temporal pulse broadening time was estimated from electron distribution models to be up to $\tau_s \sim 2000 \nu^{-4}$ s, where ν is the radiation frequency in gigahertz (Cordes & Lazio, 2002). Such “hyperstrong scattering” toward the GC, if real, would render almost any pulsar undetectable at low radio frequencies, specially those spinning fast. Since the frequency dependence of scattering is strong, $\tau_s \propto \nu^{-4}$, the paucity of pulsar discoveries at low frequencies led to more recent surveys to be carried out at higher frequencies, in order to alleviate the negative effects of scattering (e.g. Macquart et al., 2010; Eatough et al., 2013a). The main drawback of observing at high radio frequencies is that pulsars, being typically steep spectrum sources (Maron et al., 2000, $\langle \alpha \rangle = -1.8 \pm 0.2$, for $S_\nu \propto \nu^\alpha$), are much fainter and become more difficult to detect. Thus, we require of the largest and most

¹Close orbits around Sgr A* are those with orbital periods of the order of a year or less. In the case of orbits around stellar-mass black holes, close orbits refer to those with orbital periods of the order a few days or less.

sensitive radio telescopes to carry out pulsar surveys at high radio frequencies.

The hyperstrong scattering scenario toward the GC was put into question by the pulse broadening measurement of the radio emission from SGR 1745–2900 (Spitler et al., 2014), which is by far the closest pulsar to Sgr A* with a projected separation of ≈ 3 arcsec = 0.1 pc (Bower et al., 2015). Spitler et al. (2014) showed that the temporal scattering for this pulsar is much less than the one predicted by Cordes & Lazio (2002), with a measured value of only $\tau_s \sim 1.3 \nu^{-3.8}$ s (Spitler et al., 2014), making it difficult to explain the previous lack of pulsar discoveries due to hyperstrong scattering alone. With such “low” temporal broadening we should already have detected many more pulsars in past surveys, and it is not clear why this has not been the case.

In addition to scattering, other proposed causes for the non-detection of pulsars at the GC include the existence of a singular pulsar population in the region, dominated perhaps by magnetars that rarely emit in radio (Dexter & O’Leary, 2014), or MSPs that are more challenging to detect, since they exist often in binary systems and are much more affected by scattering broadening (Macquart & Kanekar, 2015). It has been even suggested that the lack of detections may be due to the rapid collapse of pulsars into black holes by accretion of dark matter (Bramante & Linden, 2014).

The absence of many more pulsars discoveries despite previous efforts, together with the high predicted number of pulsars in the GC indicates that we do not fully understand yet the scattering medium in this direction, nor the population of pulsars that may exist there. The single recent discovery of the radio magnetar SGR J1745–2900, an inherently rare object, within one parsec of the central black hole suggests the existence of a much larger GC population of more common pulsars. Despite all these uncertainties, the unique and extraordinary scientific potential of finding new pulsars located in the GC justify further and continuous efforts to survey the region; particularly as new observational hardware that can exploit larger bandwidths becomes available.

Whereas the scattering could still have hindered the detections of pulsars in previous surveys, in particular of millisecond pulsars (MSPs) due to their very short spin periods, the processing of the data did not include a full search in the acceleration parameter space. Consequently, previous works may not have been sensitive to pulsars in tight binary systems or orbiting very massive companions (such as other neutron stars, stellar-mass black holes or Sgr A*), which may be the dominant pulsar population of the GC given its high stellar densities.

With the objective of finding new pulsars in the GC, and with emphasis in highly-accelerated pulsar binary systems, we present a new, multiepoch, multifrequency Galactic Centre pulsar survey at frequencies 4.85, 8.35, 14.60, and 18.95 GHz. The observing frequencies used in our observations are high in order to alleviate the scattering effects toward the GC, and the data analysis used a newly developed searching pipeline with capabilities to detect pulsars in binary systems over a large range of accelerations.

3.2 Observations and data analysis

3.2.1 Observations

The observations analysed here were made with the Effelsberg 100-m radio telescope between February 2012 and December 2015. The data in 2012 were taken at 18.95 GHz, centred at the position of Sgr A* ($\text{RA}_{\text{J2000}} = 17^{\text{h}} 45^{\text{m}} 40^{\text{s}}.0$, $\text{Dec}_{\text{J2000}} = -29^{\circ} 00' 28''.1$), as part of a dedicated Galactic Centre survey for pulsars (Eatough et al., 2013a). After the discovery of the radio pulsations from the Galactic Centre magnetar SGR J1745–2900 in 2013 (Eatough et al., 2013c; Shannon & Johnston, 2013), a monitoring programme of this object started at Effelsberg. From that epoch, the telescope pointed at the best X-ray position of SGR J1745–2900 ($\text{RA}_{\text{J2000}} = 17^{\text{h}} 45^{\text{m}} 40^{\text{s}}.2$, $\text{Dec}_{\text{J2000}} = -29^{\circ} 00' 30''.4$; Rea et al., 2013b), with Sgr A* still within the beam. Different receivers were used to get multifrequency data, with central frequencies of 4.85, 8.35, 14.60 and 18.95 GHz. The respective beam sizes of 155, 90, 52 and 40 arcsec, still covered the Galactic Centre located approximately 3 arcsec away from the magnetar (Rea et al., 2013b). The impact on the sensitivity of the misalignment is negligible and we piggybacked the magnetar monitoring observations to continue the survey. The search data were recorded with the Effelsberg Pulsar Fast-Fourier-Transform Spectrometer (PFFTS) backend for 4.85, 8.35 and 14.60 GHz, with a sampling time of $65.536 \mu\text{s}$ and 128 spectral channels across 500 MHz of bandwidth. For 18.95 GHz, a different Fast-Fourier-Transform Spectrometer was used (namely the XFFTS backend), with a sampling time of $128 \mu\text{s}$ and 256 channels across 2 GHz of bandwidth. The flux density calibration at 4.85, 8.35, 14.60 GHz was done by using a calibrated noise diode and comparing it to NGC7027. No calibration data were taken for 18.95 GHz. The total dataset analysed is composed of 110 epochs amounting to ~ 146 hr on the GC. The repetition of the observations are a major advantage with respect to previous similar surveys because this way we increase the probability of detecting pulsars that may suffer of time-dependent effects that could hinder their detection, like for instance geodetic precession or under-optimal (for the search algorithms, see Section 3.2.2.2) orbital binary phases. Moreover, the multiepoch dataset also increase our chances to detect transient events, like giant pulse emission for example. Table 3.1 presents a summary of the observations analysed in this work.

Table 3.1: A list of the observations of the Galactic Centre analysed in this survey. The last column reports the detection of the Galactic Centre magnetar SGR J1745–2900, showing how this pulsar turned on suddenly its radio emission in April 2013.

Date	MJD	ν_{c} (GHz)	T_{obs} (hr)	SGR J1745–2900 detection?
2012 Feb 01	55958.3039699	18.95	2.2	No
Feb 02	55959.2952430	18.95	2.4	No
Feb 11	55968.2850231	18.95	2.1	No
Feb 12	55969.2641688	18.95	2.5	No
Mar 01	55987.2199189	18.95	2.5	No

Date	MJD	ν_c (GHz)	T_{obs} (hr)	SGR J1745–2900 detection?
Mar 02	55988.2158796	18.95	2.1	No
Mar 09	55995.1972800	18.95	2.5	No
Mar 16	56002.1914699	18.95	2.1	No
Mar 17	56003.1738194	18.95	2.4	No
Mar 18	56004.1702314	18.95	2.4	No
Mar 19	56005.1669675	18.95	2.4	No
Mar 20	56006.1652083	18.95	2.5	No
Mar 24	56010.1538310	18.95	2.4	No
Apr 13	56030.1062499	18.95	2.3	No
Sep 28	56198.6374305	18.95	2.4	No
Oct 08	56208.6126041	18.95	2.4	No
Dec 13	56274.4433564	18.95	2.1	No
Dec 18	56279.4483217	18.95	1.7	No
Dec 19	56280.4277777	18.95	2.1	No
2013 Apr 28	56410.0657638	4.85	1.1	Yes
Apr 28	56410.1184259	14.60	1.0	Yes
May 02	56414.0495370	8.35	2.4	Yes
May 04	56416.0458101	8.35	1.2	Yes
May 04	56416.1029976	4.85	1.0	Yes
May 05	56417.0427430	8.35	0.7	Yes
May 05	56417.0812384	4.85	1.5	Yes
May 06	56418.0395023	14.60	1.0	Yes
May 06	56418.0909606	8.35	1.1	Yes
May 07	56419.0366898	18.95	2.4	Yes
May 08	56420.0318287	8.35	1.2	Yes
May 08	56420.0808680	4.85	1.2	Yes
May 12	56424.0438194	8.35	0.6	Yes
May 12	56424.0687847	4.85	0.6	Yes
May 12	56424.0935995	4.85	0.1	Yes
May 14	56426.0163310	8.35	1.2	Yes
May 14	56426.0668865	4.85	1.2	Yes
Jun 13	56456.9318287	14.60	1.2	Yes
Jun 14	56456.9817129	4.85	1.2	Yes
Jun 17	56460.9248263	8.35	1.1	Yes
Jun 18	56460.9731249	4.85	1.1	Yes
Jul 14	56487.8749305	8.35	0.7	Yes
Jul 14	56487.9036458	4.85	1.0	Yes
Jul 21	56495.8256712	8.35	1.2	Yes
Jul 21	56495.8753009	4.85	1.2	Yes
Jul 26	56499.8194791	1.21	2.3	Yes
Aug 20	56524.7467824	8.35	1.2	Yes

Date	MJD	ν_c (GHz)	T_{obs} (hr)	SGR J1745–2900 detection?
Aug 20	56524.7990000	4.85	1.1	Yes
Aug 21	56525.7434027	1.21	2.4	Yes
Sep 12	56547.7115625	8.35	0.8	Yes
Sep 12	56547.7434027	4.85	1.0	Yes
Sep 22	56557.6565740	14.60	1.2	Yes
Sep 22	56557.7059722	8.35	1.2	Yes
Dec 14	56640.4291319	8.35	1.2	Yes
Dec 14	56640.4777083	4.85	1.3	Yes
2014 Feb 27	56715.2718171	4.85	1.3	Yes
Mar 07	56723.2400925	4.85	0.7	Yes
Mar 10	56726.1952777	8.35	1.2	Yes
Mar 10	56726.2457407	4.85	1.2	Yes
Apr 04	56751.1283333	8.35	1.2	Yes
Apr 04	56751.1794212	4.85	1.2	Yes
Apr 07	56754.1181944	8.35	1.2	Yes
Apr 07	56754.1682060	4.85	1.2	Yes
May 12	56789.0218749	8.35	1.2	Yes
May 12	56789.0727777	4.85	1.2	Yes
May 28	56804.9785185	8.35	1.2	Yes
May 28	56805.0288657	4.85	1.2	Yes
Jun 22	56830.9072106	8.35	1.2	Yes
Jun 22	56830.9579398	4.85	1.2	Yes
Jul 22	56860.8446990	8.35	0.8	Yes
Jul 22	56860.8768750	4.85	1.0	Yes
Jul 23	56861.8238541	8.35	1.1	Yes
Jul 23	56861.8737615	4.85	1.1	Yes
Jul 24	56862.8710995	8.35	1.1	Yes
Jul 24	56862.8205092	4.85	1.1	Yes
Aug 26	56895.7334490	8.35	1.2	Yes
Aug 26	56895.7822453	4.85	1.0	Yes
Sep 10	56910.6896990	8.35	1.2	Yes
Sep 10	56910.7416319	4.85	1.1	Yes
Oct 03	56933.6290509	8.35	1.2	Yes
Oct 03	56933.6824421	4.85	1.1	Yes
Oct 10	56940.6083680	8.35	1.2	Yes
Oct 10	56940.6613888	4.85	1.1	Yes
Oct 24	56954.5702777	8.35	1.2	Yes
Oct 24	56954.6232870	4.85	1.1	Yes
Nov 16	56977.5087152	8.35	1.2	Yes
Nov 16	56977.5617245	4.85	1.1	Yes
Dec 14	57005.4374305	8.35	1.0	Yes

Date	MJD	ν_c (GHz)	T_{obs} (hr)	SGR J1745–2900 detection?
Dec 14	57005.4837962	4.85	1.1	Yes
2015 Feb 01	57054.3096180	14.6	0.5	Yes
Feb 01	57054.3315856	8.35	0.7	Yes
Feb 01	57054.3664236	4.85	0.5	Yes
Mar 01	57082.2983101	4.85	0.4	Yes
Mar 04	57085.2113541	8.35	1.2	Yes
Mar 04	57085.2643749	4.85	1.2	Yes
Mar 06	57087.2193750	8.35	1.0	Yes
Mar 06	57087.2641782	4.85	1.0	Yes
Mar 08	57089.2018634	8.35	1.2	Yes
Mar 08	57089.2549074	4.85	1.1	Yes
Mar 10	57091.1945949	14.6	1.2	Yes
Mar 10	57091.2468749	8.35	1.1	Yes
Apr 11	57123.1090972	8.35	1.2	Yes
Apr 11	57123.1621527	4.85	1.1	Yes
Jul 20	57223.8326620	8.35	1.2	Yes
Jul 20	57223.8856712	4.85	1.2	Yes
Sep 11	57276.6870717	8.35	1.2	Yes
Sep 11	57276.7400925	4.85	1.2	Yes
Oct 31	57326.5546875	8.35	1.2	Yes
Oct 31	57326.6076967	4.85	1.1	Yes
Dec 30	57386.3870138	8.35	1.1	Yes
Dec 30	57386.4448379	4.85	1.1	Yes

3.2.2 Data analysis

3.2.2.1 Pulsar searching pipeline

The data were analysed using the Max-Planck-Gesellschaft Supercomputer *Hydra*² and a pulsar searching pipeline based on the PRESTO³ software (Ransom, 2001). The acceleration search step, which dominates the CPU time, is performed on the GPU-enabled version of the programme `accelsearch`⁴. The data processing was as follows.

First, the observations at 4.85 and 8.35 GHz are downsampled in time by a factor 4 and 2, to 262.144 and 131.072 μs , respectively, because of the pulse broadening expected due to the scattering toward the GC (Spitler et al., 2014). The downsampled data keeps the maximum achievable time resolution (dominated by the expected scattering), while the reduced data size speeds up the processing of these bands considerably (roughly by a factor of 4 and 2, respectively).

²<http://www.mpcdf.mpg.de/services/computing/hydra>

³<https://github.com/scottransom/presto>

⁴https://github.com/jintaoluo/presto2_on_gpu

Next, a full-length observation (usually of ~ 1.2 or ~ 2.4 hr) is recursively split into segments of half the observing time down to a minimum segment length of ~ 4.5 min. These segmentations are necessary to be sensitive to pulsars with short orbital periods because the algorithms utilized by PRESTO can best recover periodic signals with an acceleration when this acceleration is constant over the length of the observation. A good rule of thumb, applicable only for circular orbits and less valid if the orbit is eccentric or the acceleration of the pulsar is very high⁵, is to assume that the acceleration of a pulsar in a binary orbit will remain constant within portions of ~ 10 per cent of the orbit (see Johnston & Kulkarni, 1991; Ransom et al., 2003; Ng et al., 2015). Following this rule, we are most sensitive to pulsars with orbital periods longer than $\sim 0.75, 1.5, 3, 6, 12,$ or 24 hr, depending on the data segment searched (see Table 3.3). The increase in sensitivity to shorter orbital periods by reducing the observation length comes at the cost of an increase in the minimum flux densities that can be detected, as the observing length in the shorter segments is smaller (assuming radiometer noise, $S_{\min} \propto T_{\text{obs}}^{-1/2}$). This partially-coherent segmented acceleration search scheme is a good way to cover a large range of different accelerated systems and orbital periods. It was first applied to the Parkes Multibeam Pulsar Survey (Eatough et al., 2013b), and later to the the Galactic Plane region of the High-Time-Resolution-Universe South survey (Ng et al., 2015), both with time domain acceleration searches.

For each of the segments, a mask in time and frequency across the filterbank of data potentially affected by Radio Frequency Interference (RFI) is created with the programme `rfifind`. Additionally, a list of periodicities to be excluded from the analysis is prepared, including the mains frequency fundamental at 50 Hz with some strong harmonics and the magnetar SGR J1745–2900 spin frequency with its first 32 integer harmonics. The data are then barycentred and dedispersed to time series assuming different dispersive delays starting at a trial dispersion measure (DM) of $800 \text{ cm}^{-3} \text{ pc}$, with the final trial DM value, and the number and size of the steps dependent on the frequency of observation. The dedispersion plans are computed using the `DDplan.py` tool. At this stage, a search for single pulses above a threshold of 6σ is performed on the longest available dedispersed time series using `single_pulse_search.py`.

All the dedispersed time series are then Fourier transformed using the Fast Fourier Transform (FFT) algorithm, corrected for an excess of red noise and searched for periodic signals. To be sensitive to accelerated signals, PRESTO uses an estimation of the “spread” of the power of a periodic signal in the Fourier domain due to the acceleration produced by an orbital motion. The total power (or most of it) is recovered by applying the inverse effect using a matched filter (Ransom et al., 2002). The maximum of the z -value, or z_{max} parameter, of the routine `accelsearch`, which controls the maximum number of Fourier bins where to apply the matched filters, is defined as $z = a T_{\text{obs}}^2 / P c$, where a is the maximum acceleration of the pulsar on the line-of-sight, T_{obs} is the observation length, P is the shortest period to be detected (i.e. the period of the highest harmonic), and c is the speed of light. This parameter is set to 1200 in our pipeline,

⁵A very high acceleration translates into a high *jerk* in some orbital phases that can break down the assumption of the constant acceleration of “the 10 per cent rule” (see Section 3.2.2.2 for more details).

Table 3.2: Summary of the data properties and searching parameters at each frequency band. ν_c is the central observing frequency, $\Delta\nu$ the total bandwidth, t_{samp} is the sampling time, N_{ch} the number of frequency channels, DM range shows the DM values covered, and z -value the maximum number of Fourier bins used with the matched filters to recover accelerated signals (see text).

ν_c (GHz)	$\Delta\nu$ (GHz)	t_{samp} (μs)	N_{ch}	DM range ($\text{cm}^{-3} \text{pc}$)	z -value
4.85	0.5	262.144	128	800–11900	1200
8.35	0.5	131.072	128	800–15080	1200
14.60	0.5	65.536	128	800–10800	1200
18.95	2.0	128	256	800–21200	1200

the maximum allowed by the software. During the periodicity search step, harmonic summing is applied, with up to 16 harmonics summed for non-accelerated signals, and up to 8 harmonics in the other case. The filter matching algorithm of PRESTO has the advantage of being sensitive simultaneously to slow spinning pulsars with high accelerations, and fast spinning pulsars with lower acceleration ranges, because of the trade-off in the z -value between these quantities. We note that the large acceleration ranges used in this search, that are key to be sensitive to the most extreme pulsar binaries, were mainly possible thanks to the newly developed GPU-powered pipeline. Otherwise, with the computational resources available at the time⁶ the computation would have taken too long to be processed in time for this thesis. Table 3.2 shows a summary of the data and searching set-up.

After the periodicity and acceleration searches, all the detected signals are sifted to select only those above a threshold of harmonically summed power of 6σ , removing in the process the duplicated (i.e. detected at different DMs and accelerations) and the harmonically related candidates.

Finally, the folding and creation of pulsar candidate evaluation plots is done for up to 150 candidates per segment. The folding and plotting step is done twice per candidate, one time letting the programme `prepfold` to optimise the parameters of the candidate and a second time without optimisation. This is necessary because the parameter optimization step can improve the detection significance of a candidate, especially those accelerated, but it has the risk of being confused by an interference signal close to the candidate spin period, in which case the candidate is lost. This makes the folding and plotting process more robust against RFI.

3.2.2.2 Analysis of the acceleration detection capabilities of the pipeline

As already discussed, the acceleration search algorithm of PRESTO works optimally when the acceleration stays constant during the observation. The change in acceleration within an observation (i.e. the acceleration derivative, also known as *jerk*) can decrease

⁶The Fundamental Physics group of the MPIfR has recently acquired a new CPU-based computing cluster, named *Hercules*, but this was not available when the data processing was started.

the effectiveness of the matching filtering technique because it is an effect not taken into account by the software. The magnitude of the jerk mainly depends on three factors: the maximum acceleration of the pulsar, the length of the observation, and the orbital phase that the observation covers. Furthermore, to complicate further the analysis the maximum detectable acceleration in an observation also depends on the observation length through the z -value of `accelsearch`. Decreasing the length of an observation is advantageous to recover a given acceleration because it decreases the negative effects of the jerk and also the required z -value. Unfortunately, this also decreases the sensitivity to the pulsars. Therefore, with our searching method there is always a trade-off between sensitivity in terms of flux density (that increases with longer observing lengths), and in terms of acceleration correction (that improves for shorter observing lengths).

We analysed this trade-off in more detail by first calculating the theoretical maximum spin frequency (i.e. the shortest spin period) that our searching pipeline can recover. Calculated from the definition of the z -value:

$$\nu_{\text{spin}}^{\text{max}} = \frac{c z}{a_{\text{max}} T_{\text{obs}}^2} \frac{1}{N_{\text{harm}}}, \quad (3.1)$$

where $\nu_{\text{spin}}^{\text{max}}$ is the theoretical maximum *fundamental* spin frequency than can be fully recovered, c is the speed of light, z is `accelsearch`'s z -value (set to 1200 in our case), T_{obs} is the observation length, and N_{harm} is the maximum number of harmonics to be detected. Through a_{max} , there is also a dependency of the maximum recoverable spin frequency on the masses of the pulsar and the companion, the orbital inclination and, in the case of eccentric orbits, also on the eccentricity. We will focus here on circular orbits to simplify the analysis⁷. Deriving from third Kepler's law, the maximum acceleration for a circular orbit is:

$$a_{\text{max}} = \left[G (M_{\text{p}} + M_{\text{c}}) M_{\odot} (2\pi)^4 \right]^{1/3} P_{\text{B}}^{-4/3} \sin i, \quad (3.2)$$

where G is the Gravitational constant, M_{p} and M_{c} are the masses of the pulsar and the companion, respectively, P_{B} is the orbital period, and i is the orbital inclination with respect to the plane of the sky. For our calculations, we fix the mass of the pulsar to $M_{\text{p}} = 1.4M_{\odot}$ and the orbital inclination to $i = 60$ deg. For the mass of the companion we consider three different scenarios, illustrative of the kind of binaries that we aim to discover: a pulsar in orbit around Sgr A* ($M_{\text{c}} = 4.3 \cdot 10^6 M_{\odot}$), a pulsar in orbit with a stellar-mass black hole ($M_{\text{c}} = 8M_{\odot}$), and a double neutron star system ($M_{\text{c}} = 1.4M_{\odot}$). Due to the dependency of the maximum spin frequency on T_{obs} and N_{harm} (see Equation 3.1) we have considered different integration lengths, representative of different segment lengths used in our survey, and four and eight as the number of summed harmonics. Figure 3.1 shows the maximum recoverable fundamental spin frequency for the different combinations of assumed parameters. Clearly, the lower

⁷Although circular orbits are a particular case of binary orbit and it is very likely that many pulsars in the Galactic Centre are instead in eccentric orbits, we note that in such cases the pulsar will spend most of the time in the low-accelerated part of the orbit, very likely with less acceleration than in the circular orbit case that we consider.

the observing time and number of harmonics to detect, the higher the accelerations and spin frequencies that can be detected. One remarkable fact is the non-linear relation between the maximum acceleration and the orbital period. Since $a_{\max} \propto P_{\text{B}}^{-4/3}$, the increase in maximum acceleration as the orbital period decreases grows rapidly, making the detection of pulsars in the shortest orbits additionally challenging. Note that what is considered a “short” orbit depends on the maximum acceleration reached by the pulsar (related to the mass of the companion), and there is no fixed range of orbital periods than can in general be defined as short or long. This is shown by comparing the three different panels of Figure 3.1. For example, an orbital period of 5 hr will imply very different acceleration ranges if the pulsar companion is a black hole, rather than for example another neutron or a lower-mass star.

Unfortunately, for the highly accelerated pulsars that we want to detect, the jerk may affect our sensitivity to the accelerated signals significantly. The effect of the jerk is expected to be stronger at the phases of the orbit where the acceleration is lowest, because it is at those orbital phases when the jerk is higher. To estimate the jerk impact and evaluate the capabilities and limitations of our searching method, we used a modified version of SIGPROC’s `fake` to simulate a 500-ms pulsar in a 50-hr orbit⁸ around Sgr A* and applied our acceleration search for different observation lengths. We compared the σ of the detection in the Fourier search (as reported by `accelsearch`) with the σ of the same pulsar isolated. The results of the simulation are shown in Figure 3.2. We find once more than the dependency with the observation length is strong. For the case of an observing time of 0.6 hr (36 min), the acceleration is corrected and the jerk does not affect the signal recovery (see top panel of Figure 3.2). When the observing length increases, the risk of a higher jerk also increases (as the acceleration can change more in a longer segment of time). In our example with an integration length of 1.2 hr (72 min) the effect of jerk is clear, decreasing the σ of the detection at those orbital phases where the jerk is high (see middle panel of Figure 3.2). We remark that the loss of sensitivity due to jerk in this extreme case occurs even when $T_{\text{obs}} = 0.024 P_{\text{B}}$, showing that not always the assumption of the 10 per cent rule holds. In addition, this result demonstrates the importance of carrying out repeated observations in order to cover different orbital phases of potential pulsars highly accelerated. With a reduced number of observations, there is the risk of covering only an “under-optimal” orbital phase where the jerk is high enough to decrease significantly our sensitivity, with the consequent risk of missing the pulsar in the blind search.

As a final check, we simulated a 1-ms pulsar in a 1-yr circular orbit around Sgr A*, verifying that for 1-yr orbits (or longer), our searching pipeline is sensitive to even the fastest spinning pulsars. This analysis focused on three orbital phases, corresponding to the parts with maximum acceleration (minimum jerk), minimum acceleration (maximum jerk), and the intermediate orbital phase between those two cases. Those three cases are representative of the full orbit, and the results showed that the signal recovery is always above 75 per cent, with up to 8 harmonic detected. In the case that

⁸We chose a 50-hr orbit under the condition that the inspiralling time (due solely to gravitational wave emission and neglecting disturbances by interactions with other objects) is of the order of the typical lifetime of a normal pulsar, i.e. ~ 1 Myr.

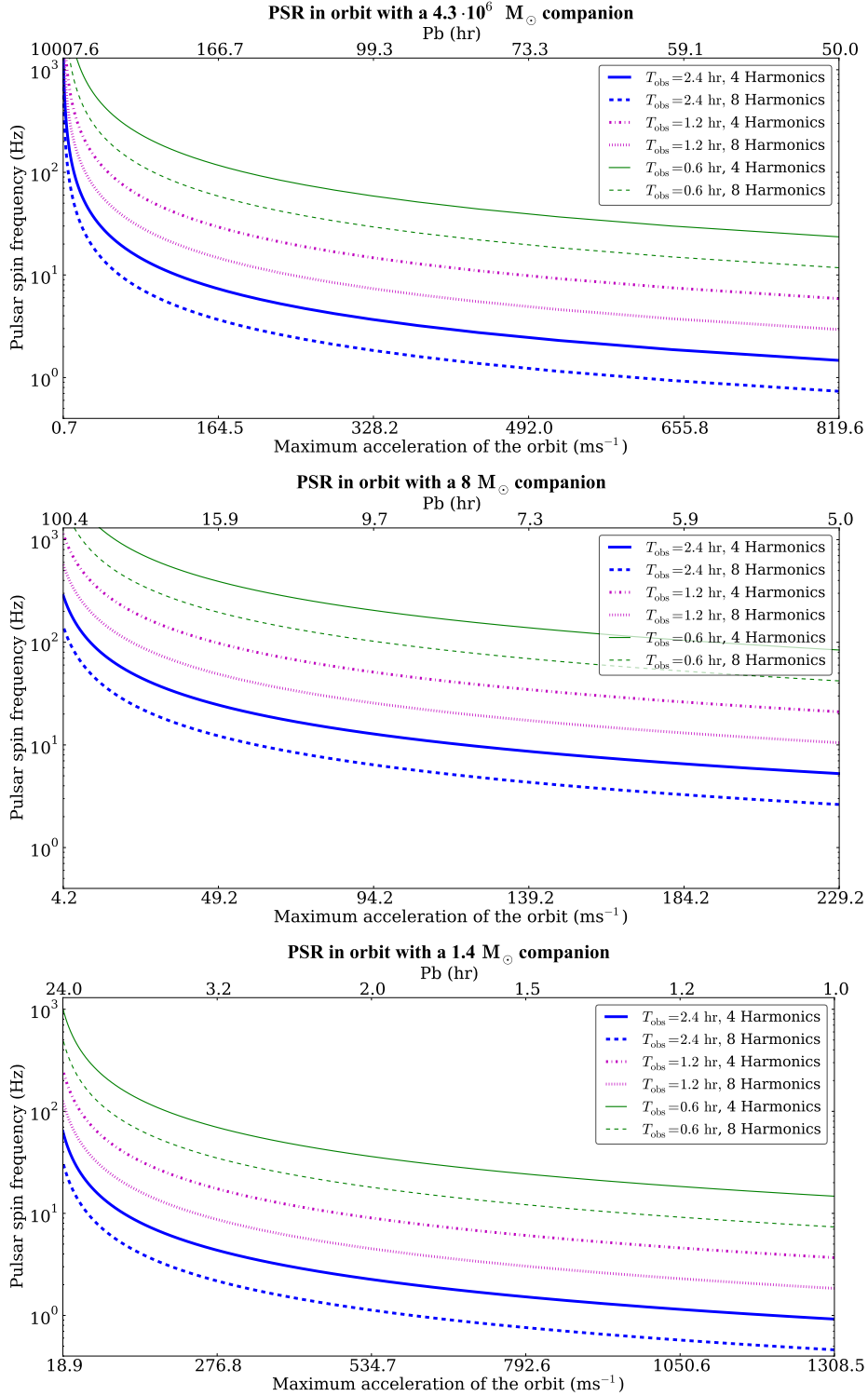


Figure 3.1: Theoretical maximum detectable pulsar spin frequency for a given orbital period, observation length, and number of harmonics recovered (see Equation 3.1). Three different scenarios are compared. *Top panel:* The pulsar orbits around Sgr A*, i.e. $M_c = 4.3 \cdot 10^6 M_\odot$. *Middle panel:* The pulsar orbits a stellar-mass black hole of $M_c = 8 M_\odot$. *Bottom panel:* The companion is another neutron star of $M_c = 1.4 M_\odot$. Note that the considered orbital periods differ in each scenario. This analysis assumes that the acceleration stays constant across the observation, which may not hold for extremely accelerated systems or long observations (see text and Figure 3.2).

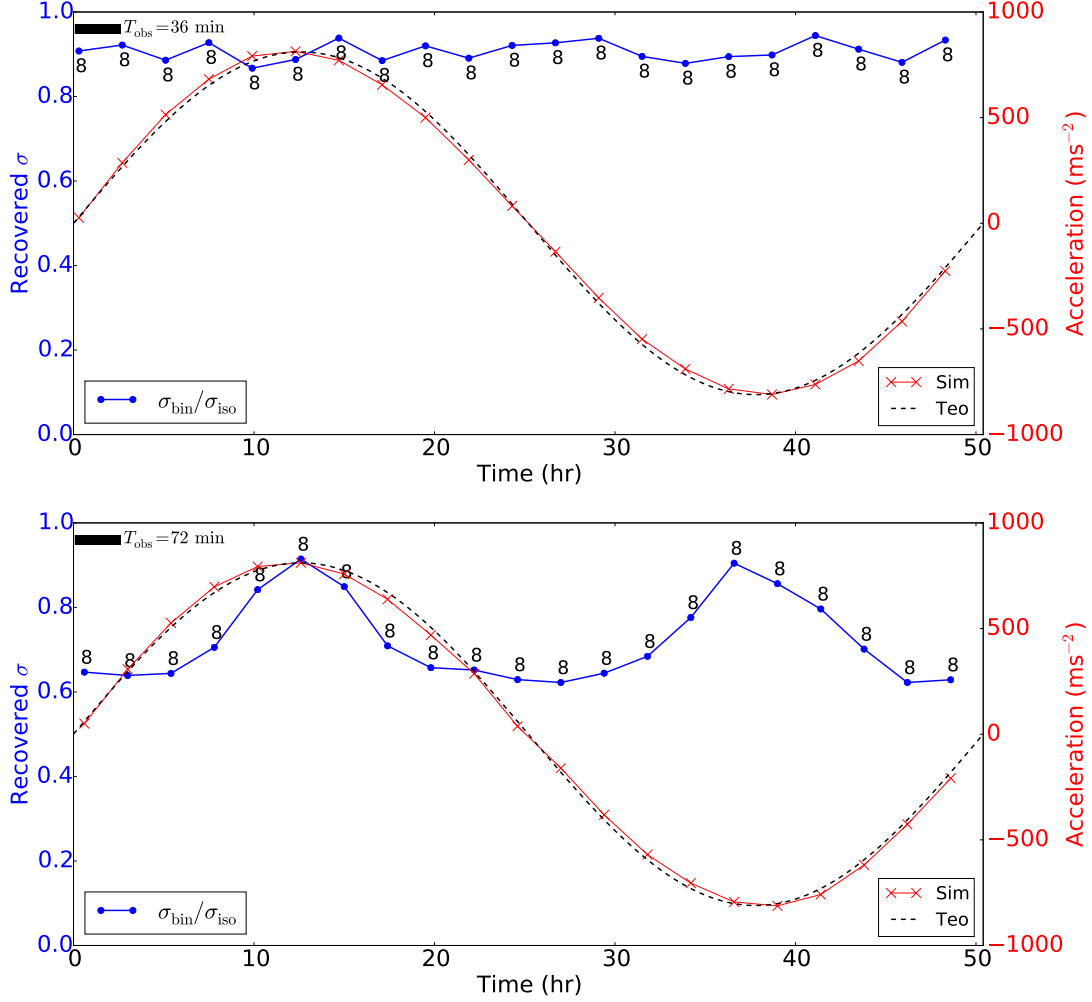


Figure 3.2: Signal recovery of an extreme binary consisting of a 500-ms pulsar in a 50-hr orbit around Sgr A*. Both the recovered σ (normalized to the optimum case of the same pulsar being isolated) and the line-of-sight acceleration (theoretical and detected) are plotted across the full orbit. The numbers near each point indicates the recovered harmonics. *Top panel*: The observation length is only 36 min (0.6 hr), the acceleration can be corrected in all the orbital phases and the jerk does not affect the sensitivity significantly. *Bottom panel*: The observing time is doubled to 72 min (1.2 hr), and even when the acceleration should be corrected completely (cf. top panel Figure 3.1), the jerk starts to decrease the sensitivity in under-optimal orbital phases, i.e. where the acceleration is low but the jerk is high.

the orbital period is longer or the pulsar spins more slowly, the recovery of the signal will be even better.

In conclusion, our searching pipeline is capable to detect the pulsar binaries considered. Nonetheless, in the most extreme cases this acceleration correction method is not capable to fully recover the pulsar signals, which mainly occurs when the integrations are too long (with respect to the orbital period), the pulsar spin period is too short, and/or the acceleration or jerk reach extremely high values (see Figures 3.1 and 3.2). In these worst-case scenarios, a considerable fraction of the sensitivity to the pulsar signal is lost, and for this reason the applied segmentation search scheme increases our probabilities to detect even the most challenging pulsar binaries.

3.2.2.3 Challenges of searching at high radio frequencies

The observations of pulsars at frequencies above a few gigahertz present some new challenges and problems compared to observations at lower frequencies. For example, the atmospheric contribution is usually neglected in typical pulsar observations between 1–2 GHz, but can have a non-negligible impact above ~ 5 GHz (see e.g. Wilson et al., 2013). The atmosphere not only contributes itself to the system noise, it also absorbs part of the astronomical signal, both effects decreasing the sensitivity of the observations. The atmospheric contribution can also increase the power of the low-frequency component of the noise (also called red noise), due to variations in the atmospheric physical conditions, that have typical time scales from fractions of a second to several minutes.

An additional issue is the Radio Frequency Interference (RFI). The *external* man-made interference at high radio frequencies is generally less prominent than at lower frequencies, but we still note important RFI signals in our datasets. At frequencies above a few gigahertz, satellite emission seems to be a common source of interference. For example, in the 18.95 GHz data we detect very strong pulses in our time series that could be due to a satellite passing through the main telescope beam or the side lobes. Because of the tiny dispersive delay corrections applied at these high frequencies (see Equation 1.20), often the RFI is detected not only at $DM=0$, but at many different dispersion values, confusing especially the single pulse search by producing false positives at $DM \neq 0$. The low dispersion, not only at 18.95 GHz, but also in the other frequency bands imposed a big challenge when discriminating celestial signals from terrestrial interference. In many cases, and specially for long period or long duty cycle signals, a detected candidate is consistent with a broad range of DM values, including very low DMs or even zero. Figure 3.3 presents one example of a strong RFI signal that is detected as a candidate at a non-zero DM. To make our signal examination more robust we required of new ways of assessing the likeliness of a signal to be celestial. Our strategy to evaluate the validity of the pulsar candidates is described in the next subsection.

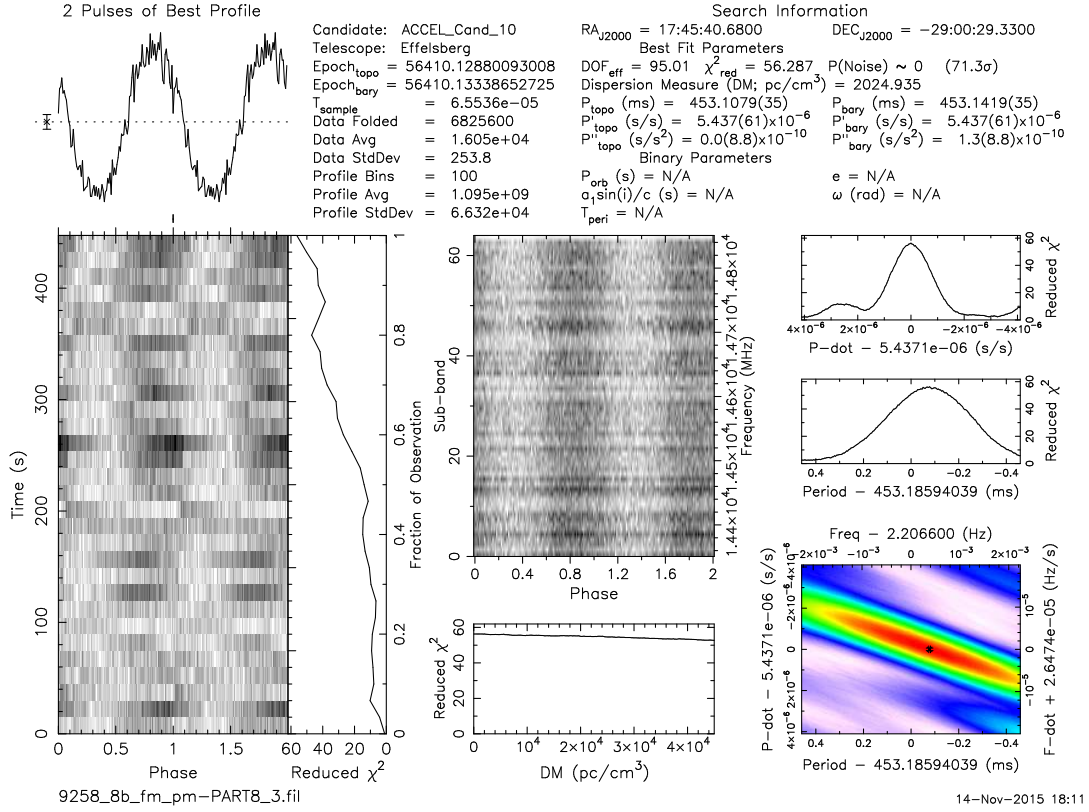


Figure 3.3: Example of candidate at a $DM \neq 0$ produced by RFI. The candidate is detected with a high DM value of $2024.935 \text{ pc cm}^{-3}$ due to the low effects of dispersion at high radio frequencies. (For a detailed explanation of the information presented in this plot, we refer the reader to Figure 2.3.)

3.2.2.4 Candidate examination

The segmented search scheme used to be sensitive to short binary orbits led to a large number⁹ of candidates per observation. To reduce the total number of candidates to be examined we applied the following methodology, which combines manual checks with computer-aided algorithms. First, we apply the UBC PICS¹⁰ pattern recognition artificial intelligence (AI) algorithm (Zhu et al., 2014) to all the candidates in one observation (i.e. to all the segments together) and we examine all the scored candidates above a threshold of 0.5. Secondly, we sift on the resulting candidates of all the segments and create a “best candidates” list with all the candidates with a harmonically summed significance above 6σ , removing the repetitions between segments. We manually inspect the 100 most significant candidates of this list. A third step is to use PEACE¹¹ (Lee et al., 2013) to score this “best candidate” list and manually inspect the 100 highest scored candidates. In a fourth step, we use a customized version of `combustible-lemon`¹², a graphical tool to plot and inspect candidate attributes, and examine the candidates that, after folding, show a significance above $\sim 10\sigma$. On each of these steps the interesting candidates are written to a database.

A final step is made after the results from different epochs have been reviewed with the previous strategy. We use the database of saved best candidates and produce a histogram with the periods found in order to look for repetitions. A real pulsar is expected to be detected several times in our large dataset, so this is a first indication on what signals are worth following up. Additionally, we create a period versus period derivative ($P - \dot{P}$) diagram of all the candidates. The objective is to exploit the barycentring conversion step and large time span of our dataset: a real, isolated pulsar should stay in the same position of this diagram, or if in a binary, would follow an elliptical curve (or a more complex curve if the system had eccentricity, see Freire et al., 2001). In contrast, local persistent signals should move exclusively on, or very close to, the period axis due to the barycentering conversion that we apply to each observation.

3.3 Results

At the moment of writing the processing of the data is completed, 100 per cent of the single pulse analysis results have been reviewed, and 23 per cent of the resulting candidates from the periodicity search have been inspected. From this subset of results, no new pulsars have been detected. The magnetar SGR J1745–2900, even when its fundamental and first 32 integer harmonics are masked in the search, is recurrently detected in the periodicity search through some of its fractional harmonics (see Figure 3.4). Furthermore, it is also detected through its single pulses in the single pulse search (see Figure 3.5). The detections of SGR J1745-2900 are a good indication that

⁹up to 18900 candidate plots per observation.

¹⁰https://github.com/zhuww/ubc_AI

¹¹<http://sourceforge.net/p/pulsareace/wiki/Home/>

¹²<https://github.com/ewanbarr/combustible-lemon>

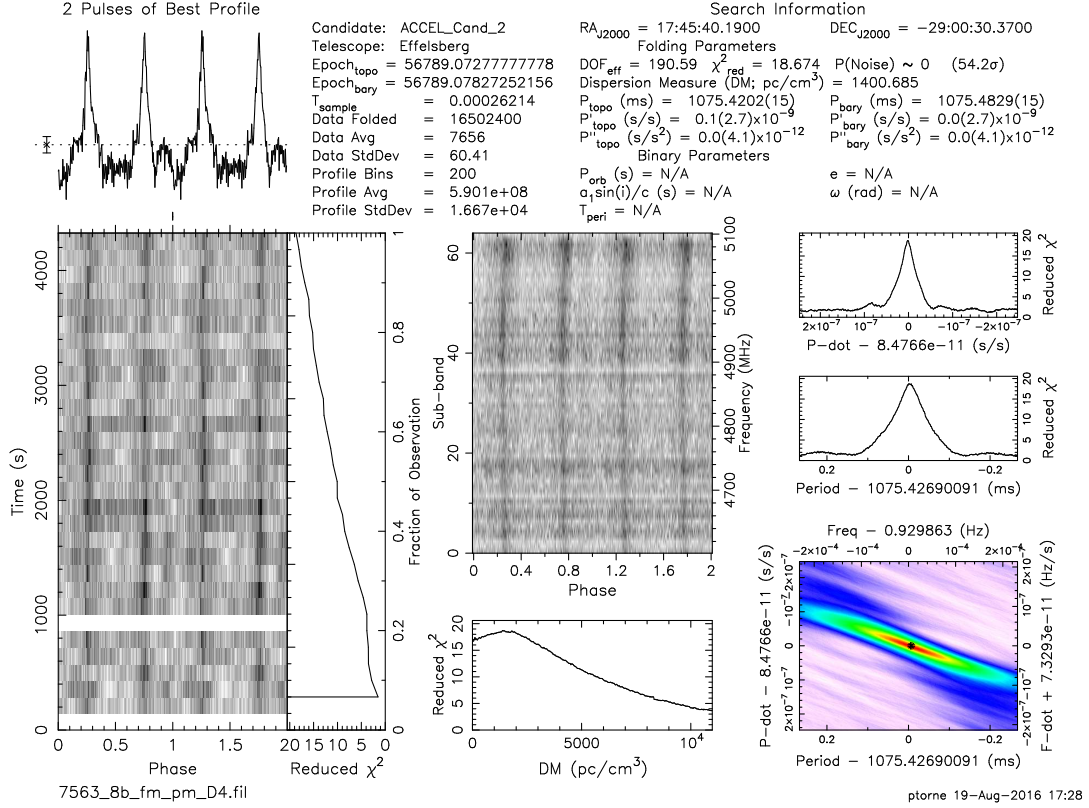


Figure 3.4: Candidate detected in our blind search corresponding to the 2/7 spin period harmonic of the magnetar SGR J1745–2900. This plot also shows how the DM is poorly constrained when using high frequency observations, since the detected DM peak of the candidate is $1400.685 \text{ pc cm}^{-3}$, far from the correct $DM = 1780 \text{ pc cm}^{-3}$. The effect of a low dispersion is also apparent from the smooth curve in the DM versus Reduced χ^2 plot shown at the bottom.

other pulsars present in the data, at least if they are luminous enough, should have been detected as well.

The flux density limits for the non-detections in each frequency band were calculated using a modified version of the radiometer equation that accounts for the pulse duty cycle (e.g.: Lorimer & Kramer, 2005):

$$S_{\min} = \beta \frac{(S/N_{\min}) T_{\text{sys}}}{G \sqrt{n_p} T_{\text{obs}} \Delta\nu} \sqrt{\frac{\delta}{1-\delta}}, \quad (3.3)$$

where S_{\min} is the minimum detectable flux density, β is a degradation factor due to digitisation and other instrumental effects ($\beta \approx 1$ for modern backends), (S/N_{\min}) is the minimum signal-to-noise to consider a detection, T_{sys} is the total system temperature, G is the telescope gain, n_p the number of polarizations used, T_{obs} the integration time, $\Delta\nu$ is the observation bandwidth, and δ is the pulsar duty cycle, being $\delta = W/P$, where

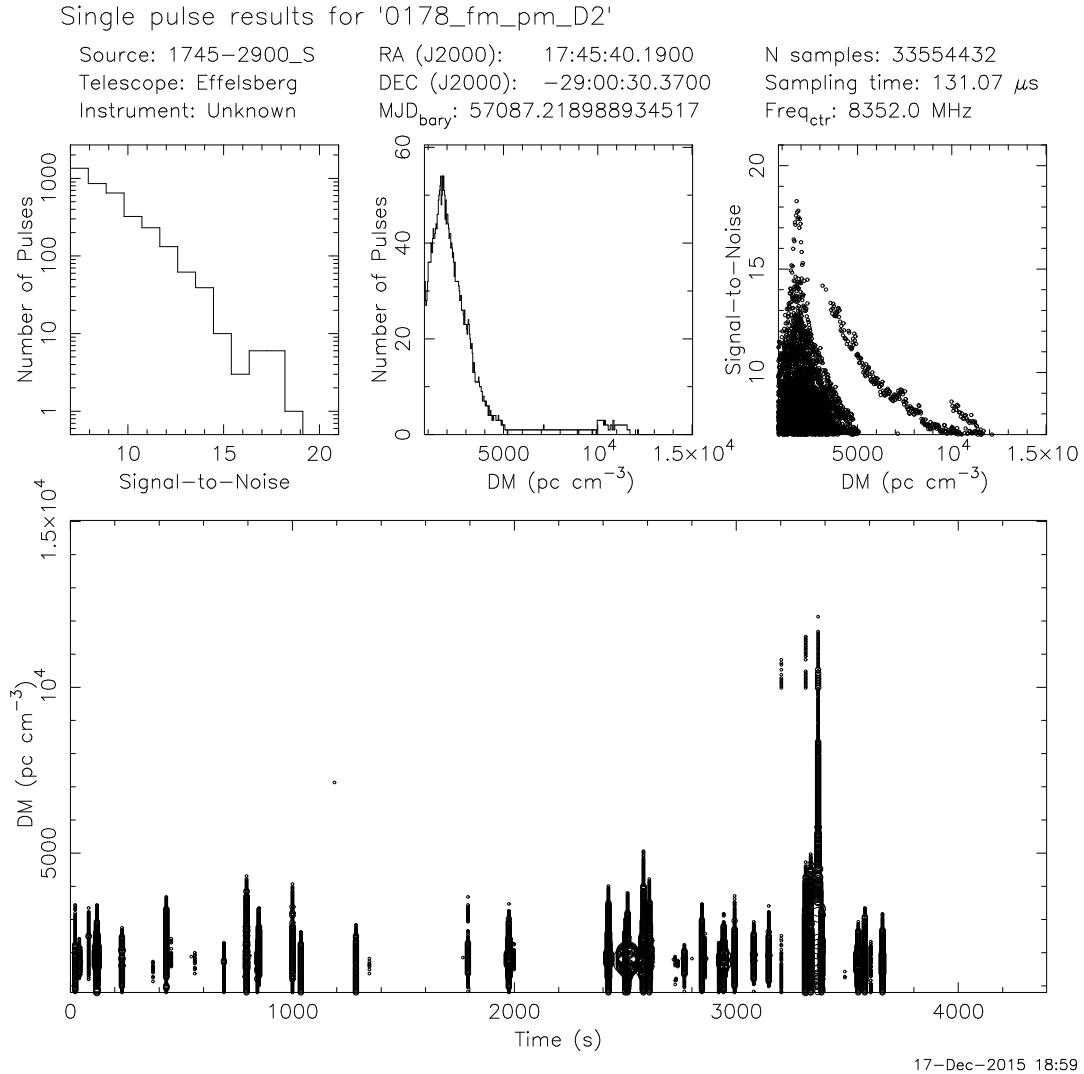


Figure 3.5: Single pulse diagnostic plot from our blind transient search on the Galactic Centre showing an example of the detection at 8.35 GHz of the single pulses from the magnetar SGR J1745–2900. We know that these pulses are produced by this source and not by another pulsar because they peak at the exact expected $DM = 1780 \text{ pc cm}^{-3}$, and the result from a periodicity analysis of the pulses coincide with the magnetar’s spin period. (For a detailed explanation of the information presented in this plot, we refer the reader to Figure 2.4.)

W is the pulse width and P the pulsar spin period. Table 3.3 shows the results from the flux density limit calculations. Figure 3.6 shows the luminosity sensitivity limits of this survey against the known pulsar population for two different GC scenarios: one including a hyperstrong scattering following Cordes & Lazio (2002), and another one with the lower scattering measured by Spitler et al. (2014).

3.4 Discussion

If the GC really harbours a large population of pulsars (e.g. Wharton et al., 2012) and scattering cannot be blamed as a sufficient cause to hinder their detection (Spitler et al., 2014), why is it so difficult to detect more pulsars in the GC¹³? It is interesting to observe the resulting sensitivity limits of this survey (Table 3.3 and Figure 3.6). Even with one of the largest radio telescopes on Earth, our sensitivity to pulsars in the GC is still remarkably low. One fundamental reason is the GC background, whose contribution to T_{sys} at frequencies $\lesssim 10$ GHz can be much greater than the contribution from all the other sources of noise (like the receiver, spillover, sky, etc.) and reduces considerably the sensitivity of the observations. A second important cause is the contribution of the atmosphere, an effect highly amplified by the extremely low elevations at which Effelsberg sees the Galactic Centre. For instance, we calculate that at 4.85 GHz the sensitivity in our survey is reduced a factor ~ 4 by the GC contribution, while the atmospheric contribution impacts a factor ~ 1.5 . Overall this is a decrease of a factor ~ 5.5 by these external effects. At 8.35 GHz, the worsening of the sensitivity reaches a factor ~ 2 by the GC background, with another factor ~ 2 by atmospheric effects. The T_{atm} is more prominent for frequencies $\gtrsim 10$ GHz. At 14.6 GHz, we calculate a decrease in sensitivity of a factor ~ 3.5 only by the sky temperature, whereas the GC contributes decreasing the sensitivity further by a factor ~ 2 . One additional motive for the low sensitivity reached in this survey, which affects all frequency bands equally, is the reduced visibility of the GC from Effelsberg, of about 2.5 hr per day. This limits the maximum integration time in a single observation, which therefore limits the minimum flux density that we may detect (see Equation 3.3). Furthermore, the distance to the GC is large, contributing to the faintness of the GC pulsar signals as seen from Earth. Taking all these facts into account, plus the additional potential loss in sensitivity to accelerated systems (see Section 3.2.2.2), we cannot rule out the possibility that the non-detections are simply due to a lack of sufficient sensitivity. Chennamangalam & Lorimer (2014) reach a similar conclusion with respect to an insufficient sensitivity as a plausible cause for the absence of more pulsar detections in previous GC surveys.

It is remarkable that our calculations of the contribution of the GC background and the atmosphere to the system noise differ from those estimated in other works (cf. e.g. Deneva et al., 2009; Macquart et al., 2010; Chennamangalam & Lorimer, 2014); estimations that also differ between these works. The clear uncertainty that exists in

¹³We recall that not all the results from this survey have been reviewed yet, but we will continue the discussion focusing on the non-detection in previous surveys and the reviewed subset of our analysed data.

Table 3.3: Flux density limits per frequency band and segmentation step. For the calculations we used Equation 3.3, and set $\beta = 1$, $n_p = 2$, $\delta = 0.15$, and $(S/N_{\min}) = 10$. P_B^{\min} corresponds to the minimum theoretical orbital period detectable, assuming the acceleration stays constant across the observation. The column T_{sys} is the total system temperature on the Galactic Centre, i.e. including the contribution from the GC background (column T_{GC}) and the atmosphere (column T_{atm}). No calibration data is available at the moment for the 18.95 GHz, indicated by the “n/a” symbol.

ν (GHz)	T_{obs} (s)	Gain (K/Jy)	T_{sys} (K)	T_{GC} (K)	T_{atm} (K)	$S_{\nu, \min}$ (μJy)	P_B^{\min} (hr)	Segmentation
4.85	4320	1.55	180	~ 116	~ 37	235	~ 12.0	Full obs.
	2160	1.55	180	~ 116	~ 37	332	~ 6.0	2 segments
	1080	1.55	180	~ 116	~ 37	469	~ 3.0	4 segments
	540	1.55	180	~ 116	~ 37	664	~ 1.5	8 segments
	270	1.55	180	~ 116	~ 37	938	~ 0.8	16 segments
8.35	4320	1.35	116	~ 49	~ 45	174	~ 12.0	Full obs.
	2160	1.35	116	~ 49	~ 45	246	~ 6.0	2 segments
	1080	1.35	116	~ 49	~ 45	347	~ 3.0	4 segments
	540	1.35	116	~ 49	~ 45	491	~ 1.5	8 segments
	270	1.35	116	~ 49	~ 45	695	~ 0.8	16 segments
14.60	4320	1.14	271	~ 48	~ 173	480	~ 12.0	Full obs.
	2160	1.14	271	~ 48	~ 173	679	~ 6.0	2 segments
	1080	1.14	271	~ 48	~ 173	961	~ 3.0	4 segments
	540	1.14	271	~ 48	~ 173	1359	~ 1.5	8 segments
	270	1.14	271	~ 48	~ 173	1921	~ 0.8	16 segments
18.95	8640	1.05	n/a	n/a	n/a	n/a	~ 24.0	Full obs.
	4320	1.05	n/a	n/a	n/a	n/a	~ 12.0	2 segments
	2160	1.05	n/a	n/a	n/a	n/a	~ 6.0	4 segments
	1080	1.05	n/a	n/a	n/a	n/a	~ 3.0	8 segments
	540	1.05	n/a	n/a	n/a	n/a	~ 1.5	16 segments
	270	1.05	n/a	n/a	n/a	n/a	~ 0.8	32 segments

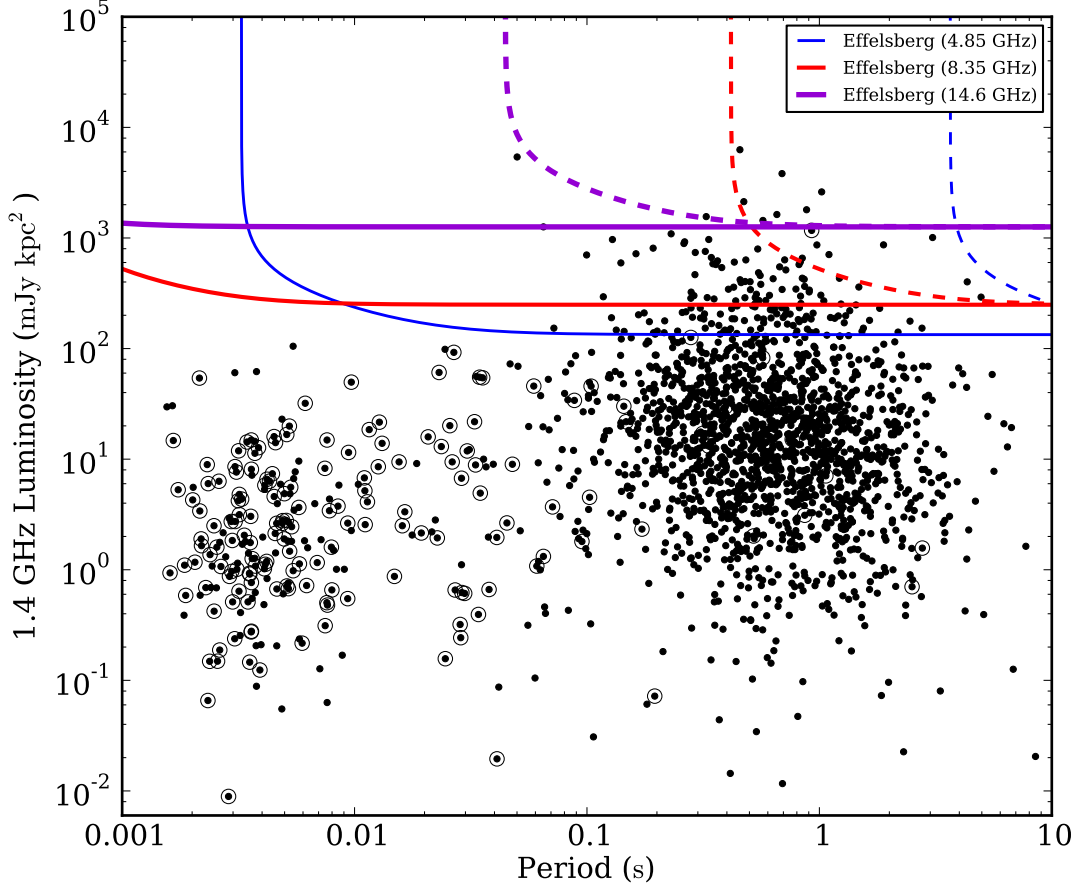


Figure 3.6: Luminosity at 1.4 GHz versus spin period of the known pulsar population with luminosity information from PSRCAT (Manchester et al., 2005). For those pulsars with no information at 1.4 GHz, we extrapolated from data at other frequencies using their measured spectral index when available, or assuming a spectral index of $\alpha = -1.7$ otherwise. The sensitivity limits of our survey at the Galactic Centre are over plotted. To extrapolate the luminosity sensitivity lines of each observing frequency to 1.4 GHz a spectral index of $\alpha = -1.7$ was assumed, with a distance to the Galactic Centre of 8.3 kpc. Only the best sensitivity for the four frequency bands is shown, i.e.: that corresponding to the longest observation in each case. The segmentation strategy decreases by $\sqrt{2}$ the sensitivity in luminosity for each division step (thereby raising the curves), but increases the minimum detectable binary orbital period (see table 3.3). Two different temporal scattering scenarios are considered: $\tau_s = 1.3\nu^{-3.8}$ s (continuous line, Spitler et al., 2014), and $\tau_s = 2000\nu^{-4}$ s (dashed line, Cordes & Lazio, 2002).

the estimated values of T_{GC} and T_{atm} in past surveys could also explain why these searches did not detect more pulsars in the GC, since their sensitivity might have been overestimated.

Implementing a stack search analysis by combining together different epochs would help to partially overcome the sensitivity limitation of our short scans. A study reveals that an incoherent stack of Fourier series increases the signal-to-noise of a periodic signal $\propto N_{stack}^{1/4}$, where N_{stack} is the number of series added together (see [Eatough et al., 2013a](#)). This technique has been already successfully used to discover very faint pulsars that would not be detected otherwise (e.g. [Pan et al., 2016](#)). Given our large dataset, we have enough observations to theoretically improve our sensitivity a factor $\sim 2-3$, which would require the incoherent addition of $\sim 16-81$ observations (the total number of epochs in this survey is 110).

Another solution to improve the sensitivity, this time focused on accelerated pulsars, is to use template matching techniques ([Knispel et al., 2013](#)). Such method has the advantage of not requiring the segmentation of the data to recover the signal of highly accelerated pulsars, avoiding the $\sqrt{2}$ loss in sensitivity that we suffer with every segmentation. The main drawback of this technique is the enormous computational cost, as it requires to search a space of up to seven variables (five to fully describe an eccentric Keplerian orbit, plus DM and spin period).

An additional effect that may be decreasing our sensitivity even further, in particular to long-period pulsars, is the red noise present in our data, similarly to what was shown recently in [Lazarus et al. \(2015\)](#) for the Arecibo P-ALFA survey. To assess quantitatively the red noise impact in our survey requires simulations not included in this work, and thus we are not accounting for this effect in our theoretical sensitivity calculations. Such analysis, however, is particularly important for surveys carried out at high radio frequencies, that tend to show an excess of red noise due to the variable atmospheric contribution, and we plan to include it in the future.

From our study of the pipeline capabilities, it is clear that long integrations are a major drawback for the acceleration correction algorithms. The next generation of radio telescopes with increased sensitivities and better visibility of the GC, like MeerKAT and, ultimately, the Square Kilometre Array (SKA), will provide short observations with very high sensitivities, improving significantly the efficiency of the searching algorithms. Moreover, the capabilities of interferometers to form tiny beams in comparison with those of single dish telescopes would be a major advantage to reduce the adverse contribution of the background emission (R. Wharton, private communication). Ideally, these higher-sensitivity data should be combined with techniques like stacked or template matching searches to maximize our sensitivity to the faintest and elusive pulsars of the GC region.

Aside from a low sensitivity, as already mentioned, other possible causes for the non-detections include time dependent effects. For example, a time varying and/or spatially complex scattering medium toward the GC could make SGR J1745-2900 visible while hindering other pulsar signals ([Spitler et al., 2014](#)). In addition, the geodetic precession due to the curved space around a massive companion could move the beamed emission of a pulsar often out (and in) of the line of sight to the Earth, or long eclipses due to the

clumpiness and density of the gas in the GC, an observation during an orbital phase with too high acceleration or jerk, or intrinsic intermittency of a pulsar emission, could all hide pulsars from us. Except for the scattering medium, which can certainly have a more complex impact, the other mentioned effects should eventually be overcome with repeated surveys like this one.

Even with all these caveats, the non-detection of a single *normal* pulsar, and instead one very rare radio magnetar, in the innermost part of the GC is really puzzling. Clearly some still unaccounted causes render the pulsar detections within the very centre of the Galaxy much more difficult than expected, but we cannot find strong enough reasons to discard the existence of more pulsars there. The exceptional science enabled by finding and studying pulsars in the GC warrants continuous efforts to survey the region.

3.5 Summary

A new survey for pulsars in the Galactic Centre at frequencies 4.85, 8.35, 14.60, and 18.95 GHz was carried out between February 2012 and December 2015 using the Effelsberg 100-m radio telescope. The various high radio frequencies utilized decrease the deleterious scattering effects, one of the major concerns when surveying this region. It is the first time that the observations are regularly repeated, covering a time span of almost four years. This long dataset increases the probabilities to find pulsars whose discovery might have been hindered previously by effects that are time variable: for example an unfavourable orbital phase, eclipses, emission intermittency, or beam precession. Our data analysis included extensive searches in acceleration to be sensitive to pulsars in binary systems, something not fully included in previous similar surveys and that makes this survey the most complete to date in terms of parameter space covered.

Within the subset of the results reviewed at the moment of writing (i.e. 100 per cent of the single pulse analysis and 23 per cent of the periodicity search) no new pulsars have been detected. While the non-detections of pulsars in the GC in this and previous surveys is quite surprising, and indicate that we do not fully understand the GC pulsar population and/or the complex scattering medium toward the centre of the Galaxy, our sensitivity still does not cover most of the expected population (if we assume that the GC pulsars resemble the population known for the Galaxy, see Figure 3.6). Therefore, a plausible explanation for the lack of more detections could simply be that our current sensitivity is insufficient.

There is still a 77 per cent of our resulting candidates from the periodicity search pending review. Therefore, our chances to discover new pulsars with this survey are not yet ruled out. In any case, the unique and remarkable scientific experiments that only pulsars located in this distinct region allow warrant additional surveys, which in the near future will be done with the next generation of more sensitive radio telescopes coming online, like MeerKAT and the SKA. Even if present surveys cannot detect new pulsars in the GC, if the reason is indeed an insufficient sensitivity, these future surveys will very likely finally uncover the elusive GC pulsar population, enabling the long-time sought GC pulsar science (see e.g. Keane et al., 2015; Eatough et al., 2015).

Acknowledgements

We thank Lorenz Huedepohl and Ingeborg Weidl for his support with the use of the MPCDF's HPC *Hydra* supercomputer, Ewan Barr for being always available to discuss about the details of the acceleration search techniques, and Gregory Desvignes for his help with the calibration of the data. We also thank Alex Kraus for sharing the script to obtain precise flux density values of NGC7027. Based on observations with the 100-m telescope of the MPIfR (Max-Planck-Institut für Radioastronomie) at Effelsberg. P.T. is supported for this research through a stipend from the International Max Planck Research School (IMPRS) for Astronomy and Astrophysics at the Universities of Bonn and Cologne.

Simultaneous multifrequency radio observations of the Galactic Centre magnetar SGR J1745–2900

This chapter is based on an article published in Monthly Notices of the Royal Astronomical Society Letters, with DOI: [10.1093/mnrasl/slt063](https://doi.org/10.1093/mnrasl/slt063). Only very minor format changes were made in order to match the style of this thesis. Information about the article (Torre et al. 2015) can be found online at: <http://adsabs.harvard.edu/abs/2015MNRAS.451L..50T>

I am the lead author of the article. My main contributions include the participation in the observations from the IRAM 30-m radio telescope, the data reduction (including the absolute flux density calibration) of the data from IRAM 30-m and APEX, and the writing of the article. I did not carry out the observations and data reduction at 2.54, 4.85 and 8.35 GHz.

The full list of authors is:

P. Torre, R. P. Eatough, R. Karuppusamy, M. Kramer, G. Paubert, B. Klein, G. Desvignes, D. J. Champion, H. Wiesemeyer, C. Kramer, L. G. Spitler, C. Thum, R. Güsten, K. F. Schuster, and I. Cognard

Abstract

We report on simultaneous observations of the magnetar SGR J1745–2900 at frequencies $\nu = 2.54$ to 225 GHz using the Nançay 94-m equivalent, Effelsberg 100-m, and IRAM 30-m radio telescopes. We detect SGR J1745–2900 up to 225 GHz, the highest radio frequency detection of pulsed emission from a neutron star to date. Strong single pulses are also observed from 4.85 up to 154 GHz. At the millimetre band we see significant flux density and spectral index variabilities on time scales of tens of minutes, plus variability between days at all frequencies. Additionally, SGR J1745–2900 was observed at a different epoch at frequencies $\nu = 296$ to 472 GHz using the APEX 12-m radio telescope, with no detections. Over the period MJD 56859.83 – 56862.93 the fitted spectrum yields a spectral index of $\langle \alpha \rangle = -0.4 \pm 0.1$ for a reference flux density $\langle S_{154} \rangle = 1.1 \pm 0.2$ mJy (with $S_\nu \propto \nu^\alpha$), a flat spectrum alike those of the other radio-loud magnetars. These results show that strongly magnetized neutron stars can be effective radio emitters at frequencies notably higher to what was previously known and that pulsar searches in the Galactic Centre are possible in the millimetre band.

4.1 Introduction

Magnetars are thought to be neutron stars with extremely strong magnetic fields (Duncan & Thompson, 1992). Further work by Thompson & Duncan (1995, 1996) theorized how the decay of the strong magnetic fields in magnetars can produce soft gamma-ray and X-ray emission and proposed that Anomalous X-ray Pulsars (AXPs) and Soft Gamma Repeaters (SGRs) could indeed be magnetars. This identification of AXPs and SGRs as magnetars was validated when pulsations with spin-down (a typical characteristic of pulsars) were first detected from one of these objects (Kouveliotou et al., 1998). At the time of writing, 23 magnetars have been discovered (for a review, see Olausen & Kaspi, 2014), and only four have conclusively shown pulsed radio emission (Camilo et al., 2006, 2007a; Levin et al., 2010; Eatough et al., 2013c; Shannon & Johnston, 2013). SGR J1745–2900, the subject of this work, is the last one discovered, and is a compelling object due to its proximity to Sagittarius A* (Sgr A*), the supermassive black hole candidate in the Galactic Centre (GC). Initially discovered at high-energies (Kennea et al., 2013; Mori et al., 2013; Rea et al., 2013b), pulsations in the radio band up to 20 GHz were also detected with different radio telescopes (Eatough et al., 2013c; Shannon & Johnston, 2013).

One peculiar characteristic of radio loud magnetars is that they tend to show shallower spectral indices than ordinary pulsars. This property makes magnetars unique sources to obtain pulsar observations at high radio frequencies, where ordinary pulsars are, with a few exceptions (Kramer et al., 1997a; Morris et al., 1997; Löhmer et al., 2008), usually too faint to be detected and studied. This under-explored region of the spectrum of emission is valuable in the study of pulsar emission physics. For instance some emission models include effects that may only be detectable at high radio frequencies, like “coherence breakdown” between the radio and infrared bands where an incoherent component of emission becomes dominant (Michel, 1982). Additionally, unexpected effects have been seen in some of the high frequency pulsar observations available to date: spectral flattening (Kramer et al., 1996), variability in flux density (Kramer et al., 1997c) or changes in polarization degree (Xilouris et al., 1996).

This particular source lies in the vicinity of Sgr A*. It has been shown that pulsars closely orbiting the black hole could be used to test General Relativity and alternative theories of gravity to the highest precision (Liu et al., 2012). Because the scattering toward the GC remains not well understood (Bower et al., 2014; Spitler et al., 2014), and scattering may still limit our chances of finding pulsars in the GC, SGR J1745–2900 is therefore a useful target for tests of high frequency observations of the GC.

We present here observations of the magnetar SGR J1745–2900 from 2.57 to 472 GHz. Section 2 describes the observations and data reduction. Our results are presented in Section 3. Finally, a summary and discussion are given in Section 4.

4.2 Observations and data reduction

4.2.1 Nançay and Effelsberg

At the Nançay radio telescope, observations were taken at a central frequency of 2.54 GHz with a bandwidth of 512 MHz. Data from dual linear polarizations were coherently dedispersed, folded modulo the magnetar period and recorded to disk. The observations were flux density calibrated using the standard `PSRCHIVE`¹ software routines that require the use of a calibrated noise diode in combination with observations of a calibration source; in this case 3C286 was used. Observations at 4.85 GHz and 8.35 GHz were made at the Effelsberg 100-m radio telescope using both a digital spectrometer, operating in a pulsar search mode, and a coherent dedispersion system. At each frequency dual circular polarizations were recorded over a total bandwidth of 500 MHz. A calibrated noise diode was used to determine the flux density scale by comparing it to NGC7027. Data were processed with the `SIGPROC`² software package.

4.2.2 IRAM 30-m

Observations in the millimetre band were made at the IRAM 30-m radio telescope and used the Eight MIXer Receiver (EMIR, [Carter et al., 2012](#)) with the Broad-Band-Continuum (BBC) backend. The BBC is connected to 4 outputs of EMIR working with dual frequency bands and dual sideband mixers. Two frequency combinations were used: centred at 87, 101, 138, 154 GHz (Mode E0/E1) and 87, 101, 209, 225 GHz (mode E0/E2). The effective bandwidth of the BBC is estimated to be 24 GHz (6 GHz per frequency band). Both horizontal (H) and vertical (V) linear polarizations were recorded. We noted a systematic lower sensitivity in the H polarization channel, the cause of which we were not able to identify. A special set-up of the backend enabled fast time sampling of the continuum signal at 1 ms. The total variations of the system temperature (T_{sys}) during the four days were between 77–183 K for the 87 GHz band, 84–208 K for the 101 GHz band, 87–257 K for 138 GHz band, 98–327 K for the 154 GHz band, 478–571 K for the 209 GHz band and 520–621 K for the 225 GHz band. Temporal fluctuations in the atmospheric water vapour are responsible for the high variations of T_{sys} . We observed in “Total Power” mode, i.e. always on source. This observing mode has the disadvantage that atmospheric and receiver gain variations are reflected in the data as variations of the mean count level. Self-produced instrumental interference was present in the data, in particular at harmonics of 1 Hz, most likely produced by the cryogenerator.

The data reduction was as follows. The dispersion delay due to the interstellar medium, even at the large $\text{DM} = 1778 \text{ cm}^{-3} \text{ pc}$ of the source, is only $\Delta t_{\text{DM}} \simeq 0.9 \text{ ms}$ across the observing frequency range. This delay is smaller than the sampling time of 1 ms and therefore negligible. The variations in the time series and interference needed to be removed because they contaminated significantly the baseline of the folded pulsar profile, reducing our sensitivity to the pulsed emission. Our solution consisted of using

¹<http://psrchive.sourceforge.net/>

²<http://sigproc.sourceforge.net/>

a sliding window of width 3 s where a sine wave of 1 Hz and baseline were fit to the data, subtracting the central 1 s of the fit from the raw data. This reduced the variations enough to produce a nearly flat-baseline folded profile. For 209 and 225 GHz, this method was less effective than a running mean filtering, that was applied twice to the time series with windows of 10 and 0.4 s, respectively. Both filtering methods subtract the continuum emission contribution from the GC. Finally, the cleaned time series were folded with the topocentric period of SGR J1745–2900, calculated from a recent ephemeris from a timing analysis performed at lower frequencies. The flux density calculations were done using interspersed hot-cold load calibration measurements at the beginning and end of each observation scan, providing the required quantities to convert counts to antenna temperature T_a^* . The methodology follows [Kramer \(1997\)](#). The conversion factor from T_a^* to flux density (S/T_a^*) was obtained from the observatory efficiency tables³. Pointing corrections were also applied between scans. In addition, due to the low telescope elevations during the observations, an elevation-dependent telescope-gain correction was applied ([Peñalver, 2012](#)). Our flux density calibration method was verified with pointings on the planets Mars and Uranus.

4.2.3 APEX

Additional millimetre and submillimetre data were taken with the APEX 12-m radio telescope. The system used was the FLASH⁺ receiver with a special version of the continuum Pocket BackEnd (PBE). FLASH⁺ worked in dual sideband mode providing simultaneously four bands centred at 296, 308, 460 and 472 GHz. The total bandwidth was 16 GHz (4 GHz per frequency band), splitting and recording one polarization at 296 and 308 GHz and the other at 460 and 472 GHz. The sampling time of the continuum signal was 0.5 ms. SGR J1745–2900 was observed on 2014 August 24 for 60 min. T_{sys} varied during the observation between 119–130 K for the 296 GHz band, 129–143 K for the 308 GHz band, 589–811 K for the 460 GHz band, and 471–3414 K for the 472 GHz band. The atmospheric water vapour content is responsible for the high T_{sys} at 460 and 472 GHz. Again, “Total Power” measurements were done. We applied the two-running-mean method with 10 and 0.4 s windows to reduce the variations in the time series and subtract the continuum contributions of the atmosphere and GC. The cleaned time series were then folded using the topocentric period of SGR J1745–2900 computed from our ephemeris. For the non-detection flux density limits, the radiometer equation with a signal-to-noise threshold of 5, duty cycle of 0.075, and telescope gain from the observatory efficiency tables⁴ is used (see e.g. [Lorimer & Kramer, 2005](#)). Factors to account for the transmissivity of the atmosphere are also included.

Within the constraints of the source visibility the observations from IRAM 30-m, Effelsberg and Nançay were simultaneous, overlapping a total of 203 min on the dates 2014 July 22 to 24. Table 1 summarizes the observations.

³<http://www.iram.es/IRAMES/mainWiki/Iram30mEfficiencias>

⁴<http://www.apex-telescope.org/telescope/efficiency/index.php>

Table 4.1: Summary of the observations of SGR J1745–2900 with flux densities and spectral indices. For July 21 the relative error bars are too large for a meaningful spectral index fit. Note that the APEX observations are one month later from the rest.

Date	Obs.	ν (GHz)	S (mJy)	α	T_{obs} (h)	
2014 Jul 21	IRAM	87	0.1(4)	–	2.0	
		101	0.6(5)		2.0	
		138	0.2(3)		2.0	
		154	0.3(4)		2.0	
2014 Jul 22	Nançay	2.54	10.5(11)	–0.3(1)	1.3	
		Effelsberg	4.85		3.9(3)	1.0
		8.35	3.3(3)		0.8	
	IRAM	87	1.5(3)		4.0	
		101	1.8(3)		4.0	
		138	2.2(3)		4.0	
		154	1.5(3)		4.0	
2014 Jul 23	Nançay	2.54	11.0(11)	–0.4(1)	1.3	
		Effelsberg	4.85		4.0(3)	1.1
		8.35	3.3(3)		1.1	
	IRAM	87	1.8(4)		2.4	
		101	1.7(5)		2.4	
		138	1.7(3)		2.4	
		154	1.9(4)		2.4	
2014 Jul 24	Nançay	2.54	3.8(4)	–0.2(1)	1.3	
		Effelsberg	4.85		2.2(3)	1.1
		8.35	4.2(4)		1.1	
	IRAM	87	2.6(4)		2.0	
		101	2.1(4)		2.0	
		138	0.8(4)		0.8	
		154	0.6(5)		0.8	
		209	1.6(11)		1.2	
225	1.0(7)	1.2				
2014 Aug 24	APEX	296	< 2.1	–	1.0	
		308	< 2.2		1.0	
		460	< 29.9		1.0	
		472	< 52.2		1.0	
Total average	Nançay	2.54	8.4(5)	–0.4(1)	3.9	
		Effelsberg	4.85		3.4(2)	3.1
		8.35	3.6(2)		3.0	
	IRAM	87	1.5(2)		10.4	
		101	1.6(2)		10.4	
		138	1.5(2)		9.2	
		154	1.1(2)		9.2	
		209	1.6(11)		1.2	
225	1.0(7)	1.2				

4.3 Results

4.3.1 Detections and profiles

The magnetar was clearly detected up to 154 GHz and more weakly detected at 209 and 225 GHz with clear peaks at the expected rotational phase. At APEX, 296 to 472 GHz, no detections were made. Fig. 4.1 shows the detected average profiles at each frequency. The profiles are generally multi-component, with a shape that varied significantly from day to day at the lowest frequencies 2.54 to 8.35 GHz. At the millimetre band the profile was more stable, showing a main peak and a precursor (pulse phase $\simeq 0.15$ in Fig. 1). The precursor seems to consist of different narrow components that appeared and disappeared randomly between observations, and was on average stronger at the highest frequencies.

4.3.2 Flux density and spectral index

In Table 1 we present the equivalent continuum flux density (also known as the “mean flux density”) from all observations. The errors were estimated taking into account the uncertainties in the calibration processes. We observed significant variations in flux density on short time-scales (of the order of tens of minutes) in the millimetre data and day-to-day variability at all frequencies. Fig. 4.2 shows the total averaged mean flux density per frequency band and a power-law fit to the data spanning more than 220 GHz. Over the period MJD 56859.83 – 56862.93 the fitted spectrum yields a spectral index of $\langle\alpha\rangle = -0.4 \pm 0.1$ for a flux density at 154 GHz $\langle S_{154}\rangle = 1.1 \pm 0.2$ mJy.

4.3.3 Single pulses

We also detected numerous single pulses at all frequencies between 4.85 and 154 GHz (at 2.54 GHz the delivered folded data did not allow to search for single pulses). At the millimetre band, the peak flux density of the strongest pulses reached 19 Jy at 101 GHz, with a pulse width of 1 ms. Following Lorimer & Kramer (2005), this is equivalent to a brightness temperature $T_B > 10^{23}$ K, for a distance to the GC of 8.3 kpc (Gillesen et al., 2009). At 154 GHz, the strongest pulse reached a peak of 8 Jy with a width of 1 ms and $T_B \simeq 2.3 \cdot 10^{22}$ K. The majority of the single pulses detected showed T_B of the order of 10^{22} K. The values calculated here are lower limits because we are limited by the coarse time resolution of the data. Fig. 4.3 shows a selection of strong single pulses from our dataset at the highest frequencies. A detailed analysis of the single pulses from SGR J1745–2900 will be presented elsewhere.

Possible reasons for the non-detections at APEX include the comparably lower sensitivity of the observations, the faintness of the source at these frequencies, and the random variability of the source. We also noted strong, periodic self-produced instrumental interference overlapping the magnetar spin frequency that could have decreased our sensitivity even further. The polarization splitting of the APEX receiver (see §2), if the magnetar is highly linearly polarized at these frequencies, could have also led to a loss in sensitivity if the radiation was misaligned with the feed at the lower

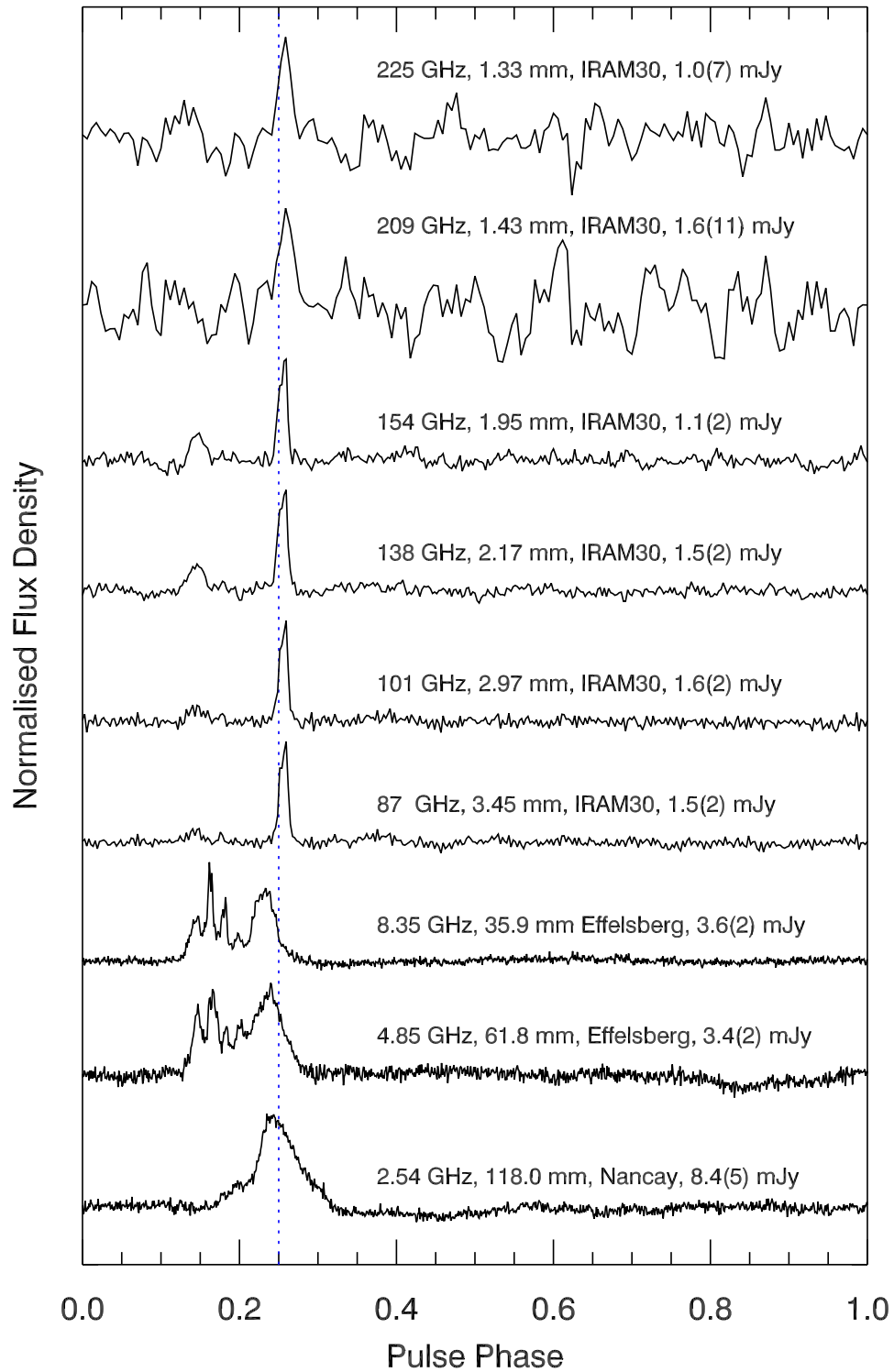


Figure 4.1: Average pulse profiles of SGR J1745–2900 at 2.54, 4.85, 8.35, 87, 101, 138, 154, 209 and 225 GHz. All profiles are generated from the sum of the observations presented here and are aligned to the same reference phase obtained from our timing ephemeris (dotted line).

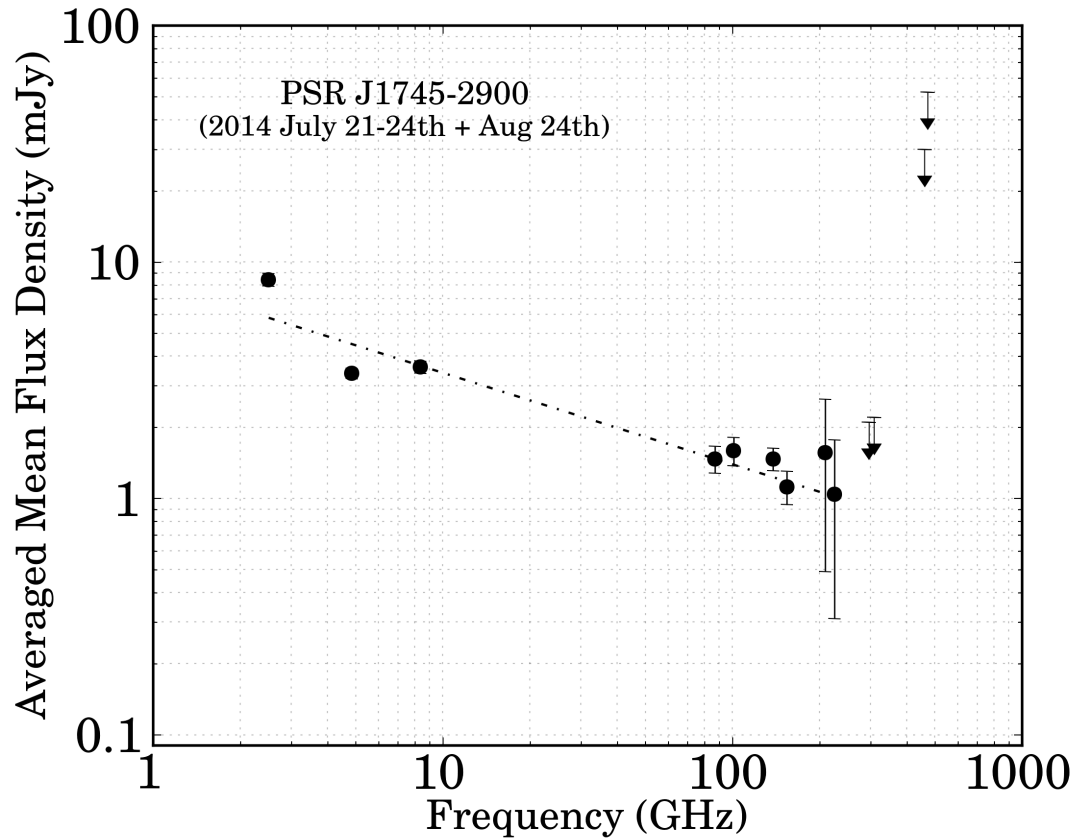


Figure 4.2: Total averaged mean flux densities. The dashed-dotted line shows the spectral index fit. The mean spectral index obtained for SGR J1745–2900 is $\langle\alpha\rangle = -0.4 \pm 0.1$, showing the unusual flatter spectrum common to magnetars in the radio band. Due to the variability of the source the APEX data (taken approximately one month later) were not used to prove or disprove the continuation of the power law beyond 230 GHz.

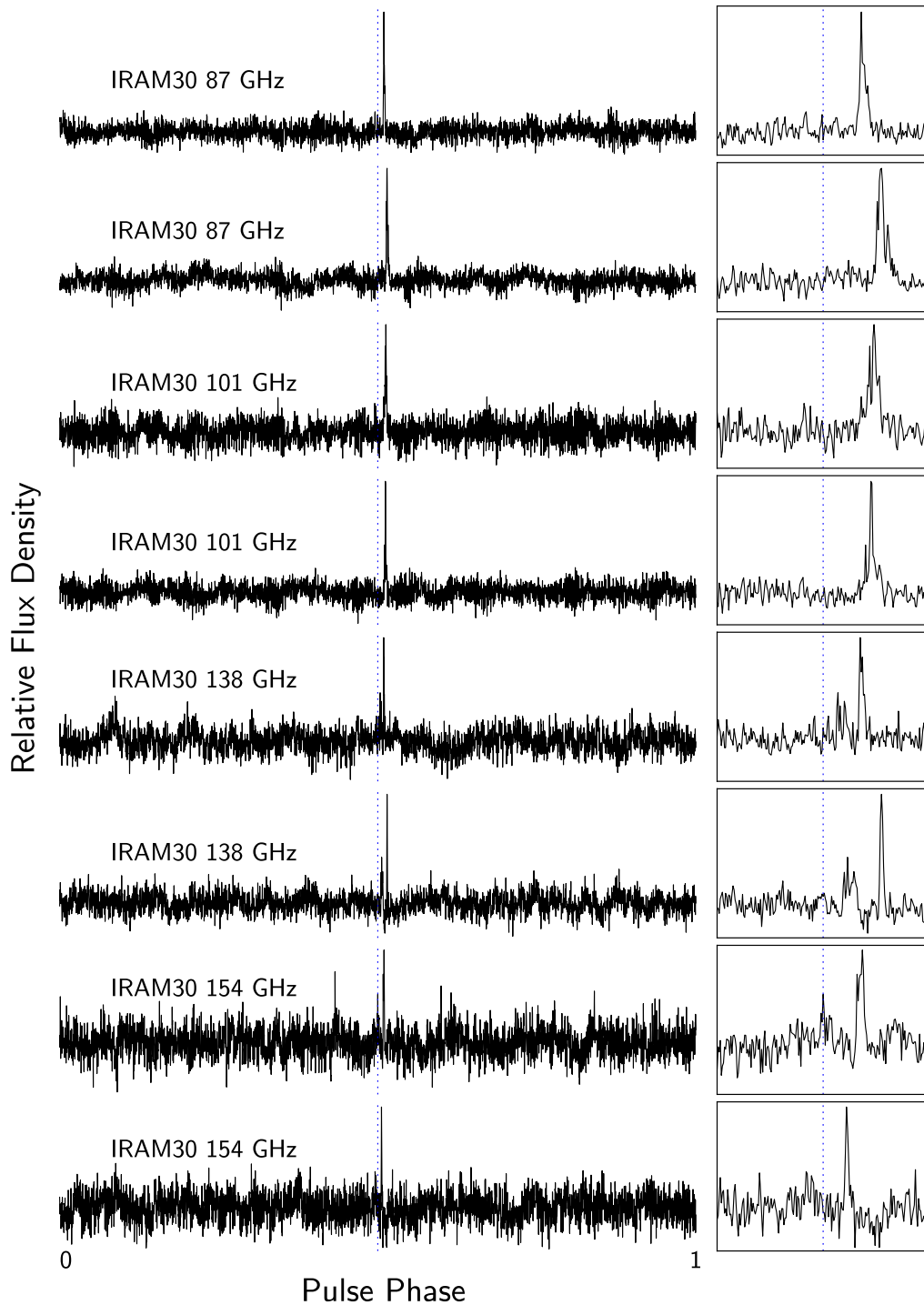


Figure 4.3: Selection of strong single pulses from our dataset in the millimetre band. The time resolution is 1 ms. The panels on the left show one rotation of the neutron star. Panels on the right show a zoom to a window of 0.2s around the reference phase computed from the ephemeris (dotted line). The width, intensity and morphology of the single pulses is diverse. The features visible in the off-pulse region are due to residual interference.

bands, 296 and 308 GHz, that were much more sensitive. Because of these uncertainties, we cannot conclusively rule out the emission of SGR J1745–2900 between 296 and 472 GHz, nor a lack of it.

4.4 Summary and Discussion

The detections of SGR J1745–2900 up to 225 GHz and its single pulses up to 154 GHz set new records for the detection of pulsed emission from a neutron star in the radio band. The high measured flux density of SGR J1745–2900 at the millimetre band between 87 and 225 GHz, $\langle S_{\text{mm}} \rangle = 1.4 \pm 0.2$ mJy, and the numerous strong single-pulses detected up to 154 GHz show that SGR J1745–2900 can be, at least during some periods of activity, an efficient producer of radiation at very high radio frequencies. In combination with the work by Camilo et al. (2007b), our detections suggest that emission at very high radio frequencies from radio loud magnetars might be a frequent characteristic of these objects.

The origin of the radio emission from magnetars is still unclear. The case of magnetars is perhaps more complex than for ordinary pulsars, which are thought to be powered entirely by their loss of rotational kinetic energy, (also called “spin-down luminosity”) \dot{E} . Some magnetars show luminosities at high-energies that are much larger than \dot{E} (see, e.g., Tables 2 and 7 in Olausen & Kaspi, 2014), requiring of additional sources to power their electromagnetic emission. Big efforts have been made trying to model processes that describe the emission from magnetars (Thompson & Duncan, 1995; Beloborodov & Thompson, 2007; Beloborodov, 2013, 2009), but the puzzle is not yet solved. From our observations, we can infer some properties of the radio emission from SGR J1745–2900. For the high brightness temperatures of the single pulses, $T_B \sim [10^{22} - 10^{23}]$ K, a coherent mechanism for the radio emission is required. Following Lorimer & Kramer (2005), its radio luminosity is estimated to be $R_{\text{lum}} \sim 10^{29}$ erg s⁻¹, assuming a duty cycle of 0.15 and an emission cone opening angle of 4°. Its spin-down luminosity is $\dot{E} \sim [10^{33} - 10^{34}]$ erg s⁻¹, depending on what timing solution is used (our own, or e.g. Kaspi et al., 2014; Lynch et al., 2014). Therefore, $R_{\text{lum}}/\dot{E} \sim [10^{-4} - 10^{-5}]$. This shows that the radio emission could be powered by its rotational kinetic energy; although this does not mean that this is the source or rule out that other mechanisms are involved. SGR J1745–2900 shows common characteristics with ordinary pulsars, and remarkable differences, like it is for the other three known radio magnetars (Kramer et al., 2007; Camilo et al., 2008; Lazaridis et al., 2008; Levin et al., 2012). The reason for this, as well as the details of the radio emission from pulsars in general, is still unknown.

Finally, the detection of SGR J1745–2900 up to 225 GHz at a distance of 8.3 kpc shows that it is, in principle, possible to search for pulsars in the GC at these frequencies. A key advantage of pulsar searches at millimetre wavelengths is that any deleterious effects caused by the GC interstellar medium (i.e. pulse scattering and dispersion) can be fully neglected. Along the same lines, any deleterious effects caused by the intergalactic medium, which are not well known, could also be neglected or will have

a minimal impact. It might therefore also be an option to search for shallow-spectrum pulsars in nearby galaxies through single-pulse emission. At 1.4 GHz, the magnetar is more luminous than 97 per cent of all known pulsars, and it is by far the most luminous in the millimetre band. This fact alone suggests a larger less-luminous population that can be detected with increased sensitivity at the millimetre band. In any case, pulsar searches with more sensitive millimetre telescopes, such as ALMA, are promising.

Acknowledgements

We are grateful to the referee S. Johnston for very useful comments, to A. Jessner and D. Riquelme for discussions, to P. Lazarus for sharing code, and to C. Ng for reading the manuscript. Partly based on observations with the 100-m telescope of the MPIfR at Effelsberg. The Nançay radio observatory is operated by the Paris Observatory, associated to the French CNRS. IRAM is supported by INSU/CNRS (France), MPG (Germany) and IGN (Spain). APEX is a collaboration between the MPIfR, the European Southern Observatory, and the Onsala Space Observatory. PT is supported for this research through a stipend from the International Max Planck Research School (IMPRS) for Astronomy and Astrophysics at the Universities of Bonn and Cologne.

Detection of the magnetar SGR J1745–2900 up to 291 GHz with evidence of polarized millimetre emission

This chapter is based on an article submitted to the Monthly Notices of the Royal Astronomical Society on the 27th of June 2016. Only very minor format changes were made in order to match the style of this thesis.

I am the lead author of the article. My main contributions include the writing of the observing proposal, doing the observations with the IRAM 30-m, the millimetre wavelength data reduction (including the absolute flux density calibration), and the writing of the article. I did not carry out the observations and data reduction at 2.54, 4.85 and 8.35 GHz.

The full list of authors is:

P. Torne, G. Desvignes, R. P. Eatough, R. Karuppusamy, G. Paubert, M. Kramer, I. Cognard., D. J. Champion, L. G. Spitler

Abstract

In [Torne et al. \(2015\)](#), we showed detections of SGR J1745–2900 up to 225 GHz (1.33 mm); at that time the highest radio frequency detection of pulsar emission. In this work, we present the results of new observations of the same magnetar with detections up to 291 GHz (1.03 mm), together with evidence of linear polarization in its millimetre emission. SGR J1745–2900 continues to show variability and is, on average, a factor ~ 4 brighter in the millimetre band than in our observations of July 2014. The new measured spectrum is slightly inverted, with $\langle \alpha \rangle = +0.4 \pm 0.2$ (for $S_\nu \propto \nu^\alpha$). However, the spectrum does not seem to be well described by a single power law, which might be due to the intrinsic variability of the source, or perhaps a turn-up somewhere between 8.35 and 87 GHz. These results may help us to improve our still incomplete model of pulsar emission and, in addition, they further support the search for and study of pulsars located at the Galactic Centre using millimetre wavelengths.

5.1 Introduction

Magnetar is the term used to refer to neutron stars whose high-energy luminosities can exceed their spin-down luminosity. These objects typically show large inferred magnetic fields ($B \gtrsim 10^{13}$ G), and it is widely accepted that they require energy from magnetic field decay to power their emission, particularly at high energies (Duncan & Thompson, 1992; Thompson & Duncan, 1995, 1996). The magnetars make up a small family within the pulsar population, with only 23 objects confirmed (see The Magnetar Catalog¹, Olausen & Kaspi, 2014). They are typically detected through their high-energy emission, but four of them have also shown radio pulsations (Camilo et al., 2006, 2007a; Levin et al., 2010; Eatough et al., 2013c).

SGR J1745–2900 is one of the radio emitting magnetars, and its location at the Galactic Centre, close to Sgr A* (Bower et al., 2015), makes it a particularly interesting object. Studying the propagation effects of its emission can provide valuable information about the environment close to the supermassive black hole at the centre of the Galaxy and along the line-of-sight (e.g. Eatough et al., 2013c; Shannon & Johnston, 2013; Bower et al., 2014; Spitler et al., 2014).

The radio emission of magnetars is similar to that of the normal population of pulsars, but shows some remarkable differences. For example, their flux density, spectral index, pulse profile shape, and polarization properties have been seen to vary on short and long time scales (Camilo et al., 2006, 2007a; Kramer et al., 2007; Lazaridis et al., 2008; Levin et al., 2012; Lynch et al., 2015). Such variability is inconsistent in most cases with propagation effects, and it is considered intrinsic to the source.

Another peculiar characteristic of magnetar radio emission is the tendency to be spectrally flat, and SGR J1745–2900 is no exception (Torre et al., 2015). This is interesting because pulsars, being typically steep spectrum sources (with mean spectral index $\langle \alpha \rangle = -1.8$, Maron et al., 2000), are difficult to detect at radio frequencies above a few gigahertz. In fact, only seven normal pulsars have been detected above 30 GHz to date (Wielebinski et al., 1993; Kramer et al., 1997a; Morris et al., 1997; Löhmer et al., 2008). SGR J1745–2900 held the record, prior to this work, with detections up to 225 GHz (Torre et al., 2015), followed by XTE J1810–197 up to 144 GHz (Camilo et al., 2007b).

The study of the characteristics of pulsar radio emission at high frequencies can help to elucidate how the emission from neutron stars is produced; a problem that remains unresolved since the discovery of pulsars almost 50 years ago (see e.g. Hankins et al., 2009; Melrose & Yuen, 2016). For instance, some models predict a possible turn-up in the spectrum at sufficiently high frequencies, due to incoherent emission becoming dominant (Michel, 1978, 1982). Observational works have reported an excess of flux density for some of the pulsars studied at millimetre wavelengths (Wielebinski et al., 1993; Kramer et al., 1996, 1997a), giving credibility to those models. However, the sample of pulsar observations at high radio frequencies is small. More observations are needed to study better the behaviour of the high frequency emission, and to check for

¹www.physics.mcgill.ca/~pulsar/magnetar/main.html

turn-ups or other unpredicted effects.

Because of its high luminosity and flat spectrum (Torre et al., 2015), SGR J1745–2900 is a superb source to be observed at very high radio frequencies, especially at the short millimetre regime where there is almost no information about pulsar radiation. This work presents the results from a multifrequency campaign for SGR J1745–2900 carried out at frequencies between 2.54 and 291 GHz (wavelengths between 11.8 cm and 1.03 mm) aiming to obtain further information about its emission properties and providing additional constraints for pulsar emission models.

5.2 Observations and data analysis

The millimetre observations were made with the 30-m radio telescope of the Institut de Radioastronomie Millimétrique (IRAM) during 2015 March 4-9. The receiver used was the Eight Mixer Receiver (EMIR, Carter et al., 2012). EMIR delivers four separated, tunable frequency bands between ~ 73 to 350 GHz (4 and 0.8 mm) in dual linear polarization². During the six days of observations different set-ups were used, mainly depending on weather, covering between 87 and 291 GHz. The Broad-Band-Continuum (BBC) backend recorded the four bands tuned in EMIR with ~ 6 GHz of bandwidth each (~ 24 GHz in total), no frequency resolution (i.e. total power mode), with a sampling time of 1 ms. After several upgrades, the intermediate frequency (IF) range of all EMIR mixers is 4 to 12 GHz which is directly fed to the BBC power detectors. However, there is a significant slope in the passband, which favours the lower frequencies, and we have therefore taken 6 GHz (instead of 8 GHz) as the properly weighted effective IF bandwidth. The sky frequency values corresponding to the centre of the 4–12 GHz IF range of the used EMIR mixers are 87, 101, 138, 154, 209, 225, 275, and 291 GHz.

In addition to the observations with the IRAM 30-m, we observed simultaneously at certain epochs with the Effelsberg 100-m radio telescope and with the Nançay 94-m equivalent radio telescope. At Effelsberg, two different observing frequencies were used, centred at 4.85 and 8.35 GHz. At Nançay, the central frequency was 2.54 GHz. The set-up, data reduction and calibration of the Effelsberg and Nançay data were identical to those already described in Torre et al. (2015). Table 5.1 summarizes the observations.

At IRAM, each observing session consisted typically of 45-min scans on SGR J1745–2900 with interspersed “hot-cold-sky” calibration measurements. Additionally, a few scans on planets were used to verify the absolute flux density calibration, obtained following the methodology in Kramer (1997), and applying elevation and frequency-dependent gain corrections (Peñalver, 2012).

Typical “switching techniques” used in millimetre observations to subtract the atmospheric contribution are not adequate for pulsar observations. Thus, the time series at millimetre wavelengths required careful processing to enhance the detections of the magnetar. This is because of a significant amount of red noise present in the data,

²For more information on the EMIR frequency combinations, see <http://www.iram.es/IRAMES/mainWiki/EmirforAstronomers>

mostly due to variations in the atmospheric water vapour content during the observations. Such effect can be particularly bad for observations of SGR J1745–2900 due to its long period and the low elevation at which the IRAM 30-m sees the Galactic Centre (elevation < 25 deg), which translates into a considerable airmass³. The data showed also periodic interference, the most prominent being at 1 and 50 Hz and some of their harmonics, most likely related to the cryogenerator and the mains power.

The cleaning process was as follows. First, the time series was Fourier transformed and prominent interference was removed by zapping a few spectral bins around each peak at 1, 2, 50, 55, 60, 100 and 200 Hz. After an inverse Fourier transform, the resulting time series was filtered by a running mean with a window length of 10 s. To prevent the filtering from degrading the magnetar pulses, we used an ephemeris from a timing model to predict the times of arrival of the pulses at the observatory, and protected a window of 0.81 s (approximately the pulse width) around each time-of-arrival. This was achieved by extrapolating 3.75 s of the running mean vector from each side of the protection window by using a third-degree polynomial. For the two highest observing frequencies, 275 and 291 GHz, we extrapolated a shorter block of running mean vector of only 0.05 s to each side, using a linear interpolation, which gave better results. Once we had a modified time series with the content of the protected windows substituted by the extrapolated data, we apply a running mean on this new time series that is then subtracted from the original one. This method is effective at cleaning the pulse, while avoiding the artefacts caused by the running mean. Next, we removed some negative spikes that occasionally appear in the time series by substituting all negative values of the time series larger than -4σ with the median of the time series. A final step was to apply a second running mean filter with a smaller window of 0.4 s, again protecting the pulse window, to remove short-term variations.

The result of the cleaning process is a high signal-to-noise folded profile with nearly flat off-pulse baseline. The mean flux density (i.e. the integrated profile intensity averaged over the full period) is calculated by summing the area under the pulse and dividing by the number of bins in the profile. Flux density errors are estimated from the off-pulse noise and also include the uncertainties in the absolute calibration factors, estimated to 10, 20 and 30 per cent for the 3, 2 and 1 mm bands, respectively.

5.3 Results and discussion

5.3.1 Detections, flux density and spectrum

SGR J1745–2900 was detected at all frequencies from 2.54 up to 291 GHz. The weather conditions at IRAM 30-m were excellent during five days of observations (zenith opacity at 225 GHz < 0.25), contributing to the successful detections at the highest frequencies. In addition, the magnetar was particularly bright in the millimetre band during this observing campaign, with a varying flux density of mean value (averaged over all the millimetre observations) $\langle S_{\text{mm}} \rangle = 5.5 \pm 0.4$ mJy. This is a factor ~ 4 brighter than

³Airmass refers to the amount of Earth's atmosphere that a celestial signal passes through along the line of sight.

in July 2014 (Torre et al., 2015). In contrast, at the lowest frequencies, 2.54 to 8.35 GHz, the magnetar was a factor ~ 6 dimmer than in July 2014.

Figure 5.1 shows the averaged pulse profiles of SGR J1745–2900 at all frequencies from 2.54 to 291 GHz. The detections at 209 and 225 GHz are now clear with peak signal-to-noise ratios of about 12, confirming the tentative detections presented in Torre et al. (2015). At the highest frequencies, 275 and 291 GHz, the detections are weaker, but the alignment of the peaks with the pulse arrival phase predicted by the timing ephemeris strengthen their significance.

Table 5.2 presents the measured mean flux densities and spectral index per day, together with the total averaged values. The high system temperatures and red noise (dominated by atmospheric effects) at 275 and 291 GHz made the detections at these frequencies challenging on individual days. Once the observations were combined, we obtained more significant detections (see Fig. 5.1) and measurements of the mean flux densities.

We remark that the flux density values presented in Table 5.2 for each frequency are averages per day. In some cases, the intensity of SGR J1745–2900 varied between different single observations by up to a factor of 2, in less than a few hours. Furthermore, within single observations, the flux density is sometimes seen to vary by a factor of a few in what seems to be a bursty behaviour. We investigated if the scintillation effect in the ISM could be responsible for this variability. Following Cordes & Lazio (1991), we calculate that the scintillation at the lowest frequencies, 2.54, 4.85 and 8.35 GHz, is negligible (and so, the variability of the magnetar at these frequencies must be intrinsic). At the millimetre wavelengths (87 GHz and above) the scintillation cannot be fully neglected, but at most it could account for an intensity modulation of a few tens of per cent. This could explain small intensity variations between consecutive days (see Table 5.2), as the refractive interstellar scintillation can have time scales down to a few days, but it cannot account for the variations of factors of a few that we also observe. Therefore, at the millimetre wavelengths the emission of SGR J1745–2900 must also have a large fraction of intrinsic variability. Furthermore, the variations of SGR J1745–2900 are not only in radio flux density and spectral index, but also in profile shape and polarization characteristics, a behaviour similar to what has been reported for this and the other known radio magnetars (e.g. Kramer et al., 2007; Camilo et al., 2007a, 2008; Levin et al., 2012; Lynch et al., 2015; Pennucci et al., 2015).

Figure 5.2 shows the observed averaged spectrum of SGR J1745–2900. Interestingly, the magnetar was clearly weaker at the lower frequencies, 2.54 to 8.35 GHz. A single power law fit yields a slightly inverted spectral index of $\langle\alpha\rangle = +0.4 \pm 0.2$. This is still consistent with a flat spectrum typical from radio loud magnetars, but it is somewhat different to the spectrum observed for the same source in July 2014 ($\langle\alpha\rangle = -0.4 \pm 0.2$; Torre et al., 2015).

It is noticeable that the single power law does not fit well all the data points (in particular 4.85 and 8.35 GHz). We can think of several possible explanations. The first is that the intrinsic variability of the source behaves differently at different frequencies and deviates the spectrum from the single power law. A second possibility is that the measurements at low frequencies suffer from some systematic error, perhaps due to

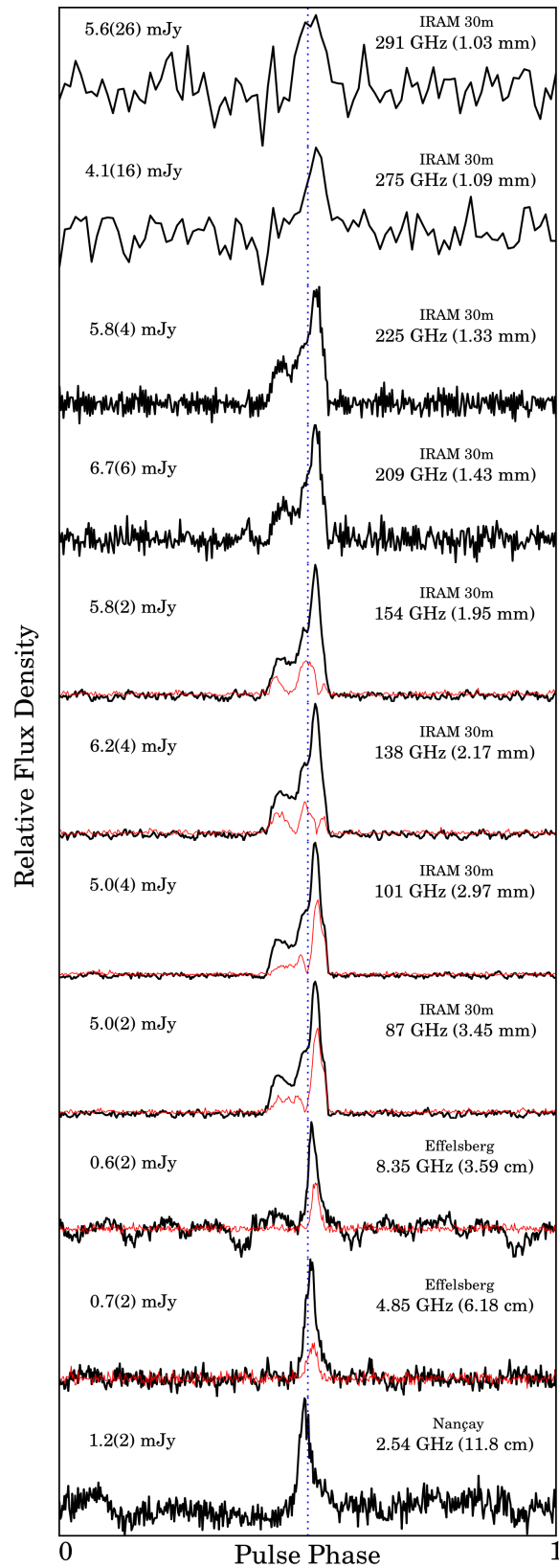


Figure 5.1: Average profiles of SGR J1745–2900 from 2.54 up to 291 GHz. The black thick line represents the total intensity profile, and the red thinner line shows the linear polarization, which is a lower limit between 87 and 154 GHz (see text). The vertical dotted line marks the predicted rotational phase from the ephemeris.

interference or red noise. The detections at Effelsberg were weaker than in the previous observing campaign in July 2014 (Torre et al., 2015) and the profile baseline showed some non-Gaussian noise (see e.g. the 8.35 GHz averaged profile in Fig. 5.1), which could lead to an under or overestimation of the flux density if the pulse lies on a dip or bump of the baseline, respectively. However, such effects would not account for deviations in the measurements larger than a few tens of per cent and are reflected in the errors at those frequencies. Thus, we consider this explanation less likely. Finally, a last possible explanation could be that there is a turn-up in the spectrum somewhere between 8.35 and 87 GHz. A turn-up might occur as a result of the decrease in the efficiency of the coherent radiation mechanism, together with an incoherent component of emission that could take over. This effect is predicted by some pulsar emission models (Michel, 1978, 1982), and hints of turn-ups have in fact been observed in some pulsars at around ~ 30 GHz (Wielebinski et al., 1993; Kramer et al., 1996, 1997a). Moreover, an incompatibility with a single power law has also been reported for the spectrum of another radio magnetar, 1E 1547.0–5408 (Camilo et al., 2008), suggesting the possibility of more complex spectra in radio magnetars than the typical single or broken power law of normal pulsars. The location of the possible turn-up in pulsar emission is not clear (it could be somewhere between radio and infrared, see Michel, 1982), and SGR J1745–2900 is at the moment the only pulsar detectable from a few up to a few hundreds of gigahertz, which could be key to detect that possible turn-up in its spectrum. Additional simultaneous multifrequency observations covering the region around ~ 30 –40 GHz would be helpful to solve the turn-up question.

5.3.2 Linear polarization

Apart from the total intensity detections, we observe evidence of linear polarization in the emission from SGR J1745–2900, including at the millimetre wavelengths. This is obvious from the comparison of the pulse profile morphology from the horizontal (H) and vertical (V) linear feeds of the IRAM 30-m, which clearly show a different profile shape in most of the observations. Figure 5.3 shows a comparison of the H and V pulse profiles at 87, 101 and 154 GHz as an example.

This pulse profile morphology inequality when recording data with orthogonal linear feeds is indicative of radiation that must have a certain degree of linear polarization. Unfortunately, the BBC backend does not provide all Stokes parameters, making it not possible to quantify the degree of both linear and circular polarization in the millimetre emission directly. However, we can calculate Stokes Q from the power of the two linear feeds and set a lower limit in the degree of linear polarization: $L = \sqrt{Q^2 + U^2} \geq |Q|$. The *lower limit* of L reaches values as high as 100 per cent for certain profile bins, and it is greater than zero for most of the pulse (see Fig. 5.3 and 5.1). Moreover, minimum values of L greater than zero are noticeable in certain profile bins up to 225 GHz, and tentatively at 275 GHz. At 291 GHz the detections are too weak to be conclusive. However, the noise levels are higher above 154 GHz, and we also note apparent correlated noise between the two polarizations for frequencies between 209 and 291 GHz. The origin of this noise is not fully understood and, for this reason, we

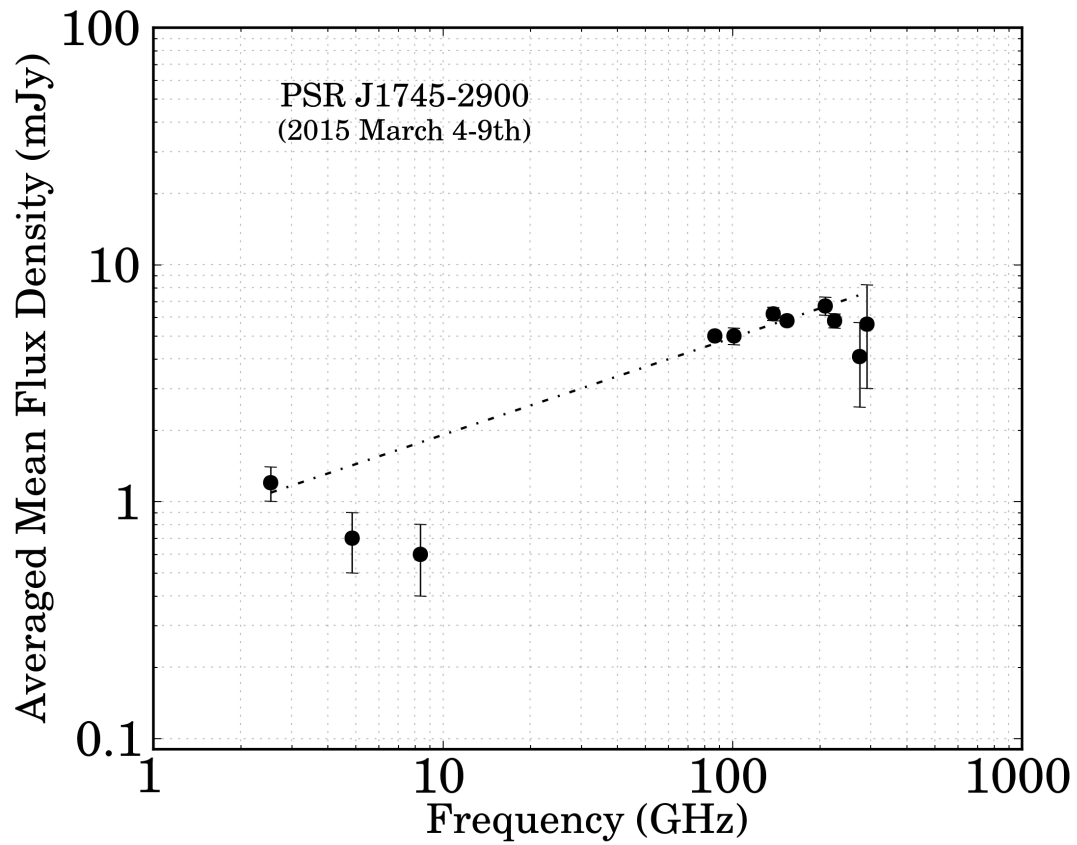


Figure 5.2: Average spectrum of SGR J1745–2900 from the observations. The dashed-dotted line shows the spectral index fit using a single power law. The mean spectral index obtained is $\langle\alpha\rangle = +0.4 \pm 0.2$. Error bars are 2σ .

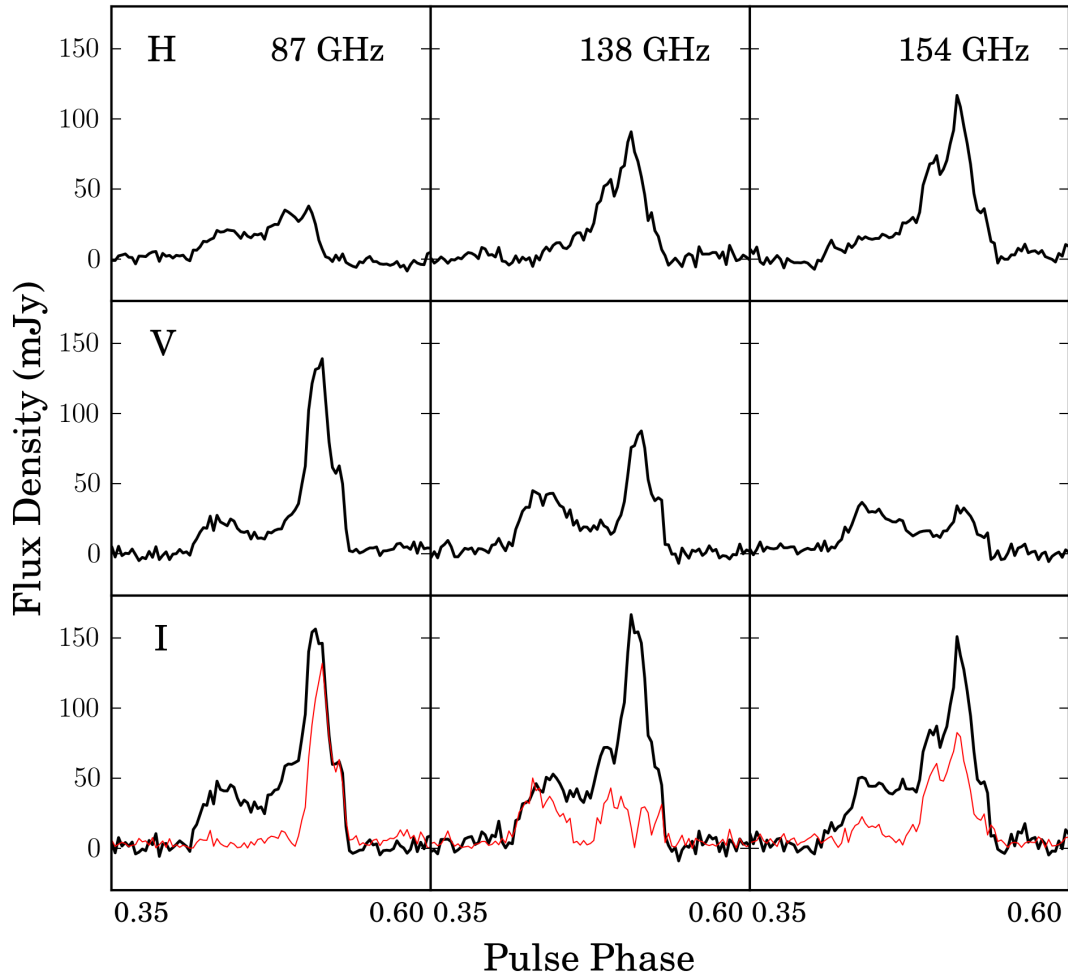


Figure 5.3: Selected examples of the pulse profile morphology differences seen in the two linear feeds of the IRAM 30-m at three different frequencies. The top panels show the profile detected on the horizontal feed (H), the middle panels on the vertical feed (V), and the bottom panels show the total intensity $I = H + V$ (black thick line), with the lower limit of the degree of linear polarization (red thin line, see text). The differences in the profile shape between the two feeds are recurrent, and the lower limit on the degree of linear polarization is greater than zero in many bins across the profile (see also Fig. 5.1), reaching values of up to 100 per cent linearly polarized emission for some profile bins.

Table 5.1: Summary of the observations. For each day and frequency (ν), the total integration time (ΔT_ν) on SGR J1745–2900 is given in minutes. The symbol “–” means that no observation was done at that frequency on that particular day. The observations at 2.54 GHz were taken with Nançay, 4.85 and 8.35 GHz with Effelsberg, and 87 to 291 GHz with IRAM 30-m.

Date	$\Delta T_{2.54}$ (min)	$\Delta T_{4.85}$ (min)	$\Delta T_{8.35}$ (min)	ΔT_{87} (min)	ΔT_{101} (min)	ΔT_{138} (min)	ΔT_{154} (min)	ΔT_{209} (min)	ΔT_{225} (min)	ΔT_{275} (min)	ΔT_{291} (min)	MJD (days)
2015 Mar 04	55	72	72	180	180	90	90	90	90	–	–	57085
2015 Mar 05	–	–	–	90	90	90	90	90	90	90	90	57086
2015 Mar 06	–	60	60	90	90	90	90	90	90	90	90	57087
2015 Mar 07	72	–	–	78	78	45	45	78	78	45	45	57088
2015 Mar 08	–	66	72	90	90	185	185	–	–	95	95	57089
2015 Mar 09	72	–	–	45	45	45	45	–	–	–	–	57090

Table 5.2: Measured flux densities and spectral indices of SGR J1745–2900. Two-sigma errors in the last digits are shown in parentheses. The symbol “–” means that no observation was done at that frequency on that particular day. “ND” indicates observations with no detection.

Date (2015)	$S_{2.54}$ (mJy)	$S_{4.85}$ (mJy)	$S_{8.35}$ (mJy)	S_{87} (mJy)	S_{101} (mJy)	S_{138} (mJy)	S_{154} (mJy)	S_{209} (mJy)	S_{225} (mJy)	S_{275} (mJy)	S_{291} (mJy)	α
2015 Mar 04	1.0(2)	0.9(2)	0.8(2)	6.2(2)	6.4(2)	7.7(2)	6.3(4)	5.9(14)	3.7(8)	–	–	+0.5(4)
2015 Mar 05	–	–	–	5.4(2)	5.0(2)	6.3(2)	5.3(2)	6.9(8)	7.0(6)	4.6(28)	4.5(38)	+0.2(6)
2015 Mar 06	–	0.7(2)	0.6(2)	3.7(2)	3.7(2)	7.5(2)	6.5(2)	5.5(10)	5.1(8)	5.9(24)	6.7(36)	+0.8(6)
2015 Mar 07	1.4(6)	–	–	6.4(2)	5.7(2)	6.4(2)	5.8(2)	8.5(12)	7.2(6)	ND	ND	+0.1(6)
2015 Mar 08	–	0.4(2)	0.4(2)	5.1(2)	5.1(2)	5.3(2)	5.9(2)	–	–	1.6(30)	ND	+0.4(6)
2015 Mar 09	1.2(2)	–	–	3.4(2)	4.3(4)	3.8(6)	4.7(6)	–	–	–	–	+0.3(2)
Total Average	1.2(2)	0.7(2)	0.6(2)	5.0(2)	5.0(4)	6.2(4)	5.8(2)	6.7(6)	5.8(4)	4.1(16)	5.6(26)	+0.4(2)

do not show here the lower limits on L for frequencies above 154 GHz. Ongoing work for a more detailed analysis of the polarized emission from SGR J1745–2900 will be presented in a future publication (Wucknitz et al. in prep.).

This is the first time linearly polarized emission up to 154 GHz (1.95 mm) has been seen in a pulsar. It is closely followed by XTE J1810–197, with inferred linear polarization up to 144 GHz (Camilo et al., 2007b). For normal pulsars, the highest radio frequency at which polarization has been detected is 32 GHz (Xilouris et al., 1996). Polarized emission at such high level and frequencies as seen for SGR J1745–2900 is unusual, as radio pulsars have been reported to depolarize at high radio frequencies (Morris et al., 1981; Xilouris et al., 1996). In contrast, radio magnetars can stay highly linearly polarized up to very high frequencies (Kramer et al., 2007; Camilo et al., 2008). Consequently, the polarized emission at millimetre wavelengths of SGR J1745–2900 is not totally unexpected. In fact, Kravchenko et al. (2016) measured an averaged linear polarization for this magnetar of about 65 per cent at ~ 40 GHz.

The polarization in pulsar emission is generally linked with a coherent radiation mechanism. The fact that high degrees of linear polarization are measured at the millimetre wavelengths for SGR J1745–2900 therefore may conflict and weaken the idea of an incoherent component of emission responsible for a turn-up in its spectrum.

5.4 Summary

We show in this paper that the radio emission from highly magnetized neutron stars can reach extremely high frequencies with detections that reach 291 GHz (1.03 mm). These new detections break the previous record recently set in Torne et al. (2015) as the highest radio frequency detection of pulsar emission, and give us more hints about the radiation mechanism of these objects. SGR J1745–2900 continues to show significant variability in its emission characteristics, and its averaged mean flux density in the millimetre band is a factor ~ 4 higher than in July 2014, while between 2.54 and 8.35 GHz is on average a factor ~ 6 dimmer. Furthermore, we show evidence for a significant degree of linear polarization in the millimetre emission from SGR J1745–2900, reaching factors up to a 100 per cent for certain profile bins, and being the polarized emission at the highest radio frequencies ever detected from a pulsar. The measured spectrum is slightly inverted, with a spectral index of $\langle \alpha \rangle = +0.4 \pm 0.2$ when a single power law is fit. The spectrum has an uncommon shape, with decaying flux density between 2.54 and 8.35 GHz and a much stronger emission at the millimetre band, which may be due to intrinsic intensity variability or indicative of the existence of a turn-up in the emission somewhere between 8.35 and 87 GHz. These new results are relevant to the development of better pulsar emission models, in particular those trying to explain the radio emission from magnetars; and are also further proof that we can detect and study pulsars located at the Galactic Centre using millimetre wavelengths.

Acknowledgements

We thank Olaf Wucknitz and Dominic Schnitzeler for discussions on the polarization analysis, Jim Cordes for discussions on scintillation effects, and the staff at the IRAM 30-m for their great support. Based on observations carried out with the IRAM 30-m, the Effelsberg 100-m, and the Nançay radio telescopes. The Nançay radio observatory is operated by the Paris Observatory, associated to the French CNRS. The Effelsberg 100-m is operated by the MPIfR (Max-Planck-Institut für Radioastronomie). IRAM is supported by INSU/CNRS (France), MPG (Germany) and IGN (Spain). P.T. is supported for this research through a stipend from the International Max Planck Research School (IMPRS). Financial support by the European Research Council for the ERC SynergyGrant *BlackHoleCam* (ERC-2013-SyG, Grant Agreement no. 610058) is gratefully acknowledged. L.G.S. gratefully acknowledges financial support from the ERC Starting Grant BEACON under contract no. 279702.

Pulsar observations at 3 and 2 mm

The work presented in this chapter is part of an ongoing project to study the characteristics of pulsar emission at short millimetre wavelengths, for the first time above 3.44 mm (87 GHz) and reaching 2.17 mm (154 GHz). I am the lead scientist of the project. I wrote two (accepted) observing proposals for the IRAM 30-m radio telescope, took most of the observations, and carried out the data reduction for the detections of PSR B0355+54 presented here. I am also the lead author of the paper that is in preparation.

When completed, this work will comprise an article that will be submitted with the following author list:

P. Torne, G. Desvignes, R. P. Eatough, G. Paubert., R. Karuppusamy, M. Kramer.

Abstract

The study of the properties of pulsar emission at very high radio frequencies is relevant for understanding the still unknown radio emission process. We present the observations of a sample of six pulsars at 3.44, 2.97, 2.17, and 1.95 mm (87, 101, 138, and 154 GHz) using the IRAM 30-m radio telescope, with simultaneous observations using the Effelsberg 100-m radio telescope at 6.18 and 3.59 cm (4.85 and 8.35 GHz) at certain epochs. The results comprise the detections of PSR B0355+54 from 87 to 138 GHz and its flux density measurements. For the other five pulsars, no obvious detections were achieved. The detections of PSR B0355+54 above 87 GHz are the highest detections of radio emission from any ordinary pulsar to date (i.e. excluding the radio magnetars). We measure an apparent fainter emission between 87 and 138 GHz, that seems to deviate from the power law extrapolated from lower frequencies. If real, this might be indicative of an inefficiency of the coherent radio emission process. However, we think that such deviation from the power law might be caused by the variability of the source, or perhaps by changes in the observing system sensitivity during the observations, for example due to weather, not taken into account in the calibration of the data. Forthcoming precise calibration information about the instrument will allow us to revisit the data providing stronger conclusions on the nature of PSR B0355+54's apparent decreasing intensity at the millimetre wavelengths.

6.1 Introduction

Almost 50 years after the discovery of pulsars, the underlying mechanism responsible for their radio emission is still unknown. Many of the theoretical radiative models for pulsars are driven by observational input and constraints (e.g. Kramer et al., 1997b, 2006a; Eilek & Hankins, 2016), but given the difficulties for studying pulsars at high radio frequencies (mainly due to their faintness and steep spectra), the vast majority of the observational studies have been carried out at frequencies between ~ 0.1 –10 GHz. However, the information obtained at higher frequencies has several advantages and can be crucial to improve the existing models. One advantage is that at sufficiently high radio frequencies the influence of the Inter Stellar Medium (ISM) and the pulsar magnetosphere in the propagation of the emission becomes negligible. Therefore, the observed characteristics of the radiation should be essentially intrinsic. Another vantage is the possibility to explore the deepest parts of the magnetosphere, arising from the apparent *radius-to-frequency mapping* in pulsar radio emission (Cordes, 1978). Very close to the neutron star surface the physical conditions may be different than at higher altitudes, for instance having larger plasma densities or by the presence of multipolar components of the magnetic field. Those changes in the physical properties of the emission region might leave a measurable imprint in the radiation characteristics (e.g. Davies et al., 1984), and may only be detectable at very high radio frequencies.

Former works studying pulsars at very high frequencies provided remarkable results, evidencing the relevance of this kind of studies (despite their difficulty) for understanding the emission process. In the first observations of pulsars at millimetre wavelengths, Wielebinski et al. (1993) reported considerably higher intensities for some pulsars at 8.7 mm (34 GHz) in comparison with the expected values extrapolated from the known spectra at lower frequencies. Further observations by Kramer et al. (1996) confirmed the unexpectedly high flux densities for PSRs B1929+10 and B2021+51, revealing what seemed to be a flattening or turn-up in their spectrum in the frequency range 27–36 GHz. Kramer et al. (1997a) re-observed some of the pulsars and expanded the spectral analysis to 7 mm (43 GHz), concluding that there is indeed an usual behaviour of the spectrum of some pulsars at the millimetre wavelengths in the form of a positive deviation from the expected power law. Nevertheless, it is interesting to note that some of the observed pulsars did follow the extrapolation of the spectrum from lower frequencies, and it is unclear why some pulsars seem to flatten/turn-up while at the same frequencies others do not. In addition to the spectral analysis, Kramer et al. (1996, 1997c) also reported unusual intrinsic variability of the emission at millimetre wavelengths and, from the the results of a polarisation analysis of the data, Xilouris et al. (1996) showed that the pulsars also suffer of a strong depolarization at these frequencies. These results triggered the observations of PSRs B0355+54 and B2021+51 at 3.44 mm (87 GHz) by Morris et al. (1997), with a detection of PSRs B0355+54 showing the same flux density (within error bars) to that measured previously at 7 mm. Thus, this was an indication that spectral flattening may occur also at much higher frequencies. Finally, Kramer et al. (1997b) used high frequency data to constrain the emission region size, discard the existence of multipolar components of the magnetic field in the

emission region of long period pulsars, and provide measurements that could potentially yield absolute emission heights. No new studies of pulsars at these frequency ranges were published until more than a decade later. Löhmer et al. (2008) carried out new observations of a larger sample of pulsars at 9 mm (32 GHz), confirming the flux density measurements of Kramer et al. (1996). The confirmed values included the higher-than-expected flux densities of PSR 1929+10 and B2021+51, giving additional credibility to the observed flattening in their spectra.

Most of these unusual effects observed at such high radio frequencies are quite interesting, in particular because they fit well only in one class of radio emission models, i.e. those based on antenna mechanisms. This class of models considers an incoherent mechanism (typically synchrotron or curvature emission) that can also produce a coherent component due to bunched particles or some kind of resonance. Such coherent process is expected to be dominant at radio frequencies. As a result, if the model applies, the emission produced by a pulsar is the superposition of the incoherent and the coherent components. That combination of components may be identifiable in the spectrum shape, that is expected to show a region where it changes from a decreasing intensity (due to the loss of efficiency of the coherent process) to an increasing intensity (due to the incoherent component taking over, see also Section 1.2.2). Measuring the frequency where the turn-up of the spectrum occurs would give us an estimation of the coherence length intrinsic to the mechanism responsible for the radio radiation at low frequencies (e.g. Michel, 1982). Despite some arguments against the viability of the antenna mechanism models (Melrose, 1992; Lesch et al., 1998), these are perhaps the most widely supported by observations (see also e.g. Rankin, 1983, 1990; Mitra & Rankin, 2011). One of the best examples is the Crab pulsar, that shows an infrared and optical emission much brighter than what would be expected from the simple extrapolation from the radio frequencies (Smith, 1977, see Figure 1.4). This characteristic highly suggests the existence of an spectral turn-up somewhere between these two frequency ranges. Although the spectrum of the Crab pulsar has been extensively studied, it still has a gap of undetected emission just in the region between radio and infrared wavelengths where the turn-up could remain yet unobserved. Furthermore, there is theoretical support for the infrared, optical and X-ray emission being indeed produced by an incoherent process (Crusius-Wätzels et al., 2001).

Finally, remark that understating better the characteristics of pulsar emission at short millimetre wavelengths has recently become important also for another reason. The paucity of pulsar discoveries in the many past surveys of the Galactic Centre, believed to be due to strong deleterious ISM effects, and in particular the scattering, has pushed the observing frequencies of the surveys in this region higher and higher in the last decade. Despite the efforts, there was no success uncovering the hidden Galactic Centre pulsar population yet (see Chapter 3). As already discussed, the ISM effects at sufficiently high radio frequencies can be fully neglected, and for this reason a new survey for pulsars in the Galactic Centre is planned under the *BlackHoleCam* project at around ~ 3.44 mm (~ 87 GHz) using the most sensitive radio telescopes of this class (e.g. the IRAM 30-m, the LMT, and ALMA, see Goddi et al., 2016). The possible spectral turn-up and intrinsic variability of pulsars at these frequencies are effects that

should be taken into account to optimally design the survey at 3.44 mm; for instance to plan repeated observations in order to average the effects of intensity variabilities, or to include spectral flattening in the estimations of the number of detectable pulsars based on the sensitivity limits of the instruments.

This chapter presents the observations of a selected sample of six pulsars at 3.44, 2.97, 2.17, and 1.95 mm (87, 101, 138, and 154 GHz) using the IRAM 30-m radio telescope. At certain epochs, we observed simultaneously with the Effelsberg 100-m radio telescope at 6.18 and 3.59 cm (4.85 and 8.35 GHz). With the exception of PSRs B0355+54 and B2021+51, observed at 3.44 mm by [Morris et al. \(1997\)](#), this is the first time that pulsars are observed at these short millimetre wavelengths. We aim to detect the sources, measure their flux densities in order to verify if the unusual spectral characteristics appear or continue at higher frequencies, study in more detail possible intrinsic intensity variabilities, and try to detect single pulses at the highest possible frequencies.

6.2 Observations and data reduction

The observations were made during three observing campaigns in July 2014, March 2015, and February 2016. During the observations in February 2016, the 100-m Effelsberg radio telescope was used to simultaneously observe the pulsars at 4.85 and 8.35 GHz, increasing our instantaneous frequency coverage to more than one decade and allowing us to obtain precise ephemeris for the pulsars to aid the data reduction of the millimetre observations. The receivers and set-ups were the same as for the observations of the magnetar SGR J1745–2900, and have been already described in Section 4.2. The only remark is that for the observations presented here only frequencies up to 154 GHz (1.95 mm) were used. In February 2016, a new fast-sampling mode of the Broad-Band Continuum backend (BBC) was available at the IRAM 30-m, enabling the recording of the time series with a sampling time of 100 μ s, i.e. ten times faster than the sampling time used in July 2014 and March 2015. The selection of PSRs B0355+54, B2021+51, B0329+54, and B1929+10 for the observations responds to two criteria: a shallow spectral index (from the catalogue of [Maron et al., 2000](#)) and the hints of flattening in their spectra reported in the literature ([Wielebinski et al., 1993](#); [Kramer et al., 1996, 1997a](#); [Löhmer et al., 2008](#); [Morris et al., 1997](#)). Furthermore, since the 100 μ s of sampling time opened the possibility of observing fast spinning pulsars with a high time resolution, in February 2016 we included in our sample the Crab pulsar (PSR B0531+21) and a recycled millisecond pulsar (PSR J1022+1001). The list of observed sources is summarized in Table 6.1, together with the total accumulated observing time on each source during the three campaigns.

The data reduction for the observations at millimetre wavelengths was as follows. First, we remove some apparently-random large negative spikes present in the time series by substituting all the negative values larger than -6σ with the median value, working in blocks of 10000 samples. Then, the time series are Fourier transformed and

Table 6.1: List of observed pulsars. The reported spin periods are taken from the ATNF PSRCAT (Manchester et al., 2005) and the spectral indices from the catalogue of Maron et al. (2000), except for PSR J1022+1001, that is taken from Kuzmin & Losovsky (2001). The columns $T_{\text{obs}}^{\text{J14}}$, $T_{\text{obs}}^{\text{M15}}$, and $T_{\text{obs}}^{\text{F16}}$ show the total observing time on each source during the observing campaigns of July 2014, March 2015, and February 2016, respectively.

PSR	P (ms)	α	$T_{\text{obs}}^{\text{J14}}$ (min)	$T_{\text{obs}}^{\text{M15}}$ (min)	$T_{\text{obs}}^{\text{F16}}$ (min)
B0355+54	156.382	-1.2	290	327	345
B2021+51	529.196	-1.5	0	135	315
B1929+10	226.517	-1.6	0	135	0
B0329+54	714.519	-2.2	0	0	22
B0531+21	33.392	-3.1	0	0	315
J1022+1001	16.452	-1.4	0	0	435

the excess of red noise is reduced using the `rednoise` routine of the PRESTO¹ pulsar analysis software. At this stage, a strong radio frequency interference at 1 Hz (likely related to the cryogenerator) is removed by zapping a few Fourier bins around 1 and 2 Hz. Then, the data are converted back to the time domain applying the inverse Fourier transform. In order to calibrate the data in flux density, it is required to undo the normalization to a standard deviation of one in the Fourier series applied by `rednoise`. This is achieved by calculating the standard deviation of both the original time series and the one after applying `rednoise` and calculating the scaling factor to be applied to the latter in order to recover the original standard deviation. To keep possible variations of the standard deviation during an observation, this scaling is done in blocks of three seconds in length. In a final step, we smooth the time series with a running mean filtering using a window of three samples. The time series are then folded topocentrically using the ephemeris of the pulsars to obtain the integrated profiles. To obtain the total averaged pulse profiles, we normalized each profile to an off-pulse root mean square of one count, averaging then the profiles at each frequency afterwards. The absolute flux density calibration factors were derived from “hot-cold-sky” calibration scans made typically just before and after each pulsar observation. We follow the methodology presented in Kramer (1997) (see also Section 2.4.2), and the required quantities are manually extracted from the calibration scans using the software MIRA². The final scaling factor applied to each observation is the value at the middle point of the observation, calculated from the linear interpolation of the factors obtained before and after the observation.

¹<https://github.com/scottransom/presto>

²<https://www.iram.fr/IRAMFR/GILDAS/>

6.3 Results and discussion

PSR B0355+54 was detected at 3.44, 2.97, and 2.17 mm (87, 101 and 138 GHz), but not at 1.95 mm (154 GHz). For the rest of the pulsars, there were no obvious detections. The total averaged pulse profiles of PSR B0355+54 are shown in Figure 6.1 together with the profiles obtained at 6.18 and 3.59 cm (4.85 and 8.35 GHz) from Effelsberg. The detections above 87 GHz are the highest detections of radio emission from any ordinary pulsar to date³. The available ephemeris for PSR B0355+54 kept the phase alignment of the profiles between July 2015 and March 2015, but deviated in February 2016. This only affected the phase of the pulsar, and not the folding period, which was correct in all epochs. The reason for the misalignment is unclear, but it could be produced by an instrumental effect, e.g. issues with the time stamps of the data. Thus, the average profiles of each observing campaign were aligned manually using their peak values. Furthermore, since the pulsar was not visible in all the observations, to increase the signal-to-noise of the total averaged profiles shown in Figure 6.1 we used only the observations with detections, discarding those where only noise was observed. This included reviewing the different frequencies and polarization channels individually. For the two highest frequencies with detections (101 and 138 GHz) the individual detections were sometimes very weak, so we only selected observations when the apparent pulse is aligned in phase with pulses seen at other frequencies observed simultaneously, and only when they align to the expected pulse phase from the ephemeris (in February 2016, when the ephemeris deviated in phase, we used simultaneous detections at Effelsberg to correct the phase offset). For the observations at Effelsberg, the data reduction (aimed to obtain the pulse profile and phase) consisted in directly folding each observation using the ephemeris.

We observed an apparent intensity variability of PSR B0355+54, since the pulsar was detectable only in certain observations, and not always at all frequencies. The observed intensity modulations showed time scales of the order of tens of minutes to hours. The diffractive interstellar scintillation (DISS) time scale and bandwidth, calculated for the distance and transverse velocity of the pulsar from [Hobbs et al. \(2005\)](#), are $\Delta t_{\text{DISS}}^{\text{strong}} \sim 20$ s and $\Delta \nu_{\text{DISS}}^{\text{strong}} \sim 100$ MHz, respectively. In the case of refractive scintillation (RISS), the time scale is larger, $\Delta t_{\text{RISS}}^{\text{strong}} \sim 1$ day. The RISS could therefore be responsible of the long modulation that we observe, but the intensity modulations of the order of tens of minutes are difficult to explain by scintillation effects. While the variations could be intrinsic to the pulsar, a stronger conclusion would require of additional data. The reason is that the pulsar is close to the sensitivity limits of the IRAM 30-m telescope, meaning that relatively small changes in the system sensitivity, for instance due to weather, could translate into the variability that we see. Moreover, the pulsar is detected typically with different signal-to-noise in the two polarization channels. While this could be explained by a different sensitivity of the two linear

³Two radio magnetars, XTE J1810–197 ([Camilo et al., 2007b](#)) and SGR J1745–2900 (Chapters 4 and 5) have been detected above 87 GHz, but we do not consider them here as ordinary pulsars. Although magnetars are accepted to be rotating neutron stars, their particular radio emission properties make not clear if their radio emission mechanism is the same as for ordinary pulsars.

feeds of the IRAM 30-m, the reason is still unclear. It could also mean that the pulsar is polarized at these high frequencies, something however not expected since this pulsar has been shown to depolarise at high radio frequencies (Xilouris et al., 1996). These uncertainties will be reduced with additional studies of the instrument noise and an improved calibration including more data, which will allow us to solve the questions about the source of this apparent variability.

Table 6.2 presents the flux density values for PSR B0355+54 at 3.44, 2.97, and 2.17 mm (87, 101 and 138 GHz), and the upper limit at 154 GHz from the radiometer equation (see e.g. Lorimer & Kramer, 2005). The values used to calculate the limit were a total weighted $T_{\text{sys}} = 132.1$ K, $T_{\text{obs}} = 53104$ s, $G = 0.15$ K/Jy, $n_p = 2$, $\Delta\nu = 6$ GHz, and $\delta = 0.1$. The uncertainty in the upper limit value is estimated to 20 per cent, mainly as a consequence of the uncertainty in the gain factor. Table 6.2 also includes the available flux density measurements for the pulsar at other frequencies from the works of Lorimer et al. (1995); Kramer (1995); Kramer et al. (1996, 1997a); Morris et al. (1997); Stovall et al. (2015). Figure 6.2 shows the full spectrum of PSR B0355+54, from 80 MHz to 154 GHz, including our new measurements. Stovall et al. (2015) provided recently an important new point at 80 MHz, adding half a decade in frequency coverage to the low frequencies. Together with the new values provided here, this is likely the spectrum with the largest frequency coverage of any known pulsar in the radio band, thus being an excellent place to look for anomalies that could give us information about the emission process.

The first thing we note is that between 80 MHz and 43 GHz the spectrum is well described by a single power law of spectral index $\alpha = -1.0 \pm 0.2$ (for $S_\nu \propto \nu^\alpha$, cf. Maron et al., 2000). However, our new measurements at 87, 101, and 138 GHz deviate from the preceding trend, decaying more rapidly. This could be indicative of a change in the pulsar spectrum in this frequency range, perhaps if the coherent emission mechanism starts to lose efficiency. As for the case of the source of the observed variability in the intensity, we are prudent not to draw any strong conclusions to explain this deviation yet. First, because we might suffer of an additional uncertainty due to the fact that our flux density calibration is based on calibration scans done just before and after each pulsar observation. This is not the optimal way to calibrate the millimetre data (although it was the best available for our observations) because during the pulsar observation (lasting between ~ 20 –100 min), any change in the atmospheric conditions affecting the sensitivity of the observation cannot be properly taken into account, and are not reflected in the error bars. Secondly, the difference of at least a 50 per cent between our measurement at 87 GHz and that reported by Morris et al. (1997) suggests that, or our calibration suffered indeed of additional unaccounted uncertainty, or there is variability of the source not taken into account. With more precise calibration information about the instrument and a detailed analysis of the source variability, we may revisit the data providing stronger conclusions on the nature of PSR B0355+54’s apparent decreasing intensity at the millimetre wavelengths.

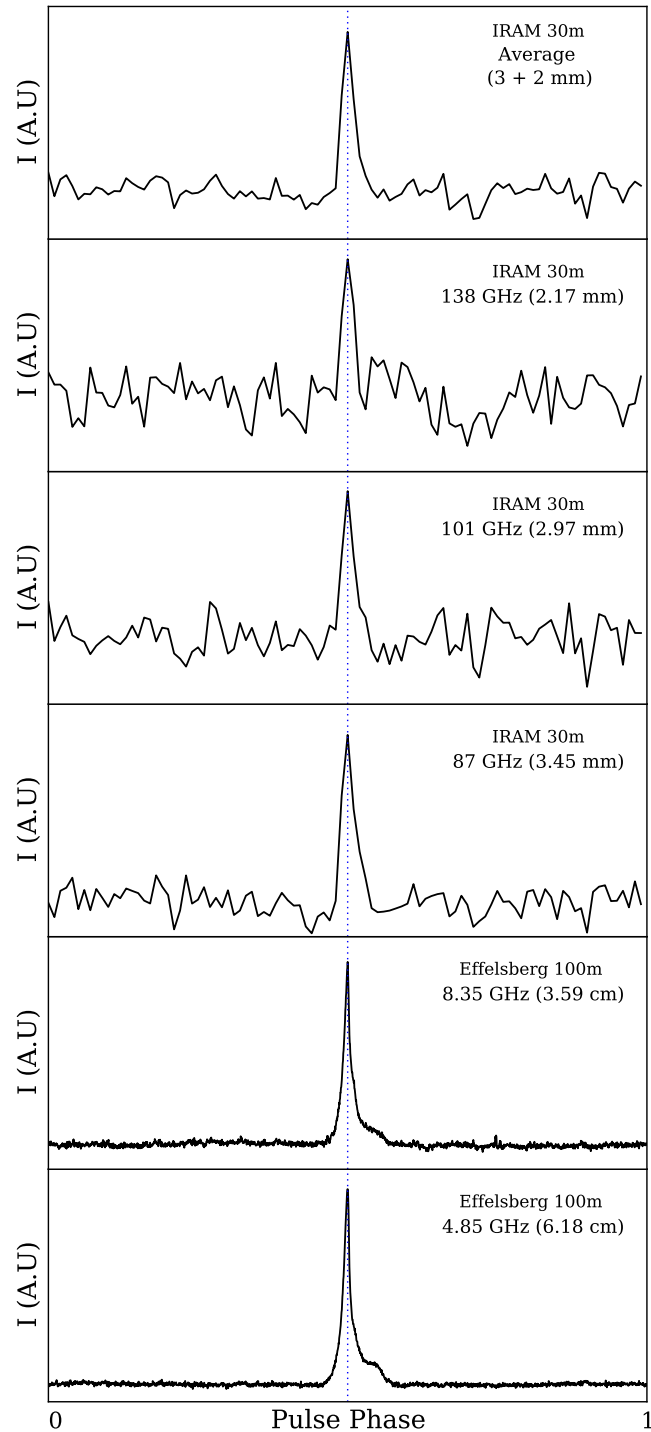


Figure 6.1: Averaged pulse profiles of PSR B0355+54 from 4.85 up to 138 GHz. The top panel shows an average of the 3.44, 2.97, and 2.17 mm bands. The profiles from IRAM 30-m result from the combination of all the observations with detection, and the profiles of different observing campaigns (i.e. from July 2014, March 2015, and February 2016) have been aligned manually to the peak value. The profiles are plotted with a resolution of 100 and 2048 bins for IRAM 30-m and Effelsberg 100-m, respectively.

Table 6.2: Flux densities for PSR B0355+54, including data at other frequencies presented in the literature (see column “Reference”). The values are presented with the maximum precision available. The σ_S column shows the 1σ errors on the measurements. For 154 GHz we provide the upper flux density limit for a detection at $S/N=5$ using the radiometer equation.

PSR	ν (MHz)	S (mJy)	σ_S (mJy)	Reference
B0355+54	79.2	450	230	Stovall et al. (2015)
	400	55.0	8.95	Kramer (1995)
	408	46.2	6.7	Lorimer et al. (1995)
	606	37.03	3.32	Lorimer et al. (1995)
	780	44.76	8.95	Kramer (1995)
	925	15.7	3.0	Lorimer et al. (1995)
	1408	22.9	6.5	Lorimer et al. (1995)
	1420	24.94	1.91	Kramer (1995)
	2700	19.18	5.11	Kramer (1995)
	4750	6.4	1.27	Kramer (1995)
	8600	3.2	1.28	Kramer (1995)
	10550	2.56	0.64	Kramer (1995)
	14600	2.0	0.5	Kramer et al. (1997a)
	14800	2.56	1.27	Kramer (1995)
	23050	0.8	0.2	Kramer et al. (1997a)
	24620	0.96	0.19	Kramer (1995)
	29300	0.83	0.19	Kramer et al. (1996)
	32000	0.83	0.19	Kramer et al. (1996)
	32900	0.84	0.05	Kramer (1995)
	33900	1.09	0.19	Kramer et al. (1996)
34800	0.70	0.19	Kramer et al. (1996)	
35400	0.89	0.19	Kramer (1995)	
43000	0.5	0.1	Kramer et al. (1997a)	
87000	0.5	0.07	Morris et al. (1997)	
87000	0.143	0.020	This work	
101000	0.102	0.026	This work	
138000	0.047	0.020	This work	
154000	<0.058	0.012	This work	

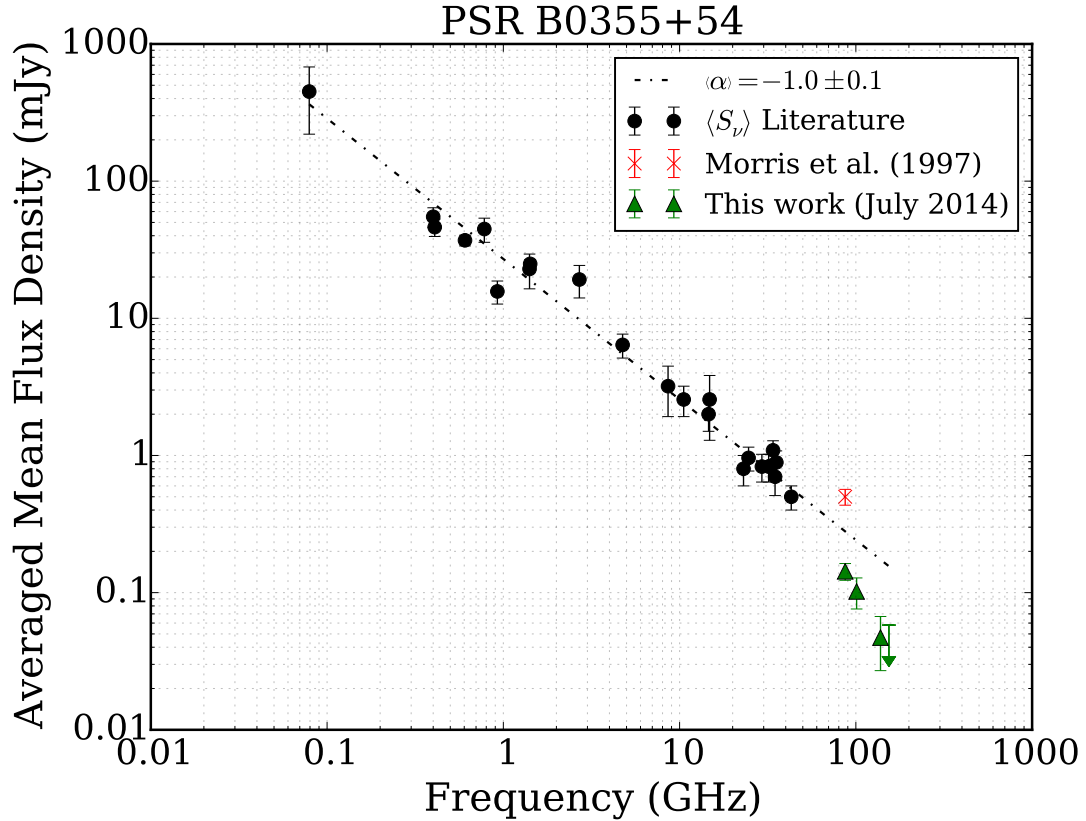


Figure 6.2: Spectrum of PSR B0355+54 from 80 MHz up to 154 GHz. The values between 80 MHz and 43 GHz are extracted from the literature (see Table 6.2). At 87 GHz we plot for comparison the value published by [Morris et al. \(1997\)](#). With our new measurements at 87 GHz and, for the first time, 101 and 138 GHz we do not see a flattening or turn-up in the pulsar spectrum. However, we note a an apparent decreased flux density at the highest frequencies that deviates from the single power law that otherwise describes the spectrum well. This deviation may be due to variability of the source at the highest frequencies, suggested from the difference between our value and the one from [Morris et al. \(1997\)](#), or perhaps by an under-optimal flux density calibration of our data (see text). We expect that the additional data will reduce the uncertainties and aid in confirming or rejecting the deviation from the power law at and above 87 GHz.

6.4 Future work

With forthcoming precise calibration information a better estimate of the flux density of PSR B0355+54 may be possible. This information is also needed to calculate precise flux density limits for the five non-detected pulsars. Moreover, a detailed study of the variability of PSR B0355+54 can provide important information that may help reducing the uncertainty of the apparent decreased flux observed at the highest frequencies. The possibility of scintillation effects due to the ISM will also be examined for the five non-detected pulsars. Finally, a search for single pulses in the millimetre data is planned. Although unexpected given the faintness of the sources at these frequencies, specially bright pulses might be observable. This is particularly interesting in the case of the Crab pulsar, known to exhibit giant pulses that can be thousands of times brighter than the average pulses, and whose emission mechanism is still under debate (e.g. [Weatherall, 1998](#); [Istomin, 2004](#); [Petrova, 2006](#)). The complete results of our analysis will be presented in a future publication ([Torre et al., in prep.](#)).

Acknowledgements

We thank Andrew Lyne and Benjamin Stappers for kindly providing precise pulsar ephemerides, and Axel Jessner for being always available for discussing about the emission physics of pulsars. We also acknowledge the staff at the IRAM 30-m for making the challenging observations successful. Based on observations carried out with the IRAM 30-m and the Effelsberg 100-m radio telescopes. The Effelsberg 100-m is operated by the MPIfR (Max-Planck-Institut für Radioastronomie). IRAM is supported by INSU/CNRS (France), MPG (Germany) and IGN (Spain). This research used the TAPAS header archive of the IRAM-30m telescope, which was created in collaboration with the Instituto de Astrofísica de Andalucía - CSIC, partially supported by Spanish MICINN DGI grant AYA2005-07516-C02. P.T. is supported for this research through a stipend from the International Max Planck Research School (IMPRS) for Astronomy and Astrophysics at the Universities of Bonn and Cologne. Financial support by the European Research Council for the ERC SynergyGrant BlackHoleCam (ERC-2013-SyG, Grant Agreement no. 610058) is gratefully acknowledged.

New instrumentation for pulsar observations

This chapter is driven by technical work in the frame of two ongoing projects to install novel receiver technologies on the Effelsberg 100-m radio telescope: a Phased Array Feed and a Ultra-Wide-Band receiver. My main contribution includes a detailed bibliographic review about Phased Array Feeds in radio astronomy (identifying the main challenges to be faced by this project), the evaluation of the impact of the local Radio Frequency Interference on the receivers, the participation in several of the commissioning tests at Effelsberg, and the design and execution of the first scientific project with the new Ultra-Broad-Band (UBB) receiver: a survey for pulsars in 54 gamma-ray sources with no associated counterparts. I am the lead author of three internal technical reports describing the details and results of the engineering tests (Torne et al., 2013; Torne, 2013; Torne & Winkel, 2014). The results of the pulsar survey with the UBB will be presented in a future publication by Wu, Torne, et al., (in prep.).

The main participating engineers and scientists were:

P. Torne, B. Winkel, C. Kasemann, G. Wieching, R. Keller, L. G. Spitler, J. Wu.

Abstract

The continuous advances in the fields of radio frequency and electronic technologies enable the construction of improved and novel receivers for our astronomical observatories. Recently, two of the main branches of technological developments applied to radio astronomy are the use of the Phased Array Feed (PAF) technology and of Ultra-Wide-Bandwidth (UWB) receivers. However, the ever deteriorating Radio Frequency Interference (RFI) environment imposes a great challenge to the operation of such technologies with optimum performance. This chapter presents different technical analysis and tests related to the ongoing installation and scientific exploitation of a PAF and a UWB receiver at the Effelsberg observatory, located at a region highly affected by RFI. The conclusion of this study is that RFI can have a severe impact on the performance of these new instruments, the biggest risks risks a significant increase of the system temperature (decreasing the sensitivity) or even frequent saturation of the receivers. Nonetheless, with adequate care in their design and usage, these new technologies should be able to operate correctly even in a strong RFI environment like Effelsberg.

7.1 Introduction

To perform adequate observations for a given astronomical experiment we rely on the capabilities of our observing facility, i.e. our telescope. The telescope's capabilities rely, at the same time, mainly on its collecting area and its electronics, which define its sensitivity to detect very faint radio signals. Apart from a good sensitivity it is desirable to have a wide field-of-view (FoV) to carry out large scale surveys or maps, while keeping a high spatial resolution. A large instantaneous bandwidth is also advantageous, as it increases the sensitivity, and would enable for instance an improved mitigation of the Inter Stellar Medium (ISM) effects, something of particular importance for high-precision timing of pulsars in the radio band. Achieving all these characteristics simultaneously is challenging, as we discuss in the following subsections. Ultra-Wide-Bandwidth receivers (UWBs) and Phased Array Feeds (PAFs) are a next generation of radio receivers that can significantly improve those observing capabilities.

7.1.1 Telescope gain and sensitivity

The main figure-of-merit for a radio telescope is its sensitivity, Γ (or G), that is commonly expressed as (see e.g. [Wilson et al., 2013](#))

$$\Gamma = G = \eta_a \frac{\pi D^2}{8k_B} = \eta_a \frac{\pi(2R)^2}{8k_B} = \eta_a \frac{\pi R^2}{2k_B} \text{ [K/Jy]}, \quad (7.1)$$

where η_a is the aperture efficiency of the antenna (the percentage of incident power that is available at the receiver feed point), D is the parabolic reflector diameter, and k is the Boltzmann constant. The units of Γ are K/Jy because it refers to the amount of incident flux density measured in Jansky ($1 \text{ Jy} = 10^{-26} \text{ Wm}^2\text{Hz}^{-1}$) that would raise the power at the receiver entrance (just after the antenna) exactly the same amount as an hypothetical resistor connected to the receiver would when its physical temperature raises one degree Kelvin (assuming all the power from the resistor is from thermal noise). This parameter is often referred as the *gain* of a telescope, G . We will also refer to it here as gain because "sensitivity" is often used in the astronomers' argot to refer to the minimum flux density that can be detected in an observation¹. The higher the gain of our telescope the weaker the signals that we can potentially detect with it. Therefore, maximizing G is an objective of all telescope designers.

Following Eq. 7.1, maximizing G can be done by increasing η_a , for example with an optimum illumination of the parabolic dish or with a good quality of the surface of the reflector. The other way is by increasing the dish diameter, D . The parameter D in Eq. 7.1 is squared, giving a special weight to the size of the collecting area in the gain of a radio telescope. This is the reason why big collecting areas are generally desirable.

From an astronomer's point of view, the interesting figure-of-merit is typically the minimum detectable flux density of an observation with a given instrument. This

¹This is a small example of why engineers and astronomers sometimes do not understand each other correctly.

limit can be calculated by using the so-called *radiometer equation* (see e.g. [Lorimer & Kramer, 2005](#)), which includes G , but also several other parameters that depends on the quality and capabilities of the electronics of a receiver,

$$S_{\min} = \beta \frac{(S/N_{\min}) T_{\text{sys}}}{G \sqrt{n_p} t_{\text{obs}} \Delta\nu} \quad (7.2)$$

where S_{\min} is the minimum detectable flux density, β is a degradation factor due to digitisation and other instrumental effects ($\beta \approx 1$ for modern backends), (S/N_{\min}) is the minimum signal-to-noise to consider a detection, T_{sys} is the total system temperature, G is the telescope gain, n_p the number of polarizations used, t_{obs} the integration time, and $\Delta\nu$ is the receiver bandwidth.

In summary, it is desirable to have good digitizers, as high-as-possible gains, as-low-as-possible system temperatures, dual polarization feeds, and as-large-as-possible bandwidths. In addition, long integration times also improve our sensitivity.

7.1.2 Field-of-View: the problem of surveying with large single dishes

From Eq. 7.1 we conclude that a larger diameter in our parabolic reflector is desirable because it will significantly increase the telescope gain. However, the diameter of the parabolic dish also affects the Field-of-View (FoV) and angular resolution of the telescope. In an approximate form for a single dish radio telescope, the FoV can be calculated from the so-called Half-Power-Beam-Width (HPBW), which is the angular width of the antenna's main beam measured at the points where the received/transmitted power is half of the maximum level. The HPBW depends on the physical size (and shape) of the collecting area, its illumination by the antenna, and the wavelength of observation. For our purposes here, we can use an approximation for typical illuminations with waveguide antennas and circular collecting areas (for detailed information see e.g. [Wilson et al., 2013](#)),

$$\text{HPBW} \simeq 1.27 \frac{\lambda}{D} \text{ [rad]} \simeq 72.7 \frac{\lambda}{D} \text{ [deg]}, \quad (7.3)$$

where λ is the wavelength of operation and D is the dish diameter. The FoV is the solid angle covered by the antenna beam with that HPBW, which is also called the mean beam solid angle, Ω_{mb} ,

$$\Omega_{\text{mb}} \simeq 1.133 \left(\frac{\text{HPBW}}{\text{rad}} \right)^2 \text{ [sr]}. \quad (7.4)$$

The solid angle Ω_{mb} is measured in steradians and is also approximately the spatial resolution of the telescope. A high spatial resolution (note that this means a small Ω_{mb}) is desirable to distinguish the details of what we observe and to be able to resolve sources which appear close to each other on the celestial sphere. This is achieved by using reflectors with a large D . However, if we want to survey or map large areas of sky, a small Ω_{mb} turns out to be a disadvantage because we would need more observing time to scan with the small beam over a large region of interest. A solution would be

to use a telescope with a smaller reflector, but that would decrease our sensitivity and angular resolution. An alternative solution is to use multi-beam receivers, that consist of several antennas illuminating the dish simultaneously.

Within the multi-beam receivers family, the PAF technology is the newest and most promising development. PAF-based receivers allow a large number of simultaneous and overlapping beams to be created, extending the instantaneous FoV (by a factor N , where N is the number of beams) while keeping at the same time the advantages of big reflectors: a high spatial resolution and a high sensitivity.

7.2 Phased Array Feeds

7.2.1 Introduction

A Phase Array Feed (PAF) is an ensemble of receiving elements working together, in which the signals of different elements are *combined coherently* to enhance the radiation capabilities of the receiver. PAFs are fundamentally different to single-beam receivers (i.e. those with only one antenna) and classic multi-beam receivers for which, although also having several receiving elements working simultaneously, their signals are not combined together (an example of such classic multi-beams is the 21 cm 7-beam receiver at Effelsberg). Moreover, in a PAF the elements are usually of smaller size than in classic multi-beam receivers, and are closely packed together to fully sample the focal plane. The key is that by combining the signals from many receiving elements, one can form a radiation beam pattern which corresponds to none of them individually, but to a new *virtual* antenna. The antenna signal combination technique used with PAFs is called *beamforming* and the beams generated with a PAF are often called *synthetic beams*. The beamforming offers *unique* capabilities to a PAF receiver. The most remarkable are:

1. Control of the spatial position of the beams, with the possibility of closely packed beams (i.e. a continuous FoV).
2. The possibility of generating a large number of beams simultaneously, that in conjunction with 1), allow for a large instantaneous spatial coverage (i.e. a large FoV).
3. Control of the beam pattern shape of the synthetic beams, allowing to modify the position and magnitude of the main beam, side lobes and nulls. This ability offer promising ways of spatially rejecting RFI.

Figure 7.1 shows a comparison of the sky coverage of single-beam, classic multi-beams, and PAFs.

A bit of history about PAFs and its application to radio astronomy

PAF technology itself is not new. It was first demonstrated in 1905 as a method to enhance the transmission of radio waves in a given direction during the telegraph era;

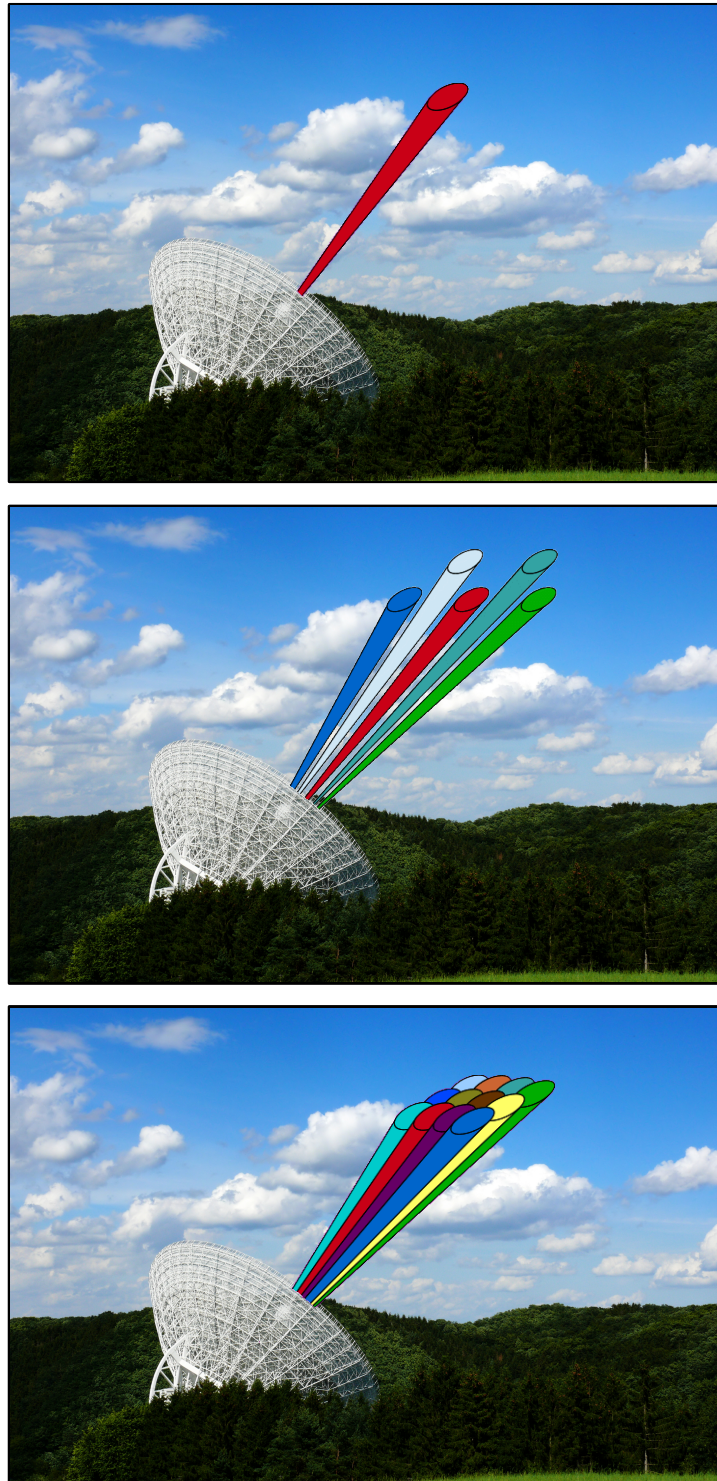


Figure 7.1: An illustration comparing the sky illumination with different receivers. The top panel shows a single-beam, that only receives radiation from one direction (we neglect the contribution from side lobes). The middle panel is an example of classical multi-beam receiver, with five beams on the sky simultaneously. The lower panel shows the wider continuous FoV that can only be achieved with PAF receivers. (Original photography of Effelsberg courtesy of Gregor Jonas).

an achievement worth of the Nobel prize (awarded to Karl Ferdinand in 1909). PAFs found great application in RAdio Detection And Ranging (RADAR), allowing much faster scanning than mechanically-scanning antennas. Apart from communication and RADAR, the PAF technology was also promptly applied in radio astronomy. The first “aperture synthesis radio telescope” (meaning a radio telescope that uses groups of antennas and beamforming to enhance its observing capabilities and point) was developed by Martin Ryle (Ryle, 1952; Ryle & Hewish, 1960) from the Radio astronomy group at Cambridge University in the late 60s and early 70s. Interestingly, those first aperture synthesis radio telescopes located in the Mullard Radio Astronomy Observatory were the instruments that discovered pulsars (Hewish et al., 1968). The Nobel Prize in Physics in 1974 was awarded to both Sir Martin Ryle and Antony Hewish, the first for bringing and exploiting the new phased array technique into radio astronomy and the second for his role in the discovery of pulsars.

What is comparably new today is the development of compact or “dense” PAFs used to illuminate the reflector of a radio telescope. The quest to equip dish radio telescopes with a PAF started in the early 2000s, when Fisher & Bradley (2000a,b) and Ivashina & van Ardenne (2002) pointed out the advantages that PAFs could bring to these facilities. Several later studies expanded and confirmed the nowadays undeniable theoretical advantages of using PAFs for radio astronomical applications, and presented the results from the first advanced prototypes (Warnick et al., 2009; Veidt et al., 2011; van Cappellen et al., 2011; Hayman, 2011), the required beamforming techniques (Jeffs et al., 2008; Landon et al., 2010; Hayman et al., 2010; Ivashina et al., 2011; Elmer et al., 2012), and promising new RFI mitigation methods with PAFs (Jeffs et al., 2005; Hasen et al., 2005; Warnick et al., 2007; Nagel et al., 2007; Jeffs & Warnick, 2008). However, the use of PAFs in radio astronomy can still be considered as being in an early stage, with much potential for improvement and exploration. For instance, current PAFs only offer limited system temperatures and beamforming schemes. The full potential of PAFs requires cryogenically cooled systems and real-time beamforming algorithms with RFI rejection capabilities. Efforts are ongoing toward such advancements, and the next-generation of PAFs will probably include most of the necessary improvements to revolutionize the observing capabilities of many radio telescopes (for a recent review of the history and last developments in PAFs, see Warnick et al., 2016). Nevertheless, the technology is already mature enough to be used for scientific purposes.

7.2.2 The Effelsberg PAF project

In 2012, the Max Planck Institute for Radio Astronomy (MPIfR) started an ambitious project to equip the Effelsberg 100-m radio telescope with a PAF. The plan consists of the acquisition of a PAF from a collaborating institution and the modification of the necessary parts to adapt it to the Effelsberg radio telescope. The selected PAF system was the Checkerboard PAF MkII, a model designed by the Australian Commonwealth Scientific and Industrial Research Organisation (CSIRO) for the 36 dishes of the Australian SKA pathfinder (ASKAP). The technical characteristics of the Checkerboard PAF MkII built for ASKAP are summarized in Hampson et al. (2012). Table

7.1 presents the characteristics of the version built for Effelsberg. The main difference is the frequency range of operation. Due to the strong RFI at Effelsberg (see Sec. 7.2.2.3 and 7.3.2.2) the frequencies below 1150 MHz are filtered out. In contrast, ASKAP’s version can operate starting at ~ 800 MHz.

Number of Antenna Elements (Signals):	188 (94 x 2 polarizations)
Available Frequency Range:	1150-1800 MHz
Instantaneous Bandwidth:	300 MHz
IF range:	Direct sampling
PAF case diameter:	~ 1.2 meters
ADC and Coarse Filterbank:	DragonFly Cards (Xilinx Kintex-7 FPGAs)
Beamforming/Correlation:	Redback Cards (Xilinx Kintex-7 FPGAs)
Number of Beams:	36 in dual polarization
Field-of-View (36 beams @ 1420 MHz)	~ 1.0 deg ²

Table 7.1: Technical specifications of the Checkerboard PAF MkII built for the Effelsberg radio telescope.

The main objectives of the MPIfR PAF project are to increase the survey speed of the 100-m at L–band, directly related with its FoV and inherently small due to the large dish (see 7.1.2), develop new capabilities against the very problematic RFI (e.g. exploiting novel spatial rejection methods), and getting experience with this new and promising receiver technology. The main science drivers of the PAF are all-sky and targeted surveys for pulsars and radio transients.

7.2.2.1 Survey speed analysis

The Effelsberg radio telescope is one of the largest and most sensitive in the world, mainly due to its enormous parabolic reflector of 100 m in diameter. As discussed in Section 7.1.2, such large diameter translates into a high angular resolution and a small FoV, affecting the *survey speed* (SVS) of the instrument. The SVS of a single dish telescope (i.e. the number of square degrees per second observable with a given flux density limit) can be estimated by (see Johnston & Gray, 2006)

$$\text{SVS} = \text{FoV} \Delta\nu n_p \left(\frac{A \eta_a \sigma_s}{2 k T_{\text{sys}}} \right)^2, \quad (7.5)$$

where FoV is the instantaneous Field-of-View, $\Delta\nu$ is the instantaneous bandwidth, n_p is the number of polarizations, A is the collecting area of the telescope, η_a is the aperture efficiency, σ_s is the point source root mean square sensitivity, k is the Boltzmann constant, and T_{sys} is the total system temperature. Eq. 7.5 shows that to increase the SVS we need to increase the FoV, the instantaneous bandwidth, the collecting area, the aperture efficiency, and achieve low system temperatures. Table 7.2 shows a comparison of the SVS of the Checkerboard PAF MkII versus different receivers at

Table 7.2: Comparison of the SVS capabilities of different receivers for the Effelsberg 100-m telescope. The last column shows a ratio against the classic technology for each case (i.e. versus the 7-beam at 1420 MHz, versus the “P300mm” receiver at 1000 MHz, and versus the “P500mm” receiver at 800 MHz). We have assumed that the aperture efficiency is the same for all receivers at each frequency band. Note that these values are estimations, as the final values for the system temperature of the PAF are not yet available.

ν (MHz)	Receiver	N_b	Ω_{mb} (deg ²)	FoV (deg ²)	$\Delta\nu$ (MHz)	T_{sys} (K)	SVS (deg ² /s)	SVS factor
1420	7-beam	7	0.0278	0.1946	250	23	0.0919	1
	PAFs	36	0.0278	1.0008	300	60	0.0834	0.91
1000	P300mm	1	0.0616	0.0616	500	50	0.0123	1
	PAFs	36	0.0616	2.2176	300	60	0.1848	15.0
800	P500mm	1	0.0779	0.0779	125	300	$0.108 \cdot 10^{-3}$	1
	PAF	36	0.0779	2.8044	300	60	0.2336	2159

Effelsberg covering different frequency bands. If we assume an observation of the same sky region (i.e. containing the same sources and obtaining the same sensitivity limits), and that η_a will be the same at each observing band, we can write

$$\text{SVS} \propto \text{FoV} \Delta\nu \left(\frac{1}{T_{\text{sys}}} \right)^2 \quad (7.6)$$

which are the three parameters used for the SVS comparison in Table 7.2.

There are several conclusions that can be obtained from Table 7.2. One is that a Checkerboard PAF MkII would perform surveys much faster than the current available receivers at 1000 and 800 MHz. Unfortunately, due to RFI those bands will not be available in the PAF installed at Effelsberg. Interestingly, the 7-beam receiver shows a slightly better performance in SVS compared to the new PAF, even having a much lower number of beams and slightly less usable bandwidth. This better performance of the 7-beam is due to the fact that this receiver is cryogenically cooled, having a considerably lower T_{sys} than the Checkerboard MkII PAF. In our study we have assumed a T_{sys} for the Checkerboard PAF MkII of 60 K, although it might be possible to achieve slightly lower values of about ~ 50 K (Chippendale et al., 2015), we prefer to be conservative in our analysis.

It must be noted that the Checkerboard PAF MkII is the first receiver of its class that will be installed at Effelsberg, and should be seen as a pathfinder. In the future, when this technology matures in its application to radio astronomy, new PAFs will very likely be cryogenically cooled, meaning that they should be able to offer very low system temperatures, comparable to those of current modern receivers. As well as the expected improvements in T_{sys} , more computing power that will allow an even larger number of beams, and the unique and promising possibilities of using beamforming to reject RFI through spatial filtering, the PAFs have a very high probability of becoming

the most versatile receivers for our radio observatories.

7.2.2.2 Challenges of the project

A detailed bibliographic review about PAFs and their use in radio astronomy was carried out as part of this PhD. This allowed us to identify the main requirements, challenges, and risks that installing a PAF on the Effelsberg 100-m dish could impose. As a summary, a list of tasks and challenges generally faced when trying to use a PAF on a radio telescope is presented in Table 7.3. Most of the tasks will simply require man power in order to be developed and solved, but some might impose significant difficulties. One particular issue was identified as a potential showstopper for the project: the possible saturation of the Low-Noise-Amplifiers (LNAs) of the new PAF by the strong RFI at the Effelsberg observatory. Because of its importance, we focused on studying and assessing this risk.

7.2.2.3 Tests of Checkerboard MkII LNA robustness against RFI

The saturation of an electronic amplifier is (usually) an undesired effect that occurs when the input power to the amplifier exceeds some limit value. The result is a non-linear behaviour of the device, producing mainly two effects. First, the output signal is no longer linearly proportional to the input signal and the form of the output signal gets distorted. Secondly, the generation of intermodulation products (IMP), copies of the input signal that appear at different frequencies at the output of the amplifier. These distortions generally mean that the receiver is practically unusable for scientific purposes.

In order to evaluate the impact that the RFI at Effelsberg could have on the future PAF, we carried out different tests on one Checkerboard PAF antenna element connected to the same amplification chain that the future PAF would have, called a “Domino” (Torne, 2013). A “Domino” includes the amplification, filtering, electronic-to-optical conversion, and optical transmission of the radio signals (see Hampson et al., 2012). Furthermore, this small front-end was installed at the prime focus of the Effelsberg telescope in order to reproduce the real RFI conditions that the future receiver will have to face. Figure 7.2 shows a picture of the Checkerboard element installed at Effelsberg.

The main test consisted on measuring the total RFI power received by the PAF antenna when the telescope is pointed at zenith (the worst case for RFI at Effelsberg because the primary focus loses completely the natural shielding by the hills surrounding the telescope). This way we could calculate if the LNAs can handle the measured RFI power levels.

We used a power meter at the output of the PAF LNA card (“Connection point A” in Figure 7.3), and measured a total power of -28 dBm (1 dBm = 0.001258925 W). By subtracting the total amplification applied between the antenna and the power meter, we calculated the power at the antenna to be -56 dBm (more details can be found in the technical report Torne (2013)). All this power can be assumed to be produced by the man-made RFI signals arriving at the antenna.

Table 7.3: Compilation of tasks and challenges for the PAF project at Effelsberg from the bibliographic review. The level of complexity and risk may vary significantly from task to task.

-
- 1) *Potential saturation of the PAF LNAs by strong RFI at Effelsberg.*
Perhaps the biggest risk for its operation in a highly polluted RFI environment. A saturated receiver is not fully functional for scientific experiments (see text).
 - 2) *The signal transport on fibres and potential saturation by RFI.*
The optical fibres have a limited dynamic range, which may not be enough to avoid saturation by strong RFI.
 - 3) *Calculation of the maximum sky coverage.*
The number of beams with a high sensitivity will be limited by the physical size of the PAF and the optics of the telescope (see [Hayman et al., 2005, 2011](#)).
 - 4) *How do gain drifts affect the efficiency of beamformed beams?*
The beamformer weights depend on the (ideally constant) complex gain of each array element (i.e. amplitude and phase). Drifts in this quantity will affect the efficiency of the beams because the applied weight will no longer be the optimum one. This issue closely relates with 5).
 - 5) *System stability: how often is it necessary to recalculate beamformer weights?*
The calculation of a new set of beamformer weights can be very time consuming. It requires measurements ON and OFF a strong calibrator per beam.
 - 6) *How does the RFI affects the calibration of weights? Opportunity or problem?*
RFI can impact the calculation of beamformer weights, specially if it is changing between the required ON and OFF measurement. It may be possible to select in the beamformer only frequency channels free of RFI to perform the weight calculation.
 - 7) *Development of real-time adaptive beamforming to reject RFI.*
Very promising technique, although the required computational requirements and control system software can be very complex and demanding.
 - 8) *Interfaces, connections between different components.*
An example of this type of issues is the conversion from optical to Ethernet interface required to use the Checkerboard PAF at Effelsberg. This conversion is solved, but similar adaptations may be needed.
 - 9) *Telescope control system.*
In particular for the calculation of new beamformer weights the backend and the telescope will need to be able to communicate and understand each other.
 - 10) *Data acquisition, storage, and processing.*
For the PAF, N beams will produce data rates of about to $N \times 74 \text{ MB/s}^a$, i.e. for 36 beams the total is 2.6 GB/s. Real-time data processing may be required for large scale surveys with the PAF.
-

^afor a typical set-up at L-band, 512 frequency channels across 300 MHz, time sampling of $54 \mu\text{s}$, and 8-bit data.

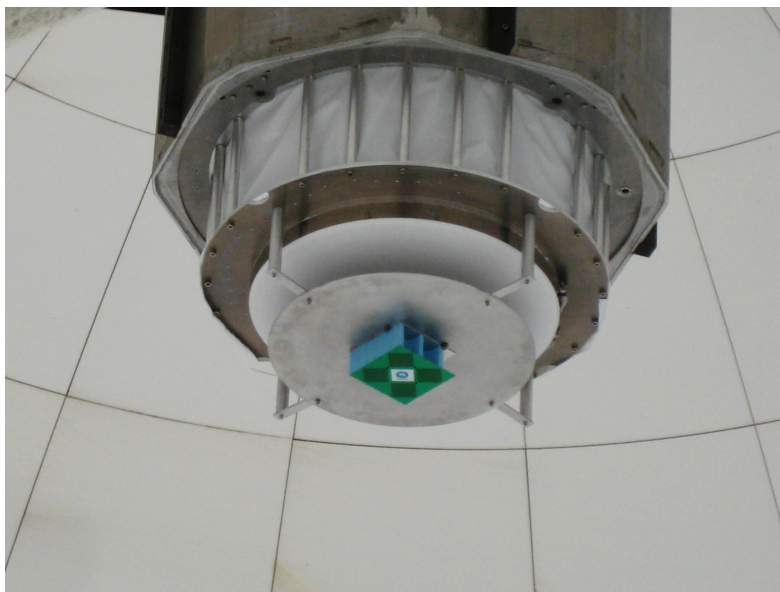


Figure 7.2: A Checkerboard PAF single element installed on the primary focus of the Effelsberg 100-m dish for testing its robustness against the local RFI.

To access the signal from the PAF element, we connected it to the receiver installed at that moment at the telescope, i.e. the Ultra-Broad-Band receiver (UBB, see Section 7.3.2). We modified one of the two polarization channels so no filtering was applied to the PAF signal, in order to check the response of the PAF LNA alone. Figure 7.3 shows a diagram of the set-up for the commissioning tests.

The Checkerboard PAF MkII LNAs consist of two Avago ATF-35143 transistors in cascade with a combined gain of 28 dB (Shaw et al., 2012; Shaw & Hay, 2015; Gough, 2010). The ATF-35143 has a 1 dB compression point² of -11 dBm at 900 MHz, with a gain of up to 18 dB (Avago-Technologies, 2012). The second transistor in the amplification chain receives the incident power on the antenna amplified by the first transistor. Therefore, -56 dBm + $(28/2)$ dB = -42 dBm is the power at the input of the second transistor in the LNA. This is still 31 dB below the 1 dB compression point. *The conclusion from this test is that the LNAs of the Checkerboard PAF MkII should be able to handle the local RFI at Effelsberg without a persistent saturation (Torre, 2013).*

It should be remarked, nonetheless, that the characteristics of the RFI at Effelsberg (like the affected frequencies and strength of the signals) are constantly changing. The fact that our measurements conclude the Checkerboard PAF MkII LNAs can handle the RFI levels measured in November 2013, does not mean that this situation will not change. It is greatly encouraged a *continuous* detailed monitoring of the RFI at the telescope to identify sources of potential problems related with saturation or under-

²A 1 dB compression point is a common characteristic of electronic transistors or amplifiers indicating an input power that will lead to an output that is deviated by 1 dB for a linear amplification. It is commonly used as a threshold of when a device is entering into the saturation regime.

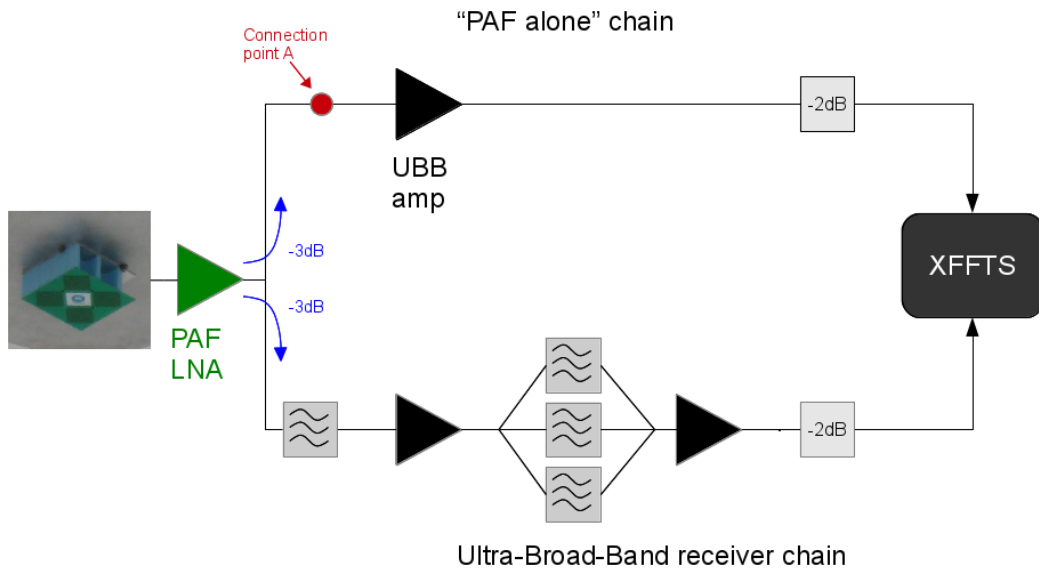


Figure 7.3: Schematic block diagram of the system set-up for the Checkerboard PAF element RFI tests (Torre, 2013).

optimal performance of the receivers, and the possible corruption of frequency ranges of interest to the observers.

7.2.3 Summary

The PAF technology is allowing the construction of a new generation of radio receivers that allow a large continuous sky coverage and novel observing techniques, everything based on the combination of signals from several closely packed antennas in a technique called beamforming. Furthermore, the unique possibility of electronically controlling of the beam shapes is very promising for RFI rejection through spatial nulling. PAFs are (compared to current classic receivers) complex systems that require significant efforts and resources to be operated and to exploit their full capabilities. The MPIfR will install a Checkerboard PAF MkII on the 100-m dish at Effelsberg by the end of 2016. Its commissioning will surely be challenging, but also exciting, as it is the first time this technology is applied to the 100-m.

RFI has been identified as a major risk as it has the potential to saturate the receiver. We have shown that the LNAs of the Checkerboard PAF MkII should in principle be able to handle the Effelsberg local RFI power levels without saturating, which is very encouraging. New tests will certainly be needed when the complete Checkerboard MkII is installed at Effelsberg to check the stability on the rest of the receiver chain (for instance the Analogue-to-Optical converters and the optical fibres, parts that could be highly affected by strong RFI levels). The RFI at Effelsberg is ever changing and generally increasing, and it is highly recommended to continuously monitor the local

RFI levels to identify related problems in the receivers and the observations.

The scientific applications of the PAF at Effelsberg surely are worth the efforts. With its large FoV new large scale surveys will be possible in less time. This is particularly important for detecting transient or variable sources, like a population of Fast Radio Bursts or the intermittent pulsar population.

It has also been shown that the Checkerboard PAF MkII will not be extremely sensitive (if compared, for instance, with the current 7-beam receiver), but it should be remarked that this is a first generation of such type of receivers, and that it operates at room temperature. Future improved versions of PAFs will likely be cryogenically cooled, with higher sensitivities. This future improvement, together with the accumulated expertise in beamforming techniques promises to be a revolution in the observing methods with single-dish radio telescopes.

7.3 Ultra-Wide-Bandwidth receivers

7.3.1 Introduction

Apart from the PAFs, another type of next-generation radio receivers are the Ultra-Wide-Bandwidth receivers (UWBs). This technology is novel in particular at the low end of the radio spectrum where, until now, bandwidths of ~ 500 to 800 MHz were challenging to achieve. UWBs can achieve instantaneous bandwidths of 2000 MHz or even more.

The advantages of these receivers are twofold: a) an increased sensitivity (see Eq. 7.2) and, b) an enhanced instantaneous measurement of the spectrum of a radio source. The latter is a fundamentally new ability because, until now, studying the radio spectrum of a source over a wide bandwidth, particularly at low radio frequencies, required of different observations with different receivers. Proposing for, obtaining, and reducing those multi-receiver observations is tedious and required expertise with the different receivers involved. UWBs facilitate enormously multifrequency studies within its radio coverage and, furthermore, allow the frequencies to be observed *simultaneously*, which is important for the study of variable sources (e.g. radio magnetars) or variable ISM effects (e.g. DM variations).

The main drawback of UWBs is generally their increased susceptibility to RFI, which can be an important issue in electromagnetically polluted areas. The data rates coming from UWBs can also be challenging to manage and store, and processing the data usually requires extra computing power due to the large file sizes.

7.3.2 An Ultra-Broad-Band (UBB) receiver for Effelsberg

The Max Planck Institute for Radio Astronomy, with support from the European Research Council under the grant BEACON (P.I.: Paulo Freire), started in 2011 one of the first developments of UWBs in the world. This new receiver was named the Ultra-Broad-Band receiver (UBB) and was designed to work at the Effelsberg 100-m radio telescope. Its main scientific objectives are: a) to improve the precision of the

timing observations of pulsars (that is proportional to the S/N of the detections, and so, to the square root of the observing bandwidth, see Eq. 7.2) and, b) to study pulsar DM variations which benefits from instantaneous multifrequency data. The latter would allow to improve even further the high-precision timing of some pulsars, reducing or eliminating the errors in the models due to time-varying DMs. The UBB was built to operate in the region of 600–3000 MHz, and it was used for several scientific experiments in this initial configuration, including a pulsar survey carried out as part of the commissioning work. Unfortunately, the strong and ever-changing RFI conditions at Effelsberg made quite challenging to operate the UBB at optimum performance within this frequency range.

From the scientific point of view, the main problems of the UBB at Effelsberg have been twofold: the loss of considerable portions of the band due to RFI (which is somewhat expected), and the decrease of its sensitivity due to the RFI power received, which added to the T_{sys} and, often, saturated the receiver.

7.3.2.1 Commissioning of the UBB at Effelsberg

The first scientific project for the UBB was designed as part of this thesis during its commissioning at Effelsberg. It consisted on a pulsar survey of gamma-ray sources detected by the Large Area Telescope (LAT) on-board the Fermi satellite with no associated counterparts. This kind of targeted survey has proved very successful in the discovery of new pulsars, in particular of young energetic ones and recycled millisecond pulsars (Ransom et al., 2011; Keith et al., 2011; Kerr et al., 2012; Guillemot et al., 2012; Barr et al., 2013a; Camilo et al., 2015; Cromartie et al., 2016). The reasons to choose this project for the UBB is that, apart from its high potential of new pulsar discoveries, the technical characteristics of the UBB addressed the major problems that were identified by Barr et al. (2013a) when performing a similar survey at Effelsberg.

Barr et al. (2013a) carried out a survey of Fermi-LAT unassociated sources using the 7-beam receiver, and pointed out that the main issues they faced were a) the small beam of the 100-m at 1.4 GHz, not fully covering the uncertain location of the gamma-ray sources, b) the possibility of missing potential pulsars due to scintillation. The lowest frequencies of the UBB band (600–900 MHz), and the fact the the UBB under illuminates the Effelsberg dish (R. Keller, private communication), contribute to a larger beam on the sky (see Eqs. 7.3 and 7.4), i.e. we had a larger FoV to cover better the uncertainty region of the Fermi-LAT sources. Additionally, the large simultaneous frequency coverage of the UBB reduced significantly the risk of non-detections due to scintillation.

A list of 54 Fermi-LAT sources with high potential of harbouring pulsars was compiled using a method to assess, from the properties of gamma-ray emission, the probability of a gamma-ray source to be powered by a pulsar (Lee et al., 2012). The selected sources were observed with the UBB between 10 to 30 min each, and searched for radio pulsations (for details on the searching methodology, see sections 2.3 and 3.2.2). After analysing the data, no new pulsars were detected (Wu, Torne, & et al., in prep.). However, during the data analysis we discovered that the strong RFI was causing major

problems with the receiver. A parallel study to understand better the impact of RFI on the receiver sensitivity was carried out, necessary because a decrease in sensitivity by the RFI could affect the yield of the pulsar survey. Moreover, it must be taken into account to correctly set the flux density limits for the non-detections.

7.3.2.2 RFI and UBB sensitivity

RFI in low radio frequency observations is endemic, in particular when the observatory is surrounded by populated areas, like it is the case for Effelsberg. Nonetheless, the amount of RFI received with the UBB was overwhelming. We used the code `rfifind` from `PRESTO` to search and mask potential RFI in the data. Focusing on the region of around 800 MHz (the optimum sub band for the pulsar survey), *in the best cases* the flagged fraction was about 40 to 50 per cent of the total. However, it often reached fractions of 80 to 100 per cent, meaning that the whole observation is lost due to RFI effects or at least the sensitivity is decreased very substantially. Figure 7.4 shows an example of an `rfifind` evaluation plot from a UBB observation at the 800 MHz sub band. To investigate in more detail what could be the cause of such large percentages of masked data, in the last observing sessions we made use of a high resolution spectrometer (namely the XFFTS) to record spectra of the data every few seconds. By analysing these spectra, it became clear that the UBB was quite often in saturation. The basis of this conclusion was, first, that the bandpass was not stable and continuous “jumps” between different power levels were evident, a sign of lack of stability of the receiver. Secondly, the RFI could be often seen everywhere across the bandwidth of the UBB, even in areas where we expected no strong RFI signals (or no signal at all). This last fact highly suggested the production of inter modulation products, a strong sign of saturation of the receiver (see Sec. 7.2.2.3). A comparison of the UBB bandpass in normal and saturation states is presented in Figure 7.5.

The UBB receiver was designed with multiple filters to reject a large amount of the strongest RFI at Effelsberg. While the receiver performed outstandingly well in the laboratory, with T_{sys} values under ~ 20 K, we showed that it was not operating as expected at the telescope. We measured the System Equivalent Flux Density (SEFD) using a set of calibrators during two commissioning runs in November 2013 and April 2014. The SEFD is related to the system temperature through the gain of the receiver ($T_{\text{sys}} = \Gamma \cdot \text{SEFD}$). The gain of the UBB is estimated to be $\Gamma = 1.2$ K/Jy with an uncertainty of 15 per cent. We obtained an average value of the $\text{SEFD} = 49.7 \pm 6$ Jy (Torre & Winkel, 2014), equivalent to a $T_{\text{sys}} \approx 60 \pm 11$ K; much higher than the $T_{\text{sys}} \approx 20$ K measured in the lab. These results are consistent with independent T_{sys} measurements obtained by another commissioning test carried out by using the moon as a calibrator (L. Spitler, private communication).

An additional few Kelvins in the system temperature at the telescope can be expected from effects like spillover, cosmic microwave background, or atmospheric contribution, but an excess of ~ 40 K is too much to be explained only by those contributions. The conclusion is that the RFI was having a large impact in the sensitivity of the UBB when installed at the 100-m dish, increasing the expected T_{sys} by a factor of ~ 3 . The

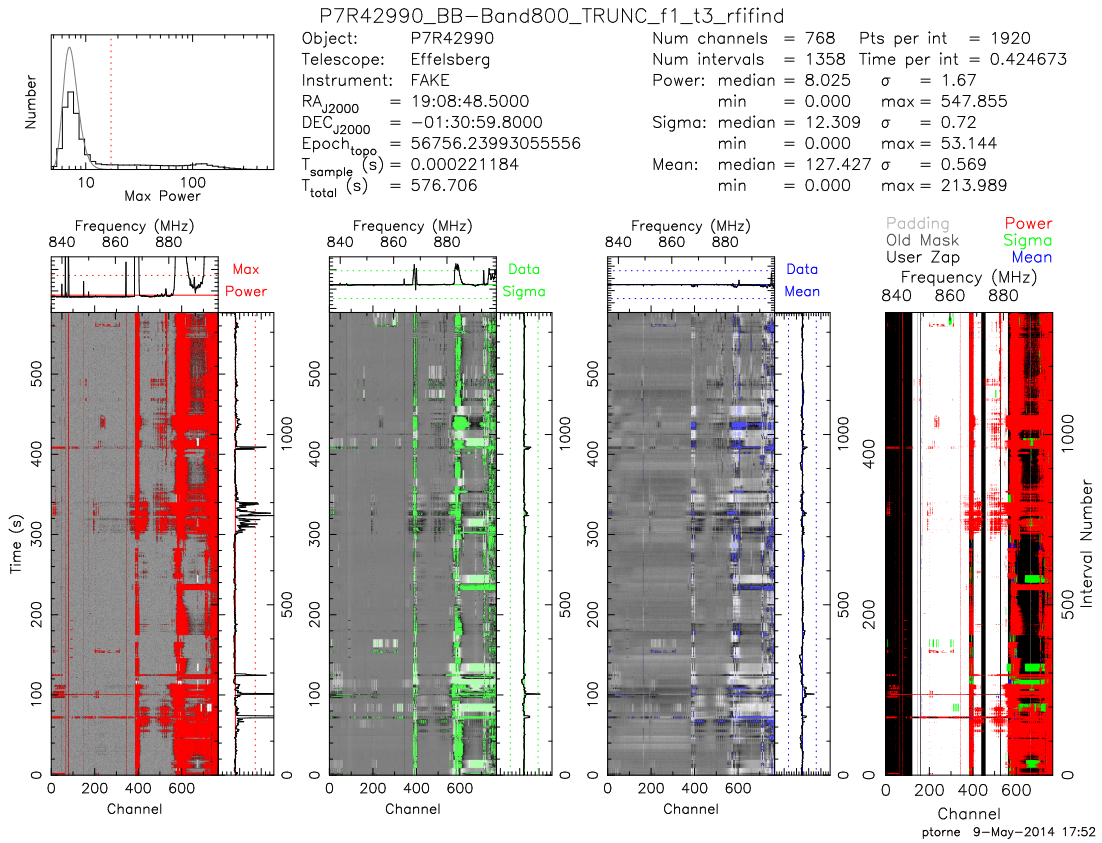


Figure 7.4: An example of `rfifind` plot of a typical observation with the UBB in the frequency range 835–898 MHz. The amount of masked data is 52.2 per cent, in addition of another 33 per cent that is truncated from the upper part of the band due to persistent RFI (898–929 MHz). In total, this observation has lost 85.2 per cent due to RFI, which is a very high fraction. Such levels of RFI have the potential to saturate the receiver, and have a significant impact in the sensitivity of an observation.

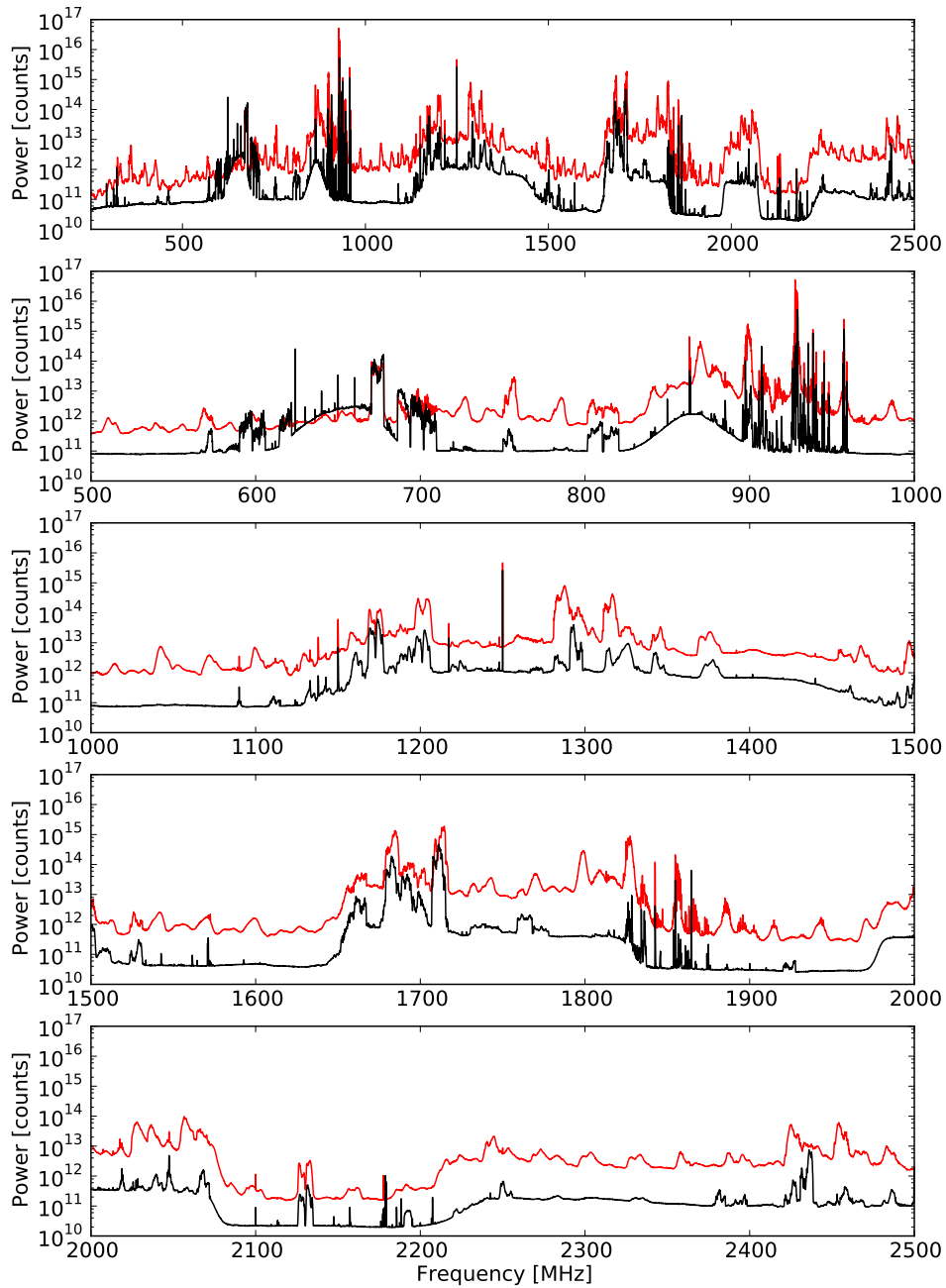


Figure 7.5: Comparison of the bandpass of the two polarization channels of the UBB during one of our commissioning tests in April 2014. One of the channels (black line) has a reduced gain in order to check if less amplification made the receiver more stable and robust against RFI. The other channel (red line) shows the standard amplification of the UBB receiver. It is clearly visible that the full amplified channel shows signs of saturation, in particular with the appearance of IMPs. A lower amplification seems to make the receiver more stable in this case, but in our full dataset this channel with less amplification also often enters into saturation. Therefore, simply reducing the gain is not a solution. The top panel shows the full recorded bandwidth, while the subsequent lower panels shows zooms between 500 and 2500 MHz, in 500 MHz intervals. The large spike at 1250 MHz is instrumental.

adopted solution, decided by the MPIfR technical department in agreement with the P.I. of the BEACON project, was to modify the UBB electronics to filter out the frequencies below ~ 1100 MHz (where it is most of the RFI power, see Figure 7.5). The development of the new necessary high-pass filters is ongoing at the time of writing, and the modified version of the UBB is expected to be at the telescope in August 2016. With the upgraded filters the total power handled by the amplifiers and the rest of the receiver chain should be substantially reduced, which should bring the T_{sys} closer to the value measured in the lab of approximately 20 K; at the expenses of losing the lower-end of the UBB original frequency band.

7.3.2.3 Focusing optimization

Another challenge for the optimum performance of the UBB receiver was to find its optimal focus point. A correct focusing of the feed is important because to maximize the aperture efficiency (and so, the gain, see Eq. 7.1) the antenna phase center (i.e. the point from which the emitted waves approach best a spherical wavefront at the reflector) must be located at the focal plane of the illuminated reflector. The phase centre, however, is not constant and depends, among other things, on the radiation frequency.

The dependence of the phase centre with frequency makes difficult to optimize the focusing of the UBB because, due to its large bandwidth, there is no unique phase centre that can be positioned at the focal point of the Effelsberg parabolic reflector. The UBB can be focused to optimize certain frequencies, optimizing the receiver gain for them, but will always be unfocused for some frequencies in its operation range³. During our observing time with the UBB, an optimum focusing set-up for the receiver was investigated.

Generally, finding the optimum focus point for a receiver is a routinary process done by the telescope control software practically automatically. Nonetheless, the standard procedure asks the observer or operator to choose a frequency to which the receiver is focused. For L-band receivers, the focusing frequency is usually chosen to be close to 1400 MHz, a frequency known to be free of RFI. This is generally a good choice for receivers with bandwidths around 300–500 MHz, but for the UBB it was not clear if this was the optimum frequency.

Figure 7.6 shows the optimum focusing set-up obtained for different frequencies across the UBB bandwidth. There is no single value that would work for all the frequencies. To investigate the optimum focus point for the UBB, we used a spectrometer as a backend and measured the gain at different frequencies for different focusing set-ups. Figures 7.7 to 7.10 summarize the measurements of these tests. The conclusion is that the high frequencies are more sensible to errors in the focusing than the low frequencies. As already discussed, with the large bandwidth of the UBB there is no

³This statement is true for the current design of the UBB. There is interest in changing the current quadrupole feed for a new design that brings the antenna phase centre between different frequencies closer, allowing an easier and optimized focusing. In addition, this problem will be reduced after the UBB frequency coverage is modified by the new high-pass RFI filters.

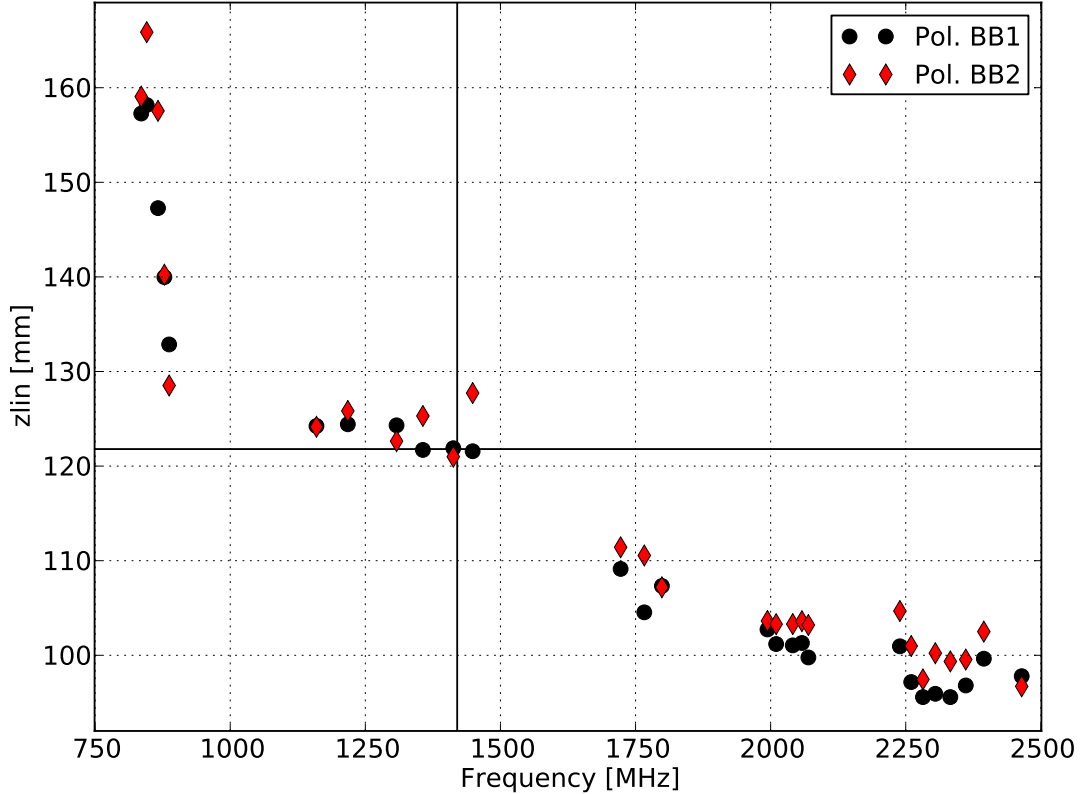


Figure 7.6: Optimum focusing set-up (represented by the offset z_{Lin}) at different frequencies across the UWB bandwidth. The black cross marks the focusing at 1400 MHz, where the receiver was usually focused. Prior to our tests there were no measurements ensuring that this was the optimum frequency where to focus the receiver and, in fact, we show that it is best to focus at the highest frequencies, around 2000 MHz (see text).

perfect focal point, but our results demonstrate that *the best focusing set-up is that one optimizing the highest frequencies, around 2000 MHz in our test.*

7.3.3 Summary

The new generation of UWBs have important applications in the timing of pulsars, the study of the interstellar medium, and for targeted pulsar searches. The MPIfR has developed one of the first UWB receivers, namely the UBB for its use at the Effelsberg 100-m radio telescope.

During its commissioning, we used this novel receiver to carry out a targeted pulsar survey on unassociated gamma-ray sources, that took advantage of the specific technical characteristics of the new receiver. No undiscovered pulsars were detected, but it was found that the RFI was causing major problems to the receiver, reducing its sensitivity. The UBB often entered often into saturation mode, and its test for measuring its T_{sys} at the telescope showed that this was highly increased by the strong RFI, reaching values

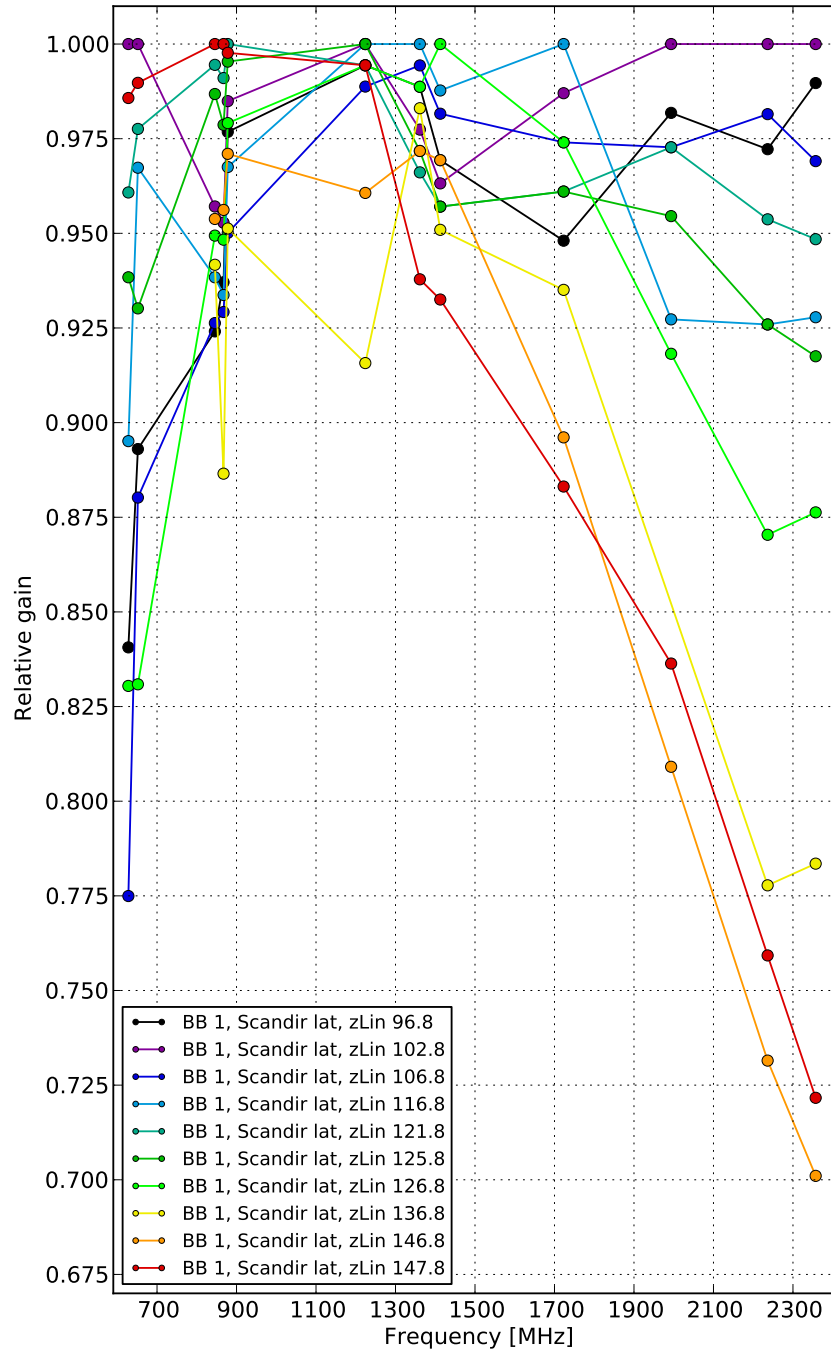


Figure 7.7: Relative gain at different frequencies for different values of the focusing point (represented by the offset z_{Lin}). The relative gain varies more at the high frequencies, showing that these are more sensitive to errors in the focusing than the low ones. The conclusion is that the best set-up is to focus close to the highest frequencies of, in this case ~ 2000 MHz. For instance, the z_{Lin} value of 102.8 mm optimizes the maximum frequency and provides a high relative gain across all the bandwidth. This plot shows the measurements from the polarization channel labelled BB1 in the latitudinal direction of the beam.

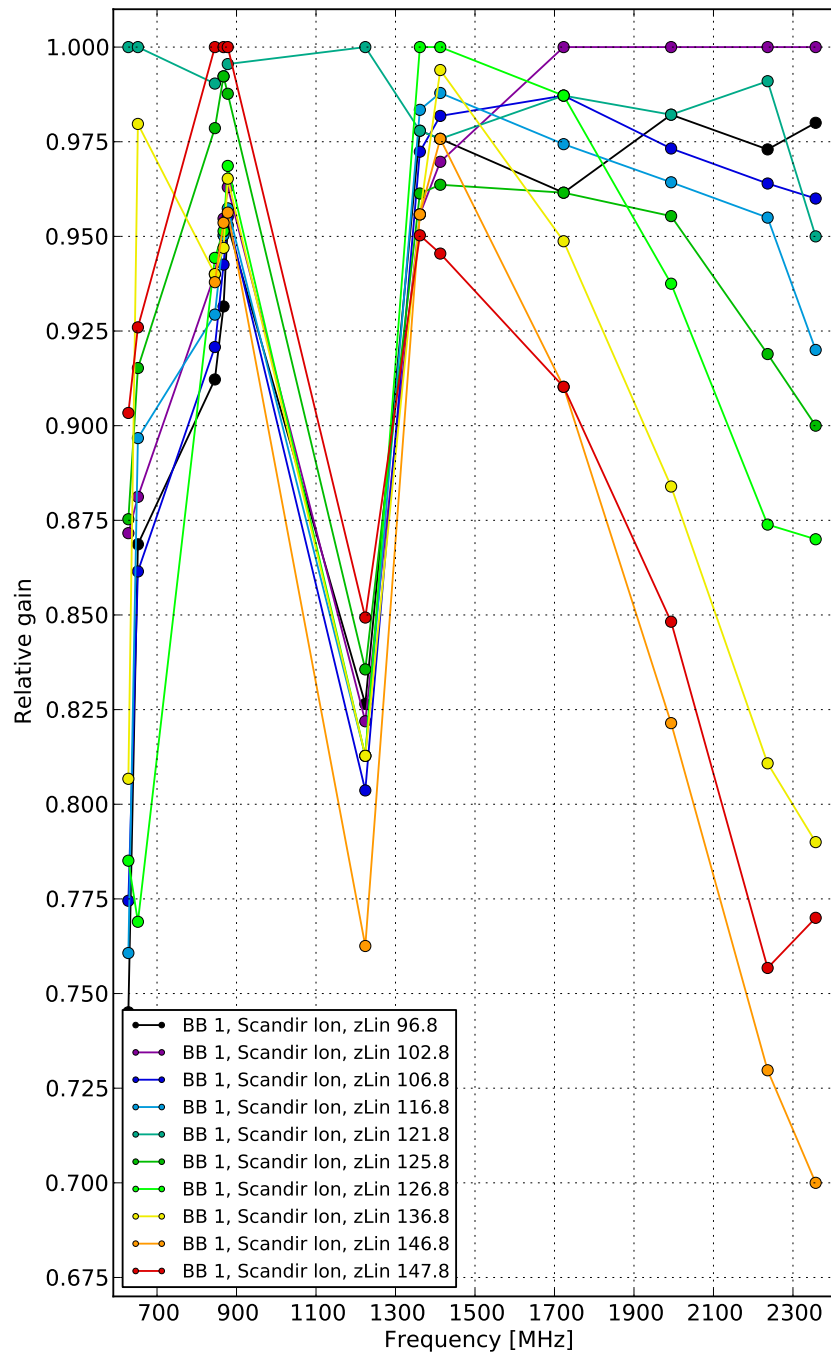


Figure 7.8: Analogous plot to Figure 7.7 for the polarization channel labelled BB1 in the longitudinal direction of the beam. The “dip” at about 1200 MHz is likely produced by RFI and it is not taken into account for the conclusions of the test.

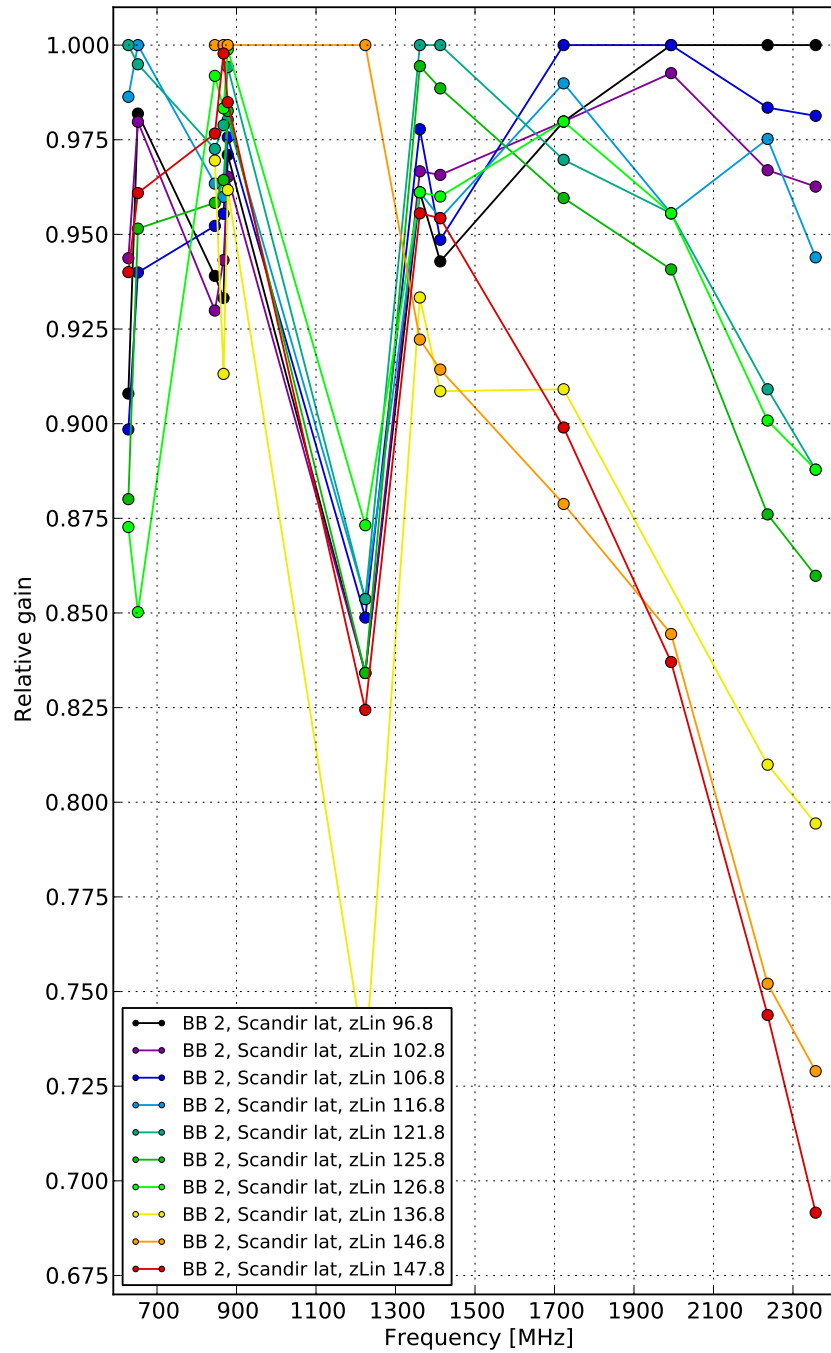


Figure 7.9: Analogous plot to Figure 7.7 for the polarization channel labelled BB2 in the latitudinal direction of the beam. The “dip” at about 1200 MHz is likely produced by RFI and it is not taken into account for the conclusions of the test.

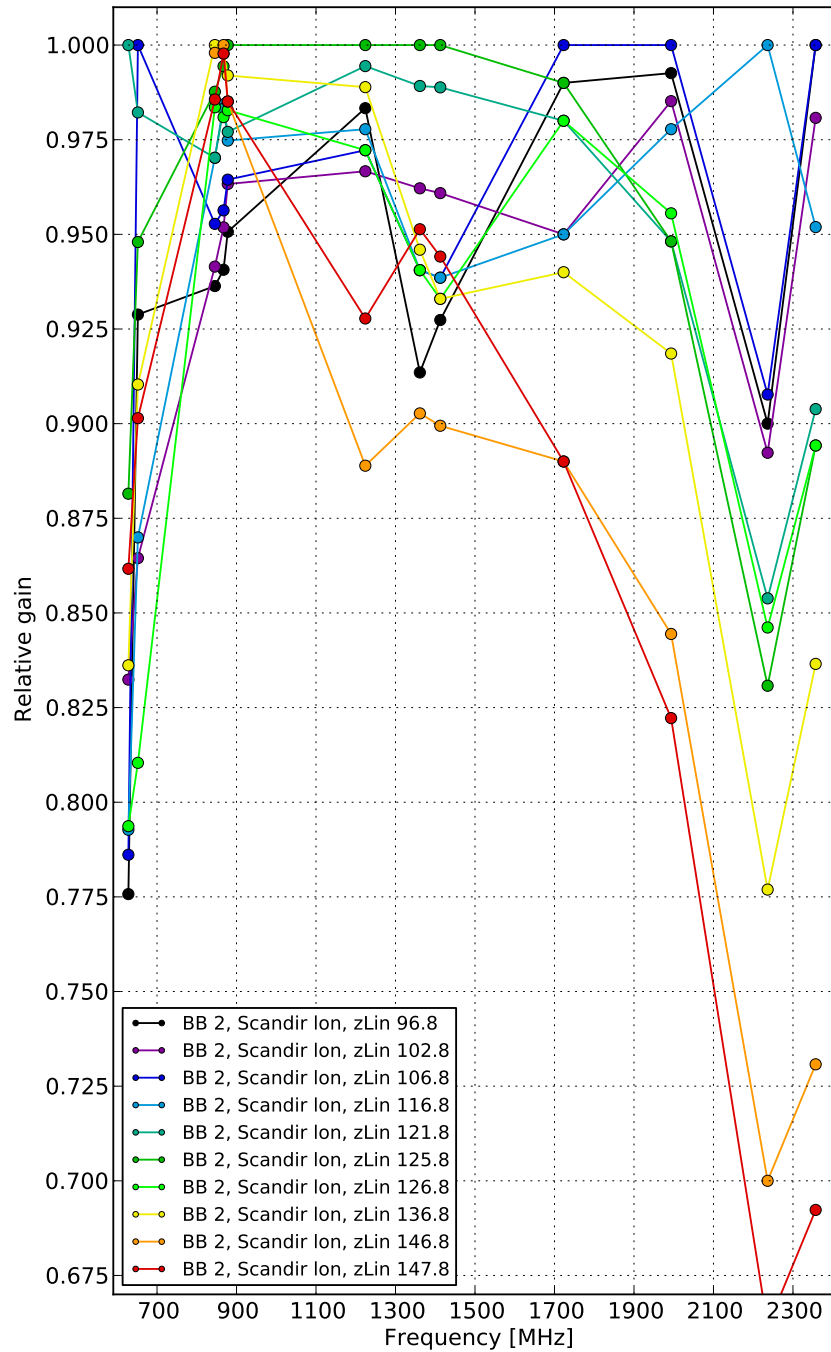


Figure 7.10: Analogous plot to Figure 7.7 for the polarization channel labelled BB2 in the longitudinal direction of the beam.

of about $T_{\text{sys}} \approx 60$ K, a factor ~ 3 higher than what is measured in the lab tests. The results from these observations and tests led to the decision of modifying the receiver to filter the parts of the bandwidth with the strongest RFI, below ~ 1100 MHz. It is expected that these changes will bring back its T_{sys} close to the expected values of around 20 K.

Last, the focussing issue of the UBB has been presented, and a test was performed to find an optimum focusing set-up. We show that the low frequencies are less affected by focusing errors than the high ones, concluding that it is preferable to focus the UBB optimizing the highest operational frequencies. This way the gain is optimized, keeping it high across most of the frequency band.

7.4 Other instruments for pulsar observations

7.4.1 Effelsberg high frequency receivers

The sensitivity of the high radio frequency receivers operating at Effelsberg together with modern pulsar backends make possible pulsar observations well above the typical $\sim 1\text{--}2$ GHz. For instance, the 6 and 3.6 cm receivers (central frequencies of 4.85 and 8.35 GHz, respectively) are being used for observing pulsars in a project to detect low-frequency gravitational waves (Lazarus et al., 2016), to monitor the Galactic Centre magnetar, and to survey the Galactic Centre for new pulsars (Torre et al., in prep.). These two receivers offer 500 MHz of bandwidth, but a newly developed receiver, named the ‘‘C+’’ is being commissioned at Effelsberg at the moment of writing, and will offer an increased instantaneous bandwidth of up to 5 GHz, between 4 and 9 GHz. The C+ receiver, together with the new ROACH2- or GPU-based pulsar backends under development will significantly improve the high frequency observations of pulsars at Effelsberg in a very near future.

7.4.2 IRAM 30-m and the Large Millimetre Telescope

Above ~ 10 GHz it becomes very difficult to detect pulsars due to their steep spectra and faintness. Nevertheless, in some cases it is scientifically interesting to observe pulsars well above that frequency (see e.g. Section 6.1). These very high frequency pulsar observations require the most sensitive facilities available at the frequency range of interest. Two outstanding examples are the IRAM 30-m radio telescope on the Pico Veleta, in Spain, and the Large Millimetre Telescope (LMT) on the Sierra Negra volcano, in Mexico.

During the work presented in this thesis, we made use of the IRAM 30-m radio telescope to successfully detect pulsars up to record frequencies of ~ 300 GHz (see chapters 4, 5, and 6). The combination of large bandwidth receivers (we remark the Eight Mixer Receiver that delivers up to 32 GHz of bandwidth and can achieve a T_{sys} as low as ~ 70 K) together with the flexibility to use different backends suitable for pulsar data recording, makes of this telescope a very valuable instrument for pulsar science.

The LMT, with its 50 m reflector, is the largest fully steerable, sub(millimetre)

single-dish telescope in the world. It is currently undergoing commissioning tests and being equipped with receivers and backends and will offer a very high sensitivity between $\sim 75\text{--}350$ GHz (4 and 0.8 mm). Its large collecting area makes it also a very promising instrument for future pulsar observations.

7.4.3 Atacama Large Millimetre/submillimeter Array

The Atacama Large Millimetre/submillimeter Array (ALMA) is the most sensitive (sub)millimetre telescope available nowadays. Consisting of 64 antennas in one of the highest, driest regions on Earth, the Atacama desert in Chile, it can operate in atmospheric windows between ~ 40 and 950 GHz⁴. To enable pulsar work with it, and also its inclusion in Global Millimetre Very Long Base Interferometry Array (GMVA), the signals from the ALMA antennas need to be combined in a so-called *phased-mode* (Fish et al., 2013). This allows the array to operate virtually as a single-dish telescope (of approximately 80 m in diameter). A project to enable this phased-mode of ALMA is already ongoing: the ALMA Phasing Project or APP (Alef et al., 2012). The first test of phased-ALMA observing a pulsar occurred in May 2016, and the processing of the data is of high priority. There is some work still required until the ALMA data can be routinely processed by pulsar software, but it is undeniable the potential that observing pulsars with ALMA can have thanks to its unrivalled sensitivity at (sub)millimetre wavelengths.

7.4.4 Square Kilometre Array

The Square Kilometre Array (SKA) will be the largest radio telescope ever built. It will consist of thousand of antennas of different types covering a wide frequency range from about 10 MHz to 20 GHz, offer a large FoV and, with an enormous collecting area, an extraordinary sensitivity. It will be deployed in two phases, namely SKA1 and SKA2. SKA1 is planned for the time line 2016-2020, and SKA2, offering the full sensitivity of the facility, for around 2030. More detailed and updated information about the SKA project can be found in the official website⁵.

With respect to pulsar science, the SKA will be able to detect practically all the Galactic pulsars beamed toward the Earth (Keane et al., 2015). This means obtaining *the* pulsar census for our Galaxy, almost certainly including some of the long-wanted pulsar-black hole system. Studying these new extreme binary systems with the sensitivity of the SKA will allow to verify if General Relativity is the correct description of gravity, or if alternatives are needed. Furthermore, the discovery of many new ultra-stable millisecond pulsars and their regular observations will improve significantly the “Pulsar Timing Array” for the direct detection of low-frequency gravitational waves (e.g. Janssen et al., 2015), accelerating and improving the results of this extraordinary astronomical experiment.

⁴At the moment of writing, ALMA Cycle 4 offers bands 3 to 10, covering between ~ 84 to 950 GHz. The rest of the frequency coverage might be added in the future.

⁵www.skatelescope.org

7.5 Conclusions

The development of novel receiver technologies for radio astronomy will significantly improve our capabilities to carry out new outstanding astronomical experiments in the upcoming years. In particular, Phased Array Feeds, with their large FoV and novel RFI rejection abilities, will allow faster surveys, surely detecting a still-undiscovered population of pulsars and radio transients. Ultra-Wide-Band receivers will allow to perform high-sensitivity multifrequency observations, improving substantially the quality of the timing analysis of pulsars, while at the same time being excellent receivers for targeted searches and spectral analysis of radio sources.

Installing and operating these new technologies in our radio telescopes requires a significant effort. It has been shown that a strong RFI environment is the major problem for the correct functioning of these new receivers. Furthermore, additional problems may arise like, for instance, the difficulties to correctly focus receivers with large instantaneous bandwidths.

As part of this thesis, I have contributed to two pioneering projects that the MPIfR is running to equip the Effelsberg 100-m dish with both a PAF and a UBB. First, I helped to identify the challenges that the projects may face, and focused on the one identified as a potential showstopper: the possible saturation of the receivers by the strong RFI at the Effelsberg site. While demonstrating that the Checkerboard PAF MkII LNAs should be able to handle the RFI power levels at Effelsberg, I also showed that the UBB receiver was highly affected by them, lowering its sensitivity and often driving the receiver into saturation. Moreover, an optimum solution to the focussing of the UBB was investigated, concluding that it is better to focus the receiver at the highest operating frequencies.

I also led the first scientific project with the UBB at Effelsberg during its commissioning time, surveying 54 gamma-ray sources with no associated counterparts and high potential of harbouring undiscovered pulsars. The project benefited from the particular technical specifications of the UBB, increasing the coverage of the uncertain positions of the gamma-ray sources, and reducing the effects of scintillation. No new pulsars were detected down to the sensitivity limits of the receiver. We remark that the RFI highly affected the observations, with about 15 per cent of the data corrupted, and the rest suffering of a significant impact in its sensitivity.

Even with the significant challenges, by watching the local RFI environment and making the new receivers robust against the strong, ever-changing undesired man made signals, the next-generation of radio receivers, like PAFs and UWB, should be capable of operating correctly in polluted RFI areas. The efforts are certainly worth, since by equipping existing radio telescopes with these new technologies their observing capabilities can be greatly improved.

Acknowledgements

P.T. wants to thank Arnold van Ardenne, Marina Ivashina, Stefan Wijholds, Douglas Hayman, Brian Jeffs, and John Ford for sharing their expertise about the PAF tech-

nology and its application to radio astronomy. The input from these discussions was extremely helpful to identify the main sources of potential issues that the installation of these kind of receivers may impose when finally applied to the 100-m telescope at Effelsberg.

Summary and future work

8.1 Summary

In this thesis, we have explored radio pulsars at different wavelengths, applying the newest receiver technology whenever possible. In particular, we presented a new, multi-epoch and multifrequency pulsar survey of the Galactic Centre, studies of the emission properties of the magnetar SGR J1745–2900 and the normal pulsar PSR B0355+54 at the highest radio frequencies to date, and technical and commissioning works related to the next generation of low-frequency radio receivers for the Effelsberg 100-m radio telescope.

The Galactic Centre survey (Chapter 3) has not yielded new pulsar discoveries in the region. The analysis of the survey sensitivity uncovered that our sensitivity to Galactic Centre pulsars is greatly reduced by the contributions to the total system noise of the Galactic Centre background and the atmosphere, and we conclude that the paucity of discoveries is likely consequence of this reduced sensitivity, and not a lack of pulsars in the region. Nonetheless, only about 50 percent of the total candidates have been inspected at the moment of writing and, therefore, the discovery of pulsars in the survey cannot yet be ruled out.

The two simultaneous multifrequency observing campaigns on the recently discovered Galactic Centre magnetar SGR J1745–2900 allowed us to measure its emission properties over a large frequency range (Chapters 4 and 5). We focused on obtaining measurements up to the highest possible radio frequencies, taking advantage of the expected flat spectrum of radio magnetars. The source was detected from 2.54 up to 291 GHz, including strong single pulses up to 154 GHz. The results include the highest-radio-frequency detection of pulsed emission from any neutron star to date, more than double the frequency of the previous highest-frequency detections. Furthermore, we showed the strong intrinsic variability of this pulsar at all frequencies, measured its flux density and its roughly-flat spectrum, and evidenced a high degree of linear polarization up to 154 GHz, the highest-frequency polarized emission reported for a pulsar. These measurements are relevant for a better understanding of the still poorly-understood radio emission mechanism of pulsars and magnetars, and set new observational constraints that any proposed emission model must be able to explain.

In addition to the magnetar SGR J1745–2900, we have presented the results of short millimetre observations of PSR B0355+54 between 87 and 154 GHz (Chapter 6). The detections for this source reached 138 GHz, pushing the limit of the highest radio frequency at which the emission from normal pulsars had been detected, and showing that normal pulsars can continue to emit in the short millimetre regime. We searched for

a flattening or turn-up in the spectrum of PSR B0355+54, a feature predicted by some emission models and that could give us information about the emission mechanism, but found none. Instead, we observed that the intensity of this pulsar apparently decreases at and above 87 GHz, deviating from the power law that described its emission very well at lower frequencies. If real, this decreased intensity could be indicative of a decrease in efficiency of the coherent radio emission process. However, uncertainties in the instrumental calibration and the possible presence of intrinsic variability in the pulsar preclude a conclusive result. Additional information about the observing instrument that will be compiled in the near future will allow us to obtain an improved calibration. With this, we will be able to obtain a stronger conclusion about the source of the apparent decreased intensity at the short millimetre wavelengths. Observations of an additional sample of five pulsars were carried out for the first time at this frequency range (87 to 154 GHz), with no evident detections. Given the expected faintness of the five pulsars at these frequencies, it is likely that the non-detections are due to an insufficient sensitivity of the observations.

Finally, technical and commissioning work on the state-of-the-art Ultra-Broad-Band (UBB) and Phased Array Feed (PAF) receivers, currently under development for the Effelsberg 100-m radio telescope, were presented (Chapter 7). These included the determination of an optimal focusing set-up for the UBB, which was identified at the highest part of its operating band, together with a multifrequency calibration and pulsar observations that concluded that the receiver was strongly affected by Radio Frequency Interference (RFI), reducing considerably (by a factor ~ 3) its sensitivity with respect to the levels measured in the laboratory. The UBB was used during its commissioning for a targeted pulsar survey of 54 unassociated *Fermi* LAT sources, with no new discoveries. For the PAF, the main focus was on the assessment of the robustness of the array against the strong RFI at the Effelsberg site. Our measurements using a test receiving element of the Checkerboard PAF MkII concluded that the front-end should be able to operate at Effelsberg without a persistent saturation (with the current RFI levels). Overall, the results confirm that these new receivers can be used in electromagnetically-polluted areas like Effelsberg, but that, in order to perform optimally, they require a careful design of the electronics so as to strongly suppress those frequency ranges particularly polluted by strong man-made radio signals.

8.2 Future Work

There are still open questions about the missing population of pulsars in the Galactic Centre and the radio emission process of pulsars and magnetars. This dissertation aimed to contribute to our knowledge in these topics, but there is still room for improving and continuing the research presented here. This section briefly describes future related research plans.

Continuing the Galactic Centre survey

The Galactic Centre survey presented here has still about 50 per cent of the pulsar candidates pending review. Completing the analysis of the results will not only enable a final conclusion about the detectability of pulsars in the region, but will also enable an improved statistical analysis of the candidate database (see Section 3.2.2.4). A quantitative assessment of the impact of the red noise on the sensitivity of our survey would allow us to calculate the true sensitivity to long-period pulsars, which is expected to be reduced by the red noise with respect to the theoretical limit based on the assumption of a purely-Gaussian system noise (e.g. Lazarus et al., 2015). New techniques to reduce the red noise applied to the raw data prior to the folding could be key to improve the detectability of the long-period pulsars (see e.g Figure 2.8).

Since uncertainties still exist with respect to the scattering in the direction to the Galactic Centre, surveys at even higher frequencies than those presented here are warranted. Some of the future surveys, like for instance those planned under the ERC-funded European collaboration *BlackHoleCam*, plan to use millimetre wavelengths to survey the Galactic Centre. Such observations will be mostly unaffected by Inter Stellar Medium (ISM) effects and have the potential to uncover a population of Galactic Centre pulsars if the scattering is the main reason for the paucity of discoveries at lower frequencies. The search process at these very high radio frequencies would be very similar to the one applied to the Effelsberg Galactic Centre survey presented in this thesis. In particular, the data processing will have to deal with the challenges of observing at high radio frequencies, like an excess of red noise in the data and a very small or negligible dispersion effect that complicates the discrimination of candidates against man-made RFI (see Section 3.2.2.3).

Apart from an improved red noise cleaning algorithm, the searching pipeline developed here could be further improved by including new searching algorithms like the Fast-Folding-Algorithm (FFA) to improve sensitivity to long-period pulsars, or by including stack and/or template matching searches that can increase our sensitivity to faint and binary pulsars, respectively. The RFI excision capabilities could also be improved. For example, a modelling of the instrument noise, or pointings off source could be used to clean the data from unwanted RFI and instrumental signals.

New observatories coming online will allow us to continue surveying the Galactic Centre with increased sensitivity and at different wavelengths. A major improvement will be obtained by using sensitive arrays instead of single dishes. With interferometric techniques, we can create small beams centred on the region of interest, filtering out most of the background contribution of the Galactic Centre that was shown here to greatly decrease the sensitivity of the observations with a single dish. Facilities like the JVLA, and the upcoming MeerKAT and the Square Kilometre Array (SKA), will be excellent tools to carry out these more sensitive surveys of the Galactic Centre. Additionally, an increased sensitivity of the observations can aid considerably the acceleration searches by reducing the integration lengths required to reach a given flux density limit (see Section 3.2.2.2).

Continuing the monitoring of SGR J1745-2900 including short millimetre wavelengths

The opportunity to measure the properties of the radio emission from magnetars is quite rare. Furthermore, these objects are variable and their emission can turn on and off rapidly. Therefore, monitoring of the Galactic Centre magnetar SGR J1745–2900 should be continued to take advantage of the long period of activity of the source, which has already lasted more than two years. Apart from giving us valuable information about the pulsar emission process through the study of its pulse profile, single pulses, intensity, spectral shape, polarization, etc., the location of this pulsar close to the centre of the Galaxy adds importance to this monitoring. The repeated observations will allow us to track possible variations in the properties of the ISM, providing information of the dynamics of the ionized gas around the Galactic Centre. The inclusion of the short millimetre wavelengths to this monitoring, in particular when the observations at low- and high-frequencies are simultaneous, may allow us to determine more characteristics of the ISM and the emission mechanism. For instance, the detection of simultaneous single pulses at different frequencies can be used to calculate how broad band the radio emission process may be, and has the potential to measure the magnetar’s DM (with its potential variations) to very high precision. Furthermore, having demonstrated in this thesis that this magnetar is highly polarized at the short millimetre wavelengths, precise polarization studies at these frequencies could provide a unique insight to the magnetic field configuration of magnetars close to the stellar surface.

Search for millimetre wavelength emission from other magnetars

The fact the magnetars can show an inverted spectrum in the radio band (see Section 5.3) opens the possibility of detection by current millimetre wavelength facilities, like the IRAM 30-m, the LMT or ALMA. If the “inverted-spectrum mode” occurs in magnetars more often than what we think, it might even be easier to detect the radio emission from these rare objects with millimetre wavelength observations rather than at low frequencies. Therefore, it could be worth carrying out a survey for high-frequency radio emission from the known population of magnetars.

Observations of pulsars at short millimetre wavelengths

As already discussed, the observations of pulsars at very high radio frequencies are relevant for developing our understating of the emission mechanism (Chapter 6). In this thesis, it was shown that PSR B0355+54 continues to emit in the short millimetre band up to 138 GHz. There are another five pulsars observed with no obvious detections, likely due to an insufficient sensitivity. Our observations of PSR B0355+54 showed that the pulsar exhibits intensity variability at the short millimetre wavelengths, making it undetectable in some of the observations. If similar variability in this frequency regime occurs for all (or most) pulsars, for instance if it is produced by an inefficient coherent emission process, a few observations with no detections may not be enough to conclusively rule out their emission at these frequencies. In this case, repeated observations

are justified. Moreover, here we made use of a 30-m telescope. Facilities like the 50-m LMT and the 80-m equivalent phased-ALMA could have enough sensitivity to uncover the radio emission from these and other pulsars at even higher frequencies than what is presented here. We also note the restriction in visibility to southern pulsars of the IRAM 30-m. The number of potential observable pulsars at millimetre wavelengths will be considerably higher if the LMT and ALMA become usable for pulsars observations.

Science with the next-generation of radio receivers at Effelsberg

The Effelsberg 100-m dish will be equipped with new state-of-the-art receivers in the very near future. The Ultra-Broad-Band (UBB) receiver is expected to be operational in autumn 2016, including the new RFI filters that should bring its sensitivity back to the expected $T_{\text{sys}} \simeq 20$ K. This receiver will offer an unprecedented precision for pulsar timing, and will at the same time be an excellent instrument for both broadband spectral studies and targeted pulsar surveys. The Phased Array Feed (PAF), on the other hand, with its increased Field-of-View, will be the instrument to use in large-scale surveys for transient emission, with a high potential of discoveries of intermittent pulsars, RRATs, and Fast Radio Bursts. Furthermore, the capabilities of the PAF to digitally and spatially reject RFI are extremely promising in a highly electromagnetically-polluted area like Effelsberg. Finally, the new broadband C+ receiver will be an excellent tool for improving the sensitivity of the Galactic Centre survey by increasing the current instantaneous bandwidth by a factor ~ 8 (neglecting the bandwidth losses due to RFI). Its broad instantaneous bandwidth will improve the measurements of frequency-dependent ISM effects, and the high frequencies of operation (4 to 8 GHz) are desirable for the study of sources highly affected by scattering, like for example the Galactic Centre magnetar SGR J1745–2900 or potential future pulsars found in this region.

Bibliography

- Abbott, B., Abbott, R., Adhikari, R., et al. 2008, *Phys. Rev. D*, 77, 062002 (Cited on page 24.)
- Abbott, B. P., Abbott, R., Abbott, T. D., et al. 2016, *Physical Review Letters*, 116, 061102 (Cited on page 23.)
- Alef, W., Anderson, J., Rottmann, H., et al. 2012, in *Proceedings of Science: 11th European VLBI Network Symposium, Bordeaux, France 10 Oct 2012*, 6 pages, 1 (Cited on page 135.)
- Alpar, M. A., Cheng, A. F., Ruderman, M. A., & Shaham, J. 1982, *Nature*, 300, 728 (Cited on page 10.)
- Antoniadis, J., Freire, P. C. C., Wex, N., et al. 2013, *Science*, 340, 448 (Cited on pages 23 and 24.)
- Archibald, A. M., Stairs, I. H., Ransom, S. M., et al. 2009, *Science*, 324, 1411 (Cited on page 24.)
- Archibald, R. F., Gotthelf, E. V., Ferdman, R. D., et al. 2016, *ApJ*, 819, L16 (Cited on page 7.)
- Arons, J., & Barnard, J. J. 1986, *ApJ*, 302, 120 (Cited on page 14.)
- Asseo, E. 1993, *MNRAS*, 264, 940 (Cited on page 14.)
- Avago-Technologies. 2012, ATF-35143, Low noise, Pseudomorphic HEMOT a surface mount plastic (Cited on page 121.)
- Baade, W., & Zwicky, F. 1934, *Proceedings of the National Academy of Science*, 20, 259 (Cited on page 3.)
- Barnard, J. J., & Arons, J. 1986, *ApJ*, 302, 138 (Cited on page 9.)
- Barr, E. D., Guillemot, L., Champion, D. J., et al. 2013a, *MNRAS*, 429, 1633 (Cited on page 124.)
- Barr, E. D., Champion, D. J., Kramer, M., et al. 2013b, *MNRAS*, 435, 2234 (Cited on page 24.)
- Bates, S. D., Johnston, S., Lorimer, D. R., et al. 2011, *MNRAS*, 411, 1575 (Cited on page 52.)
- Beloborodov, A. M. 2009, *ApJ*, 703, 1044 (Cited on page 84.)
- . 2013, *ApJ*, 777, 114 (Cited on page 84.)

- Beloborodov, A. M., & Thompson, C. 2007, *ApJ*, 657, 967 (Cited on page 84.)
- Bhattacharya, D., & van den Heuvel, E. P. J. 1991, *Phys. Rep.*, 203, 1 (Cited on page 10.)
- Bower, G. C., Deller, A., Demorest, P., et al. 2014, *ApJ*, 780, L2 (Cited on pages 76 and 88.)
- . 2015, *ApJ*, 798, 120 (Cited on pages 53 and 88.)
- Bramante, J., & Linden, T. 2014, *Phys. Rev. Lett.*, 113, 191301 (Cited on page 53.)
- Burbidge, G. R., & Strittmatter, P. A. 1968, *Nature*, 218, 433 (Cited on page 3.)
- Camilo, F., Ransom, S. M., Halpern, J. P., & Reynolds, J. 2007a, *ApJ*, 666, L93 (Cited on pages 76, 88 and 91.)
- Camilo, F., Ransom, S. M., Halpern, J. P., et al. 2006, *Nature*, 442, 892 (Cited on pages 12, 13, 76 and 88.)
- Camilo, F., Reynolds, J., Johnston, S., Halpern, J. P., & Ransom, S. M. 2008, *ApJ*, 679, 681 (Cited on pages 13, 84, 91, 93 and 97.)
- Camilo, F., Ransom, S. M., Peñalver, J., et al. 2007b, *ApJ*, 669, 561 (Cited on pages 84, 88, 97 and 104.)
- Camilo, F., Kerr, M., Ray, P. S., et al. 2015, *ApJ*, 810, 85 (Cited on page 124.)
- Carter, M., Lazareff, B., Maier, D., et al. 2012, *A&A*, 538, A89 (Cited on pages 77 and 89.)
- Chadwick, J. 1932, *Nature*, 129, 312 (Cited on page 3.)
- Champion, D. J., Ransom, S. M., Lazarus, P., et al. 2008, *Science*, 320, 1309 (Cited on page 24.)
- Chen, K., & Ruderman, M. 1993, *ApJ*, 402, 264 (Cited on page 10.)
- Cheng, A. F., & Ruderman, M. A. 1977, *ApJ*, 212, 800 (Cited on page 14.)
- Chennamangalam, J., & Lorimer, D. R. 2014, *MNRAS*, 440, L86 (Cited on page 69.)
- Chippendale, A. P., Brown, A. J., Beresford, R. J., et al. 2015, in *Electromagnetics in Advanced Applications (ICEAA), 2015 International Conference on*, 541–544 (Cited on page 118.)
- Clark, C. J., Pletsch, H. J., Wu, J., et al. 2015, *ApJ*, 809, L2 (Cited on page 39.)
- Cole, T. W. 1969a, *Nature*, 223, 487 (Cited on page 3.)
- . 1969b, *Nature*, 221, 29 (Cited on page 3.)

- Comella, J. M., Craft, H. D., Lovelace, R. V. E., & Sutton, J. M. 1969, *Nature*, 221, 453 (Cited on page 4.)
- Cordes, J. M. 1978, *ApJ*, 222, 1006 (Cited on pages 8 and 100.)
- Cordes, J. M., & Lazio, T. J. 1991, *ApJ*, 376, 123 (Cited on pages 20 and 91.)
- Cordes, J. M., & Lazio, T. J. W. 1997, *ApJ*, 475, 557 (Cited on page 20.)
- . 2002, *ArXiv Astrophysics e-prints*, astro-ph/0207156 (Cited on pages 18, 22, 52, 53, 69 and 71.)
- Cordes, J. M., & McLaughlin, M. A. 2003, *ApJ*, 596, 1142 (Cited on page 39.)
- Cromartie, H. T., Camilo, F., Kerr, M., et al. 2016, *ApJ*, 819, 34 (Cited on page 124.)
- Crusius-Wätzell, A. R., Kunzl, T., & Lesch, H. 2001, *ApJ*, 546, 401 (Cited on page 101.)
- Davies, J. G., Lyne, A. G., Smith, F. G., et al. 1984, *MNRAS*, 211, 57 (Cited on page 100.)
- Demircan, O., & Kahraman, G. 1991, *Ap&SS*, 181, 313 (Cited on page 5.)
- Demorest, P. B., Pennucci, T., Ransom, S. M., Roberts, M. S. E., & Hessels, J. W. T. 2010, *Nature*, 467, 1081 (Cited on page 24.)
- Deneva, J. S., Cordes, J. M., & Lazio, T. J. W. 2009, *ApJ*, 702, L177 (Cited on pages 52 and 69.)
- Deutsch, A. J. 1955, *Annales d’Astrophysique*, 18, 1 (Cited on page 5.)
- Dexter, J., & O’Leary, R. M. 2014, *ApJ*, 783, L7 (Cited on page 53.)
- Duncan, R. C., & Thompson, C. 1992, *ApJ*, 392, L9 (Cited on pages 13, 76 and 88.)
- Eatough, R., Lazio, T. J. W., Casanellas, J., et al. 2015, *Advancing Astrophysics with the Square Kilometre Array (ASKA14)*, 45 (Cited on page 73.)
- Eatough, R. P., Kramer, M., Klein, B., et al. 2013a, in *IAU Symposium*, Vol. 291, IAU Symposium, ed. J. van Leeuwen, 382–384 (Cited on pages 52, 54 and 72.)
- Eatough, R. P., Kramer, M., Lyne, A. G., & Keith, M. J. 2013b, *MNRAS*, 431, 292 (Cited on page 58.)
- Eatough, R. P., Molkenhain, N., Kramer, M., et al. 2010, *MNRAS*, 407, 2443 (Cited on page 36.)
- Eatough, R. P., Falcke, H., Karuppusamy, R., et al. 2013c, *Nature*, 501, 391 (Cited on pages 13, 52, 54, 76 and 88.)
- Eckart, A., & Genzel, R. 1996, *Nature*, 383, 415 (Cited on page 52.)

- Eilek, J. A., & Hankins, T. H. 2016, *Journal of Plasma Physics*, 82, 635820302 (Cited on pages 14 and 100.)
- Elmer, M., Jeffs, B. D., Warnick, K. F., Fisher, J. R., & Norrod, R. D. 2012, *IEEE Transactions on Antennas and Propagation*, 60, 903 (Cited on page 116.)
- Faucher-Giguère, C.-A., & Loeb, A. 2011, *MNRAS*, 415, 3951 (Cited on page 52.)
- Fish, V., Alef, W., Anderson, J., et al. 2013, ArXiv e-prints, arXiv:1309.3519 (Cited on page 135.)
- Fisher, J. R., & Bradley, R. F. 2000a, in *Proc. SPIE*, Vol. 4015, *Radio Telescopes*, ed. H. R. Butcher, 308–318 (Cited on page 116.)
- Fisher, J. R., & Bradley, R. F. 2000b, in *Astronomical Society of the Pacific Conference Series*, Vol. 217, *Imaging at Radio through Submillimeter Wavelengths*, ed. J. G. Mangum & S. J. E. Radford, 11 (Cited on page 116.)
- Freire, P. C., Kramer, M., & Lyne, A. G. 2001, *MNRAS*, 322, 885 (Cited on page 66.)
- Freire, P. C. C., & Tauris, T. M. 2014, *MNRAS*, 438, L86 (Cited on page 24.)
- Freire, P. C. C., Bassa, C. G., Wex, N., et al. 2011, *MNRAS*, 412, 2763 (Cited on page 24.)
- Freire, P. C. C., Wex, N., Esposito-Farèse, G., et al. 2012, *MNRAS*, 423, 3328 (Cited on page 23.)
- Gavriil, F. P., Kaspi, V. M., & Woods, P. M. 2002, *Nature*, 419, 142 (Cited on page 13.)
- Genzel, R., Eisenhauer, F., & Gillessen, S. 2010, *Reviews of Modern Physics*, 82, 3121 (Cited on page 52.)
- Gillessen, S., Eisenhauer, F., Trippe, S., et al. 2009, *ApJ*, 692, 1075 (Cited on pages 52 and 80.)
- Goddi, C., Falcke, H., Kramer, M., et al. 2016, ArXiv e-prints, arXiv:1606.08879 (Cited on page 101.)
- Gold, T. 1968, *Nature*, 218, 731 (Cited on pages 3, 4 and 5.)
- Goldreich, P., & Julian, W. H. 1969, *ApJ*, 157, 869 (Cited on page 5.)
- Gough, R. 2010, prepSKA2 meeting (Cited on page 121.)
- Greve, A., Neri, R., & Sievers, A. 1998, *A&AS*, 132, 413 (Cited on page 49.)
- Guillemot, L., Freire, P. C. C., Cognard, I., et al. 2012, *MNRAS*, 422, 1294 (Cited on page 124.)

- Halpern, J. P., Gotthelf, E. V., Becker, R. H., Helfand, D. J., & White, R. L. 2005, *ApJ*, 632, L29 (Cited on page 12.)
- Hampson, G., Macleod, A., Beresford, R., et al. 2012, in *Electromagnetics in Advanced Applications (ICEAA), 2012 International Conference on*, 807–809 (Cited on pages 116 and 119.)
- Hankins, T. H., & Eilek, J. A. 2007, *ApJ*, 670, 693 (Cited on page 14.)
- Hankins, T. H., Jones, G., & Eilek, J. A. 2015, *ApJ*, 802, 130 (Cited on page 15.)
- Hankins, T. H., Rankin, J. M., & Eilek, J. A. 2009, in *Astronomy*, Vol. 2010, astro2010: The Astronomy and Astrophysics Decadal Survey (Cited on page 88.)
- Hasen, C. K., Warnick, K. F., Jeffs, B. D., Fisher, J. R., & Bradley, R. 2005, *Radio Science*, 40 (Cited on page 116.)
- Hayman, D. B. 2011, PhD thesis, Macquarie University (Cited on page 116.)
- Hayman, D. B., Bird, T. S., Esselle, K. P., & Hall, P. 2005, in *2005 IEEE Antennas and Propagation Society International Symposium*, Vol. 3A, 371–374 vol. 3A (Cited on page 120.)
- Hayman, D. B., Bird, T. S., Esselle, K. P., & Hall, P. J. 2010, *IEEE Transactions on Antennas and Propagation*, 58, 1922 (Cited on page 116.)
- Hayman, D. B., Esselle, K. T. s., Bird, T. T. s., & Hall, P. T. s. 2011, Thesis, thesis (PhD) – Macquarie University, Faculty of Science, Dept. of Engineering, 2011 (Cited on page 120.)
- Heger, A., Fryer, C. L., Woosley, S. E., Langer, N., & Hartmann, D. H. 2003, *ApJ*, 591, 288 (Cited on page 4.)
- Hewish, A., Bell, S. J., Pilkington, J. D. H., Scott, P. F., & Collins, R. A. 1968, *Nature*, 217, 709 (Cited on pages 3 and 116.)
- Hewish, A., Dennison, P. A., & Pilkington, J. D. H. 1966, *Nature*, 209, 1188 (Cited on page 3.)
- Hewish, A., Scott, P. F., & Wills, D. 1964, *Nature*, 203, 1214 (Cited on page 3.)
- Hobbs, G. 2013, *Classical and Quantum Gravity*, 30, 224007 (Cited on page 23.)
- Hobbs, G., Lorimer, D. R., Lyne, A. G., & Kramer, M. 2005, *MNRAS*, 360, 974 (Cited on page 104.)
- Hulse, R. A., & Taylor, J. H. 1975, *ApJ*, 195, L51 (Cited on page 22.)
- Istomin, Y. N. 2004, in *IAU Symposium*, Vol. 218, *Young Neutron Stars and Their Environments*, ed. F. Camilo & B. M. Gaensler, 369 (Cited on page 109.)

- Ivashina, M., & van Ardenne, J. D. B. A. 2002, in *Microwave and Telecommunication Technology, 2002. CriMiCo 2002. 12th International Conference*, 278–281 (Cited on page 116.)
- Ivashina, M. V., Iupikov, O., Maaskant, R., van Cappellen, W. A., & Oosterloo, T. 2011, *IEEE Transactions on Antennas and Propagation*, 59, 1864 (Cited on page 116.)
- Jackson, J. D. 1962, *Classical Electrodynamics* (Cited on page 8.)
- Janssen, G., Hobbs, G., McLaughlin, M., et al. 2015, *Advancing Astrophysics with the Square Kilometre Array (AASKA14)*, 37 (Cited on page 135.)
- Jeffs, B. D., Li, L., & Warnick, K. F. 2005, *IEEE Transactions on Signal Processing*, 53, 439 (Cited on page 116.)
- Jeffs, B. D., & Warnick, K. F. 2008, *IEEE Transactions on Signal Processing*, 56, 3108 (Cited on page 116.)
- Jeffs, B. D., Warnick, K. F., Landon, J., et al. 2008, *IEEE Journal of Selected Topics in Signal Processing*, 2, 635 (Cited on page 116.)
- Jenet, F. A., Hobbs, G. B., Lee, K. J., & Manchester, R. N. 2005, *ApJ*, 625, L123 (Cited on page 23.)
- Johnston, H. M., & Kulkarni, S. R. 1991, *ApJ*, 368, 504 (Cited on page 58.)
- Johnston, S., & Gray, A. 2006, *SKA Memo 72: Surveys with the xNTD and CLAR*, Tech. rep. (Cited on page 117.)
- Johnston, S., Kramer, M., Lorimer, D. R., et al. 2006, *MNRAS*, 373, L6 (Cited on page 52.)
- Johnston, S., Walker, M. A., van Kerkwijk, M. H., Lyne, A. G., & D’Amico, N. 1995, *MNRAS*, 274, L43 (Cited on page 52.)
- Kapoor, R. C., & Shukre, C. S. 1998, *ApJ*, 501, 228 (Cited on page 5.)
- Kaspi, V. M. 2010, *Proceedings of the National Academy of Science*, 107, 7147 (Cited on page 13.)
- Kaspi, V. M., Archibald, R. F., Bhalerao, V., et al. 2014, *ApJ*, 786, 84 (Cited on page 84.)
- Kazbegi, A. Z., Machabeli, G. Z., & Melikidze, G. I. 1991, *MNRAS*, 253, 377 (Cited on page 14.)
- Keane, E. F., Kramer, M., Lyne, A. G., Stappers, B. W., & McLaughlin, M. A. 2011, *MNRAS*, 415, 3065 (Cited on page 12.)

- Keane, E. F., Bhattacharyya, B., Kramer, M., et al. 2015, *Advancing Astrophysics with the Square Kilometre Array (AASKA14)*, 40 (Cited on pages 73 and 135.)
- Keith, M. J., Jameson, A., van Straten, W., et al. 2010, *MNRAS*, 409, 619 (Cited on page 24.)
- Keith, M. J., Johnston, S., Ray, P. S., et al. 2011, *MNRAS*, 414, 1292 (Cited on page 124.)
- Kennea, J. A., Burrows, D. N., Kouveliotou, C., et al. 2013, *ApJ*, 770, L24 (Cited on pages 13, 52 and 76.)
- Kerr, M., Camilo, F., Johnson, T. J., et al. 2012, *ApJ*, 748, L2 (Cited on page 124.)
- Kijak, J., & Gil, J. 1998, *MNRAS*, 299, 855 (Cited on page 9.)
- . 2003, *A&A*, 397, 969 (Cited on page 9.)
- Klein, B. 2005, PhD thesis, University of Bonn (Cited on page 52.)
- Knispel, B., Eatough, R. P., Kim, H., et al. 2013, *ApJ*, 774, 93 (Cited on page 72.)
- Komesaroff, M. M. 1970, *Nature*, 225, 612 (Cited on page 14.)
- Kouveliotou, C., Dieters, S., Strohmayer, T., et al. 1998, *Nature*, 393, 235 (Cited on pages 13 and 76.)
- Kouveliotou, C., Strohmayer, T., Hurley, K., et al. 1999, *ApJ*, 510, L115 (Cited on page 13.)
- Kramer, C. 1997, Calibration of spectral line data at the IRAM 30m radio telescope, Tech. rep., IRAM (Cited on pages 46, 78, 89 and 103.)
- Kramer, M. 1995, PhD thesis, University of Bonn (Cited on pages 105 and 107.)
- Kramer, M., & Champion, D. J. 2013, *Classical and Quantum Gravity*, 30, 224009 (Cited on page 23.)
- Kramer, M., Jessner, A., Doroshenko, O., & Wielebinski, R. 1997a, *ApJ*, 488, 364 (Cited on pages 15, 76, 88, 93, 100, 102, 105 and 107.)
- Kramer, M., Klein, B., Lorimer, D., et al. 2000, in *Astronomical Society of the Pacific Conference Series*, Vol. 202, IAU Colloq. 177: Pulsar Astronomy - 2000 and Beyond, ed. M. Kramer, N. Wex, & R. Wielebinski, 37 (Cited on page 52.)
- Kramer, M., Lyne, A. G., O'Brien, J. T., Jordan, C. A., & Lorimer, D. R. 2006a, *Science*, 312, 549 (Cited on page 100.)
- Kramer, M., Stappers, B. W., Jessner, A., Lyne, A. G., & Jordan, C. A. 2007, *MNRAS*, 377, 107 (Cited on pages 84, 88, 91 and 97.)

- Kramer, M., Xilouris, K. M., Jessner, A., et al. 1997b, *A&A*, 322, 846 (Cited on pages 22 and 100.)
- Kramer, M., Xilouris, K. M., Jessner, A., Wielebinski, R., & Timofeev, M. 1996, *A&A*, 306, 867 (Cited on pages 15, 76, 88, 93, 100, 101, 102, 105 and 107.)
- Kramer, M., Xilouris, K. M., & Rickett, B. 1997c, *A&A*, 321, 513 (Cited on pages 76 and 100.)
- Kramer, M., Stairs, I. H., Manchester, R. N., et al. 2006b, *Science*, 314, 97 (Cited on page 23.)
- Kravchenko, E. V., Cotton, W. D., Yusef-Zadeh, F., & Kovalev, Y. Y. 2016, *MNRAS*, 458, 4456 (Cited on page 97.)
- Kuzmin, A. D., & Losovsky, B. Y. 2001, *A&A*, 368, 230 (Cited on page 103.)
- Landon, J., Elmer, M., Waldron, J., et al. 2010, *AJ*, 139, 1154 (Cited on page 116.)
- Large, M. I., Vaughan, A. E., & Mills, B. Y. 1968, *Nature*, 220, 340 (Cited on page 4.)
- Lattimer, J. M., & Prakash, M. 2001, *ApJ*, 550, 426 (Cited on page 4.)
- Lazaridis, K., Jessner, A., Kramer, M., et al. 2008, *MNRAS*, 390, 839 (Cited on pages 84 and 88.)
- Lazarus, P., Karuppusamy, R., Graikou, E., et al. 2016, *MNRAS*, 458, 868 (Cited on page 134.)
- Lazarus, P., Brazier, A., Hessels, J. W. T., et al. 2015, *ApJ*, 812, 81 (Cited on pages 24, 33, 50, 72 and 141.)
- Lee, K. J., Guillemot, L., Yue, Y. L., Kramer, M., & Champion, D. J. 2012, *MNRAS*, 424, 2832 (Cited on page 124.)
- Lee, K. J., Stovall, K., Jenet, F. A., et al. 2013, *MNRAS*, 433, 688 (Cited on pages 37 and 66.)
- Lesch, H., Jessner, A., Kramer, M., & Kunzl, T. 1998, *A&A*, 332, L21 (Cited on pages 14 and 101.)
- Levin, L., Bailes, M., Bates, S., et al. 2010, *ApJ*, 721, L33 (Cited on pages 13, 76 and 88.)
- Levin, L., Bailes, M., Bates, S. D., et al. 2012, *MNRAS*, 422, 2489 (Cited on pages 84, 88 and 91.)
- Liu, K., Eatough, R. P., Wex, N., & Kramer, M. 2014, *MNRAS*, 445, 3115 (Cited on pages 23 and 52.)

- Liu, K., Wex, N., Kramer, M., Cordes, J. M., & Lazio, T. J. W. 2012, *ApJ*, 747, 1 (Cited on pages 23, 52 and 76.)
- Löhmer, O., Jessner, A., Kramer, M., Wielebinski, R., & Maron, O. 2008, *A&A*, 480, 623 (Cited on pages 76, 88, 101 and 102.)
- Lorimer, D. R., & Kramer, M. 2005, *Handbook of Pulsar Astronomy* (Cited on pages 5, 6, 7, 9, 14, 17, 19, 20, 22, 31, 34, 37, 39, 67, 78, 80, 84, 105 and 113.)
- Lorimer, D. R., Yates, J. A., Lyne, A. G., & Gould, D. M. 1995, *MNRAS*, 273, 411 (Cited on pages 105 and 107.)
- Lorimer, D. R., Esposito, P., Manchester, R. N., et al. 2015, *MNRAS*, 450, 2185 (Cited on page 24.)
- Luo, Q., & Melrose, D. B. 1992, *MNRAS*, 258, 616 (Cited on page 14.)
- Lynch, R. S., Archibald, R. F., Kaspi, V. M., & Scholz, P. 2014, *ArXiv e-prints*, arXiv:1412.0610 (Cited on page 84.)
- . 2015, *ApJ*, 806, 266 (Cited on pages 88 and 91.)
- Lyne, A., & Graham-Smith, F. 2012, *Pulsar Astronomy* (Cited on page 12.)
- Lyne, A. G., Jordan, C. A., Graham-Smith, F., et al. 2015, *MNRAS*, 446, 857 (Cited on pages 7, 13 and 14.)
- Lyne, A. G., McLaughlin, M. A., Keane, E. F., et al. 2009, *MNRAS*, 400, 1439 (Cited on page 12.)
- Macquart, J. P., & Kanekar, N. 2015, *ApJ*, 805, 172 (Cited on page 53.)
- Macquart, J. P., Kanekar, N., Frail, D. A., & Ransom, S. M. 2010, *ApJ*, 715, 939 (Cited on pages 52 and 69.)
- Manchester, R. N. 2013, *Classical and Quantum Gravity*, 30, 224010 (Cited on page 23.)
- Manchester, R. N., Hobbs, G. B., Teoh, A., & Hobbs, M. 2005, *AJ*, 129, 1993 (Cited on pages 9, 11, 24, 71 and 103.)
- Manchester, R. N., Lyne, A. G., Camilo, F., et al. 2001, *MNRAS*, 328, 17 (Cited on page 52.)
- Maron, O., Kijak, J., Kramer, M., & Wielebinski, R. 2000, *A&AS*, 147, 195 (Cited on pages 52, 88, 102, 103 and 105.)
- McKinnon, M. M. 1997, *ApJ*, 475, 763 (Cited on page 9.)
- McLaughlin, M. A. 2013, *Classical and Quantum Gravity*, 30, 224008 (Cited on page 23.)

- McLaughlin, M. A., Lyne, A. G., Lorimer, D. R., et al. 2006, *Nature*, 439, 817 (Cited on page 10.)
- Melrose, D. B. 1978, *ApJ*, 225, 557 (Cited on page 14.)
- . 1992, *Philosophical Transactions of the Royal Society of London Series A*, 341, 105 (Cited on pages 14 and 101.)
- Melrose, D. B., & Yuen, R. 2016, *ArXiv e-prints*, arXiv:1604.03623 (Cited on pages 8, 14 and 88.)
- Michel, F. C. 1978, *ApJ*, 220, 1101 (Cited on pages 15, 16, 88 and 93.)
- . 1982, *Reviews of Modern Physics*, 54, 1 (Cited on pages 14, 15, 16, 76, 88, 93 and 101.)
- Miller, M., & Lamb, F. 2016, *Eur. Phys. J. A*, 52, 63 (Cited on page 24.)
- Mitra, D., & Rankin, J. M. 2011, *ApJ*, 727, 92 (Cited on pages 14 and 101.)
- Morello, V., Barr, E. D., Bailes, M., et al. 2014, *MNRAS*, 443, 1651 (Cited on page 36.)
- Mori, K., Gotthelf, E. V., Zhang, S., et al. 2013, *ApJ*, 770, L23 (Cited on pages 13, 52 and 76.)
- Morris, D., Graham, D. A., Sieber, W., Bartel, N., & Thomasson, P. 1981, *A&AS*, 46, 421 (Cited on page 97.)
- Morris, D., Kramer, M., Thum, C., et al. 1997, *A&A*, 322, L17 (Cited on pages 76, 88, 100, 102, 105, 107 and 108.)
- Nagel, J. R., Warnick, K. F., Jeffs, B. D., Fisher, J. R., & Bradley, R. 2007, *Radio Science*, 42, RS6013 (Cited on page 116.)
- Ng, C., Champion, D. J., Bailes, M., et al. 2015, *MNRAS*, 450, 2922 (Cited on pages 35 and 58.)
- Ng, C.-Y., & Kaspi, V. M. 2011, in *American Institute of Physics Conference Series*, Vol. 1379, *American Institute of Physics Conference Series*, ed. E. Göğüş, T. Belloni, & Ü. Ertan, 60–69 (Cited on page 13.)
- Noutsos, A., Johnston, S., Kramer, M., & Karastergiou, A. 2008, *MNRAS*, 386, 1881 (Cited on page 22.)
- Olausen, S. A., & Kaspi, V. M. 2014, *ApJS*, 212, 6 (Cited on pages 12, 76, 84 and 88.)
- Oppenheimer, J. R., & Volkoff, G. M. 1939, *Phys. Rev.*, 55, 374 (Cited on page 4.)
- Ostriker, J. P., & Tassoul, J.-L. 1968, *Nature*, 219, 577 (Cited on page 3.)
- Pacini, F. 1967, *Nature*, 216, 567 (Cited on page 5.)

- Pacini, F., & Salpeter, E. E. 1968, *Nature*, 218, 733 (Cited on page 4.)
- Pan, Z., Hobbs, G., Li, D., et al. 2016, *MNRAS*, 459, L26 (Cited on page 72.)
- Papitto, A., Ferrigno, C., Bozzo, E., et al. 2013, *Nature*, 501, 517 (Cited on page 24.)
- Peñalver, J. 2012, Antenna Technical Works, Tech. rep., IRAM (Cited on pages 49, 78 and 89.)
- Pennucci, T. T., Possenti, A., Esposito, P., et al. 2015, *ApJ*, 808, 81 (Cited on page 91.)
- Petrova, S. A. 2006, *Chinese Journal of Astronomy and Astrophysics Supplement*, 6, 113 (Cited on page 109.)
- Pfahl, E., & Loeb, A. 2004, *ApJ*, 615, 253 (Cited on page 52.)
- Pfuhl, O., Alexander, T., Gillessen, S., et al. 2014, *ApJ*, 782, 101 (Cited on page 52.)
- Portegies Zwart, S., van den Heuvel, E. P. J., van Leeuwen, J., & Nelemans, G. 2011, *ApJ*, 734, 55 (Cited on page 24.)
- Psaltis, D., Wex, N., & Kramer, M. 2016, *ApJ*, 818, 121 (Cited on pages 23 and 52.)
- Radhakrishnan, V., & Cooke, D. J. 1969, *Astrophys. Lett.*, 3, 225 (Cited on page 8.)
- Rankin, J. M. 1983, *ApJ*, 274, 359 (Cited on pages 14 and 101.)
- . 1990, *ApJ*, 352, 247 (Cited on pages 14 and 101.)
- Ransom, S. M. 2001, PhD thesis, Harvard University (Cited on page 57.)
- Ransom, S. M., Cordes, J. M., & Eikenberry, S. S. 2003, *ApJ*, 589, 911 (Cited on pages 35 and 58.)
- Ransom, S. M., Eikenberry, S. S., & Middleditch, J. 2002, *AJ*, 124, 1788 (Cited on pages 35 and 58.)
- Ransom, S. M., Ray, P. S., Camilo, F., et al. 2011, *ApJ*, 727, L16 (Cited on page 124.)
- Ransom, S. M., Stairs, I. H., Archibald, A. M., et al. 2014, *Nature*, 505, 520 (Cited on pages 11 and 24.)
- Rea, N., Viganò, D., Israel, G. L., Pons, J. A., & Torres, D. F. 2014, *ApJ*, 781, L17 (Cited on page 13.)
- Rea, N., McLaughlin, M. A., Gaensler, B. M., et al. 2009, *ApJ*, 703, L41 (Cited on page 12.)
- Rea, N., Esposito, P., Pons, J. A., et al. 2013a, *ApJ*, 775, L34 (Cited on page 13.)
- Rea, N., Esposito, P., Israel, G. L., et al. 2013b, *The Astronomer's Telegram*, 5032, 1 (Cited on pages 54 and 76.)

- Rea, N., Israel, G. L., Pons, J. A., et al. 2013c, *ApJ*, 770, 65 (Cited on page 13.)
- Richards, D. W., & Comella, J. M. 1969, *Nature*, 222, 551 (Cited on page 3.)
- Ruderman, M. A., & Sutherland, P. G. 1975, *ApJ*, 196, 51 (Cited on page 14.)
- Ryle, M. 1952, *Proceedings of the Royal Society of London Series A*, 211, 351 (Cited on page 116.)
- Ryle, M., & Hewish, A. 1960, *MNRAS*, 120, 220 (Cited on page 116.)
- Saslaw, W. C., Faulkner, J., & Strittmatter, P. A. 1968, *Nature*, 217, 1222 (Cited on page 3.)
- Scheuer, P. A. G. 1968, *Nature*, 218, 920 (Cited on page 19.)
- Schnitzeler, D. H. F. M., Eatough, R. P., Ferrière, K., et al. 2016, *MNRAS*, 459, 3005 (Cited on page 52.)
- Sesana, A., Vecchio, A., & Colacino, C. N. 2008, *MNRAS*, 390, 192 (Cited on page 23.)
- Shannon, R. M., & Johnston, S. 2013, *MNRAS*, 435, L29 (Cited on pages 13, 52, 54, 76 and 88.)
- Shaw, R. D., & Hay, S. G. 2015, in 2015 9th European Conference on Antennas and Propagation (EuCAP), 1–4 (Cited on page 121.)
- Shaw, R. D., Hay, S. G., & Ranga, Y. 2012, in *Electromagnetics in Advanced Applications (ICEAA)*, 2012 International Conference on, 438–441 (Cited on page 121.)
- Sigurdsson, S., Richer, H. B., Hansen, B. M., Stairs, I. H., & Thorsett, S. E. 2003, *Science*, 301, 193 (Cited on page 11.)
- Smith, F. G. 1977, *Pulsars* (Cited on pages 16 and 101.)
- Spitler, L. G., Lee, K. J., Eatough, R. P., et al. 2014, *ApJ*, 780, L3 (Cited on pages 53, 57, 69, 71, 72, 76 and 88.)
- Staelin, D. H., & Reifenstein, III, E. C. 1968, *Science*, 162, 1481 (Cited on page 4.)
- Stappers, B. W., Archibald, A. M., Hessels, J. W. T., et al. 2014, *ApJ*, 790, 39 (Cited on page 24.)
- Stovall, K., Ray, P. S., Blythe, J., et al. 2015, *ApJ*, 808, 156 (Cited on pages 105 and 107.)
- Sturrock, P. A. 1971, *ApJ*, 164, 529 (Cited on page 14.)
- Taylor, J. H., & Cordes, J. M. 1993, *ApJ*, 411, 674 (Cited on page 18.)
- Taylor, J. H., & Weisberg, J. M. 1982, *ApJ*, 253, 908 (Cited on pages 22 and 23.)

- Thompson, C., & Duncan, R. C. 1995, *MNRAS*, 275, 255 (Cited on pages 13, 76, 84 and 88.)
- . 1996, *ApJ*, 473, 322 (Cited on pages 76 and 88.)
- Thorne, K. S., & Ipser, J. R. 1968, *ApJ*, 152, L71 (Cited on page 3.)
- Tolman, R. C. 1939, *Phys. Rev.*, 55, 364 (Cited on page 4.)
- Torne, P. 2013, Effelsberg RFI tests on Checkerboard Phased Array Element, Tech. rep. (Cited on pages 111, 119, 121 and 122.)
- Torne, P., Desvignes, G., Eatough, Paubert, G., et al. in prep., *MNRAS* (Cited on page 109.)
- Torne, P., Eatough, R. P., Karuppusamy, R., Kramer, M., & Klein, B. in prep., *MNRAS* (Cited on page 134.)
- Torne, P., Knittel, G., & Wieching, G. 2013, CSIRO Phased Array Feed (PAF) for Effelsberg, Tech. rep. (Cited on page 111.)
- Torne, P., & Winkel, B. 2014, UBB Calibration Memo - SEFD calculations, Tech. rep. (Cited on pages 111 and 125.)
- Torne, P., Eatough, R. P., Karuppusamy, R., et al. 2015, *MNRAS*, 451, L50 (Cited on pages 87, 88, 89, 91, 93 and 97.)
- Turolla, R., Zane, S., & Watts, A. L. 2015, *Reports on Progress in Physics*, 78, 116901 (Cited on page 12.)
- van Cappellen, W. A., Bakker, L., & Oosterloo, T. A. 2011, in *General Assembly and Scientific Symposium, 2011 XXXth URSI*, 1–4 (Cited on page 116.)
- Veidt, B., Hovey, G. J., Burgess, T., et al. 2011, *IEEE Transactions on Antennas and Propagation*, 59, 2047 (Cited on page 116.)
- Warnick, K. F., Jeffs, B. D., Landon, J., et al. 2009, in *Antenna Technology and Applied Electromagnetics and the Canadian Radio Science Meeting, 2009. ANTEM/URSI 2009. 13th International Symposium on*, 1–4 (Cited on page 116.)
- Warnick, K. F., Maaskant, R., Ivashina, M. V., Davidson, D. B., & Jeffs, B. D. 2016, *Proceedings of the IEEE*, 104, 607 (Cited on page 116.)
- Warnick, K. F., Waldron, J., Landon, J., et al. 2007, in *Antennas and Propagation, 2007. EuCAP 2007. The Second European Conference on*, 1–5 (Cited on page 116.)
- Weatherall, J. C. 1998, *ApJ*, 506, 341 (Cited on page 109.)
- Weltevrede, P., Stappers, B. W., Rankin, J. M., & Wright, G. A. E. 2006, *ApJ*, 645, L149 (Cited on page 12.)

- Wex, N., & Kopeikin, S. M. 1999, *ApJ*, 514, 388 (Cited on pages 23 and 52.)
- Wharton, R. S., Chatterjee, S., Cordes, J. M., Deneva, J. S., & Lazio, T. J. W. 2012, *ApJ*, 753, 108 (Cited on pages 52 and 69.)
- Wielebinski, R., Jessner, A., Kramer, M., & Gil, J. A. 1993, *A&A*, 272, L13 (Cited on pages 15, 88, 93, 100 and 102.)
- Will, C. 2001, *Living Reviews in Relativity*, 4, gr-qc/0103036 (Cited on page 22.)
- Wilson, T. L., Rohlf, K., & Hüttemeister, S. 2013, *Tools of Radio Astronomy*, doi:10.1007/978-3-642-39950-3 (Cited on pages 17, 64, 112 and 113.)
- Wu, J., Torne, P., & et al. in prep., *MNRAS* (Cited on page 124.)
- Xilouris, K. M., Kramer, M., Jessner, A., Wielebinski, R., & Timofeev, M. 1996, *A&A*, 309, 481 (Cited on pages 76, 97, 100 and 105.)
- Zhelezniakov, V. V., & Shaposhnikov, V. E. 1979, *Australian Journal of Physics*, 32, 49 (Cited on page 14.)
- Zhu, W. W., Berndsen, A., Madsen, E. C., et al. 2014, *ApJ*, 781, 117 (Cited on pages 37 and 66.)

Acknowledgements

This thesis would not have been possible without the help and support of many people, to whom I would like to express my gratitude in the following lines.

First of all, I am mostly indebted to *Prof. Dr. Michael Kramer*. He gave me the opportunity to carry out a PhD in the topics of my major interests, guiding me but at the same time giving me the freedom and time to explore the ideas that intrigued me the most. I deeply appreciate his efforts to be available for discussions and always find the time to answer my questions and e-mails about any topic.

I am grateful to *Prof. Dr. Frank Bertoldi* for co-supervising this thesis, even knowing the difficulties and risks that a thesis with so much instrumentation load could have. He always made sure to keep the science in the main focus of the thesis, which was certainly helpful, specially in the first two years where the technical works were perhaps absorbing too much of the available PhD time.

I also thank *David Champion*, that gladly accepted the challenge of being my advisor. His advices and ideas have been invaluable for the completion of this work.

I do not forget my initial advisors *Reinhard Keller* and *Olaf Wucknitz*. It was a pity that the Phased Array Feed for Effelsberg got delayed and we could not make this unique receiver see its first light in Germany during this thesis work.

I thank *Benjamin Winkel* for his willingness to help me any time, and for showing me the use of Python to process FITS files and how the calibration of broad-bandwidth radio data is (properly) done. My thanks to *Peter Müller* for nicely providing the custom code that I needed to record high-quality RFI data at Effelsberg.

I want to thank *Gundolf Wieching* and *Christoph Kasemann* for answering all my questions during the technical works. I learnt much from them about state-of-the-art radio receivers and the management of such challenging projects.

I want to express my gratitude to *Andre Gunst* for inviting me to ASTRON to learn from their expertise with PAFs, and to *Graeme Carrad* for organizing my short stay at CASS/ATNF. Both visits were certainly key to identify the main challenges that this new technology imposes when applied to radio telescopes. I also appreciate the kindness sharing with me their great knowledge about PAFs of *Arnold van Ardenne*, *Marina Ivashina*, *Stefan Wijnholds*, *Brian Jeffs*, *John Ford*, *Douglas Hayman*, *Ron Beresford*, *Aidan Hotan*, and *Andrew Brown*.

All the *staff at Effelsberg* should be recognised for making of the observatory such a lovely place and, more importantly, for making the telescope so easy to use. I would like to particularly thank *Alex Kraus* for his excellent job scheduling the simultaneous observations with other telescopes, sometimes with a short notice. For the observations from other observatories, I have to thank the *staff at APEX*, and in particular *Bernd Klein* for his help in the most ambitious observations of pulsars done in this thesis. The *staff of the 30-m telescope at Pico Veleta* were of vital importance for the success of this PhD, in particular *Gabriel Paubert* for his amazing job making the BBC a powerful pulsar instrument even when not initially designed for that purpose, and

Carsten Kramer for his input during the calibration of the data.

My gratitude goes also to all the *colleagues of the Fundi group* for being so open and always available to help or answer questions, plus for the most bizarre conversations during the coffee breaks. I want to particularly mention *Ramesh Karuppusamy* for teaching me the details about the functioning of pulsar backends, *Norbert Wex* for his explanations of the fascinating effects of extreme regimes of Gravity, *Laura Spitler* for her collaboration in the magnetar and single pulse works, and *Paulo Freire* for his interesting explanations about literally anything. *Ralph Eatough* and *Gregory Desvignes* deserve their own acknowledgement as well. They have been invaluable collaborators in the projects that led to the main scientific contribution of this thesis, and kindly proofread parts of the dissertation. Without them things would have been much more difficult for me. Thank you very much for your help and patience guys.

I also benefited much from discussions with *Axel Jessner*. His knowledge and explanations about pulsar emission mechanisms were certainly helpful. During their visits to Bonn, I also had the great opportunity to query *Don Melrose* about pulsar emission, and to discuss the effects of scattering and scintillation on pulsar emission with *Jim Cordes*. I appreciate much their explanations.

The IT department (*rz-support*) of the MPIfR, and in special *Jan Behrend*, deserves a recognition for their efficiency solving computer and network issues. They allowed me to focus on my research, not having to worry at all about any computer-related problem. Furthermore, Jan's replies (and solutions) would never take more than a few minutes. Thank you Jan also for showing me the fantastic Linux commands "screen" and "sshfs".

I must acknowledge our former secretary *Gabi Breuer* for taking care of most the administrative obligations when I arrived to Bonn. I am as well very grateful to our secretary *Kira Kühn* for her continuous help with all kind of administrative requirements. I also want to thank *Simone Pott* for being so nice and helpful during the application process to the IMPRS, and to the IMPRS former and current coordinators, *Manolis Angelakis* and *Rainer Mauersberger*.

A particular big thank goes to all the other students that have put up with me on a daily-basis during all this time. I want to specially thank my two-time officemates *Ewan Barr* and *Patrick Lazarus* for many discussion on how to search for pulsars, and for answering my many questions about the details of the searching software. It was quite nice to share offices with so many people during these years, in particular in the large office of the basement (that I liked much). Thanks to *David Mulcahy*, *René Gissuebel*, *Jana Koehler*, *Charlotte Sobey*, *John Antoniadis*, *Lijing Shao*, *Marina Bereniza*, *Philip Schmidt*, *Alice Pasetto*, *Carolina Mora*, *Ancor Damas*, *Nicolas Caballero*, *Joey Martinez*, *Leon Houben*, *Andrew Cameron*, *Nataliya Porayko*, *Jason Wu*, *Alessandro Ridolfi*, and *Eleni Graikou*, for never allowing the atmosphere to get too boring. I enjoyed much our lunch conversations about any topic, in particular contrasting how the different nationalities and cultures analyse and confront different ideas.

One of my most special thanks goes to *Cherry Ng* for many reasons, but in particular for showing me how my priorities can drastically change when you meet the right person. These years in Bonn would simply not have been the same without her.

I cannot finish these acknowledgements without giving thanks to *Antxon Alberdi* for advising me to come to the MPIfR in Bonn, and mentioning to me the name of Michael Kramer for the first time.

My family, and in particular *my parents Mercedes and Pablo and my sister Mercedes*, deserve a large part of the credit for this thesis. They always supported me when I pursue my dreams, and I know that it has not been easy for them to see me leave Spain for such a long time. This thesis would have been impossible without their love and help.

Finally, thank you to all the curious people that keep asking questions without answers. This is essentially what drives research and the fundamental reason why this thesis exists.

Erklärung

Ich versichere, dass ich die von mir vorgelegte Dissertation selbständig angefertigt, die benutzten Quellen und Hilfsmittel vollständig angegeben und die Stellen der Arbeit – einschließlich Tabellen, Karten und Abbildungen –, die anderen Werken im Wortlaut oder dem Sinn nach entnommen sind, in jedem Einzelfall als Entlehnung kenntlich gemacht habe; dass diese Dissertation noch keiner anderen Fakultät oder Universität zur Prüfung vorgelegen hat; dass sie noch nicht veröffentlicht worden ist sowie, da ich eine solche Veröffentlichung vor Abschluss des Promotionsverfahrens nicht vornehmen werde. Die Bestimmungen dieser Promotionsordnung sind mir bekannt. Die von mir vorgelegte Dissertation ist von Prof. Dr. Michael Kramer betreut worden.

Unterschrift: Pablo Torne Torres

Datum: 08.09.2016

Curriculum Vitae

Personal data

Name: Pablo Torne Torres
Place of birth: Granada, Spain

Education

from May 2012 PhD candidate at the Max Planck Institute for Radio Astronomy with dissertation in the subject of Astronomy about *Exploring Radio Pulsars with New Technologies*

2010-2012 Master's degree in Physics and Mathematics: specialization in Astronomy and Astrophysics at the University of Granada, with completion of master thesis entitled *Implementation of Classical Methods of Magnetic Field Measurements in a FPGA*

2003-2010 Superior degree in Telecommunication Engineering at the University of Granada with engineering thesis about the *Design and Implementation of a IEEE 802.15.4 Low Power Wireless Sensor Network Node Control*

2008-2009 Two semesters of Elektrotechnik und Informationstechnik at the Universität Stuttgart as part of the Erasmus student exchange programme

2001-2003 Bachillerato at Mulhacen School, Granada (Spain)

1997-2001 Secondary education at Mulhacen School, Granada (Spain)

Teaching experience

Feb 2013 - Feb 2015 Tutor of the Advanced Radio Lab Course at the Argelander-Institut für Astronomie of the University of Bonn

Professional experience

from May 2012 Scientist at Max Planck Institute for Radio Astronomy

Mar. 2011 - Jan. 2012 Research engineer at Instituto de Astrofísica de Andalucía

Nov. 2009 - May 2010 (Internship) Product manager assistant at Airbus Defence & Space

Dec. 2008 - June 2009 IT developer in innovation project for the University of Granada

Publications

Refereed

Ridolfi A., Freire P. C. C., **Torne, P.**, Heinke C. O., van den Berg M., Jordan C., Kramer M., Bassa C. G., Sarkissian J., D'Amico N., Lorimer D., Camilo F., Manchester R. N., Lyne A., “*Long-term observations of the pulsars in 47 Tucanae - I. A study of four elusive binary systems*”, Monthly Notices of the Royal Astronomical Society, Volume 462, Issue 3, p.2918-2933 (2016)

Clark C. J., Pletsch H. J., Wu J., Guillemot L., Ackermann M., Allen B., de Angelis A., Aulbert C., Baldini L., Ballet J., Barbiellini G., Bastieri D., Bellazzini R., Bissaldi E., Bock O., Bonino R., Bottacini E., Brandt T. J., Bregeon J., Bruel P., and 99 authors including **Torne P.**, “*PSR J1906+0722: An Elusive Gamma-Ray Pulsar*”, The Astrophysical Journal Letters, Volume 809, Issue 1, article id. L2, 8 pp. (2015)

Torne P., Eatough R. P., Karuppusamy R., Kramer M., Paubert G., Klein B., Desvignes G., Champion D. J., Wiesemeyer H., Kramer C., Spitler L. G., Thum C., Güsten R., Schuster K. F., Cognard I., “*Simultaneous multifrequency radio observations of the Galactic Centre magnetar SGR J1745-2900*”. Monthly Notices of the Royal Astronomical Society: Letters, Volume 451, Issue 1, p.L50-L54 (2015)

Proceedings

Goddi C., Falcke H., Kramer M., Rezzolla L., Brinkerink C., Bronzwaer T., Deane R., De Laurentis M., Desvignes G., Davelaar J. R. J., Eisenhauer F., Eatough R., Fraga-Encinas R., Fromm C. M., Gillessen S., Grenzbach A., Issaoun S., Janßen M., Konoplya R., Krichbaum T. P., Laing R., Liu K., Lu R.-S., Mizuno Y., Moscibrodzka M., and 14 authors including **Torne P.**, *BlackHoleCam: fundamental physics of the Galactic center* to be published in the International Journal of Modern Physics D (IJMPD), & Proceedings of the Fourteenth Marcel Grossman Meeting on General Relativity edited by Massimo Bianchi, Robert Jantzen, Remo Ruffini, (2016)

Keane, E. F., Bhattacharyya, B., Kramer, M., Stappers, B. W., Bates, S. D., Burgay, M., Chatterjee, S., Champion, D. J., Eatough, R. P., Hessels, J. W. T., Janssen, G., Lee, K. J., van Leeuwen, J., Margueron, J., Oertel, M., Possenti, A., Ransom, S., Theureau, G., **Torne, P.**, “*A Cosmic Census of Radio Pulsars with the SKA*” in Proceedings of Advancing Astrophysics with the Square Kilometre Array (2015).

Antoniadis J., Guillemot L., Possenti A., Bogdanov S., Gelfand J., Kramer M., Mignani R., Stappers B., **Torne P.**, “*Multi-wavelength, Multi-Messenger Pulsar Science in the SKA Era*” in Proceedings of Advancing Astrophysics with the Square Kilometre Array (2015).

Technical reports

Torne P., Winkel B, *UBB Calibration Memo - SEFD calculations*, MPIfR Internal technical report (2014)

Torne P., *Effelsberg RFI tests on Checkerboard Phased Array Element*, MPIfR Internal technical report (2013)

Torne P., Knittel G, Wieching G., *CSIRO Phased Array Feed (PAF) for Effelsberg*, MPIfR Internal technical report (2013)

Submitted

Torne P., Desvignes G., Eatough R. P., Karuppusamy R., Paubert G., Kramer M., Cognard I., Champion D. J., Spitler L. G., “*Detection of the magnetar SGR J1745–2900 up to 291 GHz with evidence of polarized millimetre emission*”. Monthly Notices of the Royal Astronomical Society, *submitted*

In preparation

Torne P., Eatough R. P., Karuppusamy R., Kramer M., Klein B., “*Searching for pulsar binaries in the Galactic Centre with the Effelsberg 100-m radio telescope*”. To be submitted to Monthly Notices of the Royal Astronomical Society, 2016.

Torne P., Desvignes G, Eatough R. P., Paubert G., Karuppusamy R., Kramer M., “*Pulsar observations and 3 and 2 mm*”. To be submitted to Monthly Notices of the Royal Astronomical Society, 2016.

Oral & Poster contributions

“Probing the Galactic Centre and its Supermassive Black Hole”

Torne P., on behalf of the Fundamental Physics in Radio Astronomy Group

Oral contribution

MPIfR Fachbeirat, Bonn, Germany (2016)

“Observations of Pulsars up to 472 GHz”

Torne P., Desvignes G., Eatough R. P., Karuppusamy R., Klein B., Kramer M.

Poster contribution

MPIfR Fachbeirat, Bonn, Germany (2016)

“Pulsars in Globular Clusters”

Ridolfi A., Freire P, Kramer M., **Torne P.**, Desvignes G.

Poster contribution

MPIfR Fachbeirat, Bonn, Germany (2016)

“Pulsed Emission at Millimetre Wavelengths”

Torne P., Desvignes G., Eatough R. P., Karuppusamy R., Liu K., Wex N., Kramer M.

Oral contribution

BlackHoleCam F2F Meeting, Bonn, Germany (2016)

“Pulsar Observations at Millimetre Wavelengths”

Torne P., Desvignes G., Paubert G., Kramer M.

Oral contribution

Pulsars in the Galactic Centre, Bonn, Germany (2016)

“Observing Pulsars at Millimetre Wavelengths”

Torne P., Desvignes G., Eatough R. P., Klein B., Kramer M.

Oral contribution

9th Neutron Star Workshop, Bonn (2016)

“Searching for pulsar-black hole systems in the Galactic Centre”

Torne P., Eatough R. P.

Oral contribution

MPIfR Lunch Colloquium, Bonn, Germany (2015)

“Applications and Challenges of Multi-frequency and Millimetre Pulsar Observations”

Torne P., Desvignes G., Eatough R. P., Kramer M.

Oral contribution

4th RadioNet/ERATec Technical Forum Workshop, Florence, Italy (2015)

Oral & Poster contributions (cont.)

“The magnetar SGR 1745–2900, an unexpected (very welcomed) guest”

Torne P., Desvignes G., Eatough R. P., Spitler L. G., Karuppusamy R., Liu K., Wex N., Falcke H., Kramer M.

Oral contribution

BlackHoleCam Plenary Meeting, Bonn, Germany (2015)

“The seek for pulsars in the Galactic Centre”

Torne P.

Oral contribution (Invited)

IAA Seminar, Granada, Spain (2015)

“Searching and Timing of Pulsars in the Globular Cluster M15”

Ridolfi A., Freire P, Kramer M., **Torne P.**

Poster contribution

XXVI Winter School of Astrophysics, Tenerife, Spain (2014)

“A new, large Field-of-View receiver for the Effelsberg 100-m”

Torne P., and the Fundamental Physics Group

Poster contribution

Royal Astronomical Society Meeting, London, U.K. (2014)

“High-frequency Radio Observations of the Galactic Centre Magnetar”

Torne P., Desvignes G., Eatough R. P., Klein B., Kramer M.

Oral contribution

6th Neutron Star Workshop, Bonn, Germany (2014)

“SKA technology for Effelsberg”

Torne P., and the Fundamental Physics Group

Poster contribution

Arecibo Single Dish Summer School, Arecibo, Puerto Rico (2013)

“Looking for pulsars with new receivers”

Torne P.

Oral contribution

IMPRS Monday Seminar, Bonn, Germany (2013)

“Detection Systems for Low-Frequency Radiation”

Torne P.

Oral contribution

IMPRS Annual Retreat, Bremen, Germany (2013)

Oral & Poster contributions (cont.)

“RFI Effects on Phased Array Feeds for Radio Astronomy”

Torne P.

Oral contribution

1th RadioNet/ERATec Technical Forum Workshop, Bonn, Germany (2013)

“Biography of Physics Nobel Prize Winners: Pieter Zeeman”

Torne P.

Oral contribution

IMPRS Retreat, Hirscheeg, Kleinwalsertal, Austria (2012)

“Focal Plane Array for the Effelsberg 100-m radio telescope”

Torne P., Kramer M, Keller K.

Poster contribution

CASPER Workshop, Green Bank Observatory, West Virginia, U.S.A. (2012)

“SKA technology for the Effelsberg 100-m”

Torne P., Kramer M, Keller K.

Oral contribution

IMPRS Monday Seminar, Bonn, Germany (2012)